^{36}Cl analysis of bedrock fault scarps in central Italy and western Turkey

Huw Goodall

Submitted in accordance with the requirements for the degree of
Doctor of Philosophy

The University of Leeds
School of Earth and Environment

September 2020

Declaration

The candidate confirms that the work submitted is her own, except where work which has formed part of jointly authored publications has been included. The contribution of the candidate and the other authors to this work has been explicitly indicated below. The candidate confirms that appropriate credit has been given within the thesis where reference has been made to the work of others.

The work in Chapter 4 of this thesis is a manuscript to be submitted to Tectonics Huw J. Goodall, Laura C. Gregory, Richard P. Shanks, Luke N.J. Wedmore, Ken McCaffrey, Ruth M.J. Amey, Gerald P. Roberts, Richard J. Phillips, Andrew Hooper. Determining reliable cosmogenic slip histories on bedrock normal faults.

The idea for this paper was developed by myself and the co-authors, and methodology was developed by myself and Laura Gregory. I collected samples from sites CF2, CF3 and RP2, and co-authors provided samples from sites CF1 and RP1. I processed samples from CF1 and RP1 before starting my PhD, and I processed the other samples during my PhD. Richard Shanks made the AMS measurements, Stephen Reid at the University of Leeds made the ICP-OES measurements. Some terrestrial laser scans were collected by myself and co-authors during fieldwork in Italy, and some scans were provided by the other co-authors. I processed the results, wrote and produced all figures for the manuscript, which was improved by suggestions and comments from all co-authors and my supervisors, Greg Houseman, Tim Wright and Richard Walters.

Copyright © 2020 The University of Leeds and Huw Goodall. The right of Huw Goodall to be identified as Author of this work has been asserted by her in accordance with the Copyright, Designs and Patents Act 1988.

Acknowledgements

For someone reading this at the start of their PhD, I want you to know two things. Firstly staying happy is the most important thing! Secondly, nothing goes to plan. Military coups, earthquakes, spiky bushes and a pandemic messed up my PhD plans. Something will mess up yours, but dont worry about it, and dont forget that life goes on outside of work! Some bits are really grim, but I have had some unique, amazing experiences that I wouldnt have had anywhere else.

Whilst this thesis only has my name on the front, this work could not have been completed without the help and support of many others, who I will try and thank here. Sorry for any omissions! My primary supervisor Laura Gregory. No one could ask for a better supervisor. Incredibly helpful and encouraging, you have always had time for a chat and to hear my latest problem. You are understanding when I have made mistakes in the lab, enthusiastic when I have come to you with ideas, and a well of optimism when it seemed like I was never going to finish this thesis. It has been a pretty wild ride at times, and a good adventure, thanks for being a really fun, all round nice person to share it with, and giving me a chance to crush some rocks 5 years ago!

I also would like to thank my other supervisors: Greg Houseman, for many insightful conversations and sharing of ideas, Tim Wright, for helping me with some tricky (and not so tricky!) maths, and Rich Walters, for inspiration during intense rapid-fire catch ups.

My work has revolved around ideas and code developed by Patience Cowie. Whilst I sadly never had the opportunity to work with Patience, I have been following in her footsteps since I began my PhD, and I would like to thank her for the incredible body of work she produced. I would also like to thank Leo Zijerveld who worked with Patience to develop the code my thesis is based on.

My first field work was particularly memorable given the M_w6 earthquake which woke me up one morning, and Id like to thank the team for looking out for me. Thanks to Laura, Max Wilkinson, and Luke Wedmore, who was a final year PhD student at the time, and provided me with a role model for the kind of scientist I hoped to be by the time I got to fourth year, as well as teaching me how to create and analyse TLS data.

My work in Turkey would have been impossible without the assistance of Hasan

Sozbilir and his research group at Dokuz Eylül University, with particular thanks to Bora Uzel, Okmen Sumer, Mustafa Softa, Elif Çakir and Irem Avcu and their families, who introduced me to the many delights of Turkey (Köfte!) and made my research easier with their expansive knowledge of Geology. You all made me feel at home and proved to be a very handy team of diggers and negotiators.

Ken McCaffrey provided invaluable help with the TLS and GNSS data, and Katie Farrell and Tim Craig provided enthusiastic field support. I would like to thank John Elliott for his continuous 'support' both in the field and at every opportunity.

I would also like to thank Franco, his team and the local people of Italy, as well as the local people of western Turkey, for allowing me to work on their land, and their generous hospitality at every turn. Thanks to Shasta Marrero for helping me hack her CRONUScalc, Silke Mechernich for the encouragement, data, and discussions about ^{36}Cl since before I started my PhD, and Richard Shanks and the team at SUERC, for making the AMS measurements that my work is based on, and giving me the tour. Thanks to Gerald Roberts for providing some of the Italy data, and along with Andy Hooper, helping prepare my Italy paper. Jonathan Weiss was both a charming, calming influence and provided good conversations and ideas about western Turkish geodesy.

One of the most helpful people I met during my PhD is Richard Rigby. He is an all-powerful computer wizard disguised as the nicest man you could possibly meet. Thanks for always having time and solving countless random IT issues, always with a smile. Id like to apologise to Harri Williams, for using that bloody tile cutter for days on end in his lab, and thank him for always having a minute to chat and help whenever needed. Stephen Burgess and Antony Windross always managed to get me out of a fix, and the two Andys (Conolly and Hobson) helped me undo any unplanned experiments I undertook in the clean lab. Thanks to Stephen Reid for putting up with our fuss and measuring our ICP-OES samples.

My fellow PhD students have been an enormous source of help, without them I would still be trying to work out GMT, matlab, inverse theory, python, where I get a pen from. the list is endless! My co-residents of 8.153, particularly the ones who were there from the start: Lin Shen, Pawan Piromthong, Jeanne Giniaux and Matt Gaddes. Thanks to the first three for showing me what hard work really looks like, and Matt, for reminding me that life isnt all about work (though you have to still do it!). Thanks to the ever evolving lunch bunch (particularly regulars Tingleby , Ass. Prof. Harnett, and Meme Dr. Ben Todd), bake-off crew (sorry about the rice crispy buns), and beers regulars (shout out to Dinko for his long standing dedication there). The COMET community has been great to be a part of, Ive enjoyed every meeting, including the late nights (thanks to Austin Elliott for those!).

Without the help of my family, Id never have got close to where I am today, thanks to my parents for their support (good effort in reading the paper Dad!), Im not even going to list the things you have done for me, I bet I dont even know half of them. I

will try and be a better brother now Imo, now that I have a bit more free time!

My long suffering partner Ruth. I dont really know where to start, so just to give anyone reading an idea of how awesome she has been, not only has she been an incredible supportive partner with all that entails, but she came on field work to Italy and dug holes in the blazing sun, co-authored a paper with me, helped me debug code, and kept me sane and happy whilst locked in a house with me for 6 months whilst doing more than her fair share so that I could focus on getting this thesis done. Thanks Ruth!

(I told you there were many others!)

Contents

List of Figures

List of Tables

Chapter 1

Introduction

"The beginning of knowledge is the discovery of something we do not understand"
Frank Herbert

1.1 Background

1.1.1 Motivation

Earthquakes have been a problem for humanity for millennia (*Ambraseys*, 2009), they can cause incredible devastation in a matter of seconds, producing many casualties. With world population increasing, a greater number people are now living in areas that are prone to large earthquakes. The location of potential earthquake sources is generally well known around plate boundaries, however earthquake sources in interior continental settings are often less well defined. These earthquakes occurring in continental settings are responsible for a greater number of deaths than their plate boundary counterparts (*England and Jackson*, 2011). Understanding how earthquakes occur and where they are likely to occur is key in reducing the hazard they pose to affected populations. Due to the often long time periods (commonly hundreds or thousands of years) between large earthquakes on a single fault, reliable observations of how continental faults behave over multiple earthquake cycles are difficult to make. Whilst the historical record can assist with this, the details of the observation and pinpointing which exact fault ruptured in an historical earthquake can be difficult if not impossible. The geometry, slip and growth of faults and fault networks can be observed on million year time scales using seismic reflection data, at relatively low spatial and temporal resolution. We also have good records during the last 50-100 years, with seismology, field mapping of modern ruptures and remote sensing data allowing us to observe how faults have moved over the last century or so, as well as further illuminating their geometries. This thesis will focus on demonstrating the reliability of ^{36}Cl dating of limestone bedrock normal faults, and the information we can gain by using this method to bridge this spatial and temporal

gap in our understanding of normal fault behaviour over millennial timescales.

1.1.2 Lithospheric extension

Many areas of the continental lithosphere are extending and these extending regions can produce large deadly earthquakes on normal faults (*Middleton et al.*, 2016, *Ward and Valensise*, 1989, *Walters et al.*, 2009). The lithosphere can deform in a brittle or a ductile manner and which mode of deformation occurs is a function of temperature, stress, composition and pore fluid pressure. The top 10-20 km typically deforms in a brittle manner potentially causing earthquakes, with ductile deformation occurring at greater depths (*Jackson*, 2001). The exact depth of the base of the seismogenic zone varies through the lithosphere due to the changes in lithology, heat flow and structural history (*Bürgmann and Dresen*, 2008). The rheology of the crust is not particularly well known as it cannot be directly observed. Experiments in rock mechanics, observations of exhumed lithosphere and fault zones, and geodetic observations have allowed indirect calculation of lithospheric rheology (*Bürgmann and Dresen*, 2008). The question of rheology is a 4 dimensional problem, in that the rheology will change both through 3d space and in time. There are three classic models of continental crustal rheology, which all assume there is strong horizontal layering of the rheology due to increasing pressure and temperature with depth, as well as compositional layering (1.1). The jelly sandwich model assumes a strong upper crust and upper mantle, with a weak lower crust (*Hirth and Kohlstedt*, 2003), the crème bûlée model proposes that the lithosphere is strong whilst the upper mantle is weak (*Jackson*, 2002), and the banana split model which proposes that activity along major fault zones is controlled by the rheology of these relatively weak zones rather than the bulk rheology of the lithosphere (*Bürgmann and Dresen*, 2008). The lateral heterogeneity in continental lithospheric strength is proposed to be caused primarily by variation in heat flow, which controls lithospheric thickness, and presence of pore fluids may vary and also have significant influence (*Vauchez et al.*, 1998).

The earthquake cycle was first described following observations of the 1906 earthquake in San Francisco (*Reid*, 1910). The proposed model is that on a locked (not slipping) fault, the continuing relative motion of blocks on either side of the fault builds up elastic strain in the medium surrounding the fault, aswell as stress on the fault over time until a threshold stress is met and an earthquake occurs, resulting in a drop in stress on the fault. This cycle then repeats. Due to increase in the availability of high precision long time period measurements, it is now known that there is commonly a third period in the cycle, where after the earthquake there is period (*Stein and Lisowski*, 1983, *Shen et al.*, 1994, *Li et al.*, 2018; Figure 1.2) of higher strain rates, known as the post-seismic period. Faults can also slip much more slowly, producing lower frequency seismic radiation in slow earthquakes (*Szeliga et al.*, 2004) or tremor (*Katsumata and Kamaya*, 2003), which typically have a longer timer period and cause

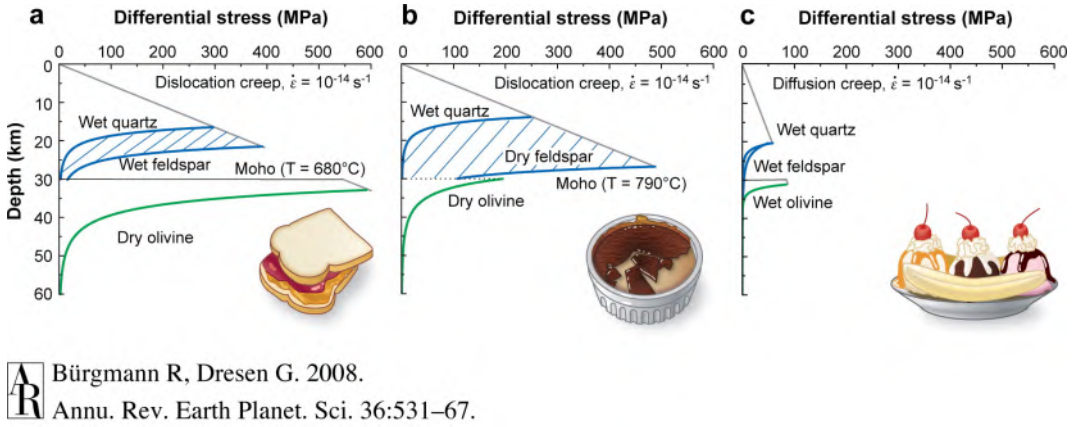

Bürgmann R, Dresen G. 2008.
Annu. Rev. Earth Planet. Sci. 36:531–67.

Figure 1.1: The three first order models of continental lithospheric rheology, from *Bürgmann and Dresen* (2008).

little damage to infrastructure. Faults can also creep, where they deform aseismically (*Cakir et al.*, 2005), and creep rates themselves can vary in time *Wei et al.* (2013), *Shirzaei and Bürgmann* (2013).

1.1.3 Surface faulting

How coseismic displacement is distributed on a fault at the Earth's surface is becoming increasingly well documented in the modern era, as the number and quality of detailed surface rupture studies increases (e.g. *Civico et al.*, 2018), and novel techniques such as LiDAR (*Nissen et al.*, 2014, *Wedmore et al.*, 2019), GNSS (*Wilkinson et al.*, 2017), InSAR and other remote sensing techniques are developed (*Simons et al.*, 2002, *Lindsey et al.*, 2015, *Walters et al.*, 2018, *Bao et al.*, 2019). Conceptual models of long term displacement on faults typically have simple geometric shapes, with either a uniform displacement along the length of the fault, or displacement at a maximum in the center of the fault (*Rotevatn et al.*, 2018), though real data typically show greater along strike variation over thousand to million year timescales (*Nicol et al.*, 2005; Figure 1.3). A meta-study of co-seismic earthquake surface displacement indicates ruptures are more commonly asymmetric than the symmetric model used for long term fault growth (*Wesnousky*, 2008). Measured surface displacements from single events also do not adhere to these smoothed models. They commonly show deviation from the conceptual models with multiple peaks and troughs in displacement (*Barka et al.*, 2002, *Haeussler et al.*, 2004, *Wesnousky*, 2008, *Walters et al.*, 2018, *Wedmore et al.*, 2019) (Figure 1.4). These complex displacement patterns are seen in geological (*McLeod et al.*, 2000) and geomorphic records of normal fault of displacement. On some faults, the similarity between coseismic displacement and geomorphic records of displacement accrued over multiple earthquake cycles indicates that areas of high coseismic surface fault slip align with areas of high geological time-scale slip over length-scales of a few km, and are therefore representative of long term slip processes at depth (*Brozzetti*

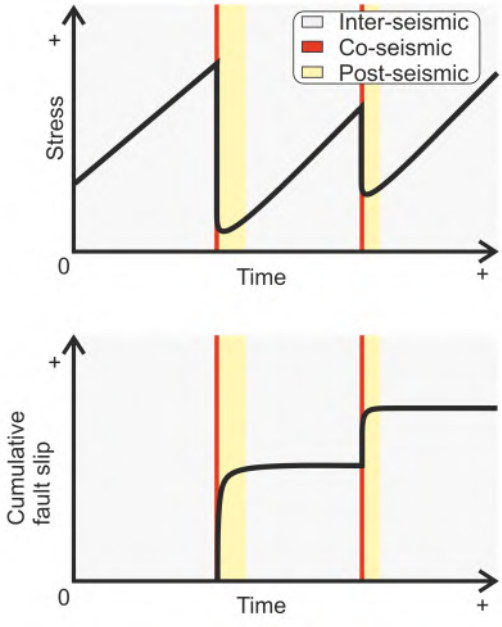

Figure 1.2: An idealised schematic of stress on a fault, and slip on a fault during the earthquake cycle.

et al., 2019). Shorter wavelength coseismic variations appear to average out over time, and are therefore variable between coseismic events and are effectively noise (*Walsh and Watterson*, 1987). To further complicate the situation, coseismic surface displacement commonly occurs on multiple discrete fault planes on structures both synthetic and antithetic to the main faults (*Barka et al.*, 2002, *Hamling et al.*, 2017, *Civico et al.*, 2018).

Deformation of the surface by earthquakes can dramatically affect landscapes. Surface ruptures can produce fault scarps, in the case of normal faults, this is where the hanging wall moves down relative to the footwall, exhuming the face of the fault plane. When these scarps form through relatively incompetent material the fresh face can degrade quickly (*Wallace*, 1980), but can leave long term markers on the landscape if they are large (Figure 1.5). If many events occur on the same fault they can produce large topographic effects over time, the nature of which is a function of lithology that is being uplifted (*Goldsworthy and Jackson*, 2000). Uplift of the softest lithologies, such as sediments, results in low relief, low angled badland topography as rivers rapidly incise the soft material. Harder lithologies produce a steeper topography, with flat iron features (*Goldsworthy and Jackson*, 2000). Limestone is one of the most competent lithologies, which typically produces relatively steep slopes and can sometimes preserve exposure of the fault plane itself (figure 1.6).

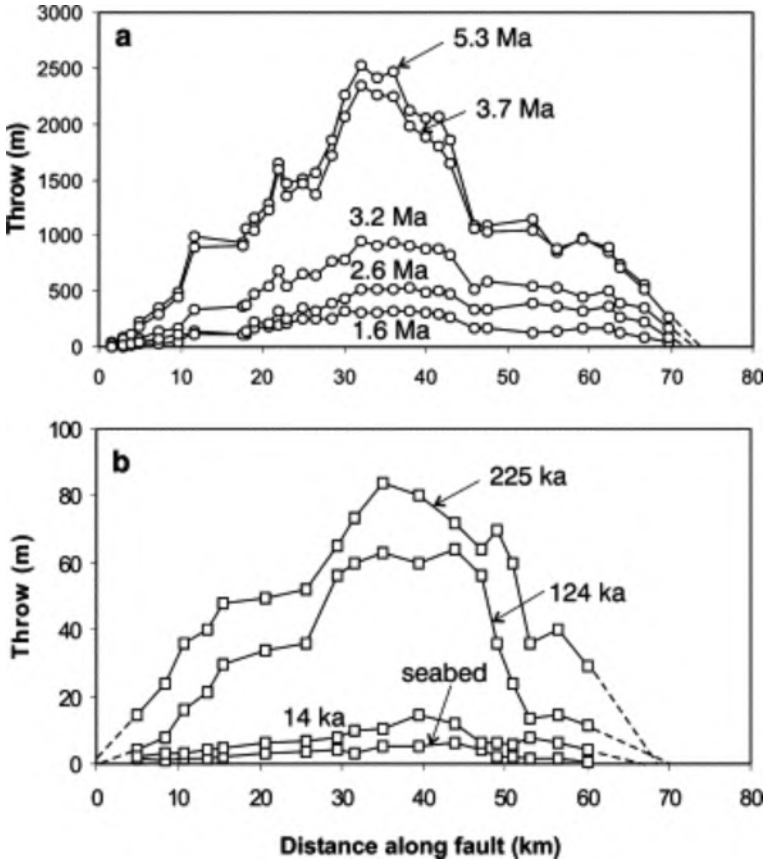

Figure 1.3: Along strike profiles of throw for the Cape Egmont normal Fault, New Zealand, showing the evolution of throw with time. Data is from interpreted seismic-reflection data tied to wells and seabed bathymetery. Note the overall pattern remains similar, with a central peak, however there is clear variation through time in the distribution of throw. From *Nicol et al.* (2005).

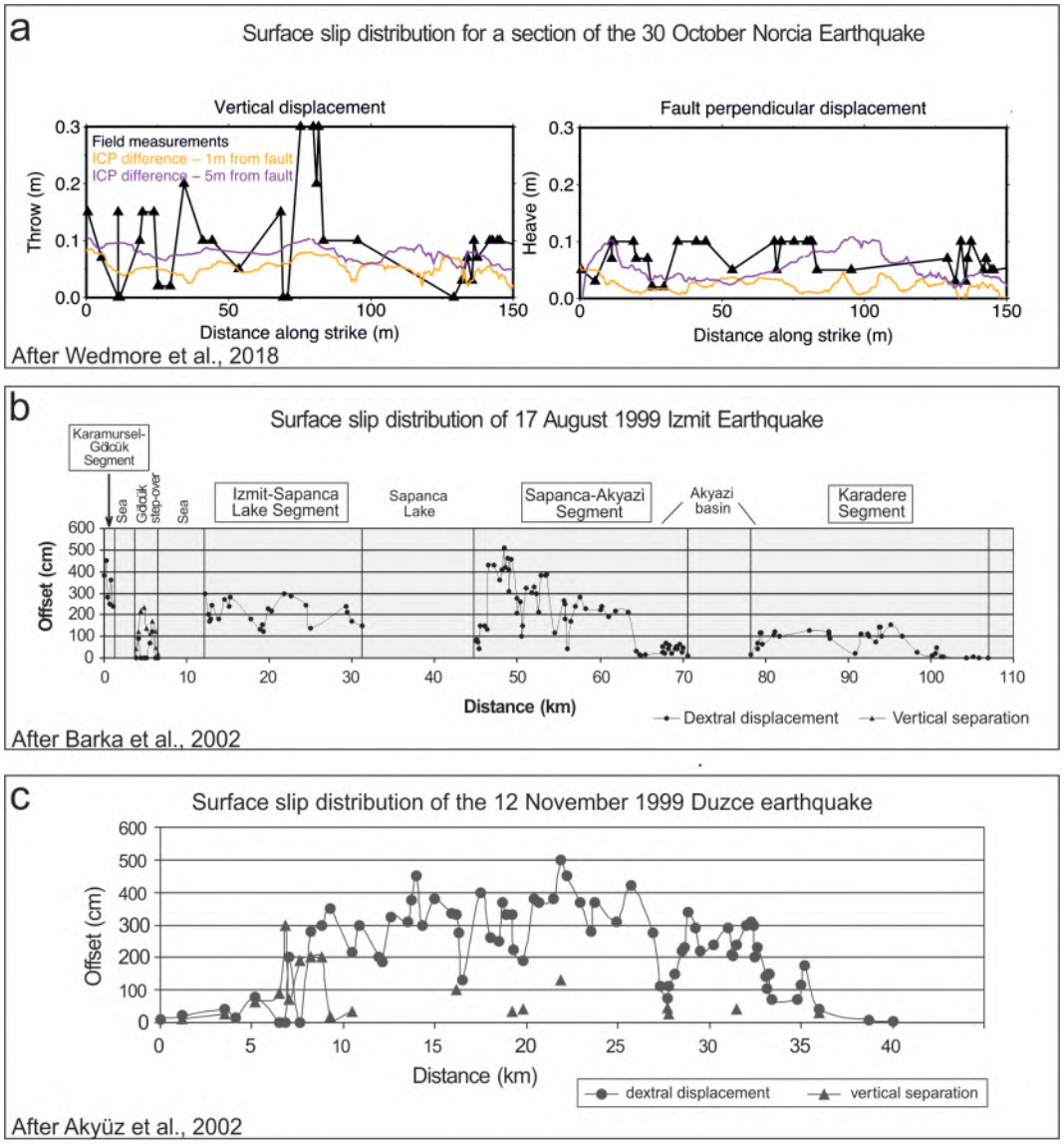

Figure 1.4: a) Coseismic displacements for a section of fault that ruptured during the Mw 6.6 normal faulting Norcia Earthquake in Central Italy, measured using terrestrial laser scanner and using an iterative closest point algorithm to calculate the difference between before and after scans of the fault earthquake after *Wedmore et al.* (2019). b) Surface slip distribution for the M7.4 Izmit strike slip earthquake on the North Anatolian fault, after *Barka et al.* (2002).c) Surface slip distribution for the M7.1 Duzce strike slip earthquake on the North Anatolian fault, after *Akyuz et al.* (2002).

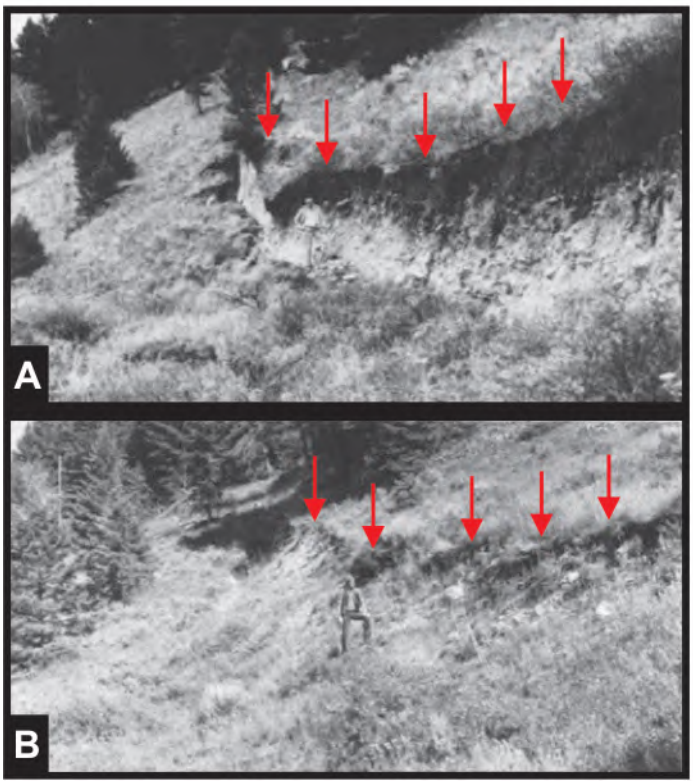

Figure 1.5: Series of photos showing degradation of normal fault scarp over time. A) Photo from 1959 of Hebgen fault scarp in Montana USA which ruptured on the 17/8/1959 in a M7.1 earthquake B) A photo from the same position in 1978, 19 years later. Red arrows show line of the top of the scarp. After *Wallace* (1980) and references therein.

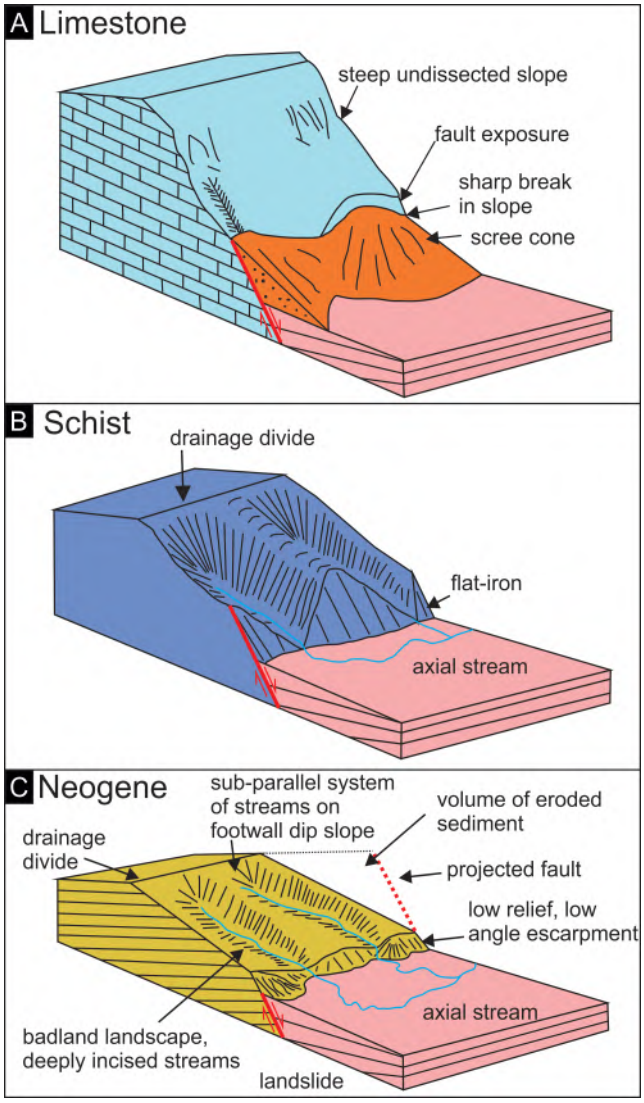

Figure 1.6: Schematic of the morphology of normal faults, which show variation depending on the competence of the lithology. Competence is highest in limestone and lowest in the Neogene sediments. These particular examples are from Greece, figure after *Goldsworthy and Jackson* (2000).

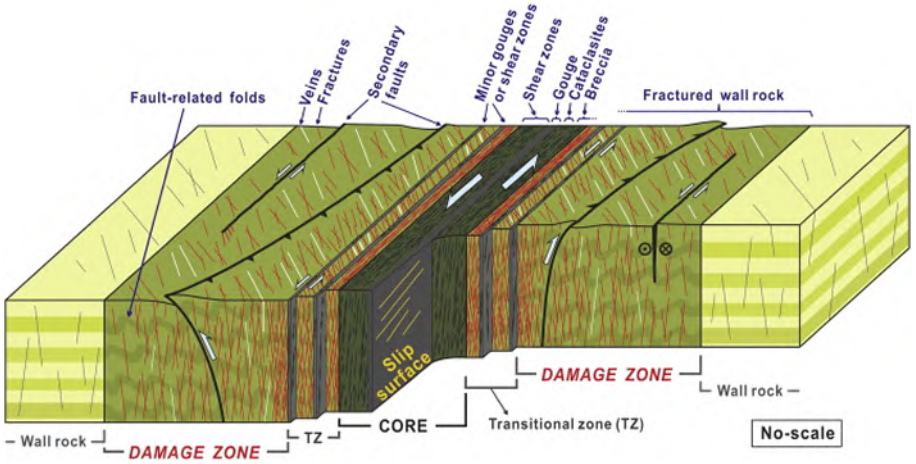

Figure 1.7: A conceptual model of a fault, from *Choi et al.* (2016) and references therein.

1.1.4 Faults below the surface

Evidence for the geological make up of faults in the brittle domain is primarily in the form of exhumed fault zones and data from boreholes crossing fault zones. Remaining in the brittle domain a fault can be either a single high strain core surrounded by a damaged zone, or a series of anastomosing high strain cores within the damage zone, or somewhere inbetween (*Faulkner et al.*, 2010). The fault core is typically composed of gouge on the major slip surface, surrounded by cataclasites and breccia. The damage zone is composed of wall rock which has been fractured, and contains secondary faulting and veining, and there is a transition zone between the two (Figure 1.7). The width of this damage zone does correlate somewhat with displacement; fault linkage and branching also effect the width of the fault zone (*Choi et al.*, 2016). Furthermore the damage zone width is often asymmetric between the hangingwall and footwall and may have complex 3 dimensional geometries (*Choi et al.*, 2016).

How faults slip at depth in a single earthquake is an open question. Geodetic (*Elliott et al.*, 2016, *Walters et al.*, 2009, *Pollitz et al.*, 2011, *Walters et al.*, 2018, *Amey et al.*, 2019) and seismological (*Baumont et al.*, 2002, *Rhie et al.*, 2007, *Romano et al.*, 2010, *Walters et al.*, 2018) data are commonly inverted to show the distribution of slip at depth for individual earthquakes, however these inversions commonly rely on assumptions such as how slip can be realistically distributed on a fault (*Amey et al.*, 2018) and assumptions of fault zone geometry at depth. These studies commonly find that slip is distributed in an un-even manner on the fault plane, and that previous earthquakes and other subsurface structural features can effect the distribution of slip (*Walters et al.*, 2018). The subsurface geometry of individual active faults is commonly poorly constrained, however seismology can provide insight, revealing that faults can have complex geometries, such as ramp-flat-ramp geometries (*Wang et al.*, 2017), and that normal faults typically have planar down dip geometries through the seismogenic

crust, though listric down dip rupture geometries do occur in minor or antithetic faults (*Reynolds and Copley*, 2017).

1.1.5 Determining strain rate, slip rate and fault activity

Determining a strain rate, slip rate or activity of a fault can be approached using a plethora of methods, covering a range of timescales (*Searle et al.*, 2011). Slip rates can be estimated over the longest time scales (10^5-10^7 years) using offset of geological units, sediment thickness and tilting of strata from field mapping or seismic reflection data (*Nicol et al.*, 1997, *McLeod et al.*, 2000, *Contreras et al.*, 2000, *Yin and Harrison*, 2000). Offsets of dated geomorphological markers can be used to determine average slip rates, including slip rates based on offsets of surfaces of known age (*Roberts and Michetti*, 2004), and offset of sedimentary features such as river terraces (*Gold et al.*, 2017), fans (*Chevalier et al.*, 2016) and channels (*Noriega et al.*, 2006). The response of rivers to uplift can be quantified to determine slip rates on normal faults (*Boulton and Whittaker*, 2009), as can the uplift or down-throw of coastlines if there are datable markers such as marine terraces (*De Martini et al.*, 2004), sea level notches (*Cooper et al.*, 2007) or ancient constructions (*Koukouvelas et al.*, 2017). Excavation and analysis of paleoseismic trenches across faults can assist in constraining fault activity over 10^3-10^4 year timescales (*Galli et al.*, 2008, *Ran et al.*, 2010, *Malik et al.*, 2010). Typically paleoseismic trench studies attempt to identify the time at which discrete events occur. Cosmogenic isotope dating of limestone bedrock fault scarps is another increasingly common tool that can be used to determine slip rates over 10^3-10^4 year time scales (*Cowie et al.*, 2017). This method will be described in greater detail in subsequent sections.

As well as directly offsetting existing features, individual earthquakes can produce shaking which can result in many secondary effects. If a secondary effect can be dated it can be used to build a catalogue of earthquake activity. Effects that have been used to do this include dating of seismically triggered landslides (*Jibson*, 1996), turbidites (*Noda et al.*, 2008), tsunami deposits (*Mörner*, 1996, *Kelsey et al.*, 2002), and seismites, which are soft sediment deformation structures formed due to earthquake induced shaking (*Rodriguez-Pascua et al.*, 2000). Precariously balanced rocks (PBR) have also been used as evidence for a lack of fault activity (*Briggs et al.*, 2013). One challenge in using secondary effects is that it can be difficult to attribute an effect to a specific fault, or in some cases it may not be certain that the effect was seismically induced. Historical accounts (*Ambraseys*, 2009, *Tan et al.*, 2008, *Wedmore et al.*, 2017) as well as archaeo-seismology (offset and damage to ancient structures) (*Sintubin and Stewart*, 2008, *Altunel et al.*, 2009, *Stewart and Piccardi*, 2017) can provide evidence of fault activity (Figure 1.8). Again, it can be difficult to identify the responsible fault or in some of the older records, if the deformation described is even due to an earthquake.

The development of new technologies at the beginning of the 20th century started

Figure 1.8: a) A 1st century aqueduct offset in a normal sense by the Manisa fault and subsequently repaired (N38.616647N, E27.319535). b) An offset temple in the ancient city of Knidos, western Turkey (N 36.688903, E 27.373262). The responsible fault is seen in the form of a limestone fault scarp in the background. The offset can be traced through the ancient ruins.

what is known as the instrumental period. The development of our understanding of seismology and the ever increasing number and quality of seismometers deployed (*Deschamps et al.*, 1982, *Chiaraluce et al.*, 2017) has resulted in seismologists being able to accurately and precisely locate seismic signals that were previously undetectable, allowing identification of active faults as well as significantly improving our understanding of fault systems (*Brodsky*, 2019). Geodetic techniques, including Interferometric synthetic aperture radar (InSAR) and Global Naviagation Satellite Systems (GNSS, previously GPS), can provide measurements of deformation during the co-seismic (*Wilkinson et al.*, 2017, *Sreejith et al.*, 2016), post-seismic (*Barbot et al.*, 2008, *Biggs et al.*, 2009) and inter-seismic periods of the earthquake cycle (*Cavalié et al.*, 2008, *Hussain et al.*, 2016).

As previously described, the high competence of limestones can result in the formation and preservation of bedrock limestone fault scarps. There have been numerous methods applied to these fault scarps to measure slip rates and/or distribution on the normal faults. Firstly studies have used offset of post-Last Glacial Maximum (LGM) slopes to calculate average slip rates on the faults over the last approximately 15 kyr (*Piccardi et al.*, 1999, *Roberts and Michetti*, 2004, *Papanikolaou et al.*, 2005, *Wilkinson et al.*, 2015). These studies provide a single slip rate for the 15 kyr period. To try and identify slip rates at a higher resolution or individual earthquakes, various studies have used increase in roughness up dip to identify periods of rapid exhumation and quiescence or displacement due to individual earthquakes on the faults (*Giaccio et al.*, 2003, *Wiatr et al.*, 2015, *He et al.*, 2016). Studies have also measured variation of

concentration of rare earth elements up the dip of the fault scarp to identify individual earthquakes on faults (*Carcaillet et al.*, 2008, *Manighetti et al.*, 2010, *Tesson et al.*, 2016). Exhumation of these fault scarps is not always only due to tectonic exhumation, but can be attributed to other processes like erosion and depostion on the hangingwall slope and landslides, meaning that exhumation rate is not always the same as slip rate on the fault, so care should be taken to undertake analysis on sections of scarp where these other processes are not occurring or where they can be properly accounted for (*Bubeck et al.*, 2015).

1.2 Methodology

The primary method I use in this thesis is cosmogenic isotope dating of limestone bedrock fault scarps, which can be used to determine Holocene slip rates on normal faults. In this section I introduce cosmogenic nuclides, and how they can be used to determine fault slip rates.

1.2.1 Cosmogenic Nuclides

Cosmogenic nuclides (or cosmogenic isotopes) are produced by the interaction of cosmic rays with material on the Earth's surface (*Gosse and Phillips*, 2001). Cosmic rays are a series of charged particles, primarily atomic nuclei, as well as electrons, positrons and other sub-atomic particles (*Dunai*, 2010). The cosmic rays have energy levels of between $1x10^{6}$eV and $1x10^{20}$eV (*Dunai*, 2010). Cosmic rays with energy levels that are pertinent to cosmogenic nuclide production are produced by supernova. The flux of cosmic rays in the galaxy is thought to have been fairly constant over the last 10 Ma (*Leya et al.*, 1998). The flux of cosmic rays reaching the Earth's surface is dependent on solar winds, magnetic field strength and atmospheric thickness (*Gosse and Phillips*, 2001). Magnetic field strength, atmospheric thickness and solar winds vary through time, and magnetic field strength and atmospheric thickness also vary with latitude and longitude. The type of cosmic rays that reach the surface of the earth is controlled by interaction with the ionosphere and atmosphere (figure 1.9) and there is a significantly reduced selection of primary cosmic rays at the Earth's surface, compared to the large variety found in space. The majority of the cosmogenic nuclide producing cosmic rays are secondary cosmic rays, composed primarily of neutrons but also muons.

Cosmogenic isotopes are produced via a number of different reaction pathways. The focus of my study is chlorine 36 (^{36}Cl) and the production mechanisms are (in order of importance); spallation of ^{39}K and ^{40}Ca (and to a lesser extent Ti and Fe), thermal neutron capture and negative muon (μ^-) capture (*Gosse and Phillips*, 2001; and references therein). The relative contribution of each pathway is a function of rock composition and burial depth. For example the attenuation rate of μ^- is lower than that for neutrons so the relative contribution of μ^- capture increases with depth

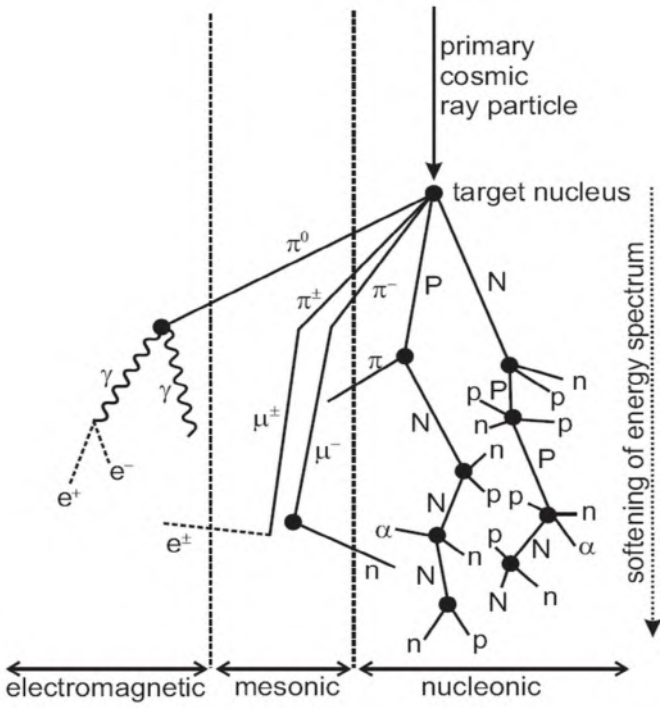

Figure 1.9: The interaction of cosmogenic rays with the atmosphere produces a range of secondary cosmogenic particles. n = neutron, p = proton (capital letters used for those continuing the nuclear cascade) From *Dunai* (2010) and references therein.$\pi^{\pm 0}$=pion, $e^{\pm}$ = electron or positron, $\mu^{\pm}$ = muon and γ = gamma ray photon.

below the surface. There is some uncertainty in the production rates and this must be considered when analysing the data. ^{36}Cl can also be produced by capture of thermal neutrons produced within the rock by radioactive elements. The neutron flux of a sample must therefore be calculated based on the major/trace element composition of the rock. Limestone is typically low in these radioactive elements (U,K,Th) so has a low or negligible background ^{36}Cl production from non-cosmogenic sources.

Cosmogenic isotopes have been used for exposure dating of terrestrial material for over half a century (*Davis and Schaeffer*, 1955). The longer a material is exposed at the surface the more atoms of the cosmogenic isotope it contains. These isotopes are useful if they are almost entirely otherwise absent on earth. The most useful cosmogenic isotopes are radio-nuclides, and as a result have a working age limit that is a function of the half life of the isotope (*Dunai*, 2010). It was only with the discovery that an acceleratory mass spectrometer (AMS) could be used to determine isotopic abundance (*Muller*, 1977) that cosmogenic isotopes came into widespread use (*Budzikiewicz and Grigsby*, 2006). ^{3}He, ^{21}Ne, ^{22}Ne, ^{10}Be, ^{26}Al and ^{36}Cl are currently used, with a range of other possible isotopes awaiting development or application (*Dunai*, 2010). On Earth, ^{36}Cl has been used for exposure dating of glacial deposits (*Phillips et al.*, 1997) and dating offsets of alluvial fans to determine slip rates on strike slip faults (*Daëron et al.*, 2004, *Frankel et al.*, 2007).

1.2.2 Exposure analysis of normal fault scarps

Cosmogenic ^{36}Cl can be used to determine detailed exhumation histories on normal fault scarps (e.g. *Zreda and Noller* (1998), *Benedetti et al.* (2002)). Slip on the fault plane exhumes the footwall and if the rate of slip outpaces erosion rates, the footwall fault scarp is preserved (Figure 1.10). When the fault plane is exposed at or near to the surface of the earth it is subjected to cosmogenic radiation, producing cosmogenic isotopes through reactions outlined in the previous section. By measuring a series of cosmogenic isotope concentrations up the scarp, an exposure history of the scarp can be modelled (figure 1.11).

Exposure dating of the scarp requires the scarp to be competent and resistant to weathering so that any surface exposed is due to the movement of the fault and not erosion of the fault surface once exposed. It also requires a lithology that produces a measurable amount of a cosmogenic isotope once exposed. Limestone fulfills both these criteria, often being competent and producing measurable amounts of ^{36}Cl due to high Ca concentration.

The concentration of ^{36}Cl in a rock varies as a function of exposure time (t) and burial depth (*Schlagenhauf et al.*, 2010, *Gosse and Phillips*, 2001).

$$\frac{\Delta N(z,t)}{\Delta t} = P(z,t) - \lambda N(z,t)$$

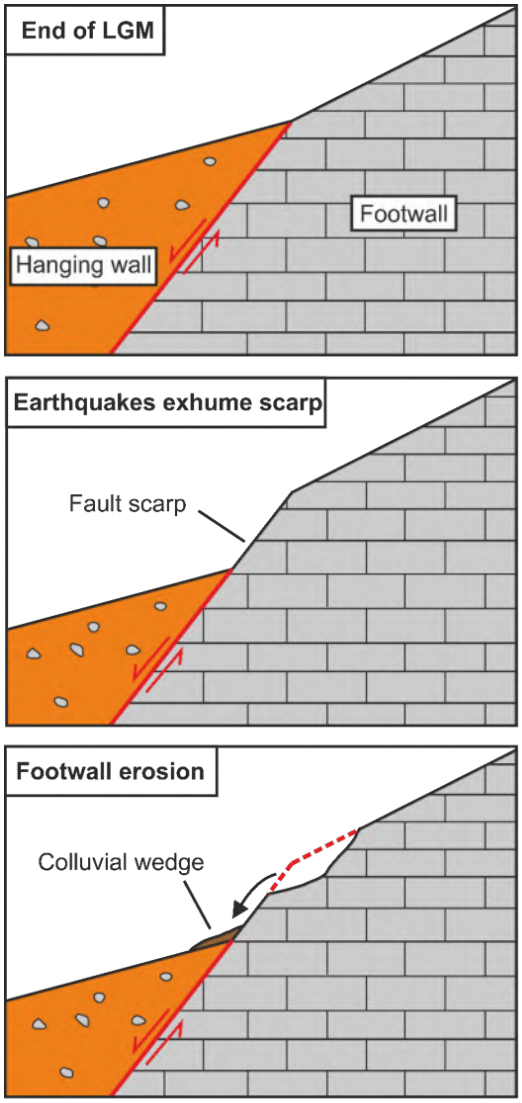

Figure 1.10: Before the end of the LGM erosion rates were much higher than present, and kept pace with exhumation rates producing slopes as in the top panel. This results in zero slope offset at the end of the LGM. Frame 2 shows the effect of 0 erosion, and frame 3 shows the result of fault exhumation when exhumation rate is greater than erosion rate. Limestone fault scarps commonly weather with with the morphology of frame 3 in areas of competent limestone.

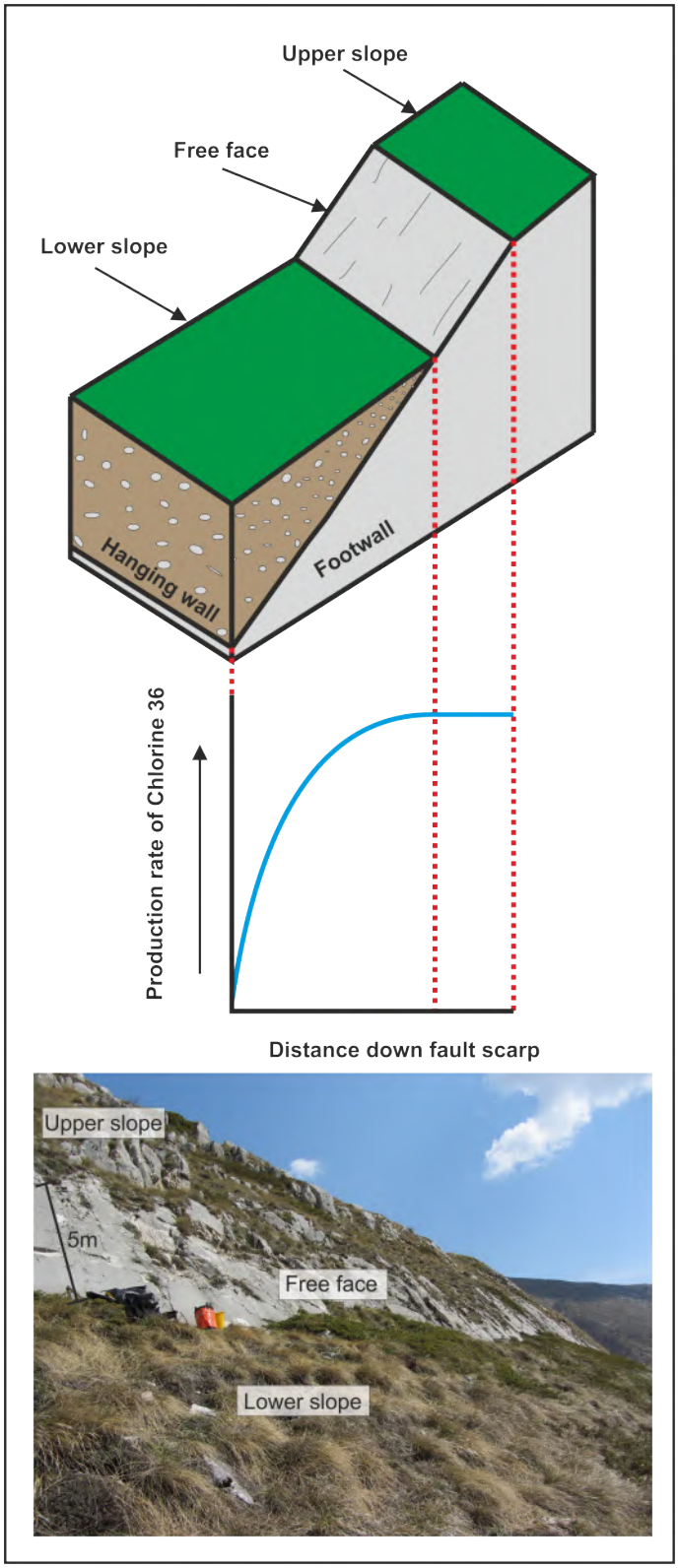

Figure 1.11: A schematic figure of relationship between scarp geometry and ^{36}Cl production rates. Production rates decrease in an exponential like way to around 3m depth, due to shielding of colluvium in the hangingwall. Below is a photo of the Campo Felice fault showing the fault scarp, upper and lower slopes.

- N Number of atoms of isotope
- P Isotope production rate
- λ Decay constant
- $\frac{\Delta N}{\Delta t}$ Rate of change of Number of atoms of isotope
- z Burial depth
- t Exposure time

The production rate P_{total} at a given depth z is given by:

$$P_{total}(z) = S_{el,s}F_sQ_sP_{mu}(z)+S_{el,\mu}F_\mu Q_\mu P_{mu}(z)+S_{el,s}F_n[Q_{eth}P_{eth}(z)+Q_{th}P_{th}(z)]+P_{rad}$$

Subscripts refer to reaction type: s = spallation, μ eth = epithermal neutron capture, th = thermal neutron capture and rad for radiogenic production. $S_{el,s}$ and $S_{el,\mu}$ are scaling factors to account for the effects of lattitude and elevation, F is a scaling factor to sum shielding corrections for the geometry, topography and cover shielding. P_i is sample specific ^{36}Cl production rate resulting from reaction i, which is a function of chemical composition, Q_i is the sample thickness integration factor for the reaction i. Equation from *Schlagenhauf et al.* (2010), *Schimmelpfennig et al.* (2009) and *Gosse and Phillips* (2001).

1.3 Overview of regional tectonics

The Mediterranean is a large and tectonically complex area (Figure 1.12). In my thesis I focus on two distinct regions of extension, the central Italian Appennines and western Anatolia.

1.3.1 Central Italain Appennines

The Italian Appennines is in the convergence zone of the Northward moving African plate and the Eurasian plate (*Anderson and Jackson*, 1987; Figure 1.12). As a result of this convergence the Tethys ocean was subducted under Eurasia, and collision occurred between Eurasia and fragments of continental crust producing thrusting (*Roberts and Michetti*, 2004). This compressional regime is still present east of the Italian Apennines, and thrusting continues there today(*Farolfi and Del Ventisette*, 2017). In the Central Italian Appennines thrusting halted in the Pliocene (*Patacca et al.*, 1990) and an extensional regime began which is thought to be due to mantle upwelling through a slab window (*D'agostino et al.*, 2001). The upwelling has produced a 700 km by 90 km long wavelength topographic high (*Faure-Walker et al.*, 2012), which is currently extending NE-SW at 2.7 mm/yr between the Tyrrhenian and Adriatic seas(*D'Agostino et al.*, 2011). This extension has resulted in a network of NW-SE trending <40 km

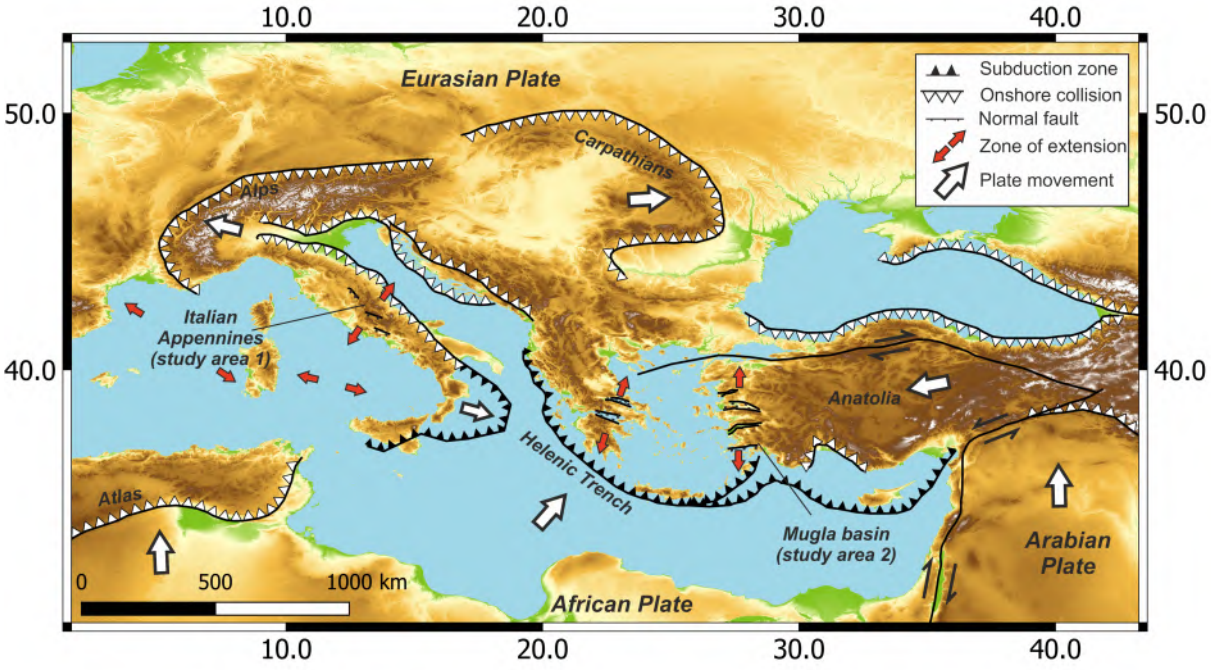

Figure 1.12: A simplified overview of tectonics in the Mediterranean. The regions which are the focus of this thesis are the Central Italian Appennines and Western Anatolia. Simplified from *Robertson and Grasso* (1995),*Faccenna et al.* (2001) and *Nocquet* (2012).

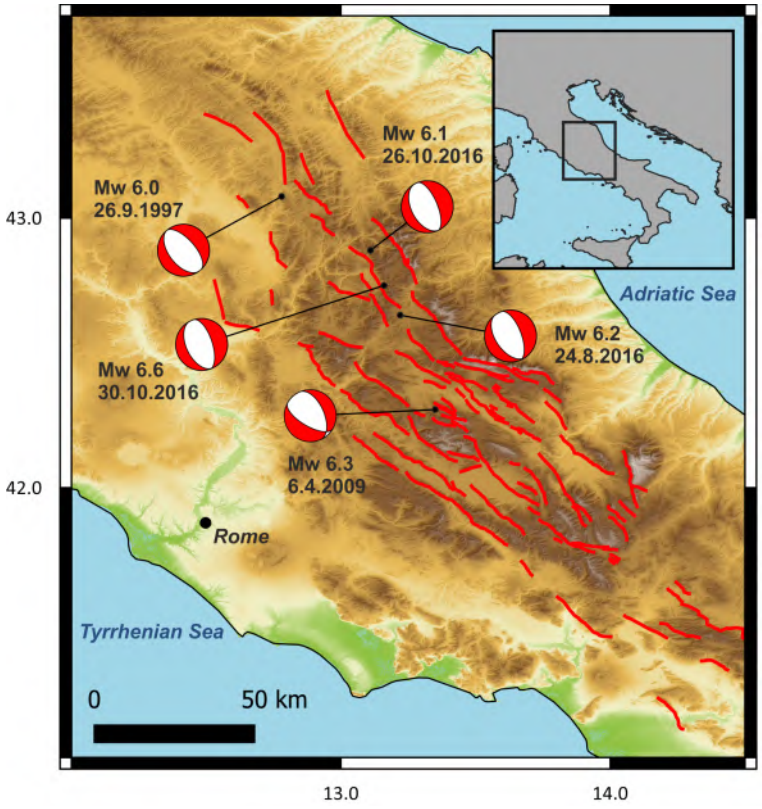

Figure 1.13: A map of active faults in the central Italian Appennines, earthquake moment tensors are from www.globalcmt.org, fault map is from *Roberts and Michetti* (2004). DEM from 1 arcsecond (30m) SRTM data. Yellow box shows location of Figure 3.2.

long normal faults (Figure 1.13), which have ruptured in $>M_w6$ earthquakes (*Roberts and Michetti*, 2004, *Wedmore et al.*, 2017, *Walters et al.*, 2018).

1.3.2 Western Turkey

My second region I focus on in this thesis is western Anatolia. A period of continental collision between the Pontide and Tauride Terrains from the Cretaceous to the Miocene transitioned into east-west extension during the Miocene (*Yilmaz et al.*, 2000). North-south extension began in the Late Miocene and continued until present, with a brief extensional hiatus in the late Miocene (*İnci*, 1984, *Yilmaz et al.*, 2000). It is proposed that present day extension is either due to; back-arc extension because of slab roll-back (*McKenzie*, 1978) and westward escape of Anatolia (*Şengör et al.*, 1985), differential convergence rates across the subduction zone in the Aegean (*Doglioni et al.*, 2002), or an internal gravitational potential energy gradient from east to west across all of Anatolia (*England et al.*, 2016). Currently western Anatolia is extending at at a rate of 20 mm/yr (*Aktug et al.*, 2009), and this combined with the multi-stage tectonic history, has produced a pattern of active faults, with faults in a range of orientations (Figure 1.14). The major active grabens in the region are oriented E-W and are commonly

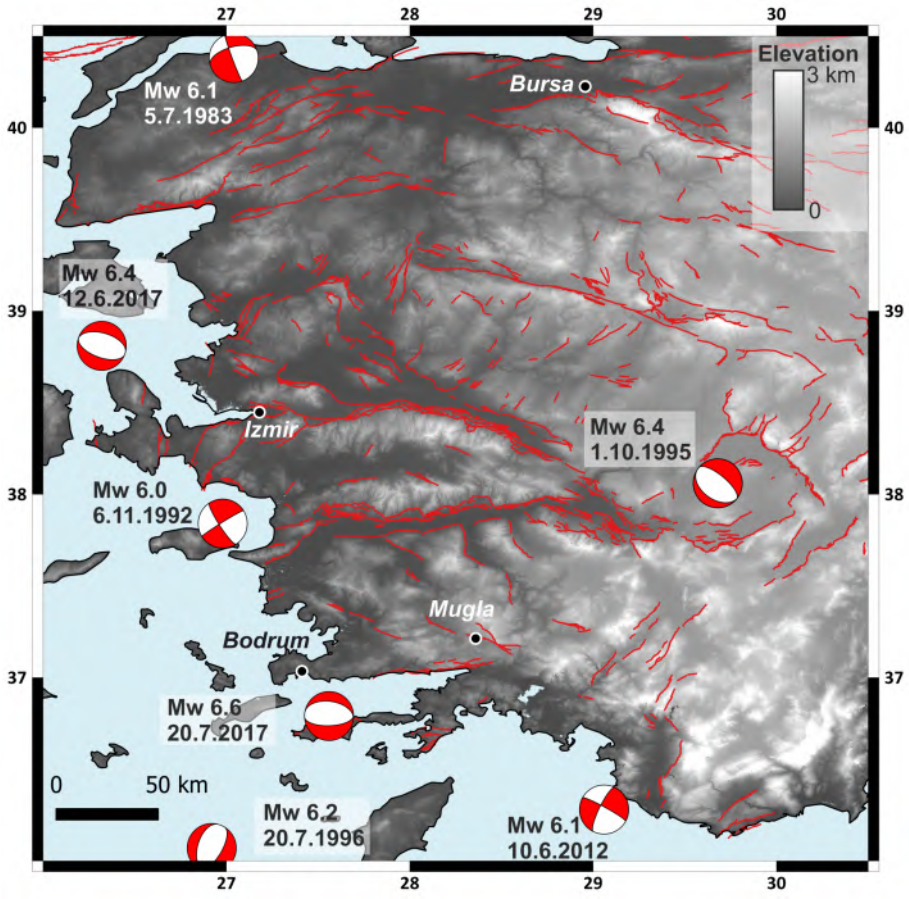

Figure 1.14: Active faults, shown in red are from (*Emre et al.*, 2018), earthquake moment tensors are from www.globalcmt.org and run from DEM from 1 arcsecond (30m) SRTM data.

bounded by fault networks >100 km long. Other active grabens trend NW-SE and NE-SW and are still seismically active (*Yilmaz et al.*, 2000). Since 1974 there have been 7 earthquakes > $Mw6$, with a range of focal mechanisms, and there is a long record of destructive earthquakes in the area, going back millennia (*Tan et al.*, 2008, *Ambraseys*, 2009).

1.4 Thesis Outline

1.4.1 Aims and objectives

There are two major aims in my thesis. The first is primarily a methodological focus. Cosmgenic istope dating of bedrock normal fault scarps is being increasingly used to determine slip rates on normal faults. These slip rates often form the basis of geodynamic and seismic hazard models, however it has not been determined that it is a consistent method for measuring slip rate. I aim to test whether it is a robust technique for determining slip rate by cosmogenic isotope; investigating the reproducibility of the method at multiple sites along a single fault. This will provide greater confidence in the method. I have chosen to undertake this study in the central Italian Apennines, because there it has the highest concentration of existing ^{36}Cl fault scarp studies, which I can integrate with my studies.

To understand how fault networks behave requires information on their slip rates, and by determining slip rates on faults that are next to each other, I may gain insight into how faults are interacting over millennial timescales. Quaternary slip rates on faults in western Turkey are not constrained in many areas, and it is one of the most rapidly extending regions on earth. I aim to determine slip rates on some of these normal faults using cosmogenic isotope dating of limestone fault scarps, and see what information this can provide on how faults are interacting in the region. I have chosen to work in the Muğla-Yatağan basin because no Quaternary slip rates have been determined on the faults which lie close to a major city, and the close proximity of 3 faults may provide insight into how faults interact over km scales. Finally there are also appropriate sample sites on each of the major faults, allowing the ^{36}Cl fault scarp dating method to be use.

- Review the current state of knowledge of cosmogenic isotope dating of bedrock fault scarps and the modelling methods used to analyse it.
- Use data from a previous study in the central Italian Apennines to determine if multiple closely spaced sample sites on a single fault produce similar slip rates.
- Collect and complete cosmogenic isotope analysis at multiple closely spaced sample sites on two separate faults in the Central Italian Apennines.
- Sample and generate cosmogenic isotope data for a small network of normal faults in western Turkey.

- Model the slip rate of these faults over thousand year time scales
- Compare geodetic and cosmogenic based slip rates on normal faults in western Turkey

1.4.2 Outline of work

In chapter 2 I provide an overview of ^{36}Cl analysis of bedrock fault scarps, discussing the importance of appropriate sample sites and how they can be identified. I give examples of previous studies where the selection of inappropriate sample sites brings their results into question. I go on to explain how modelling of cosmogenic fault scarp data has evolved through time and justify the modelling methods I will use in future chapters. In my next chapter I show that previous work, which demonstrated that cosmogenic isotope dating of fault scarps produces similar slip histories at multiple sample sites along strike, used arbitrary changing of a parameter with no justification. I re-model the data in a way which treats each site the same and conclude that the slip histories are significantly different between sites, most likely due to non-tectonic exposure of the fault scarp, indicated by the geomorphology of the sample site. I propose that a new study is required to determine if ^{36}Cl dating of fault scarps produces similar slip histories at multiple sites along strike, using data from sites where the geomorphology indicates only tectonic exhumation of the fault scarp. Chapter 4 is this new study, where I hypothesis that if multiple sample sites produce similar slip histories along strike, then ^{36}Cl dating of bedrock fault scarps is a reliable method for determining representative slip rates on normal faults. I generate and use ^{36}Cl data from two faults in the central Italian Apennines, the Campo Felice fault where I use 4 sample sites including 1 sample site from a previous study, and the Rocaprettura fault, where I use 2 new ^{36}Cl sites and 1 sample site from a previous study. Comparison between sites on the Campo Felice fault shows similar slip histories at all sites, supporting my hypothesis. In contrast I find variable rates between the Rocaprettura sites, which I conclude are due to slip partitioning between fault segments at one site, and non-tectonic exhumation of the fault scarp at the sample site from the previous study. These findings lead me to conclude that ^{36}Cl analysis of limestone bedrock fault scarps is a reliable method for determining a representative slip rate on normal faults, given careful site selection, and indicate that it is a tool that can be provide insight into Holocene along-strike variation in slip rates. I then apply this same method to three faults in western Anatolia in chapter 5, to determine 15 kyr slip histories of the major faults in the Mugla basin. I produce an updated active fault map for the basin using satellite imagery and digital elevation models, and compare the 15 kyr slip rates on the faults to GNSS derived extension rates, and find that there is agreement between the two methods. I also use deterministic modelling of the seismic hazard of the faults to demonstrate the hazard they pose to the region. Finally I discuss my results in the

context of the evolution of fault activity in the Mugla basin, and the wider context of basin evolution.

Chapter 2

An appraisal of the current state of ^{36}Cl fault scarp dating

"Coming back to where you started is not the same as never leaving"
Terry Pratchett

2.1 Summary

The objective of this chapter is to introduce where and how previous ^{36}Cl fault scarp studies have been undertaken. The initial focus is on the geomorphology of sample sites from previous studies, and I cite examples where poor selection of sample locations has resulted in exhumation histories that are a product of processes other than earthquakes. I then describe the evolution of modelling of ^{36}Cl fault scarp data and provide justification for the modelling methods used throughout this thesis. A previous study (*Schlagenhauf et al.*, 2011) attempted to constrain along-strike variability in slip using multiple ^{36}Cl sample sites on the same fault, they then go onto correlate events they identified at the different sites. I find they arbitrarily varied important parameters in the modelling to force the identified events to correlate. I propose the data from *Schlagenhauf et al.* (2011) should be re-modelled using an approach which which treats each site identically, to determine if there is correlation between slip histories at each site.

2.2 Background

2.2.1 Previous ^{36}Cl fault scarp studies

There are a number of previous ^{36}Cl fault scarp studies (*Akar et al.*, 2012, *Benedetti et al.*, 2002, 2003, 2013, *Mechernich et al.*, 2018, *Mitchell et al.*, 2001, *Mouslopoulou et al.*, 2014, *Mozafari et al.*, 2019a,b, *Palumbo et al.*, 2004, *Schlagenhauf*, 2009, *Schlagenhauf et al.*, 2010, 2011, *Tesson et al.*, 2016, *Tesson and Benedetti*, 2019, *Zreda and*

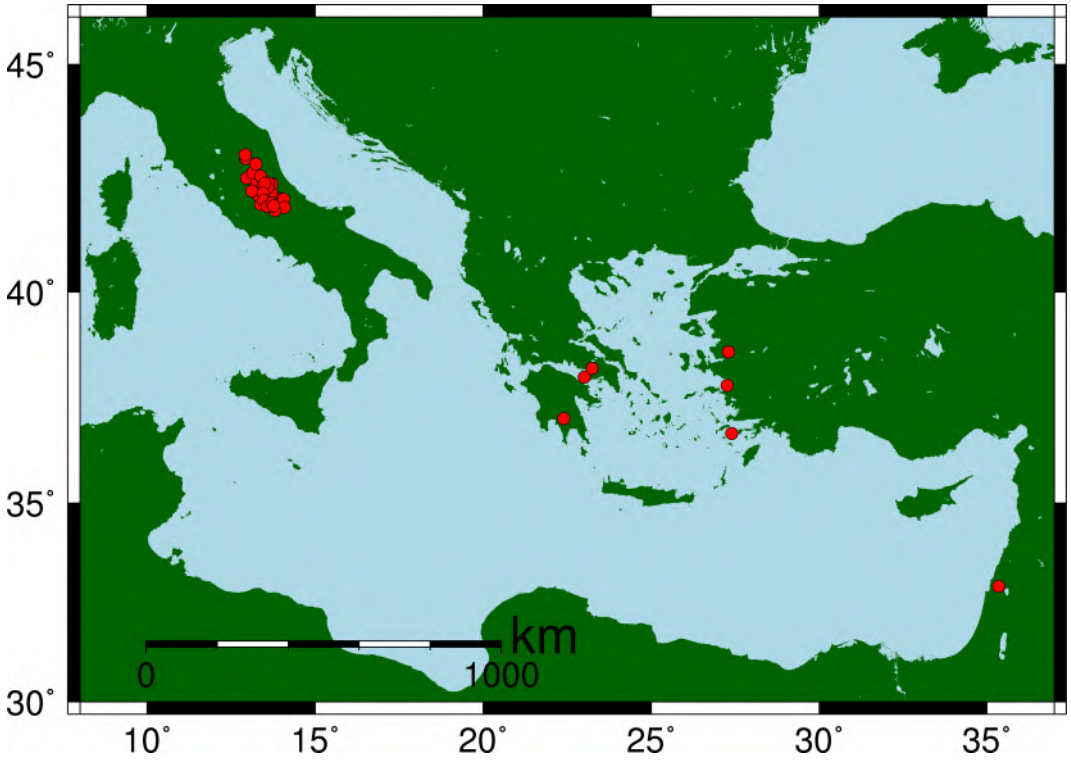

Figure 2.1: A map of all known published and unpublished (Gregory, personal comms.) limestone bedrock fault scarp ^{36}Cl sample sites in the Mediterranean, not including those sampled in this study. Studies are located in Italy (*Palumbo et al.*, 2004, *Schlagenhauf*, 2009, *Schlagenhauf et al.*, 2010, 2011, *Benedetti et al.*, 2013, *Tesson et al.*, 2016), Greece (*Benedetti et al.*, 2002, 2003, *Mechernich et al.*, 2018), Turkey(*Akar et al.*, 2012, *Sahin et al.*, 2016, *Mozafari et al.*, 2019b) and Israel (*Mitchell et al.*, 2001). The site of *Zreda and Noller* (1998) is not shown, but is located in Western USA.

Noller, 1998), the majority of which are located in the Mediterranean (Figure 2.1). This is because the Mediterranean hosts large areas of limestone where extension is actively occurring, producing the limestone fault scarps necessary for ^{36}Cl fault scarp studies. As the method has been increasingly used, understanding of how best to collect, model and interpret the data has evolved.

When collecting samples from limestone fault scarps it is vital to understand the geomorphology of the sampled section of fault scarp and how it has been exhumed. Limestone fault scarps form by progressive exhumation of limestone in the footwall by multiple normal faulting earthquakes (*Tucker et al.*, 2011). These earthquakes offset the limestone bedrock by up to 100's of meters, producing a characteristic morphology (Figures 2.2, 1.10 and 1.11).

^{36}Cl can only provide an exhumation history of fault scarp, whether the exhumation history is representative of the slip rate of the fault or not depends upon what processes have caused the exhumation. Careful study of the sample site geomorphology can reveal whether earthquake slip or slope processes affect exhumation of the scarp. If the fault scarp has been exhumed purely by tectonic processes over multiple earthquake cycles,

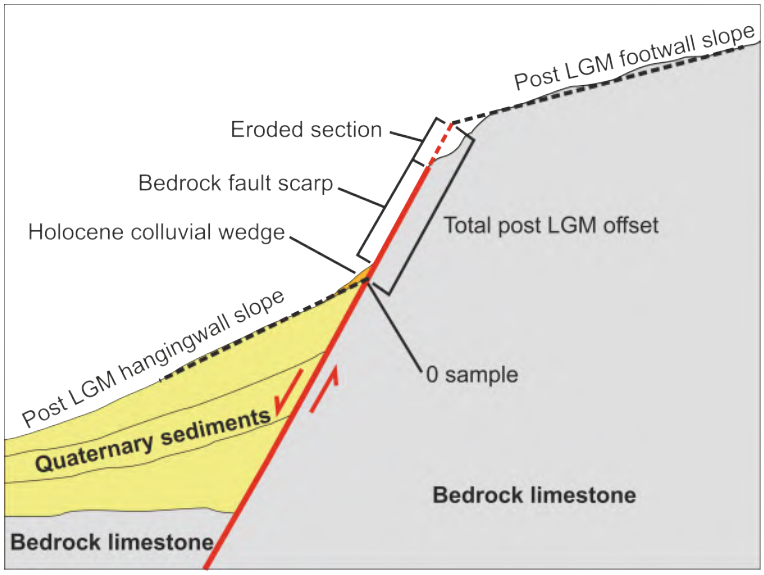

Figure 2.2: Idealised morphology of bedrock limestone fault scarps. The total offset on the fault can be up to 100's of meters, the post-LGM offset is typically <20 m. When sampling for ^{36}Cl dating, the 0 height up the scarp sample is taken where the stratified Quaternary sediments meet the bedrock scarp. All sample heights are reported relative to this.

the along strike variation in offset of the slope should be consistent over 10-1000 m scales (*Bubeck et al.*, 2015). Any large deviation from this can be assumed to be a result of other exhumation or depositional processes. The character of the hangingwall slope can also indicate which processes are exhuming the fault plane. An idealised purely tectonically exhumed scarp produces a hangingwall slope which dips uniformly along strike, with a change in gradient where the hangingwall slope flattens in the bottom of the valley/basin and a change in gradient where it meets the limestone fault scarp (Figure 2.2). Any deviation from this indicates other processes may contribute to exhumation of the fault plane, and so the exhumation rate does not equal the slip rate. An ideal site for sampling would therefore have a planar footwall slope and hangingwall slope, with a consistent total post LGM offset along strike for at least 10's of meters, because this implies that there has likely only been tectonic exhumation of this section of fault scarp since the LGM.

2.2.2 Sample site selection

Sometimes processes exhuming the fault plane are anthropogenic, either modern or ancient. If studies are undertaken using data from sites affected by anthropogenic processes, the exhumation rates are unlikely to be representative of the fault slip rate, unless the modelling accounts for these processes. The colluvium that commonly composes the hangingwall has in some regions been used for construction material, which leaves quarries exposing sections of fault plane up to 30 m in height (Figure 2.3). In other areas, terracing for agriculture has modified the hillslope, exhuming the fault

plane, as has construction, and erosion due to human or animal traffic. Parts of the Mediterranean have been populated for over 10 kyr, which can make finding appropriate sample sites difficult in this region. The large time and monetary costs associated with producing ^{36}Cl fault scarp data sets makes it imperative that sample sites are carefully chosen, picking areas where exhumation is affected by tectonic processes not anthropogenic, erosional or depositional processes. For example, if a terrace was excavated 2000 years ago, revealing 2 m of fault scarp, it would appear that there was a 2m event 2000 years ago in the ^{36}Cl data. It would be impossible to differentiate between an earthquake and an excavation using the ^{36}Cl data alone. Mapping and understanding the geomorphology of the sample site can provide insight into how the fault scarp formed. If the scarp was only exhumed by earthquakes it would have a very different morphology from a scarp which had also been excavated. Whilst the change in geomorphology between pre-excavated and excavated could be mitigated for in the modeling of ^{36}Cl concentrations, it would require knowledge of the age of excavation, the pre-excavation slope geometry and knowledge that the pre-excavation slope was stable. If this information was available, the ^{36}Cl concentrations on the scarp could be modeled by running a two part model, with the first part running the pre-excavation geometry, and the second part taking the output of that model and using it has starting conditions for the post-excavation geometry. If the information is not available or taken into account then the slip rate or events identified will have a component of human excavation/burial which add events/increase the slip rate, and skew the ages of the events or changes in slip rate.

I identify examples of published sampling localities that are partially exhumed through anthropogenic or other non-tectonic processes, and are therefore unlikely to provide good estimates of normal fault activity. The first ^{36}Cl fault scarp study was undertaken by *Zreda and Noller* (1998) on the Hebgen lake fault scarp in Montana, USA, which produced a surface rupture during a M_s 7.5 earthquake with a normal fault mechanism, in 1959 (*Myers and Hamilton*, 1964). The sample site is located approximately 20 m from a road, which is oriented parallel to fault strike (Figure 2.4). The scarp does not seem to be entirely natural as the bedrock section is continuous for 300 m at most. Using imagery from the Google Maps street view, it appears that the preserved fault scarp rapidly degrades northwest along strike and the preserved scarp height does not appear consistent. The site appears to have been partially excavated as part of construction of the road that runs along strike, evidenced by similar road cuts, which can be seen in aerial imagery 2-3 km North and South along the road.

The second example is a site on the Kaparelli fault which is located near the Gulf of Corinth, Greece, and was sampled by *Benedetti et al.* (2003). It is not clear in the paper of *Benedetti et al.* (2003) but there is a section of horizontal ground on the hangingwall immediately next to the fault scarp (Figure 2.5). This extends for approximately 8 m perpendicular to the fault dip direction before the angle increases

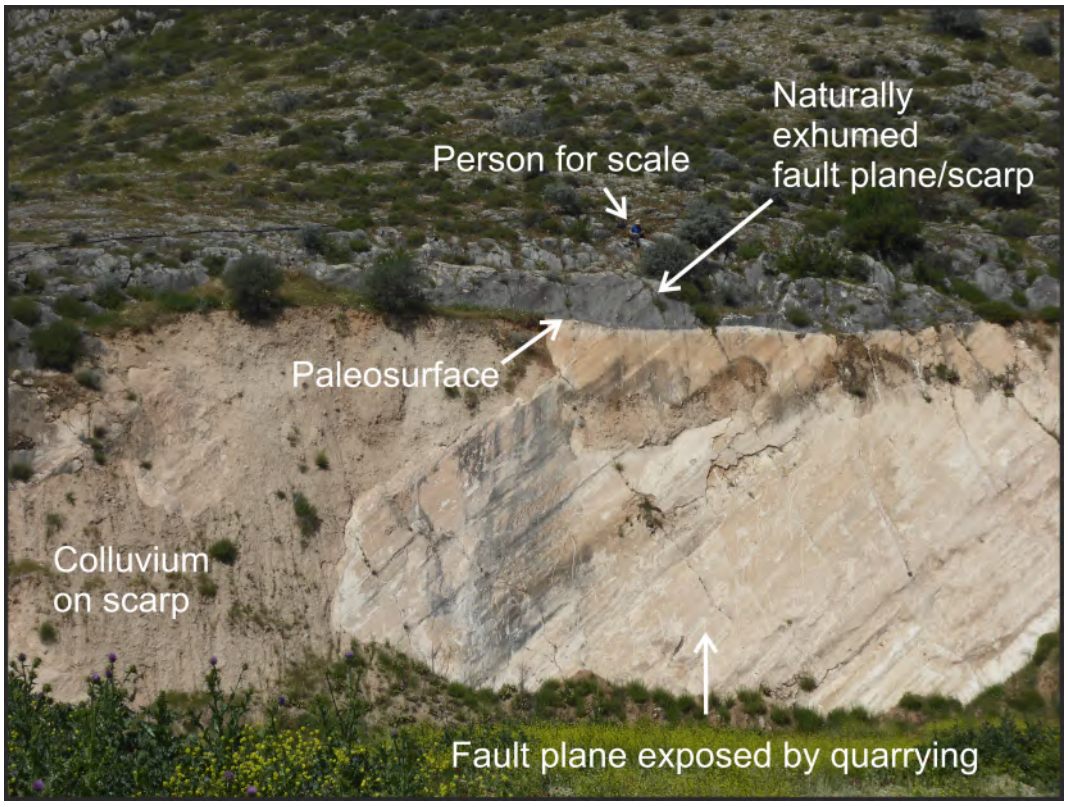

Figure 2.3: A limestone normal fault scarp on the Rahmiye fault that has been exposed by quarrying of the colluvium in front of the scarp. The pre-quarry paleosurface can be seen at the border between the light and dark sections of the fault scarp. These kind of excavations can be found throughout Western Turkey and Greece.

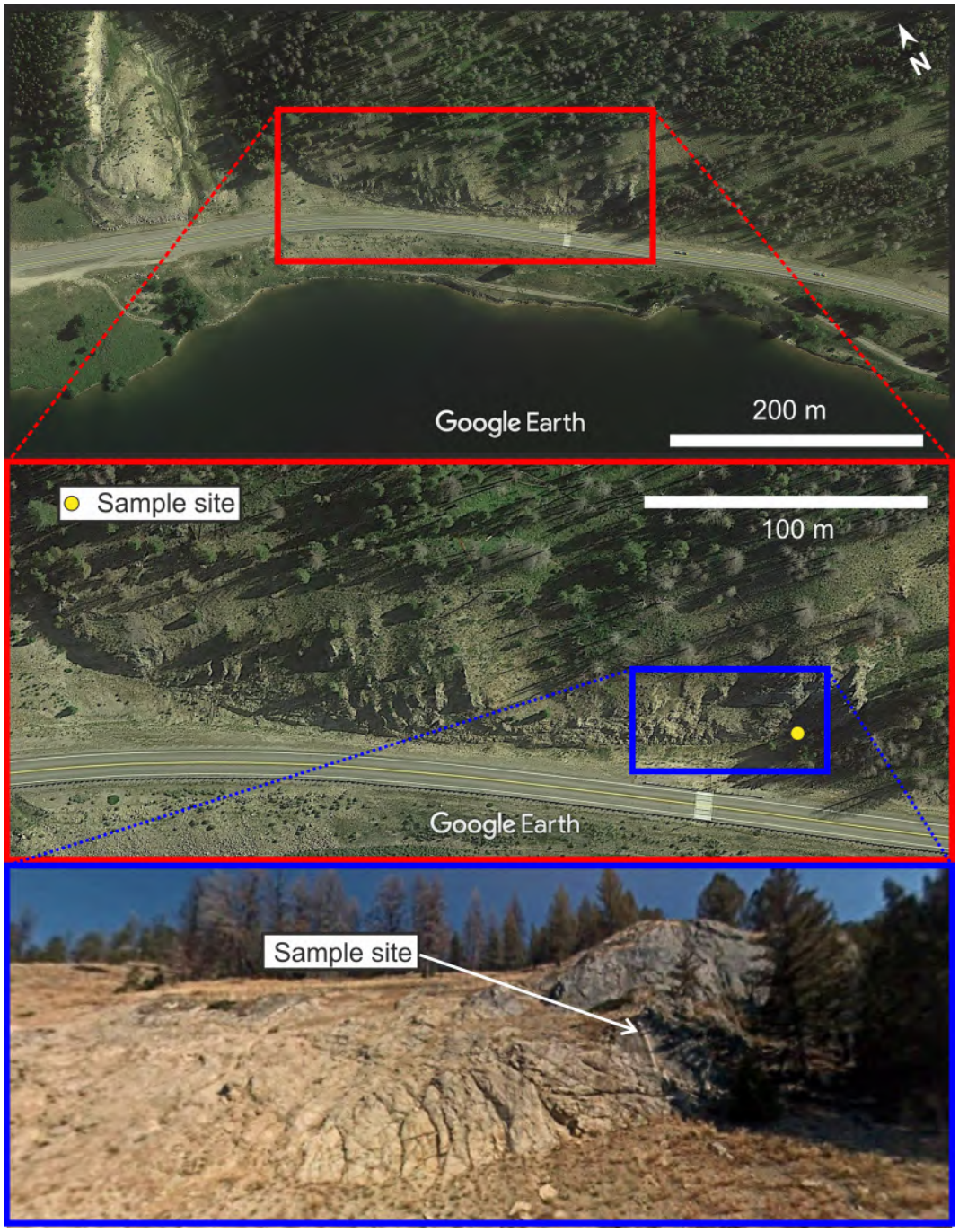

Figure 2.4: The first cosmogenic fault scarp sample site, sampled by *Zreda and Noller* (1998). Top two pannels show aerial imagery, bottom pannel shows google maps view of the sample site captured in 2008, field of view approximately 20 m.

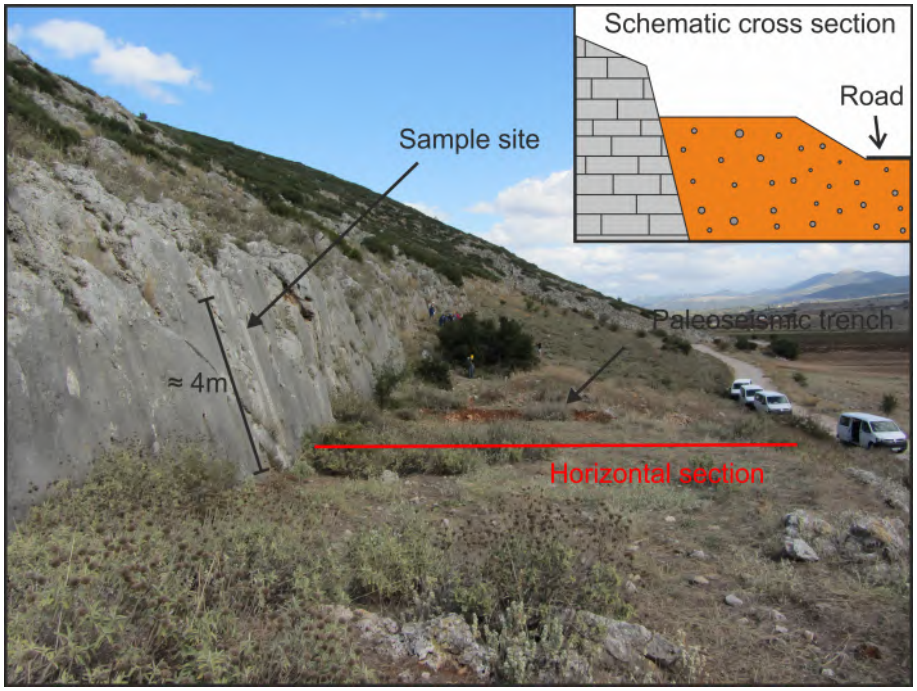

Figure 2.5: One of the sample sites on the Kaparelli fault which ruptured in a noral faulting earthquake in 1981 and was sampled by *Benedetti et al.* (2003) for ^{36}Cl analysis. The inset panel shows a schematic cross section perpendicular to fault strike, which deviates significantly from the ideal sample site location in it's hangingwall morphology (Figure 2.2).

down towards the basin. This indicates that the hangingwall has been modified such that material has been excavated from the fault to form the terrace. Further evidence of the anthropogenic slope modification is that the fault scarp is significantly higher at the sample location than 100 m along strike and you can see in the photo that the hangingwall is sloping not horizontal along strike. These features were not identified in the paper and are only apparent when visiting the sample site, which highlights the need to more quantitatively and clearly record and discuss sample site geomorphology and any existing problems with it. This study was found to be in disagreement with a paleosiesmic trench study conducted at a later date on the same fault (*Kokkalas et al.*, 2007), the trench data suggesting 2 events, the oldest between 9490 and 7150 ka, the youngest between 5710 and 1060 ka, and the ^{36}Cl data indicating 3 events at 20±3 ka, 14.5±0.5 ka and 10.5±0.5 ka. The poor geomorphology of the sample site is likely to have made a contribution to this discrepancy by changing the apparent timing of exhumation.

More recently *Mozafari et al.* (2019a) published two sites in western Turkey, one of these was on the Yavansu fault, which I visited in 2017. There is a paved road running along strike approximately 3 m from the base of the sample site (Figure 2.6). The slope is stepped because of the road and building construction that has occurred down slope. This indicates the fault scarp has been exhumed at least partially by non-tectonic processes. This is not accounted for or discussed by *Mozafari et al.* (2019a), and is not

at all apparent when reading the paper. East along strike, the fault plane does outcrop in areas where the slope appears unmodified, however I did not identify any section with appropriate geomorphology to sample due to morphological modifications of the hangingwall or footwall slopes, or poor preservation of the free face itself.

Occasionally it can be apparent in the ^{36}Cl data collected from a sample site that the scarp exposure can't be explained by tectonic exhumation. I visited an unpublished sample site 1.2 km from the sample site of *Akar et al.* (2012), which was sampled by the same group (Figure 2.7). Here I was informed by one of the co-authors that they were unable to successfully model the data. The site is characterised by a very steep fault which has a horizontal footwall slope for up to 8 m, which hosts a small building. Beyond the horizontal section the footwall slopes down to a large quarrying operation to the north. Satellite imagery shows quarrying in close proximity to the scarp began between 2002 - 2008, however the small building was present from before 2002 (the earliest Google Earth image) and is most likely the reason for the levelling of the ground immediately in front of the fault scarp. The fault scarp continues only for around 250 m along strike, and is excavated for a line of similar buildings to the one seen close to the sample site. The site published in *Akar et al.* (2012) has been excavated or built over, and no longer exists. Conclusions regarding both seismic hazard and our understanding of fault behaviour based on the datasets discussed above, are likely incorrect.

2.2.3 Evolution of modeling cosmogenic fault scarp data

Technological, scientific and mathematical advances mean that solving complex problem of using ^{36}Cl data to determine slip rates on normal faults has changed significantly in the last two decades. Here I will summarise how the modelling of this problem has become more sophisticated, with a particular focus on the methods that I will use in the rest of this thesis.

The earliest cosmogenic fault scarp study was undertaken by *Zreda and Noller* (1998) on the Hebgen Lake fault scarp in Montana, USA. To model the exhumation history of the fault scarp they used horizontal bands that vary in appearance and morphology up the scarp. *Zreda and Noller* (1998) suggest these bands represent offsets in paleo-earthquakes, and the variety in appearance and morphology is due to varying time exposed to weathering. They define 6 different zones with widths that are plausible coseismic offsets given the fault length using this method. They then calculate the average exposure age for the samples in each of these bands. The modelling accounts for four ^{36}Cl production pathways, neutron activation of ^{35}Cl, spallation of ^{39}K and ^{39}Ca and negative muon capture by ^{40}Ca. Exposure ages were calculated for samples in each of the weathering bands and then corrected for subsurface production. Whilst some exposure of the fault surface may be non-tectonic due to being located next to a road as previously discussed, this study demonstrated the potential of ^{36}Cl dating of

Figure 2.6: The site sampled by *Mozafari et al.* (2019a) on the Yavansu fault. Top panel: Google Earth imagery of the Yavansu fault, showing proximity to road and construction. The steep nature of the slope below the road suggests large scale anthropogenic modification. Bottom panel: Photograph of the sample site, view east along-strike.

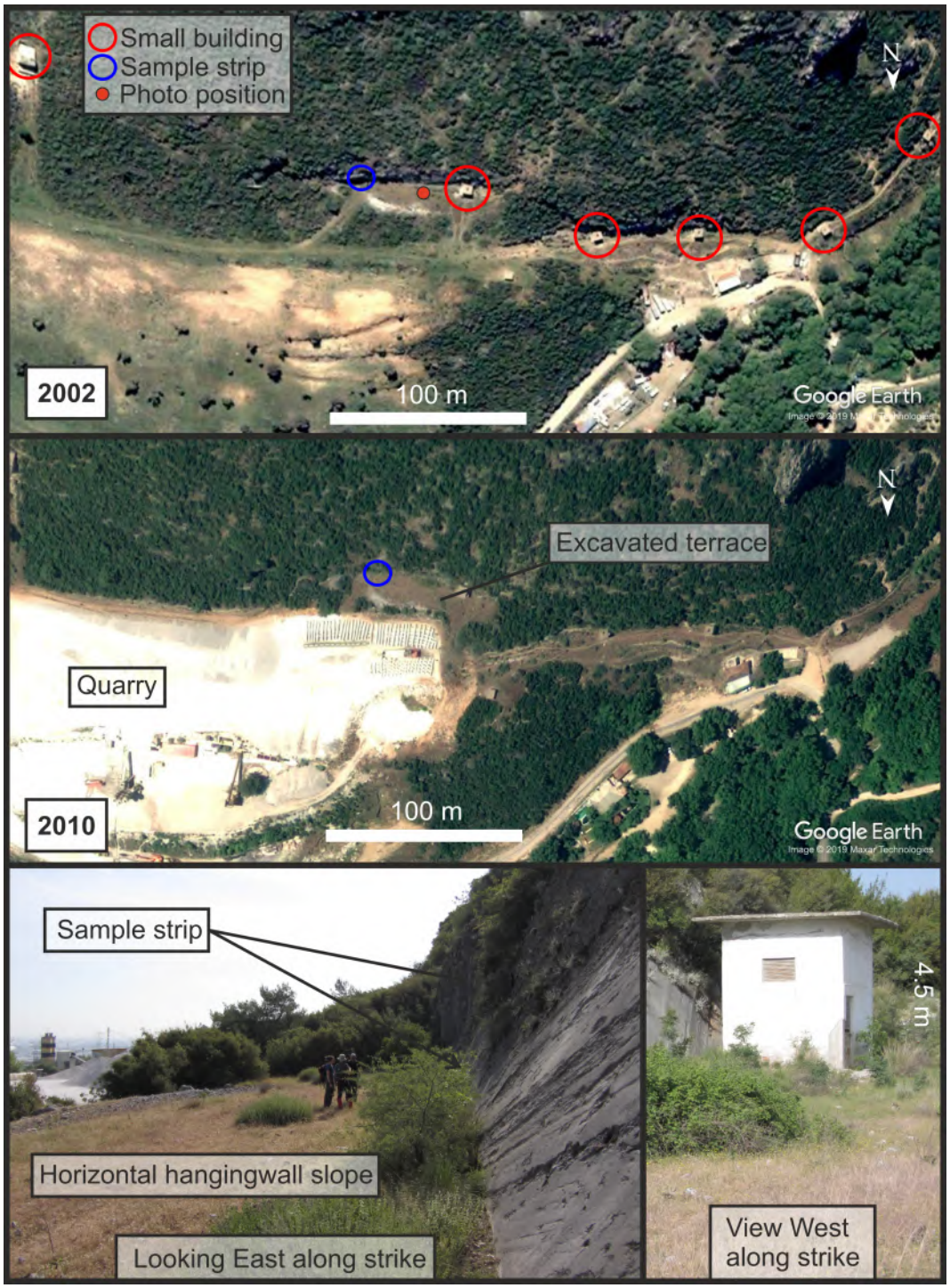

Figure 2.7: The unpublished site sampled by *Akar et al.* (2012) close to Manisa, Western Turkey. Top two panels: Google Earth imagery of the Yavansu fault, from 2002 and 2010 showing infrastructure affecting the sample site. Bottom left: Horizontal hangingwall slope indicates excavation of the fault scarp. Bottom right: Small building, possibly a pumping station, likely the reason for excavation and leveling by sample site. Photos taken from: N38.612114 E027.298128.

bedrock fault scarps.

Mitchell et al. (2001) developed a matlab code to model cumulative ^{36}Cl for given offsets at given times on the fault scarp. This code accounts for 7 production pathways for ^{36}Cl (Section 1.2.1) and requires manually entering the offsets and timing of the offsets into the code. *Mitchell et al.* (2001) demonstrated that their samples from the Nashef East normal fault in northern Israel can be fit by many different exhumation histories due to the complex production rate below the ground. Instead of trying to identify individual events they attempted to identify a robust temporal pattern of displacement, i.e. periods of relatively fast exhumation, and periods of slower exhumation. They demonstrated that with this modeling technique weathering bands are not required, as they were by *Zreda and Noller* (1998). *Mitchell et al.* (2001) used a 'goodness-of-fit' F to compare the fit to data of models, with a lower 'F' indicating a better fitting model.

$$F = \sum (^{36}Cl_{measured} - ^{36}Cl_{model}) \tag{2.1}$$

Benedetti et al. (2002) modelled ^{36}Cl data from two sites on the Sparta fault in southern Greece using a different method, in which the production rate changes with depth due to increased shielding, so the buried fault scarp develops a characteristic exponential like curve in concentration of ^{36}Cl with depth below the ground. This curve is then exhumed by an earthquake, producing a step change in ^{36}Cl concentration (Figure 2.8). By identifying the number and height of steps on the scarp, the number of earthquakes can be identified and then the age of these changes can be modelled by using a forward model. Manual searching of the timing of these events was then undertaken to find a best fit model. *Benedetti et al.* (2002) defined the best model as the model with the lowest root mean square (RMS) value of the difference between the measured data and modeled data, where n is the number of data, which is essentially identical to the approach of *Mitchell et al.* (2001).

$$RMS = \sqrt{\sum_{n} (^{36}Cl_{measured} - ^{36}Cl_{model})^2 / n} \tag{2.2}$$

The forward model was not published, but it is described as similar to that of *Mitchell et al.* (2001). Steps in the data were identified in this study by visually assessing the data. One problem with this step identification method is that in the study of *Benedetti et al.* (2002) the ^{36}Cl concentrations have not been adjusted for Ca concentration or other elements relevant to the production of ^{36}Cl, meaning that these step changes may just be a function of variable rock chemistry, and therefore production rate, of individual samples.

Benedetti et al. (2003) used a similar method of modelling two ^{36}Cl sites on the Kaparelli fault in Greece, but they added an estimate of the initial abundance of ^{36}Cl

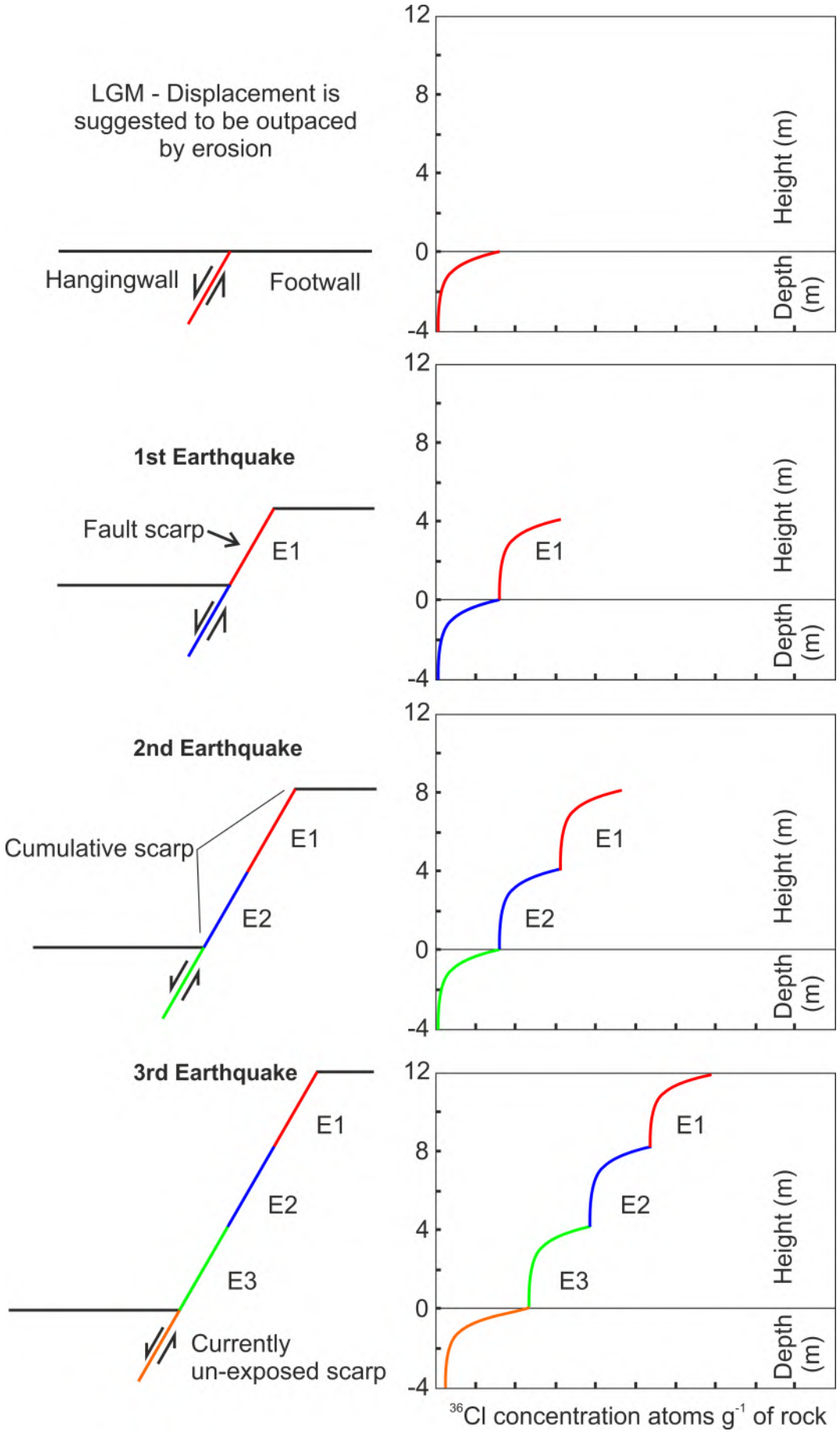

Figure 2.8: Schematic ^{36}Cl profiles of a scarp exhumed in three 4 m events, at regular intervals. *Benedetti et al.* (2002) pick events by picking step changes in the data, noted by change in colour in this figure. After a synthetic test in *Palumbo et al.* (2004).

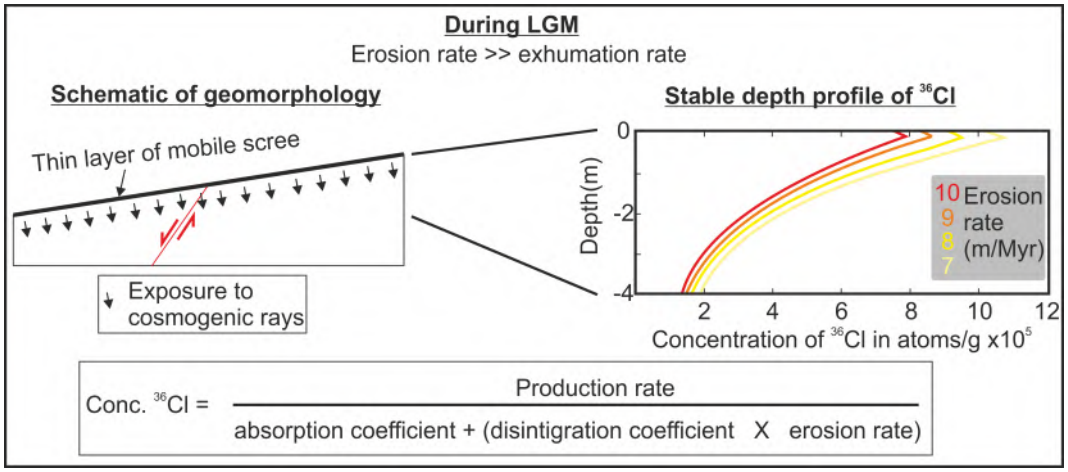

Figure 2.9: Schematic of the pre-exposure charateristic described by *Benedetti et al.* (2003). Production rate exponentially decreases with depth, and the disintigration co-efficient is 2.303 10^{-6} yr^{-1}. The absorption co-efficient is equal to the density of the material divided by the absorption mean free path (*Lal*, 1991). Over a period of a few 100 kyr, a ^{36}Cl profile similar to those shown on the right plot will build up, the form of which is varies depending on erosion rate, and other constants shown in the equation. After *Benedetti et al.* (2003).

as a function of depth below the maximum sample height up the scarp, prior to preservation of displacement on the fault. This abundance depends on the interplay between the accumulation of ^{36}Cl and erosion (Figure 2.9). *Benedetti et al.* (2003) used the highest of their samples to calculate a maximum erosion rate for this calculation in their model, though they advise that ^{36}Cl concentration from a sample in the footwall would further reduce this maximum bound.

Palumbo et al. (2004) sampled one site on the Magnola fault in the Central Italian Apennine. They model the data using the same method as *Benedetti et al.* (2003); however, as well as calculating a best fit model by considering the RMS of the fit to the data of the model as previous studies have done (*Benedetti et al.*, 2002, 2003; Equation 2.2). *Palumbo et al.* (2004) also calculate a 'best' model, using the Akaike Information Criterion (AIC), which takes into account the number of data n, the goodness-of-fit and the number of independent parameters p , which in this case is the number of exhumation events (*Akaike*, 1974).

$$AIC = n \log \left[\sum_{n} \left((^{36}Cl_{measured} - ^{36}Cl_{model})^2 \right) / n \right] + 2p \tag{2.3}$$

Using the AIC allows modellers to evaluate if the complexity of the model is justified by the data. *Palumbo et al.* (2004) find that whilst there was a lowest AIC value for 6 events, the value was almost as low for the range of 4 - 8 events.

A model was developed and published by *Schlagenhauf et al.* (2010) and tested on data from the site on the Magnola fault sampled by *Palumbo et al.* (2004), as well as samples at the same site taken from the buried scarp surface. This model builds

on previous models and provides a matlab package that calculates the ^{36}Cl for each sample for a given scarp exhumation history and a given pre-exposure age (the time which the pre-faulted surface was buried before it was faulted). The model calculates the weighted RMS (RMSw), where $\sigma^{36}Cl_{measured}$ is 1 sigma uncertainty of the ^{36}Cl AMS measurement, determined by the accuracy of the AMS.

$$RMSw = \sqrt{\sum_{i=1}^{n} \left[\left(\frac{^{36}_{i}Cl_{measured} - ^{36}_{i} Cl_{model}}{_{i}\sigma^{36}Cl_{measured}} \right)^2 \right] /n} \tag{2.4}$$

the chi-squared value,

$$\chi^2_{red} = \frac{1}{n-p-1} \sum \left[\left(\frac{^{36}Cl_{measured} - ^{36} Cl_{model}}{\sigma^{36}Cl_{measured}} \right)^2 \right] \tag{2.5}$$

and a version of the AIC, known as the AICc that has been modified for use where the ratio of the number of data n to the number of free parameters p is ≤ 40 (*Burnham and Anderson*, 2002).

$$AICc = n \log \left[\sum_{n} \left((^{36}Cl_{measured} - ^{36} Cl_{model})^2 \right) /n \right] + \frac{2pn}{n-p-1} \tag{2.6}$$

Schlagenhauf et al. (2010) used individual Ca concentration measurements for the samples collected in their study, and used average values for the samples from *Palumbo et al.* (2004). Instead of visually identifying steps in the data, *Schlagenhauf et al.* (2010) calculated the probability density functions (PDF) of each individual ^{36}Cl measurement based on the analytical error, stacked them and used peaks in the stacked PDF to identify earthquakes (Figure 2.10). This approach is based on the hypothesis that concentrations overlap due to the exponential-like decrease in production rate during the buried portion of the exposure history, and is done on data which has not been normalised for Ca concentration. *Schlagenhauf et al.* (2011) use the same modelling techniques to construct slip histories for 4 sites on the Magnola fault, and one site on the neighbouring Velino fault. This study will be discussed in more detail in the next section. *Benedetti et al.* (2013) use the modelling method of *Schlagenhauf et al.* (2010) to determine earthquake ages on 7 faults in the Central Italian Apennines, however they use average Ca values in the modelling. *Mouslopoulou et al.* (2014) also use the same method of to determine earthquake ages on the Spili Fault, on the island of Crete, Greece, and it is unclear if average Ca values were used.

Aside from the method to determine the best fit model, or best model, the primary change in models since the work of *Schlagenhauf et al.* (2010) is the method for searching parameter space. Until the work of *Tesson et al.* (2016), searching parameters was undertaken manually by users selecting parameters to trial. The increase in availability and development of computational power has resulted in the ability to search parameter

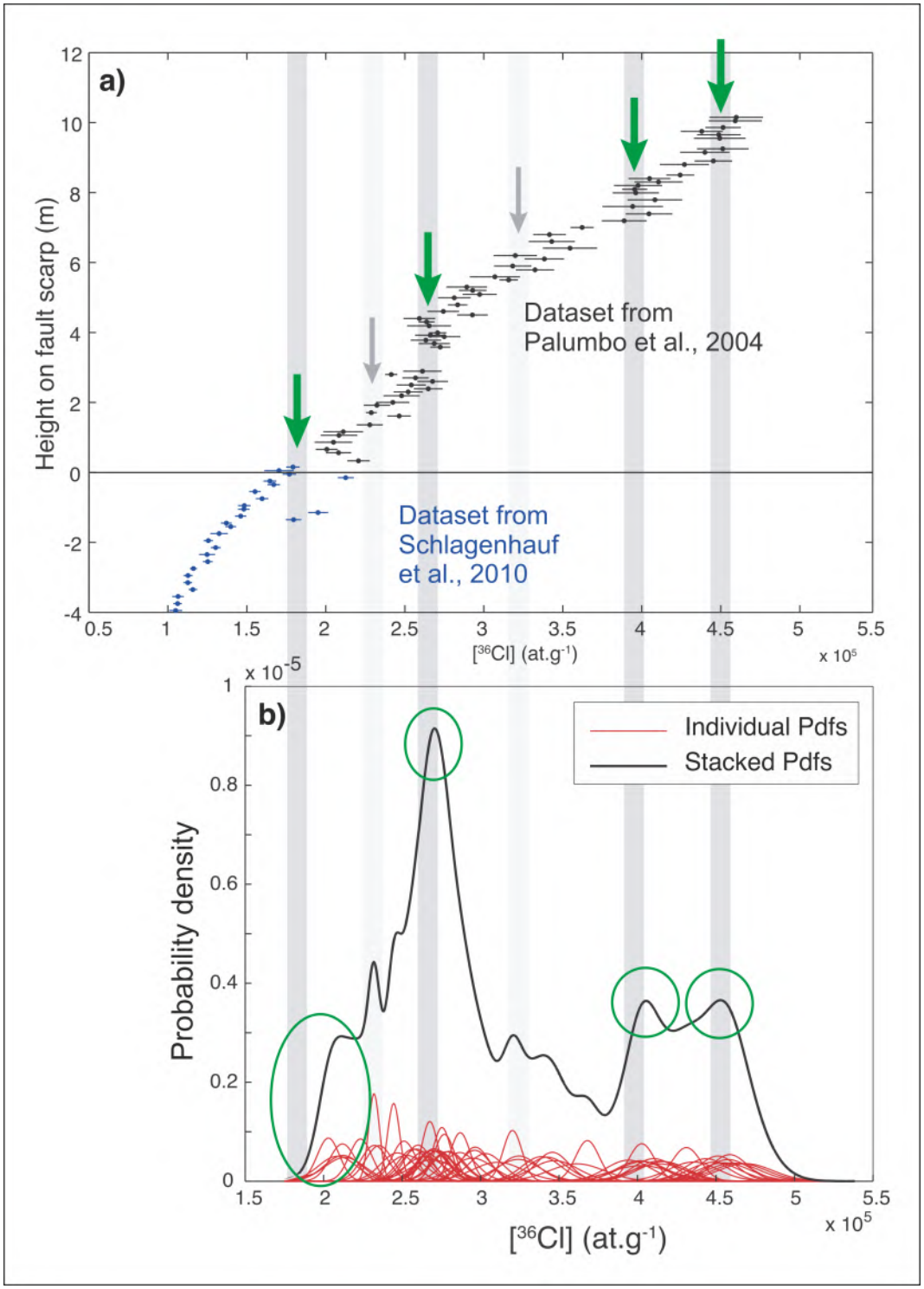

Figure 2.10: a) Measured ^{36}Cl from *Schlagenhauf et al.* (2010) and *Palumbo et al.* (2004) and their associated 1 sigma errors. b) The individual PDFs for each measurement and the stacked PDF. Grey bands and arrows show peaks in stacked PDF identified by *Schlagenhauf et al.* (2010). Modified from *Schlagenhauf et al.* (2010).

space in a more rigorous and effective manner. *Tesson et al.* (2016) use a Monte Carlo (MC) framework, using the code of *Schlagenhauf et al.* (2010) for the forward model. A random sample is drawn from the range of assumed acceptable values (prior distribution) for each parameter using an MC framework, which are then used as input parameters for the forward model (Figure 2.11). The modelled parameters for each earthquake are slip per event (with a boxcar prior distribution between 10-360 cm) and the ages of the events (a boxcar prior distribution between 500-10000 years), however the reasoning for these a priori distributions was never stated. If there are two events then two random ages must be generated, and one random event slip must be generated. The second event size is not independent because the summed event size of both events must equal the total displacement. They ran 9 separate MC inversions for scenarios from 2-9 events, on a ^{36}Cl data set from the Pizzalto fault in the Italian Apennines, and evaluated the goodness of fit using RMSw and χ^2_{red}.

Cowie et al. (2017) present 3 different methods for modeling new data from 7 fault in the Italian Apennines. They all use the code of *Schlagenhauf et al.* (2010) as a forward model. The first and most simple is constant rate. When *Cowie et al.* (2017) implement this they keep the slip size and inter-event time constant to produce a constant slip rate (Figure 2.12). To vary the slip rate between different models they change the inter-event time, which results in a different time when the oldest earthquake occured, which they define as scarp age. The forward model calculates the RMSw and the AICc, and a minimum value can be found by searching a range of scarp ages (or slip rates).

When the data are not fit well by a constant slip rate, the timing of the change in slip rate must be inferred, as well as the scarp age. *Cowie et al.* (2017) infer that the change in slip rate occurs at the height where there is a change in morphology of the scarp, which they call a change point. They define this by identifying discrete changes in roughness measured from terrestrial laser scan (TLS) data. They assume that a discrete change indicates a sudden exposure of a more fresh surface that is less weathered than the portion of the scarp above, and therefore a discrete change in slip rate. If there is only a continuous change in roughness, this would imply exposure of the fault at a constant rate. *Cowie et al.* (2017) assume a constant slip rate between the change points and the first and last event.

To model slip histories where they have TLS roughness data *Cowie et al.* (2017) use a more complex Bayesian Markov chain Monte Carlo (MCMC) framework, which is based on the Metropolis Hastings algorithm (*Metropolis et al.*, 1953, *Hastings*, 1970, *Sambridge et al.*, 2006). The Metropolis Hastings algorithm starts with an arbitrary set of parameters and passes them into the forward model, which calculates the fit to data using the likelihood function. During each iteration a small random perturbation is proposed to one of the parameters and the resulting fit is either accepted or rejected based on the ratio of the likelihood of the new model versus the previous accepted model (Figure 2.13). If the MCMC model is run for enough iterations, the distribution

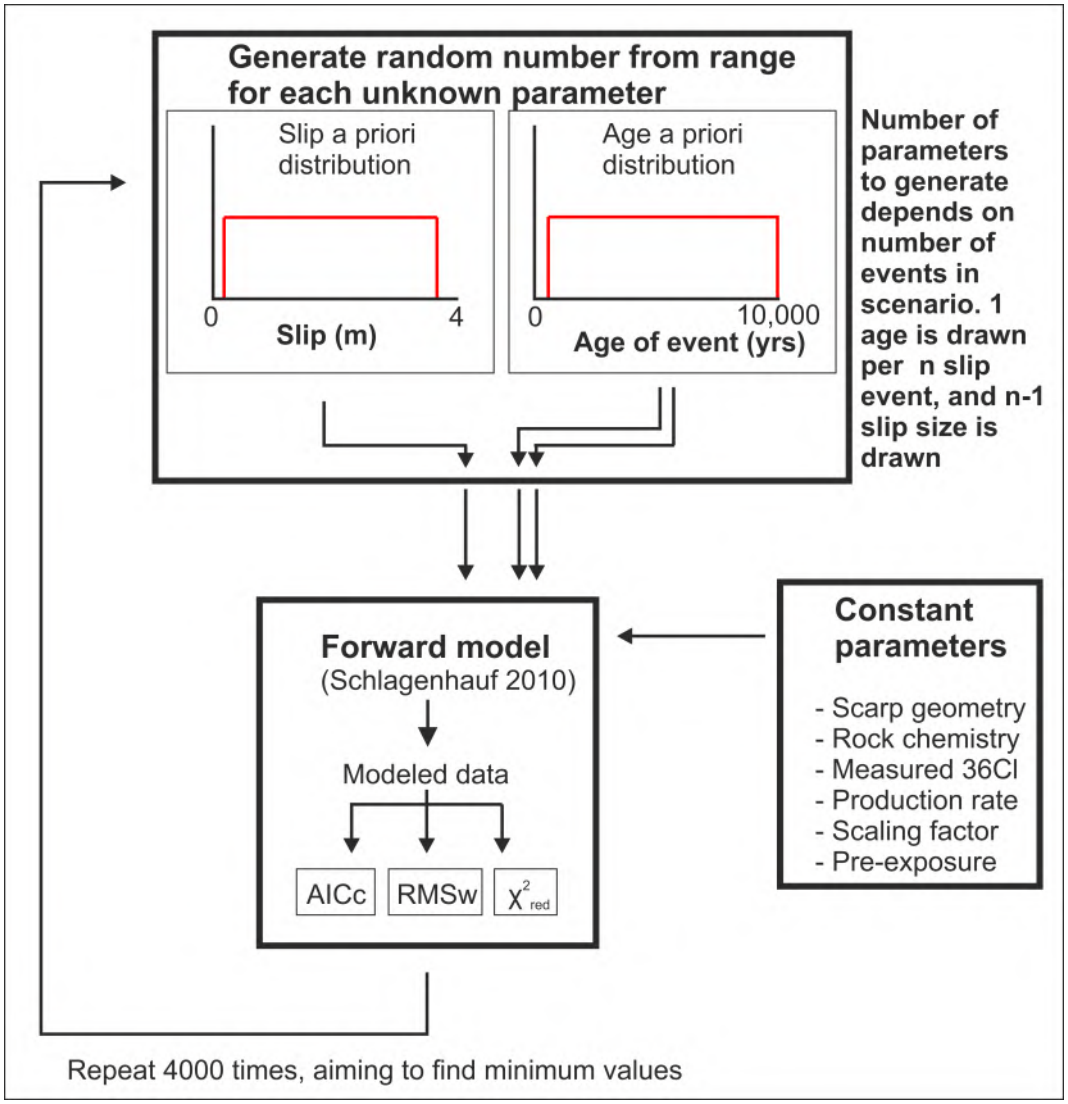

Figure 2.11: Schematic of the Monte Carlo framework used by *Tesson et al.* (2016) to explore parameter space for timing and age of earthquakes. This version is for a schematic for the 2 earthquake scenario. In this case a slip size parameter is only generated for event 1 because $event2 = (totalheight - event1slipsize)$. This means that the size of events 1 and 2 are not independent variables.

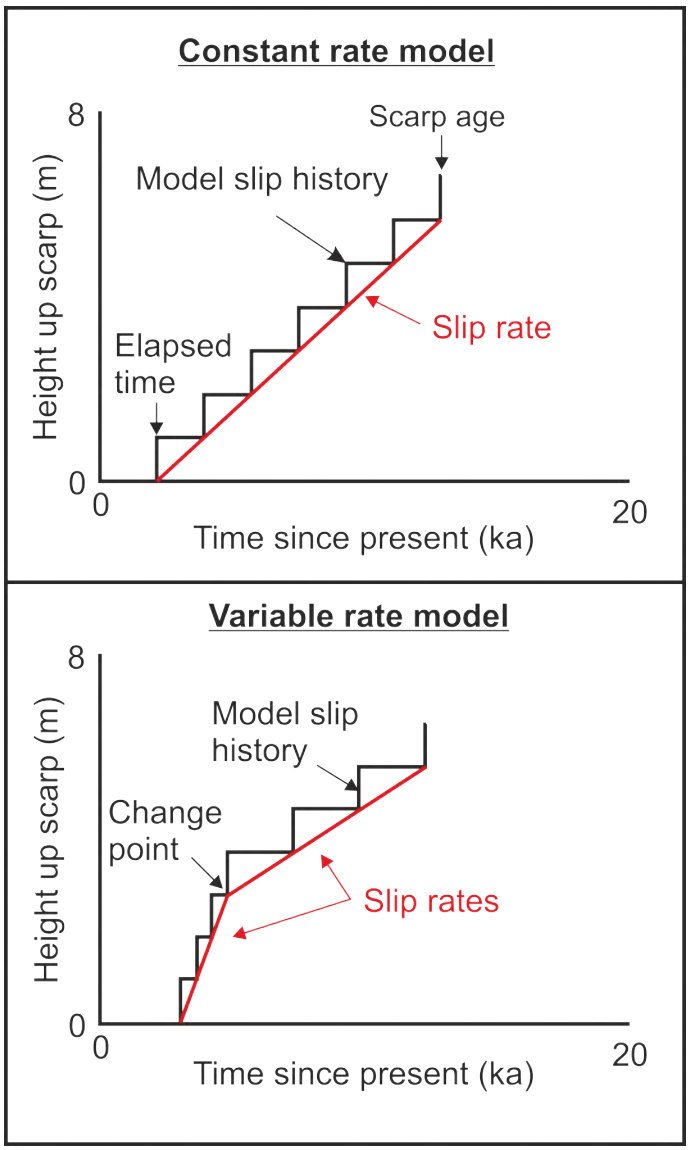

Figure 2.12: Top panel: how constant slip rate models are generated in the constant slip rate code of *Cowie et al.* (2017). Slip rate is varied by changing the scarp age. Bottom panel: how variable rates are modeled in the fixed and flexible change point models of *Cowie et al.* (2017) by changing length of time between exhumation events.

of parameters of accepted models will converge and represent the posterior distribution of parameters. Using this algorithm allows the inclusion of both data and independent information (priors). In the study of *Cowie et al.* (2017) the priors are timing of the most recent earthquake and the timing of the scarp age. The scarp age is when the first offset of the post LGM-slope occurred, the scarp may no longer be preserved, but the offset of the footwall slope and hangingwall slope is preserved (Figure 2.2). The parameters that are solved for in the MCMC model are the timing of the change points (changes in slip rate), elapsed time (time since last earthquake), and scarp age. Constant slip rates are modelled between these change points, using a stepped model as in the constant slip rate model of *Cowie et al.* (2017). When analysing the model output *Cowie et al.* (2017) remove models affected by the arbitrary start parameters, known as removing the burn in. This code is henceforth referred to as the fixed change point code, as the number and height up the scarp of the change points are fixed.

When there is no prior information on the number of changes in slip rate *Cowie et al.* (2017) use the flexible change point code, which is based on the reversible jump MCMC algorithm (*Green*, 1995). This trans-dimensional inversion allows for both the parameters and the number of parameters to be solved for, and produces an inherently parsimonious solution (*Bodin and Sambridge*, 2009). In the case of modelling ^{36}Cl data, this means that the number of changes in slip rate (change points) can vary, as well as the height on the fault scarp and the timing of change points. Theoretically there can be any number of change points, however the algorithm favours simple slip histories with low numbers of change points (generally <10). The 3 different inversions (constant rate, fixed change point and flexible change point) were applied to 7 faults in the Central Italian Apennines by *Cowie et al.* (2017).

Beck et al. (2018) developed a modeling code that also uses a MCMC algorithm to determine exposure histories from ^{36}Cl fault scarp data. They incorrectly suggest that the models of *Cowie et al.* (2017) do not consider uncertainties in the timing of the end of the LGM, when it is accounted for in the normally distributed prior for scarp age of 15 ±2.5 ka. *Beck et al.* (2018) use a more complex method to determine the shielding factors than those used in *Schlagenhauf et al.* (2010), in that they pre-compute a sparse grid of shielding factors using piecewise exponentials, but this method requires the assumption of a constant-in-time production rate. The end result is a code which runs in a similar but more efficient way than that of *Schlagenhauf et al.* (2010). *Beck et al.* (2018) also consider events that occur before the end of the LGM, they assume the scarps that form before the LGM are immediately eroded. The inversion solves for a series of fault displacement and event time values, which can both vary, unlike in the code of *Cowie et al.* (2017) where only event time can vary and displacement is kept constant. The inversion also allows inclusion of uncertainties in production rates, the timing of the end of the LGM and the density of the colluvium.

Beck et al. (2018) applied this code to the Fiamignano and Frattura faults in the

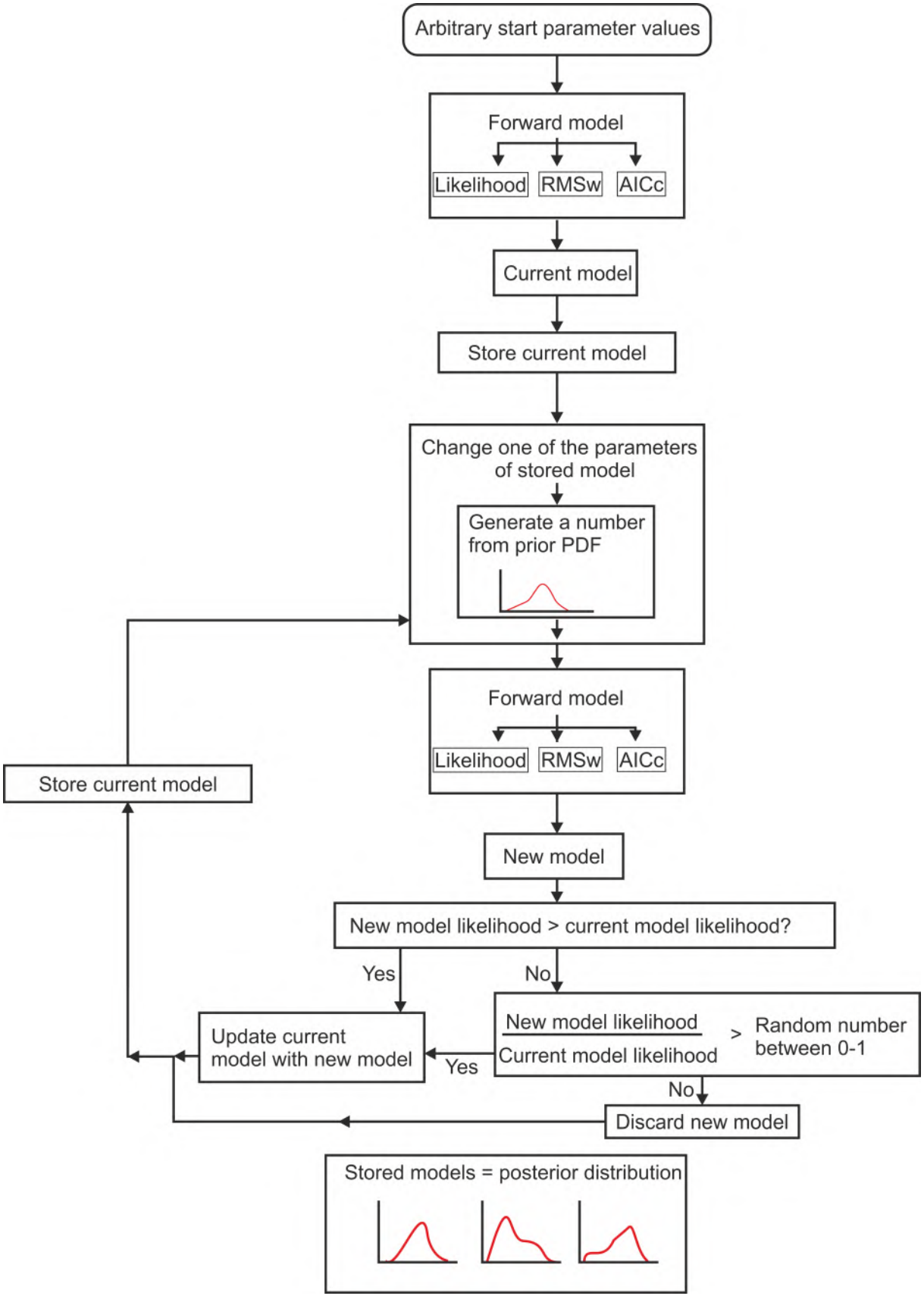

Figure 2.13: A schematic of the Bayesian modeling method used by *Cowie et al.* (2017).

Italian Appennines, remodelling data from *Cowie et al.* (2017). The modeling method of *Beck et al.* (2018) is similar to the method of *Cowie et al.* (2017) in that they only resolve periods of relatively fast slip and slow slip on a fault, meaning the inversion can not determine if a single large slip event occurred or if multiple smaller earthquakes occurred.

A third code has been developed by *Tesson and Benedetti* (2019), which also uses an MCMC reversible jump approach. They use an updated forward calculation, based on that in *Schlagenhauf et al.* (2010), but with updated muon production rate calculations from *Balco* (2017) and *Lifton et al.* (2014) which incorporate a more accurate model of muonic production rate with depth at the cost of increased computational expense. The *Tesson and Benedetti* (2019) code also solves for the long term inheritance, which similar to the pre-exposure used by *Schlagenhauf et al.* (2010, 2011) and others. This algorithm solves for the following parameters and *Tesson and Benedetti* (2019) use the stated ranges as boxcar priors; number of events (1 - 20), an event age (0 - 20000 years), event slip (0 - scarp height), the pre-LGM demise slip-rate (0,5mm yr^{-1}). Synthetic tests of the model of *Tesson and Benedetti* (2019) indicate that individual events can not be identified, though modelling may be able to identify a minimum number of surface rupturing events.

Most recently *Tikhomirov et al.* (2019) published a matlab code, which inverts for a user defined number of slips, parametrised by slip size and timing. There are 2 versions, one which uses a random walk algorithm and one which uses classical Monte Carlo algorithms, similar to *Tesson et al.* (2016). This method uses chi square value to determine goodness of fit. It is not a trans-dimensional inversion, so the inversion must be run multiple times to get results for multiple numbers of events (i.e. a seperate inversion must be run for each of 1 event, 2 events etc.). *Tikhomirov et al.* (2019) suggest using the AICc to determine the optimum number of events. The forward model is similar to *Schlagenhauf et al.* (2010), and the MC inversion method is similar to *Tesson et al.* (2016), however it is implemented differently. The inversion is undertaken in two steps; firstly particle fluxes, shielding factors and are calculated for 3D grid of all possible positions of a sample. This database is then used in the second step where the code randomly generates slip histories via either a Monte Carlo or random walk algorithm. Notably the authors do not cite any previous ^{36}Cl modelling codes in their paper, despite their similarity and the large body of work already undertaken in this field.

This range in approaches to modelling is due in part to the range of assumptions that can be made when approaching the problem of determining exhumation histories of fault scarps using ^{36}Cl data. Some methods rely on scarp roughness data to provide size of slip events, however these methods assume that slip events occurred in one earthquake. Given the knowledge that a fault can experience surface rupture multiple times in <12 months (e.g. Mt. Vettore in the 2016 earthquake sequence *Walters*

et al. (2018)) and the resolution of the ^{36}Cl data, this roughness data provides only a minimum number of events. On many faults roughness data is either not available, or changes in roughness are not observed in the TLS data. Modeling methods which rely on extra data cannot be applied universally, however when it is available it is useful to include, because while it may not be indicative of individual earthquakes, discrete changes in roughness may imply changes in slip rate or climatic conditions (*Cowie et al.*, 2017, *Mechernich et al.*, 2018).

Some methods rely on fitting subsurface curves or cusps in the data (*Benedetti et al.*, 2002, 2003, *Schlagenhauf et al.*, 2010), however it is not certain that cusps are formed due to the decay of production rate at depth. Variation in colluvium density through time due to water, large boulders or other similar uncertainties may explain some of these cusps, and quantifying this would be very difficult. In cases where the ^{36}Cl data have not been corrected for the chemistry of individual samples, cusps could be just due to variation in bulk chemistry between samples on the same scarp.

The resolution of ^{36}Cl data and inherent uncertainties that cannot be captured by current modelling makes identification of individual events difficult to do with any certainty. The methods of *Tesson and Benedetti* (2019) and *Beck et al.* (2018) work around this by attempting to fit the data with a large number of events of varying size. Unsurprisingly, they get a good fit to the data, however it appears unwanted complexity in the model is made to fit measurement noise rather than actual signal. The field has generally moved toward inversion processes that can quantify uncertainties using trans-dimensional Monte Carlo or similar algorithms (*Cowie et al.*, 2017, *Beck et al.*, 2018, *Tesson and Benedetti*, 2019), the changing nature of production rate with depth below colluvium makes the problem one which does not have a unique solution, which makes using a modelling method which can provide indication of uncertainties vital. These do however have a penalty of being computationally expensive due to the iterative nature, though evolving computing power and improving code will eventually negate this. *Cowie et al.* (2017) take one of the simplest approaches by reducing the number of variable solved for compared to that of *Beck et al.* (2018) and *Tesson and Benedetti* (2019) and using periods of constant slip rates between discrete changes in rate. This approach has the opposite problem in that it is likely over-simplifying the real exhumation history, however it is much less likely to overfit the data than models with a greater number of parameters. The code of *Tesson and Benedetti* (2019) has the advantage that it attempts to solve for pre-exposure, which is not really addressed in any of the other Bayesian inversions, however this comes at the price of a a greater number of parameters. A table of the four most recent modelling methods, with a summary of their key features, and the main pros and cons for their use is shown in Figure 2.14.

To summarise, there is currently no modelling method which can convincingly determine the timing and/or magnitude of individual earthquakes using ^{36}Cl fault scarp

Model	Features	Pros/cons
Cowie et al., 2017	~ 3 methods used ~ All use Schlagenhauf, 2010 as a forward model ~ All used fixed exhumation sizes ~ Constant rate model tries a range of constant slip rates at equal spacings and calculates fit of each model ~ Other method uses Schlagenhauf, 2010 in a Bayesian Markhov chain Monte Carlo (MCMC) framework. ~ Solves for timing and position of changes in slip rate ~ Can either use roughness/morphology data to determine where change in slip rate occurs ~ Or use trans-dimensional MCMC method to determine number, timing and position of changes in slip rate ~Outputs each model and its fit to data (Likelihood, RMSw, AICc)	**Pro** ~Range of inversions of increasing complexity ~ Does not require scarp morphology data but can use it ~Statistically robust method f or searching parameter space ~ Does not use cusp ~ Generally uses fewer parameters to fit models ~ Allows time varying production scaling factors **Con** ~ Doesn't solve for individual events ~ Computationally expensive ~ Fixed pre-exposure age. ~ Uncertainties in model inputs not considered like in Beck 2018 ~ Uses simple "pre-exposure" to consider time before scarp preservation ~ Written in Matlab (license required)
Beck et al., 2018	~ Tran-dimensional Bayesian MCMC with reversible jump ~ More efficient forward model ~ Solves for timing and size of indiviual events ~ Cannot resolve individual events ~ Includes uncertainties for production rate, timing of LGM and colluvium density. ~ Assumes constant in time production rate at given depth (i.e. non time varying scaling factor)	**Pro** ~ Efficient forward problem ~ Attempts to resolve individual events ~ Only needs fault scarp data ~ Considers pre-scarp-preservation period in more sophisticated way ~ Written in python (open) **Con** ~ Greater number of parameters used than Cowie 2017 ~ Cannot vary production factor in time ~ Output difficult to interrogate ~ Complex proposal functions and a-priori means that care must be taken. If the chosen priors are incorrect, then the model output will be incorrect. The greater number of priors can compound this.
Tesson et al., 2019	~ Tran-dimensional Bayesian MCMC approach ~ Forward model has updated muon production vs Cowie 2017 ~ Considers pre-scarp-preservation ~ Relative speed unknown ~ Solves for timing and position of individual events ~ Cannot resolve individual events, but can resolve minimum numbner of events	**Pro** ~ Simple proposal mechanism ~ Better muon production model ~ Considers pre-preservation period ~ Written in python (open) **Con** ~ Greater number of parameters used then Cowie 2017 ~ Better muon model is more computationally expensive
Tikhomirov et al., 2019	~ Monte-Carlo, or random walk inversion ~ Solves for timing of a user defined number of events ~ Different method of forward model ~ Speed unknown	**Pro** ~ Simple proposal mechanism **Con** ~ Not-transdimensional, so comparison between scenarios requires multiple inversions ~ Unlikely to be efficient in searching parameter space ~ Relies on knowing number of slip events, which is not typically known. ~ Matlab (license required) ~ Authors do no compare at all to any previous modelling

Figure 2.14: A table showing the major features, pros and cons of the four most recently published ^{36}Cl fault scarp modelling methods, from *Cowie et al.* (2017), *Beck et al.* (2018), *Tesson and Benedetti* (2019) and *Tikhomirov et al.* (2019). It is worth noting that only *Cowie et al.* (2017) was published when I began work on this thesis.

data, despite the majority of studies attempting to do so. However, one or two changes in slip rate over a period of 10-15 kyr can be resolved. This is because whilst there can be a 'best' model, there are many models which fit the ^{36}Cl data almost as well. Going forward, uncertainties on parameters such as colluvium density, scarp geometry etc., should be incorporated into the model of *Cowie et al.* (2017). The field has generally moved from trying to identify individual earthquakes, which appears wise given the non-unique nature of the problem, and inherent uncertainties. Any future modelling method should continue to move away from the use of 'cusps' first identified by *Benedetti et al.* (2002), and should use an efficient and statistically robust method to search parameter space. Testing of any modelling method should be undertaken using real world data and a similar general method to *Schlagenhauf et al.* (2011). The hypothesis should be that, if the method is reliable, then multiple closely spaced sites along strike on a single fault should result in similar slip histories. In the next chapter I will test this hypothesis using data from the Magnola fault in Italy from *Schlagenhauf et al.* (2011), and the modelling method from *Cowie et al.* (2017).

Chapter 3

^{36}Cl dating of the Magnola fault

"With four parameters I can fit an elephant, and with five I can make him wiggle his trunk"
John von Neumann

3.1 Summary

The objective of this chapter is to determine if multiple ^{36}Cl sample sites along the same fault produce similar slip histories, when modelled in a way which treats all sites identically. To achieve this I model ^{36}Cl data from the Magnola fault because this is the only published data set with four sample sites on a single fault. The study on the Magnola fault was published by *Schlagenhauf et al.* (2011), who used a modelling approach which does not treat each site uniformly. *Schlagenhauf et al.* (2011) say that the 4 sample locations on the Magnola fault produce similar slip histories, however I find that when using a more appropriate modelling method that the 4 sample sites produce 4 surprisingly different slip histories. I indicate that this difference between closely spaced sites is because the sample sites have been affected by geomorphic processes other than tectonic exhumation. I propose a new study should be undertaken using data from sample sites where the geomorphology indicates that the the footwall and hangingwall slopes have been stable since the end of the LGM.

3.2 Background

If cosmogenic isotope dating of bedrock normal fault scarps is a reliable tool for determining slip rates or timings of earthquakes on normal faults, multiple closely spaced sample sites should give similar exhumation histories because earthquakes in general cause surface rupture along the length of the fault in a consistent pattern (though deviations will be discussed later). Two studies have sampled two sample sites on the same fault to see if they are in agreement (*Benedetti et al.*, 2002, 2003), however

(*Benedetti et al.*, 2003) arbitrarily vary the pre-exposure at different sites on the same fault, without explaining the process that would contribute to variable pre-exposure at closely spaced sites on the same fault. The sample sites of *Benedetti et al.* (2003) have also been partially exhumed by anthroprogenic processes (*Benedetti et al.*, 2003), as discussed in Section 2.2.1.

Schlagenhauf et al. (2011) present data from 4 sites on the Magnola fault and one on the neighbouring Velino fault, located in the Central Italian Apennines. They modelled the data using the code of *Schlagenhauf et al.* (2010) and in order to fit the data from the 5 sites with similar slip histories they varied the pre-exposure between sites, ranging from a value of 2.5 ka to 13 ka. Pre-exposure is a way to parameterise the time period the scarp has been preserved close to the surface before the first modelled earthquake. If climatic conditions and earthquake slip are the same along fault, which approximately they should be, then the pre-exposure period should also be approximately the same. The 10 kyr variation in pre-exposure is not justified by the authors, and I would expect that there is not a large variation in pre-exposure (up to 10 ka) between sample sites spaced a few km apart. The duration of pre-exposure directly sets the timing of the events, and *Schlagenhauf et al.* (2011) have varied the pre-exposure until the timing of events correlated between sites. Figure 3.1a demonstrates the effect of pre-exposure by using either 100 or 10,000 year pre-exposure in a model, the same exhumation history will produce very different ^{36}Cl concentrations. This means that if the pre-exposure is varied by 10 kyr, the timing of exhumation events, or changes in slip rate of the best fitting model will vary by thousands of years (Figure 3.1b).

3.3 Method

To test whether the sites on the Magnola fault can be modelled using similar parameters along strike with the same exposure history, I re-modelled the data from the Magnola fault using the Markov chain Monte Carlo (MCMC) flexible change point code of *Cowie et al.* (2017). I chose this modeling method because the simple nature of the code means there is limited opportunity to over fit the data, and the simplicity makes it easier to compare between sites than the more complex MCMC codes of *Tesson and Benedetti* (2019) and *Beck et al.* (2018). The code of *Cowie et al.* (2017) also writes out all accepted models, allowing full interrogation of the data, which gives it a significant advantage over the code of *Beck et al.* (2018). Also there seems to be little difference in the resolution of the modeling methods of *Cowie et al.* (2017),*Beck et al.* (2018) and *Tesson and Benedetti* (2019), so using the simplest model that can fit the data is the best start. For these reasons I used the *Cowie et al.* (2017) model in my modelling in this chapter and in chapters 4 and 5. I used the same input parameters as *Schlagenhauf et al.* (2011), but I kept the pre-exposure constant between sites at 100 years, because I model the full height of the scarp (total post LGM offset Figure 2.2) rather than the

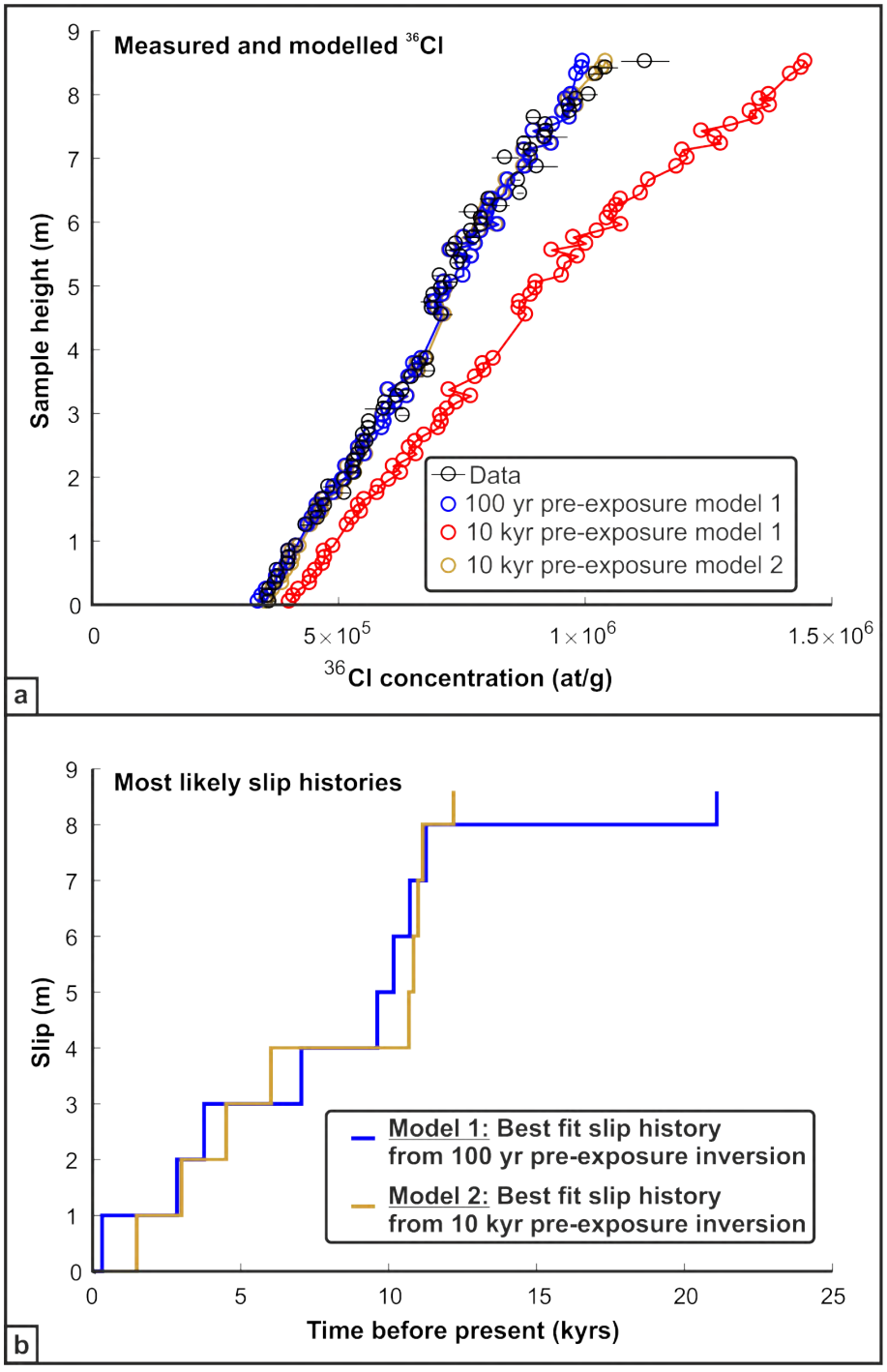

Figure 3.1: a) Data from site MA2, along with a best fitting slip history generated using the flexible change point code of *Cowie et al.* (2017) using a pre-exposure value of 100 years, in blue, and 10 kyr in gold. The red points are the ^{36}Cl concentrations generated by using the same best fitting model that produced the concentrations in blue, but with a pre-exposure age of 10 kyr. b) shows the best fit exhumation history for site MA2 that produced the models in the top panel in blue, and gold shows the best fit slip history produced if the flexible change point code is run assuming and pre-exposure age of 10 kyrs. Note that the slip histories vary in their timing of changes in slip rate, and therefore events, depending on the value of pre-exposure used. The largest effect is in the oldest part of the slip history.

height of the highest sample. 100 years is the minimum value the *Schlagenhauf et al.* (2011) code, which is used as the forward model in the codes of *Cowie et al.* (2017), will accept. This pre-exposure and the the method for modeling, which more thoroughly explores the available slip-rate parameter space, are therefor the key differences between this study and the work of *Schlagenhauf et al.* (2011). I also do not try to force the results to be the same along strike.

3.3.1 Method of comparison between sites

Comparing between the output of the MCMC code of *Cowie et al.* (2017) for different ^{36}Cl sites is difficult to do in a quantifiable way. Whilst the MCMC inversion does produce a best-fit model, this model will vary depending on how best-fit is defined. The inversion outputs the likelihood, the RMSw and the AICc calculated for each slip history, and the highest likelihood model will not necessarily have the lowest RMSw values etc.. Another consideration is that all MCMC codes produce a posterior distribution, and in this case, a distribution of possible slip histories. Whilst there is a 'best' model, there are commonly many models that fit the data almost as well. This means that to compare between sample sites requires comparison between multivariate distributions. To further complicate matters I must use the transdimensional code of *Cowie et al.* (2017) rather than the the fixed change point code, because I have no independent information for the height of the change points (such as surface roughness). This means I may either compare varying-dimensional distributions, or choose an arbitrary number of change points. To allow the number of change points to be informed by the data I will use the variable change point code, which means I must compare between solutions of varying dimensions.

To determine whether two distributions are identical, tests such as the ANOVA (*Fisher*, 1992) or Kruskal-Wallis test (*Kruskal and Wallis*, 1952) can be used. These tests allow rejection of null hypothesis, i.e. are two populations of models drawn from the same distribution. These tests work only if the null hypothesis is that the two distributions that models are drawn from are identical. However, in the case of comparing slip histories betweens sites, the distribution of slip histories from each site can not be identical, because the scarp height varies between sites meaning they must have experienced different slip histories. This variation in height may be due to either random noise during each rupture as well as more permanent variations in slip over multiple events, as discussed in Chapter 1. These along strike variations in slip, which are known to occur from observations of modern earthquake ruptures, mean that any relatively simple comparison of distribution tests, like the ANOVA or Kruskal-Wallis, is not appropriate. As a result I use a more qualitative approach to comparing between sites. I compare the slip history distributions by plotting the 95% confidence intervals of the slip history distributions, along with the most likely slip history and determine if these are similar in their magnitude and timing of changes in slip rate.

3.3.2 Morphology of the Magnola Fault

The Magnola fault is 10 km long and located approximately 1-2 km from the Velino fault to the NW and sample sites are spaced at ∼1-2 km distance along strike (Figure 3.2). The fault strikes ∼110 degrees and dips to the south west. ^{36}Cl concentrations from above ground samples at site MA3 were published by *Palumbo et al.* (2004) and all other sites and results from the below ground samples from MA3 were published by *Schlagenhauf et al.* (2011). Assessing the quality of the sample sites is difficult as I have not visited them, but there are photos of each site in *Schlagenhauf et al.* (2011). Site MA1 has a white stripe along the base of the scarp (Figure 3.3A), which suggests recent exposure of the bottom of the scarp, along with a non-horizontal hangingwall-footwall contact. Given the lack of recent earthquakes along the fault and the discontinuous nature of this white line, it suggests that hangingwall material may be being removed locally by non-tectonic processes, such as recent removal of decaying vegetation, or more long-lived slope processes. Lens distortion in the photo makes it difficult to asses how level the contact between the fault scarp and the hangingwall is. Site MA2 has non-ideal geomorphology, as the contact between the fault scarp and the hangingwall slope is not horizontal (Figure 3.3B), suggesting active removal or deposition of material on the hangingwall slope. Colleagues have visited site MA2, and report that it is located in an ephemeral stream, so material is likely being removed by this. The sample ladder is offset laterally at several points, which may increase the effect of an uneven fault scarp/hangingwall contact. The geomorphology of site MA3 looks reasonable given the limited photos available, though material may have been removed from the hangingwall by large gully east along strike, exposing the free face in a non-tectonic process (right in Figure 3.3C). MA4 has a sloped hangingwall/faultscarp contact and the ladder steps along strike to above a section which appears to have a much higher contact between the fault scarp and hangingwall (Figure 3.3D). I did not model their other site VE, as it is located on a different fault which adds further complication to interpretation, as the relationship between the Velino and Magnola fault may not be temporally correlated as one may rupture without the other.

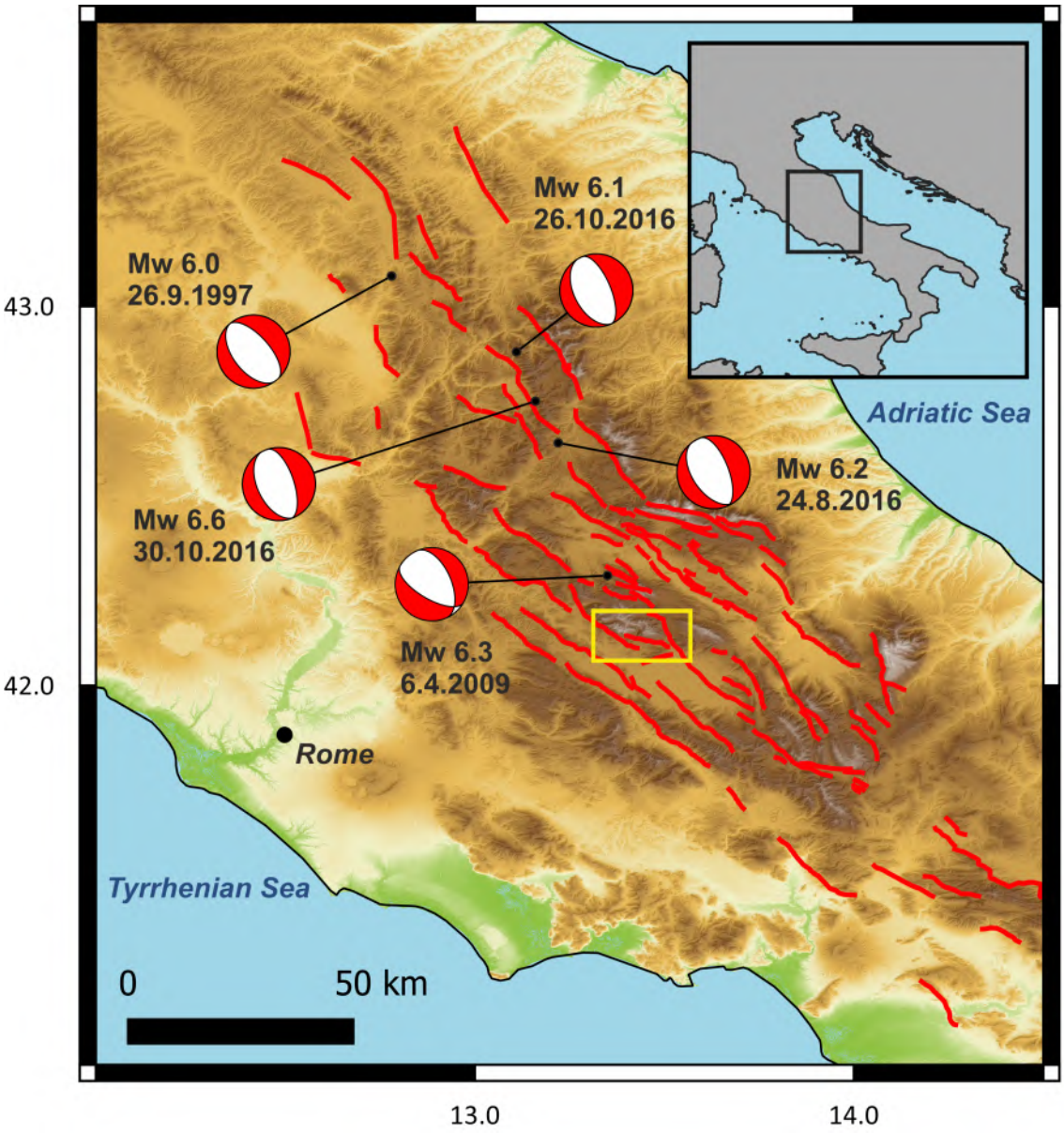

Figure 3.2: Map of ^{36}Cl sample sites on the Magnola and Velino faults. Faults from *Roberts and Michetti* (2004), site locations from *Schlagenhauf et al.* (2011). Location of figure is shown in Figure 1.13.

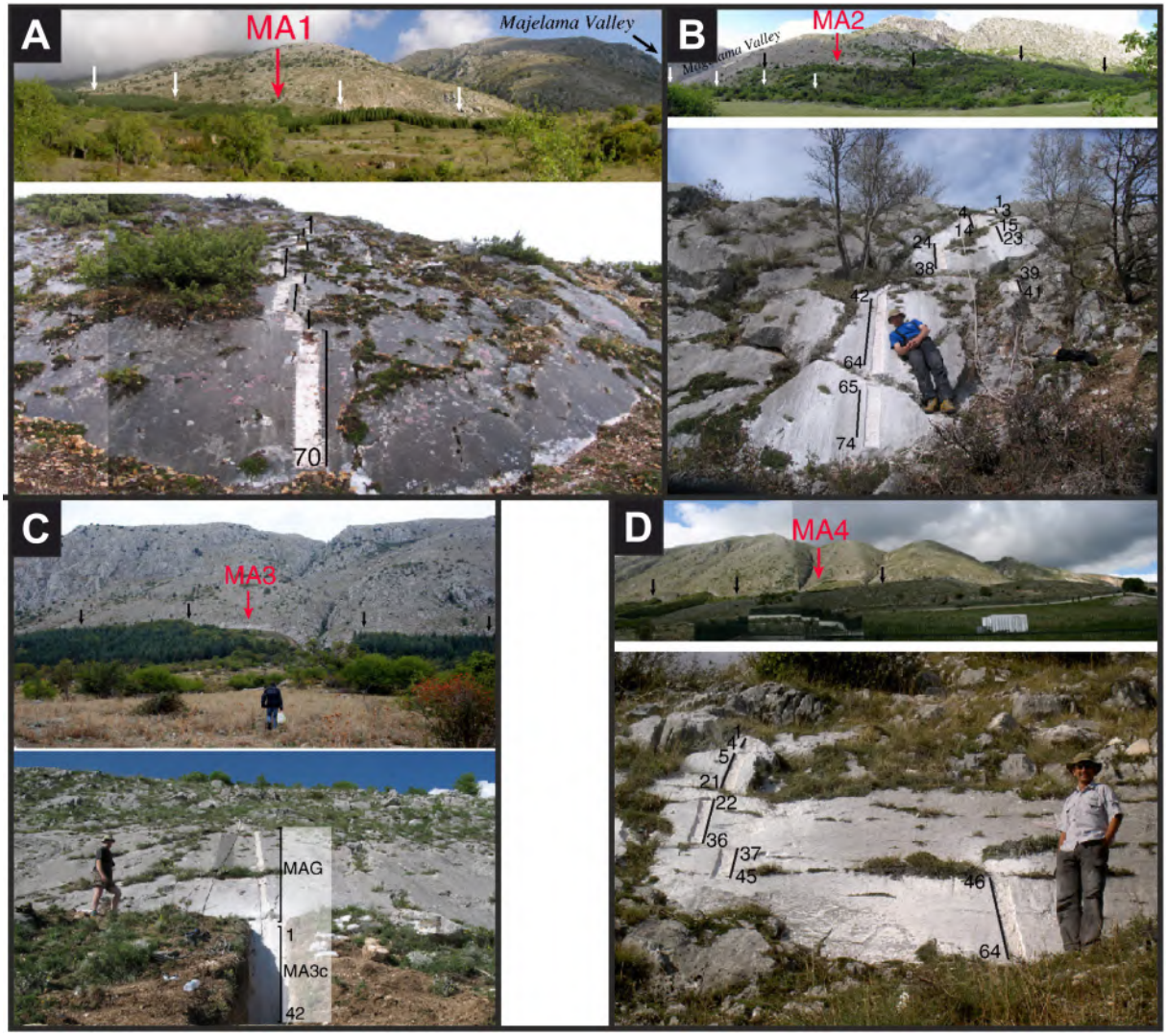

Figure 3.3: Photos of ^{36}Cl sample sites on the Magnola fault, sampled by *Schlagenhauf et al.* (2011) and *Palumbo et al.* (2004). Photos from *Schlagenhauf et al.* (2011). A) Site MA1, note the light grey stripe at the base of the fault scarp. B) Site MA2, note the stepped ladder located above the sloping contact between fault scarp and hangingwall. C) Site MA3, the upper picture shows how this section is close to an erosive gully. D) Site MA4, note uneven scarp/hangingwall contact, and the sample ladder which steps to an area with a higher scarp/hangingwall contact.

3.4 Results of modelling ^{36}Cl data on the Magnola fault

^{36}Cl concentration vs height for sites Ma1-Ma4 is plotted in Figure 3.4. Results of the constant slip rate modelling for the same sites is plotted in Figure 3.5 and the results for the variable slip rate modelling are plotted in Figures 3.6 and 3.7.

The gradient of ^{36}Cl concentration versus height varies between sites, whilst data are not corrected for Ca concentration the gradient of ^{36}Cl with height is a function of the slip rate on the fault (Figure 3.4). A high gradient (steep slope) indicates a faster slip rate, a lower gradient indicates a slower slip rate. Site 3 has the highest gradient,

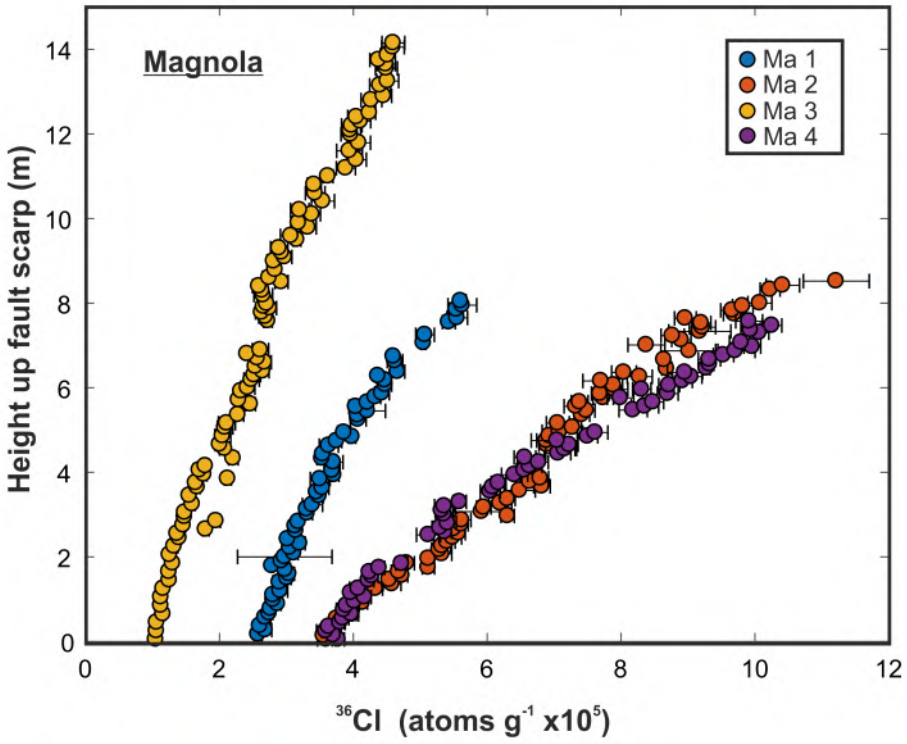

Figure 3.4: Data from *Palumbo et al.* (2004) and *Schlagenhauf et al.* (2011) with analytical uncertainties of the AMS measurement plotted.

and site 1 has a similar gradient to site 3, whilst sites 2 and 4 lower gradients (Figure 3.4).

To determine if the data can be fit with a constant slip rate, I used the constant slip optimisation code from *Cowie et al.* (2017) (discussed in Section 2.2.3, Figure 2.12). I set the model to search scarp ages at 200 year increments, where scarp age is defined as the time at which the the oldest event occurred that is preserved in the post-LGM offset (Figure 2.2). The site that can be most closely modelled with a constant slip rate is MA1, however there is still a systematic misfit, with modeled values being too low at 0-2 m and too low at 7-8 m (Figure 3.5). Data from site Ma2 can be modelled using a constant slip rate up to a sample height of around 6 m, where the model no longer fits the data, and Ma3 and Ma4 also have increasing misfits above 5 m and 4 m respectively. Best fit scarp ages vary by 9000 years between sites, and the resultant constant slip rates range from 0.6 mm to 2.7 mm (Table 3.1), which suggests that these sites have undergone different exhumation histories. These results suggest variable slip rates are required to properly model the data, because constant slip rate histories produce systematic misfits (Figure 3.5). The optimisation curves can be seen in the right panels in figure 3.5.

In an attempt to get a better model fit, I modelled each site using the MCMC flexible change point code from *Cowie et al.* (2017), again fixing the pre-exposure at

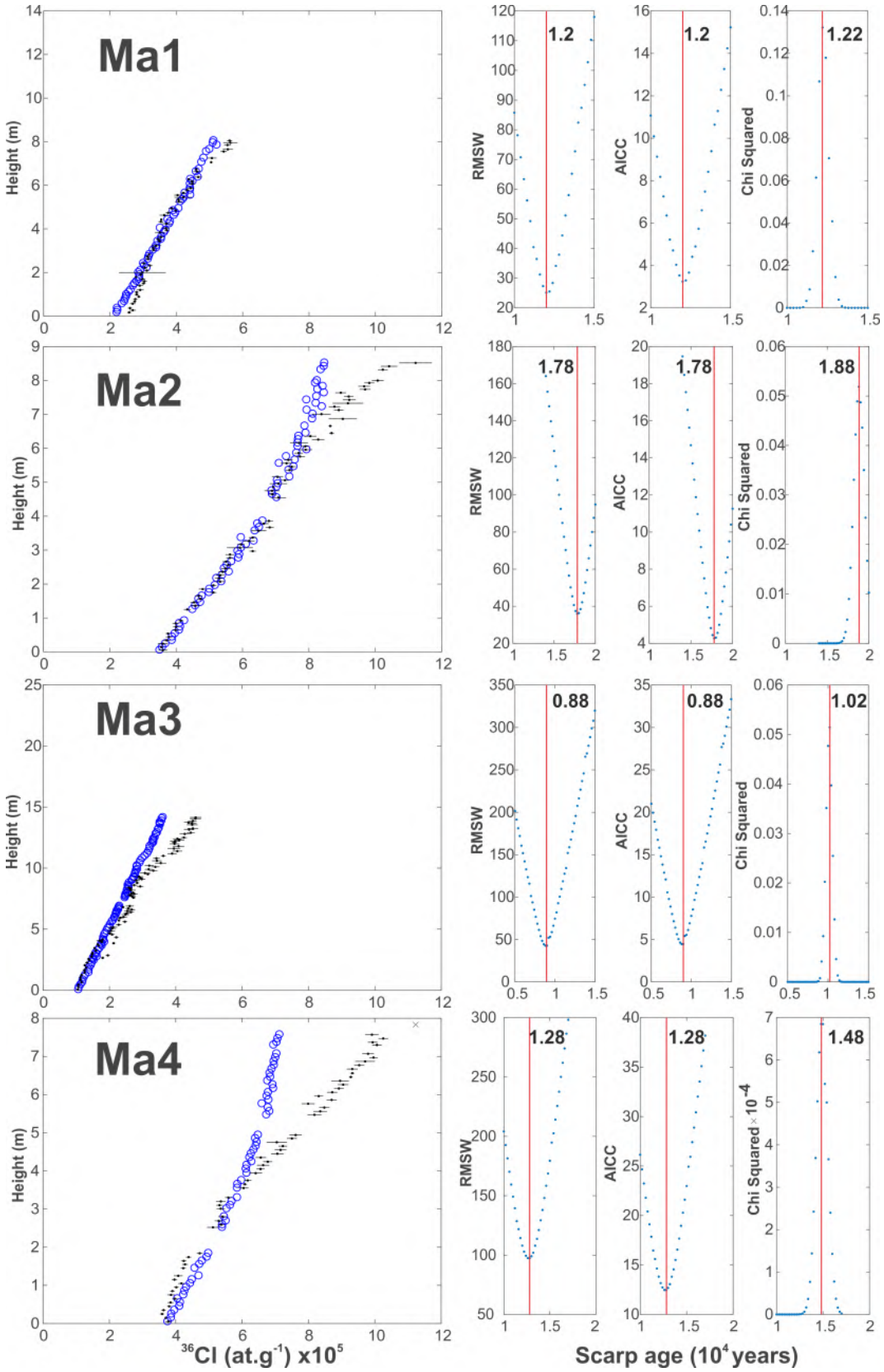

Figure 3.5: Left column shows the data (black) and model (blue circles) for the lowest RMSw constant rate slip history. Plots on the right show the RMSw, AICC and χ^2_{red} values for constant slip rates with different scarp ages, with the optimum value shown by red line and values. Note the x and y axis values vary between scarp age plots.

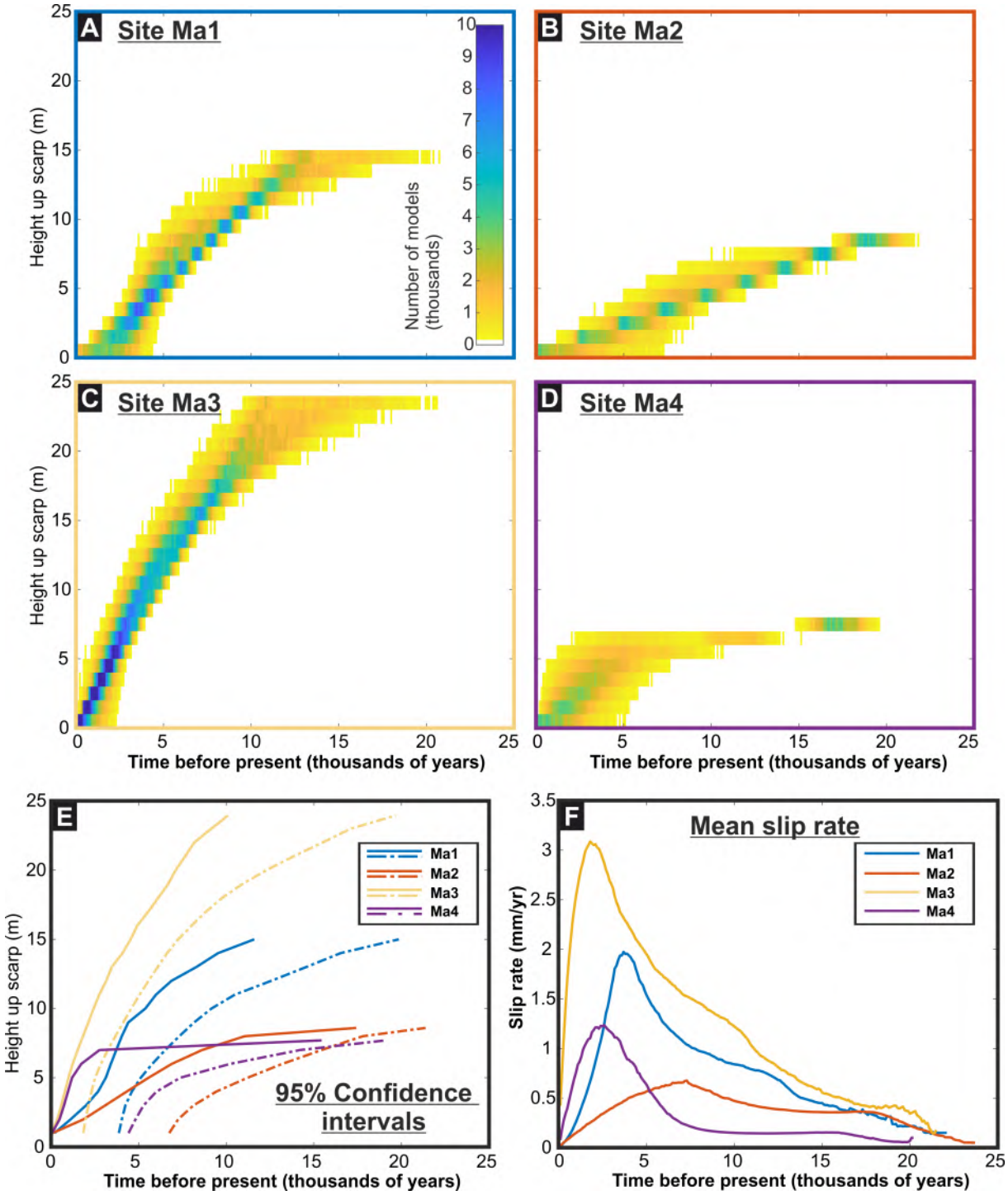

Figure 3.6: Results of remodelling the sites on the Magnola fault, using the data from *Palumbo et al.* (2004) and *Schlagenhauf et al.* (2011), and the model of *Cowie et al.* (2017). Plots A-D) Distribution of slip histories, binned into 200 year bins. A burn in of 10,000 has been removed in this and other plots in this figure. E) 95% confidence intervals of plots A-D. F) Average incremental slip rate of model distribution.

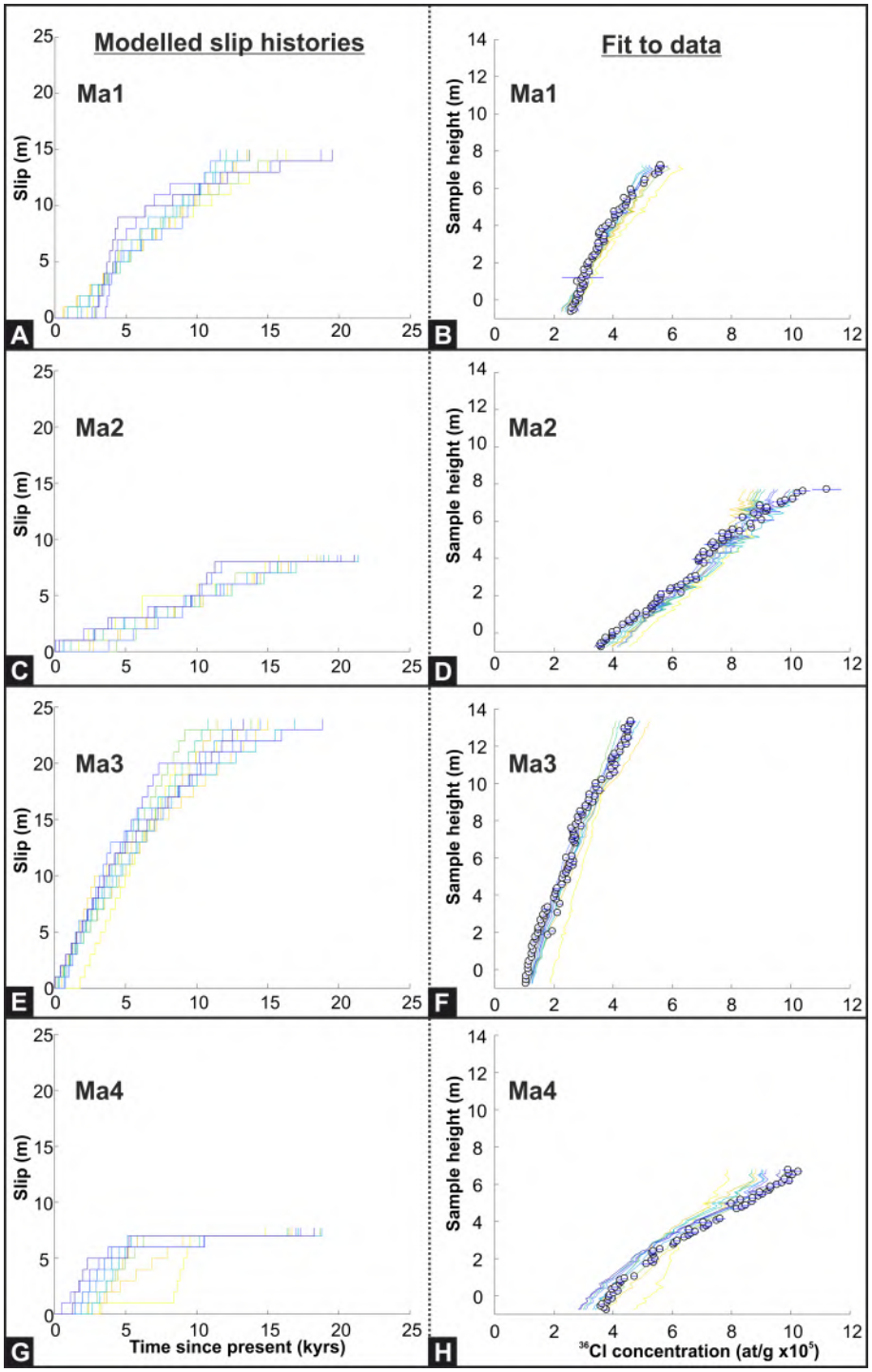

Figure 3.7: Plots A,C,E and F show slip histories of a selection of accepted models. I present 10 models from each site, ranging from the highest to lowest likelihood at equal intervals, represented by the variation from darker to lighter colours. Plots B,D,F and H show corresponding fit to data of accepted models (coloured lines, with darker colours showing the most likely and lighter colours showing the least likely) and models (black circles, with horizontal blue lines showing analytical error).

Site	Scarp height (mm)	Scarp age (years)	Average Slip rate (mm/yr)
Ma1	15000	12000	1.25
Ma2	8600	17800	0.48
Ma3	23950	8800	2.72
Ma4	7700	12800	0.60

Table 3.1: Lowest RMSw models from constant slip rate modelling for the sites on the Magnola fault.

100 years. All sites apart from Ma2 show a preference for a variable slip rate, which is reflected in both the 2D histograms of slip histories and in the mean slip rate plot (Figure 3.6). The slip rate is different between each sample site, shown by the varying gradients in the first 5 kyr at all sites (Figure 3.5A-E), as well as the difference in timing and magnitude of peak mean slip rates (Figure 3.5F). The data are better fit by the variable slip rate models; Ma1 is well fit by the best fitting models, in that there is no systematic missfit, (Figure 3.7A-B), Ma2 has a small systematically misfit, in that the last 4 data points are not well fit even in the best fitting model (Figure 3.7C-D), Ma3 has a systematic missfit below around 3 m(Figure 3.7E-F), and the clearest missfit is in models of site Ma4, which struggle to fit the majority of the data points(Figure 3.7G-H). Models of all sites show a relatively slow slip rate before 5-10 kyr BP, with an increase in slip rate, peaking at ≈3-8 kyr BP depending on the site, before declining to the present (Figure 3.6). The slip rates in the last ≈ 2 kyr BP would change significantly if there was an earthquake in the near future, so the slowing of slip rates in this time period should be ignored.

3.4.1 Discussion

Given the uncertainties that are not captured by the model, sites Ma1-3 are fit reasonably well by the slip histories shown in Figure 3.6, but site 4 is not being captured well by the modelling due the systematic misfit of the majority of the data (Figure 3.7). Sites Ma4 and Ma2 have higher ^{36}Cl concentration at the same height on sites Ma1 and Ma3. Sites Ma4 and Ma2 also have sloping contacts between the fault plane and the hangingwall slope, and therefor they may have undergone similar non-tectonic exhumation of the scarp such as drainage removal of hangingwall material, resulting in a similar ^{36}Cl vs height profile (Figure 3.4). It may be that Ma4 has undergone a more complex exposure history, in that it has been exposed and then re-buried before being exposed again, possibly multiple times, resulting in a ^{36}Cl vs height profile that can not be reproduced in models which do not allow re-burial of the scarp. Aside from the fit of the models, there are differences between the distributions of slip histories at the 4 sites on the Magnola fault. On the first order, the total Holocene scarp offset ranges from 7.7 m to 24 m. This variation in scarp height does not occur in any systematic way such as the maximum displacement in the centre of the fault. Low slip at the western end of the

Magnola fault could be explained by strain being accommodated by the Velino fault, which is located southwest of the Magnola fault (Figure 3.2), but a systematic trend of increasing slip away from the Velino fault would be expected. It seems more likely that the variation in scarp height is due to removal of hangingwall material by erosion, leading to taller section of exposed bedrock fault plane. Site Ma3 has the largest scarp height (24 m) and is located in an area where there is active erosion in the hangingwall, indicating that this erosion contributes significantly to the exposure of the fault scarp. This erosional signal cannot be accounted for by simply varying the scarp age or pre-exposure parameters, because the temporal history of exhumation/burial due to erosion is unknown. Given the concerns with site geomorphology at the other sites on the Magnola fault, discussed in previous sections, it is not possible to deconvolve the exhumation due to earthquakes and the exhumation caused by other slope processes, using the current dataset. There may be some variation in slip histories between sites due to genuine variation in millenial and longer term slip rates along strike on the fault, such as those described by *Brozzetti et al.* (2019) on the Mt. Vettore fault. Determining if there is long term variation in along strike slip rate requires collection of new ^{36}Cl datasets from sample site where the geomorphology indicates that exhumation of the limestone fault scarp is solely due to tectonic processes, because as previously discussed, deconvolving the tectonic and non-tectonic exhumation adds significant complexity to modelling with a greater number of unknowns. Given the variation in slip histories between sample sites on the Magnola fault, as well as the problems with site selection at all sites, it is difficult to know which, if any, of these sites provides a reliable record of slip on the Magnola fault.

3.4.2 Conclusion

Whilst it is not quantifiable, there should be significant overlap between slip history distributions of closely spaced sample sites on the same fault. This is not the case for the sample sites on the Magnola fault. This is either because, the fault scarp at the sample sites has been exhumed by non-tectonic processes and therefore they do not represent tectonic exhumation of the fault, or there is large variation in slip rate along strike on the fault over a distance of ≈4 km. Given the geomorphology indicates non-tectonic processes contribute significantly to exhumation of the bedrock scarp at the sites as previously discussed, I believe this to be the cause of the discrepancy. The variation in behaviour along strike required does not appear reasonable, and there is no clear reason why ^{36}Cl dating of bedrock fault scarps should not be reliable. To demonstrate the reliability, a new experiment is required, sampling multiple sample sites along strike on the same fault using only data from sites where the geomorphology indicates that the scarp has only been exposed by tectonic processes.

Chapter 4

Determining reliable cosmogenic slip histories on bedrock normal faults

Huw J. Goodall[a], Laura C. Gregory[a], Richard P. Shanks[b], Luke N.J. Wedmore[c], Ken McCaffrey[d], Ruth M.J. Amey[a], Gerald P. Roberts[e], Richard J. Phillips[a], Andrew Hooper[a]

[a]*COMET,School of Earth and Environment, University of Leeds, UK*
[b]*Scottish Universities Environmental Research Centre (SUERC), East Kilbride, UK*
[c]*Department of Earth Sciences, University of Bristol, Bristol, UK*
[d]*Department of Earth Sciences, Science Laboratories, Durham University, Durham, UK*
[e]*Department of Earth and Planetary Sciences, Birkbeck, University of London, UK*

Corresponding Author, Huw J. Goodall, ee09hg@leeds.ac.uk

Foreword

This paper was submitted by myself and the co-authors listed below for publication. I collected, processed and analysed all data for sample sites Cf2 and Cf3, and Rp2. Samples and data from sites Cf1 and Rp1 were collected by co-authors before I started my PhD, and I processed Cf1 and Rp1 whilst working for Laura Gregory as a research assistant before beginning my PhD. ^{36}Cl samples were measured by Richard Shanks, and ICP-OES measurements were undertaken by Stephen Reid at the University of Leeds. I produced all writing and figures within the following chapter, with comments from co-authors, and I would like to thank all co-authors for assisting with this study. This work was supported by the UK Natural Environment Research Council (NERC) through the Leeds-York NERC Doctoral Training Program NE/L0025274/1, standard grant NE/I024127/1, and NERC IRF NE/M019020/1. I am grateful to Greg Houseman, Tim Wright and Richard Walters for providing their insight and discussion at all stages, and Tim Craig for his assistance in producing two of the figures.

4.1 Summary

The objective of this study is identify if multiple ^{36}Cl sample sites on a single fault produce similar slip histories when modelled. I chose to work on the Campo Felice and Rocapretura faults in the central Itallian Apennines because both faults had existing data sets, meaning that I could compare results between research groups and maximise the number of sites in the study. In my study I used samples from four sites on the Campo Felice fault, and three sites on the Rocapretturo fault. I find that if a sample site with appropriate geomorphology is used, then the method is a repeatable and reliable method for determining slip rate. I also find that the method can resolve both spatial and temporal variations in slip rate. The implications of this are that the method is a powerful, reliable tool for investigating fault behaviour, and that future studies should consider taking multiple sample sites on a single fault.

4.2 Background

Activity of normal faults during the late Quaternary is key to understanding current earthquake hazard along faults. Knowledge of fault slip histories also aids investigation of fundamental questions of how faults interact and how they behave on timescales longer than the instrumental record. Slip rates can be measured using a wide variety of tools. Where faults have limestone bedrock scarps, the cosmogenic isotope ^{36}Cl can be used to determine not only the average slip rate over a certain period, but also a more complete history of exhumation by earthquakes over multiple seismic cycles (*Benedetti et al.*, 2002, *Schlagenhauf et al.*, 2010, *Akar et al.*, 2012, *Cowie et al.*, 2017, *Mechernich et al.*, 2018). The technique has been exploited most in the Mediterranean area as geologic conditions mean limestone fault scarps are common and well preserved in the region (*Benedetti et al.*, 2002, *Schlagenhauf et al.*, 2010, *Akar et al.*, 2012, *Cowie et al.*, 2017, *Beck et al.*, 2018). Previous ^{36}Cl based studies on these scarps have concluded that significant slip rate variations occur over thousand year time scales (*Cowie et al.*, 2017, *Schlagenhauf et al.*, 2011).

Interpreting fault scarp cosmogenic isotope data is complex, due to challenges in modelling the data, the multiple pathways which ^{36}Cl is accumulated, and how fault scarps are preserved. The exhumation history must be modelled, because the ^{36}Cl data do not directly reflect an exposure age because cosmogenic isotopes accumulate while the fault is partially buried. Careful study of sample site geomorphology is key in determining if the fault scarps have been exhumed by earthquakes, or if other geomorphic processes contribute (*Bubeck et al.*, 2015).

Data collected from multiple closely spaced sites along one fault should have similar slip rates. *Schlagenhauf et al.* (2011) attempted to compare between multiple sites on a single fault, by sampling multiple sites on the Magnola fault in Central Italy. In

order to fit the data from different sites with a similar slip history, they varied the pre-exposure age of the samples at each site, from 2.5 ka to 13 ka. The pre-exposure age is used to correct for the time period in which samples were exposed to cosmogenic radiation, and thus accumulating ^{36}Cl, prior to a regional reduction in erosion rates at the demise of the last glacial maximum (LGM) (*Schlagenhauf et al.*, 2011, *Tucker et al.*, 2011). Therefore, it's unlikely that sites spaced at ≈1 km along strike on the same fault will have pre-exposure ages that differ by 10 ka.

Seismic hazard assesments and models of tectonic deformation are based on Quaternary fault slip rates, so thorough evaluation and validation of the method is required. In this study I investigate whether ^{36}Cl derived slip histories are repeatable and therefore reliable measures of Late Quaternary normal fault activity. I do this by building on the work of *Schlagenhauf et al.* (2011), using multiple sample sites on a single fault to determine whether data from different sites can be modelled by similar slip histories. The hypothesis that ^{36}Cl derived slip histories are repeatable and therefore reliable assumes that the earthquake exposure history should be the same along the length of the fault, so sample sites should be located away from fault tips, where slip is likely to be less than in the center. I use the modeling methods of *Cowie et al.* (2017), which do not require a variable pre-exposure age, and I take into account geochemical variability of the samples. This approach fixes the slip size, allowing us to focus on the effects of differing geomorphic parameters between multiple sites, compared to the more complex modeling approaches (e.g. *Beck et al.*, 2018, *Tesson and Benedetti*, 2019).

I use the central Italian Apennines as our study area because limestone fault scarps are common in the region. They generally have excellent exposure, are well mapped and easily accessible. There are a 19 published ^{36}Cl sample sites in the region (*Schlagenhauf et al.*, 2010, *Benedetti et al.*, 2013, *Tesson et al.*, 2016, *Cowie et al.*, 2017; Figure 4.1). The existing sample sites also provide data for this study as I have remodeled data from some previous studies (*Schlagenhauf*, 2009, *Benedetti et al.*, 2013).

I present five new ^{36}Cl sampling sites from the Italian Apennines, three on the Campo Felice fault and two on the Roccapreturo fault. I selected sites paying attention to the geomorphology and test whether ^{36}Cl measurements at these sites give consistent slip histories over the last 10 ka. I also re-model data from *Benedetti et al.* (2013) for a site on the Campo Felice fault and data from *Schlagenhauf* (2009) for a site on the Roccapreturo fault, in order to directly compare with our new data. Previously published data further support the repeatability and reliability of ^{36}Cl derived slip histories. I discuss the conditions under which ^{36}Cl can be used to elucidate along strike slip rate variation and earthquake displacement on normal faults. Our chosen samples also provide evidence of how relay zones interact over 10 ka timescales.

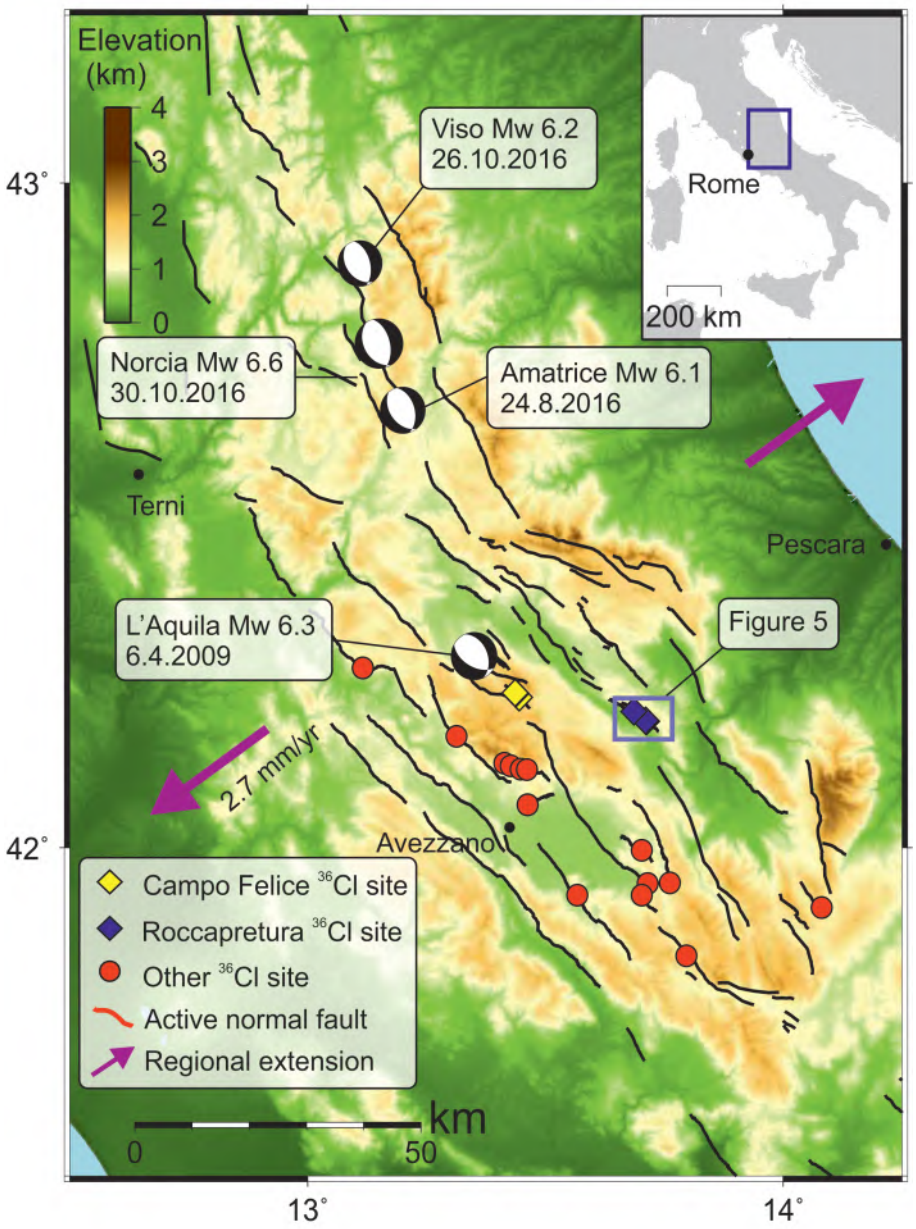

Figure 4.1: An overview of the region and sample sites used in this study. Sample site locations are from *Palumbo et al.* (2004), *Schlagenhauf* (2009), *Schlagenhauf et al.* (2011), *Benedetti et al.* (2013), *Tesson et al.* (2016), *Cowie et al.* (2017), earthquake moment tensors are from www.globalcmt.org and the fault map is modified from *Roberts and Michetti* (2004). The regional extension direction is based on *D'Agostino et al.* (2011). Colours show elevation from 1 arcsecond (30 m) SRTM data. Note the L'Aquila earthquake occurred on the Paganica fault, located North West of the Roccapreturo fault (*Walters et al.*, 2009).

4.3 Geological Setting

GPS measurements indicate the central Italian Apennines is extending NE−SW at a rate of 2.7±0.2 mm yr^{-1} (*D'Agostino et al.*, 2011) (Figure 4.1). This extension has produced a series of NW-SE trending normal faults (Figure 4.1), which host >M_w6 surface rupturing earthquakes in both instrumental and historical records (*Rovida et al.*, 2016, *Walters et al.*, 2018). Extension rate estimates for the region based on the offset of postglacial slopes by active faults since the LGM are 3.1 ± 0.7 mm yr^{-1} (*Roberts and Michetti*, 2004, *Faure-Walker et al.*, 2012) and are similar to average extension rates calculated using offset stratigraphy, indicating the total extension rate across the region may have remained constant for the last 2-3 Ma (*Roberts and Michetti*, 2004). Time variable fault slip rates and spatio-temporal earthquake clusters have been inferred in the region based on models of ^{36}Cl cosmogenic data (*Schlagenhauf et al.*, 2011, *Benedetti et al.*, 2013, *Cowie et al.*, 2017).

Bedrock fault scarps form along Mediterranean normal faults when bedrock exhumation rates, normally as a result of footwall uplift during earthquakes, are greater than erosion rates (*Tucker et al.*, 2011). In the Italian Apennines fault scarps are observed in Mesozoic limestone, but scarps are poorly preserved where faults pass into other lithologies. Preferential formation and preservation of fault scarps is due to the strong resistance of the limestone to erosion and has been well documented in regions with similar lithologies (*Goldsworthy and Jackson*, 2000, *Akar et al.*, 2012). Fault scarps in the Italian Apennines are generally preserved since the end of the LGM 15 ka ± 3 ka (e.g. *Roberts and Michetti* (2004), *Bubeck et al.* (2015)). During the LGM the region experienced cooler climatic conditions producing increased weathering, hence the erosion rate exceeded the rate of exhumation by normal fault slip (*Tucker et al.*, 2011).

Our study is focussed on two faults, the first is the Campo Felice fault which is ∼15 km long. It is composed of two overlapping segments, an ∼6 km southern section striking on average 130° and an ∼8 km northern section with an average strike of 120°. The Campo Felice fault has been the focus of numerous studies (*Giaccio et al.*, 2003, *Giraudi et al.*, 2011, *Giraudi*, 2012, *Benedetti et al.*, 2013, *Wilkinson et al.*, 2015). The Campo Felice fault may have ruptured during an event in 1300 AD (*Salvi et al.*, 2003), but this is not certain as the data is from a paleoseismic trench on a fault segment 5 km north, which *Salvi et al.* (2003) propose is linked to the Campo Felice fault. The footwall slope has active drainage channels and gullies that feed debris fans and gullies in the hangingwall slope, varying in scale from ∼1 m - ∼100 m. Away from active drainage the hangingwall, footwall and fault scarp have planar profiles perpendicular to slope strike (Figure 4.4), similar to the idealised model (Figure 4.3). The hangingwall slope is composed of well cemented colluvium.

The bedrock fault scarp is generally well exposed and has a morphology typical of

normal fault scarps in the region. It intersects the hill slope between ∼ 60-200 m above the basin floor. Preservation of the planar fault scarp varies along strike, becoming more degraded near the fault tips due to less Holocene slip being accommodated at the ends of the fault and on average slower slip rates allowing erosion rates to overcome exhumation rates. Further details of each site location and characterisation can be found in Supplementary Materials.

There is one pre-existing ^{36}Cl sample site on the fault which was published by *Benedetti et al.* (2013), referred to here as site CF4. I consider the geomorphology at this sample site good as it fullfills our site selection criteria, outlined below. In this study I present results from three additional sites. All sites are located on the southern segment of the fault along a ∼1 km section (Figure 4.5). The distribution of sample sites was dictated by the geomorphology of the fault.

The second fault in this study is the Roccapreturo fault, part of the Middle Aterno Valley Fault system (MAVF), which is 21 km long (*Galadini and Galli*, 2000). The Roccapreturo fault is composed of two segments, the southern segment is ∼8 km long, and the northern segment is ∼3 km long, with a relay zone of 1 km length and a separation between the segments varying between 400–900 m (Figure 4.2). The footwall is composed of colluvium and is characterised by planar slopes incised by gullies ≤300 m wide(Figure 4.5). A paleoseismological study of the Roccapreturo fault identified two events (Figure 4.2), the most recent event occurring between 1879–2009 BP and 3787–6055 BP and the penultimate event occurring between 3787–4055 BP and 7329–7499 BP(*Falcucci et al.*, 2015). *Falcucci et al.* (2015) used the offset of Pleistocene breccias to calculate a slip rate on the Roccapreturo fault of between 0.23–0.34 mm yr^{-1}. The fault has been seismically inactive during the time period covered by the historical record (*Galadini and Galli*, 2000).

Schlagenhauf (2009) sampled one ^{36}Cl site on this fault(herein referred to as RP3). They find that the scarp formed in multiple events of unknown number and magnitude. They interpreted that the most recent event occurred 2.0-3.0 ka and the entire scarp was exhumed between 2 ka and 6 ka BP and they propose an average slip rate to be 1.7 mm yr^{-1} over the period of exhumation.

The geomporphology of this site does not meet the site selection criteria that I use; it is located close to a gully that appears to have contributed to exhumation of the fault scarp. I include this site to identify the effects of the non-ideal geomorphology on resulting models. I sampled two additional sites on the Roccapreturo fault, the first (RP1) located 180 m northwest along strike from site RP3 and the second (RP2) a further 2.5 km northwest along strike (Figures 4.5 and 4.2). Details of sites can be found in Supplementary Materials A2.

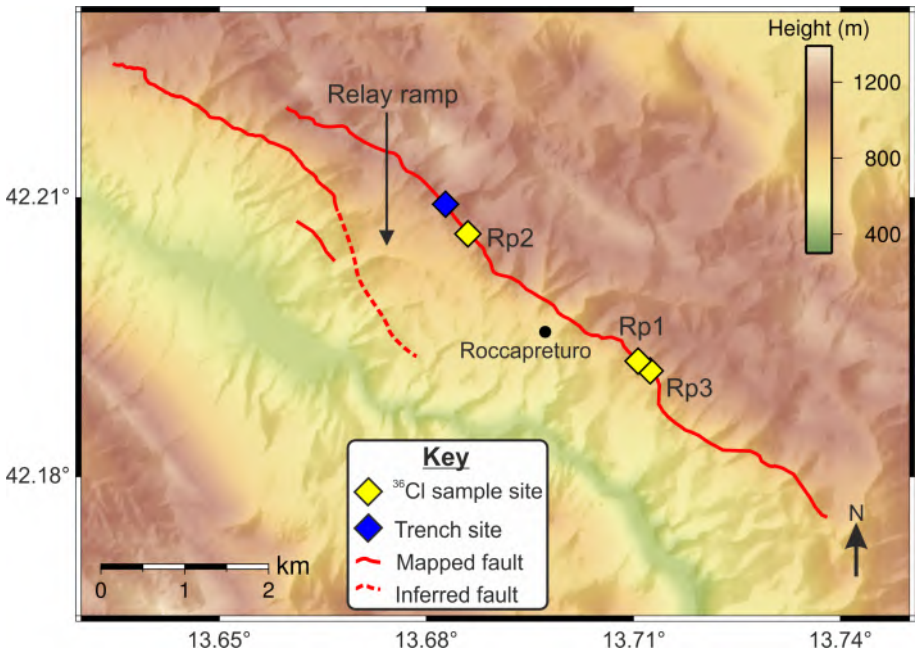

Figure 4.2: Topographic map of Roccapreturo fault with two overlapping fault segments. Trench sites are from *Falcucci et al.* (2015) and site RP3 that is reported by *Schlagenhauf* (2009). Location of map shown in Figure 4.1. DEM from *Tarquini et al.* (2012)

4.4 Methods

4.4.1 Sample site selection

If ^{36}Cl derived exposure histories provide reliable estimates of normal fault slip rates, then data from different sample sites along strike on a single fault should be able to be modelled successfully by similar slip histories. I identify sites where I am confident that the hangingwall and footwall slopes have been stable since the demise of the LGM. I follow the criteria set out by *Bubeck et al.* (2015) to identify cosmogenic sampling sites, minimising non-tectonic exhumation. The sites fullfill the following five criteria: 1) the footwall and hangingwall slopes are intact and planar and show no evidence of incision; 2) the hangingwall slope is free of post LGM sediments; 3) the site is located away from relay zones; 4) the fault plane surface is well preserved; and 5) the contact between the fault plane and the lower slope is horizontal, ruling out along strike mass movement. I identify areas that conform to the first three of these criteria by investigating the footwall slope - fault scarp and fault scarp - hangingwall contacts. Horizontal contacts consistent over a distance of 10 meters or more indicate a lack of significant erosion or deposition since the demise of the LGM (Figure 4.3). I identify appropriate areas for sampling using a combination of satellite image analysis (Google earth), analysis of terrestrial laser scanner (TLS) derived point clouds and fieldwork.

The limestone fault scarps in the region are composed of fractured limestones with an increase in fracture density into the fault core where an indurated carbonate fault

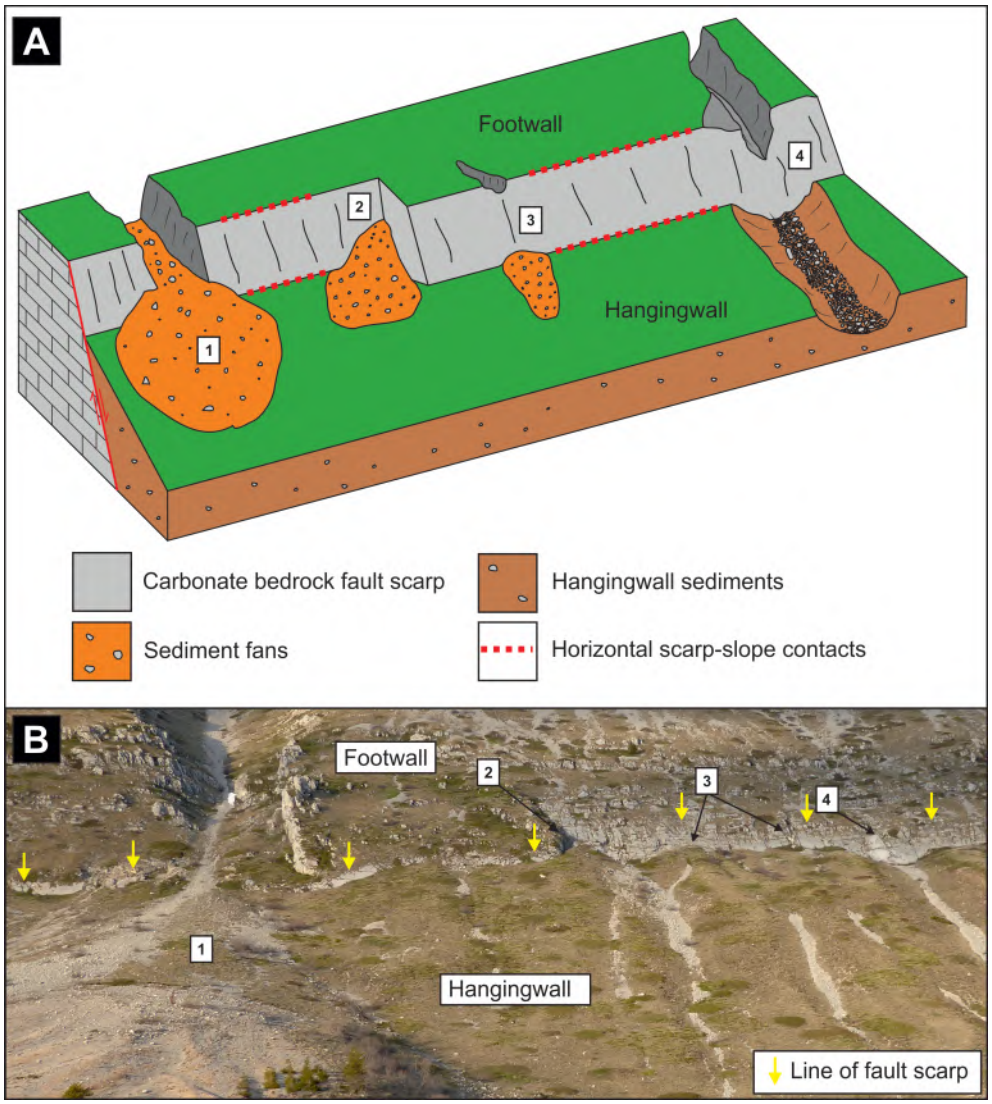

Figure 4.3: A) A schematic diagram of slope processes that can produce non tectonic exhumation and burial of active limestone fault scarps. Labels 1-4 indicate areas of hangingwall erosion or deposition that would be inappropriate to sample. 1)Major incision into the footwall and deposition of material in a large alluvial fan. 2) Erosion of the fault scarp at a step in the fault, with material deposited on the footwall. 3) Small localised hangingwall erosion with related footwall deposition. 4) Incision of both the hangingwall and footwall. Ideal sample sites are located away from areas affected by depositional and erosional slope processes, where the scarp-slope contacts are horizontal, after *Bubeck et al.* (2015). B) The Campo Felice fault with features from A indicated. Photo taken from (42.2308° N, 13.4343° E) looking northeast. Horizontal scale is approximately 320 m across image at height of scarp.

gouge is situated. The limestone scarps generally have planar surfaces with slickensides and striations commonly visible on the surface. I use these indicators to identify areas where the fault plane is well preserved as erosion will destroy fault surface features. I avoid areas of fault plane that are intensely fractured or areas with eroded scarp, as well as areas with obvious secondary precipitation of calcite. I avoid fractures and secondary calcite in an attempt to sample fault rocks that are not contaminated with vadose carbonate cements that will contain chlorine derived from atmospheric processes (*Dunai*, 2010).

4.4.2 Sample collection and preparation

Sampling involves excavating a trench in the hangingwall against the fault scarp to a depth of 1 - 2 m and at most sites I measure the density of the excavated colluvium using a simplified version of the method of *Muller and Hamilton* (1992; Supplementary Materials). Samples are cut from the exposed fault plane along a line parallel to the slip vector on the fault (typically parallel to dip direction). Some samples on the ladder are sometimes offset to avoid eroded parts of the fault plane. I collect a 3D point cloud dataset using TLS at each sampling site and extract the geometry of the slip parallel profile of the slope using the Matlab® code *crossint* (Figure 4.4 *Wilkinson et al.*, 2015, *Cowie et al.*, 2017).

Sample preparation and measurement is undertaken at the Leeds University Cosmogenic Isotope Laboratory, following standard methods of *Cowie et al.* (2017) and references therein. Prepared samples are measured on an accelerator mass spectrometer at the Scottish Universities Environmental Research Centre. Bulk rock chemistry is constrained by inductively coupled plasma optical emission spectrometry at the University of Leeds. More detailed description of the sampling and laboratory processes are located in the Supplementary Materials.

4.4.3 Modeling of the data

Generating a slip rate from ^{36}Cl data on fault scarps requires modeling the data as an exhumation history, as ^{36}Cl concentrations do not represent direct exposure ages because ^{36}Cl is accumulated while the fault is partially buried. The choice of how I model the exhumation must be consistent to facilitate comparison. I use the Matlab® code from *Schlagenhauf et al.* (2010) to forward model the ^{36}Cl concentration that results from a user defined exhumation history and parameters such as site geometry, sample composition and cosmogenic particle flux to simulate exhumation of a normal fault plane. I use a time varying cosmogenic particle flux calculated in the online cosmogenic calculator *CRONUS* (*Marrero et al.*, 2016). Previous studies use a constant value of colluvium density (*Cowie et al.*, 2017) and, given the poorly quantified uncertainties associated with mean colluvium density, the method of measurement and

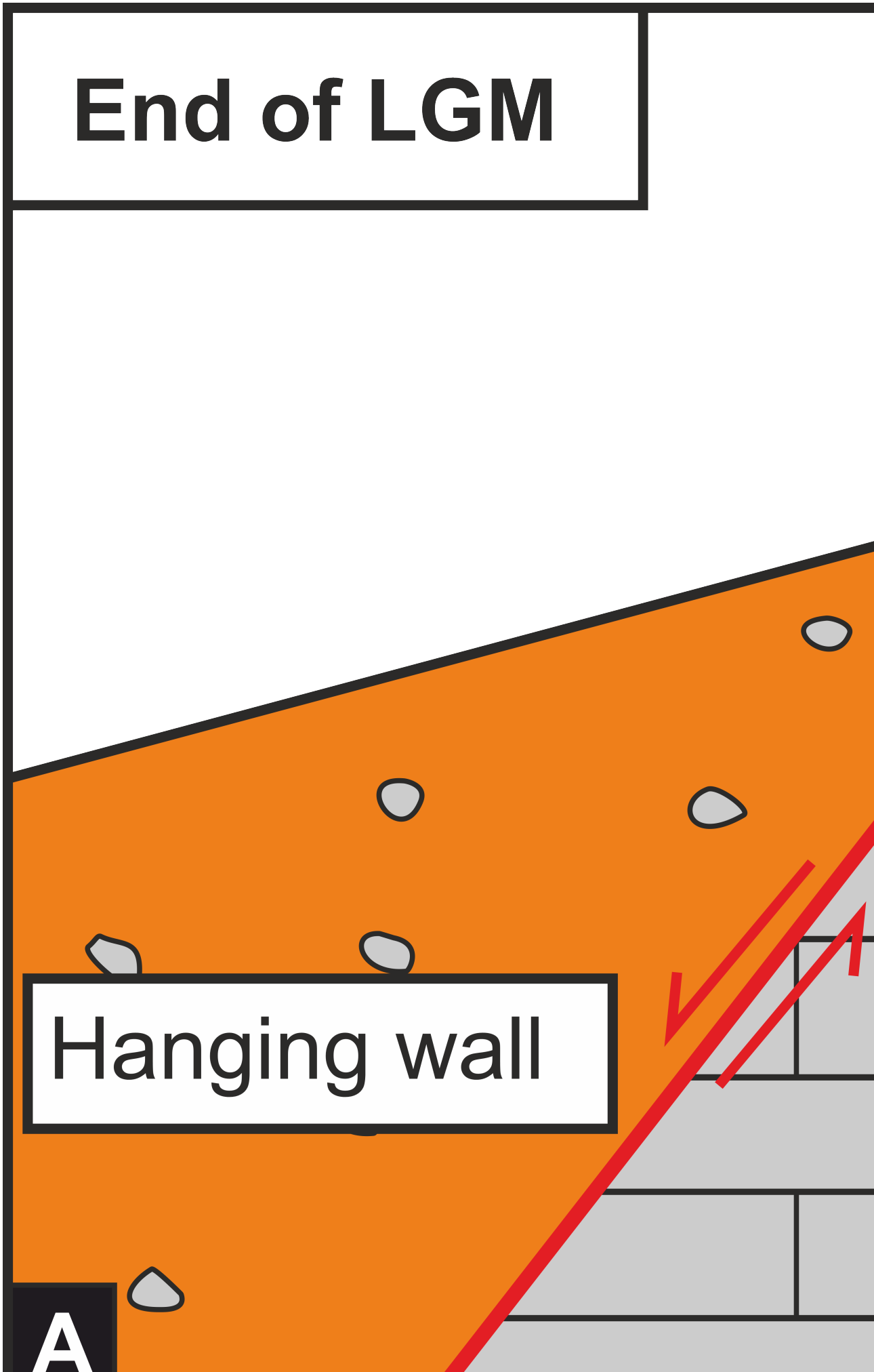
End of LGM
Hanging wall
A

the agreement of our measured values with the value typically used, I also use a mean value of 1.5 g cm^{-3}. Further details on production rate scaling can be found in the Supplementary Materials (Section B).

I use a Bayesian Markov chain Monte Carlo (MCMC) approach developed by *Cowie et al.* (2017), which runs the forward model iteratively, to find all slip histories that adequately explain the ^{36}Cl measurements within uncertainties. A Bayesian approach incorporates independent priors (timing of the LGM, timing of the most recent surface rupturing earthquake) into the modeling and produces the posterior probability of models, including a best fit model. This approach also allows us to explore trans-dimensional parameter space, letting us solve for both slip rate and the number of changes in slip rate. The Bayesian algorithm generates a slip history conditioned on the prior probabilities, runs it through the forward model and produces a series of modeled ^{36}Cl values. It then calculates the likelihood of the proposed slip histories given the comparison between the modelled ^{36}Cl values relative to the measured data. The algorithm then varies one or more of the parameters used to define the slip history and runs the forward model again. The new slip history is accepted if it has a higher likelihood than the previous model or if the ratio of new/current likelihood is higher than a random number drawn from a uniform distribution between 0 and 1, otherwise the new model is rejected, as per the Metropolis Hastings algorithm. I run this for 10^5 iterations.

The model parameters for which I solve to define a slip history are: 1) Scarp age (time of the first event that produced preserved fault scarp), 2) Elapsed time (time since last earthquake), 3) Timing of change points (timing of change in slip rate), 4) Height up fault scarp of a change point and 5) A hyper-parameter, the number of change points. The actual number of parameters I solve for can vary between each iteration, dependent on how many change points are defined. Further details can be found in (*Cowie et al.*, 2017). I use the flexible change point method of *Cowie et al.* (2017) rather than the fixed change point model (where the change point height up the fault scarp is fixed) because I have no additional data such as fault roughness to fix the height of the changes in slip rate up the scarp. The flexible change point model allows timing and number of changes in slip rate to vary between iterations, whilst favoring simpler models with fewer changes in slip rate through implementation of a reversible jump algorithm.

The Bayesian MCMC algorithm produces a distribution of possible slip histories and their likelihood and misfit. I use a constant slip size of 1 m to exhume the scarp incrementally in our modeling as I find that using a smaller constant slip size has little effect on the overall model results but does make the inversion process more computationally expensive (Figure SB2).

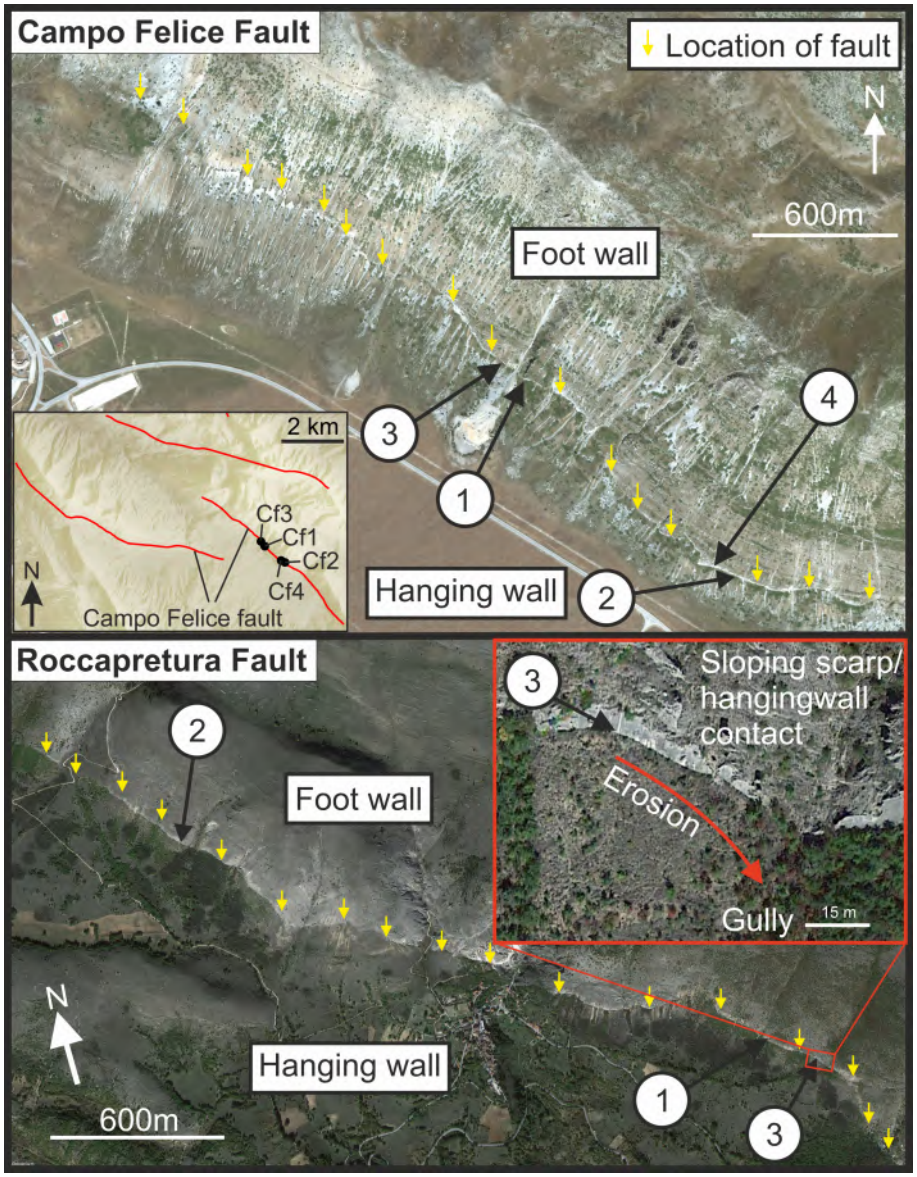

Figure 4.5: Location of sites used in this study, inset in a) shows length of the Campo Felice fault. Campo Felice sites 1, 2, 3 were sampled during this study, site 4 was sampled and processed by *Benedetti et al.* (2013). On the Roccapreturo fault sites 1 and 2 were sampled during this study, site 3 was sampled and processed by *Schlagenhauf* (2009). Inset in b), shows the fault scarp/hangingwall slope contact is not perpendicular and indicates material is being removed from the hangingwall and transported towards the gully south-east along strike. The sample site can be seen as a light strip on the grey fault scarp. Imagery from Google Earth, 2018.

4.5 Results

4.5.1 Campo Felice fault

I present ^{36}Cl data for the Campo Felice and Roccapreturo faults (Figure 4.6). ^{36}Cl concentration profiles are similar for sites CF2, CF3 and CF4 whilst concentrations are greater at site CF1 for samples at similar heights. The ^{36}Cl concentration vs height gradient is related to the slip rate on the fault, with steeper gradients indicating faster slip rates. On Campo Felice all profiles show a change in gradient at ∼3 m.

I present histograms of all accepted exhumation models for each site (Figure 4.7a-d). The histograms show the distribution of ages at which a section of currently exposed fault surface was initially exposed to the surface in our models. To aid comparison between sites I plot the 95 percentile range of these same exhumation histories for all sites on one plot (Figure 4.7e). All models are poorly constrained above 7-10 m due to the lack of samples on the degraded part of the scarp, and as a result the older portions of the slip model have higher variability (Figures 4.6 and 4.7a-e). Fits to the data of a selection of accepted models are plotted in Figure 4.8.

For each site, I calculate slip rates in mm yr^{-1} for the models that fit the data within the equivalent weighted RMS (RMSw) value of 2 standard deviations. Data from CF4 are not fit within 2 standard deviations, due to the lack of sample-specific calcium values available in *Benedetti et al.* (2013), and I instead plot models that fit within 3 standard deviations. Slip rates are plotted in Figure 4.7 as an average of the models that fit the data to within 2 standard deviations (3 in the case of site CF4), binned into 100 year increments. Because one of the modeled parameters is the time elapsed since the last earthquake, each model has a period of time between the present day and the last proposed earthquake during which the incremental slip rate is zero. If another earthquake occurred today, the average slip rate between the present day and what would then be the penultimate earthquake would change to accommodate the ‘new‘ slip, but modeled slip rates previous to the penultimate event would remain the same. Therefore, the apparent drop to zero mm yr^{-1} in our slip rate calculations reflects the modeled elapsed time, and does not imply that the fault is inactive - an important consideration if time-varying fault slip rates are to be incorporated into earthquake hazard assessments.

Models show agreement in exposure history between the sites (Figure 4.7). Models of sites 1-3 show peak slip rates of 4-4.5 mm yr^{-1} between 1 and 3 ka ago, with a reduced slip rate of <1 mm yr^{-1} before approximately 3-4 ka (Figure 4.7f). Models of site 4 show a higher peak slip rate of 6 mm yr^{-1} occurring more recently than at sites 1-3. Models of sites 2 and 4 show a second longer period of increased slip rate which ends at approximately 8 ka. This period of period of high slip rate suggest the fault was relatively active between 1-3 ka and relatively inactive between 4-8 ka.

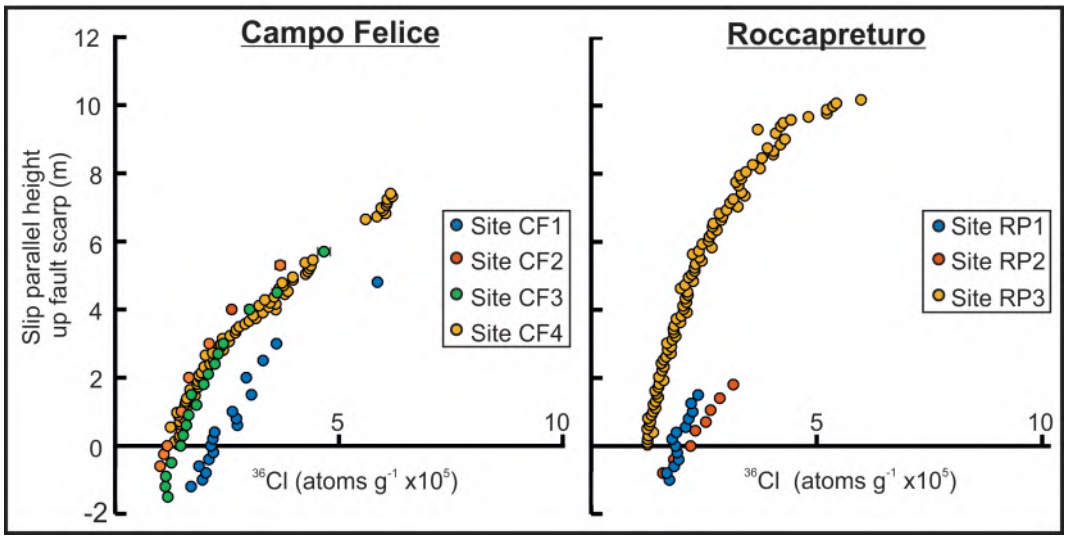

Figure 4.6: Concentration of ^{36}Cl vs height in the plane of slip. Data from Campo Felice Site CF4 are from *Benedetti et al.* (2013), and Roccapreturo Site RP3 from *Schlagenhauf* (2009). 1 sigma uncertainties for ^{36}Cl are in most cases smaller than the plotted points.

4.5.2 Roccapreturo

^{36}Cl profiles have the expected increase in ^{36}Cl concentration up the Roccapreturo fault scarp (Figure 4.6). Site RP3 has lower ^{36}Cl concentrations for the same height than at sites RP1 and RP2, and has a steeper gradient at the base of the scarp compared to sites RP1 and RP2. The gradient at site RP3 gradually reduces with height. Sites RP1 and RP2 have similar ^{36}Cl concentrations with minor differences in gradient. Site RP3 samples a section of preserved scarp that has an offset of 10.2 m, compared to sites RP1 and RP2 which have offsets of 7.2 m and 4.7 m respectively.

There is a clear difference between modelled slip histories at each site on the Roccapreturo fault (Figure 4.9a-d). I present the average incremental slip rate of models that fit the data within the RMSw equivalent of 3 standard deviations of the distribution (Figure 4.9e). Models of all sites include a period of rapid exhumation occuring at approximately 4 ka, with the maximum slip rates being 1.2, 0.5 and 2.4 mm yr^{-1} for sites RP1-3 respectively. Models of site RP2 show a maximum slip rate around 6 ka with a broad peak. A subset of the models used to calculate average incremental slip rate are plotted in Figure 4.10.

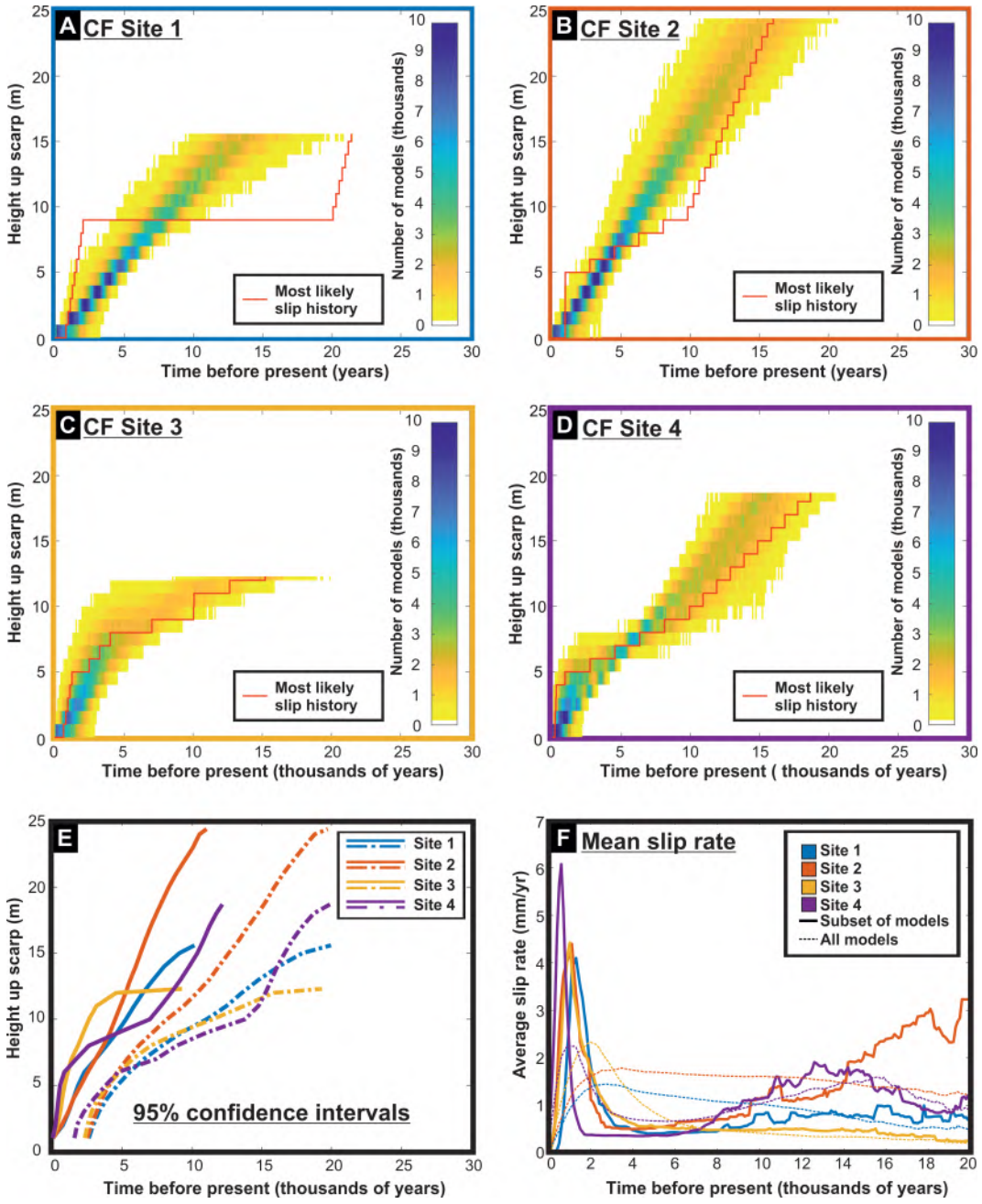

Figure 4.7: Results from the modeling of the Campo Felice ^{36}Cl data. Plots show 10^5 iterations, minus the burn in of 10,000 iterations. Plots A-D) Distribution of slip histories, with the ages in 100 year bins. E) shows the 95% confidence intervals of plots A-D. F) Average incremental slip rate of models that fit the data to within 2 standard deviations at sites 1-3 and 3 standard deviations at site 4.

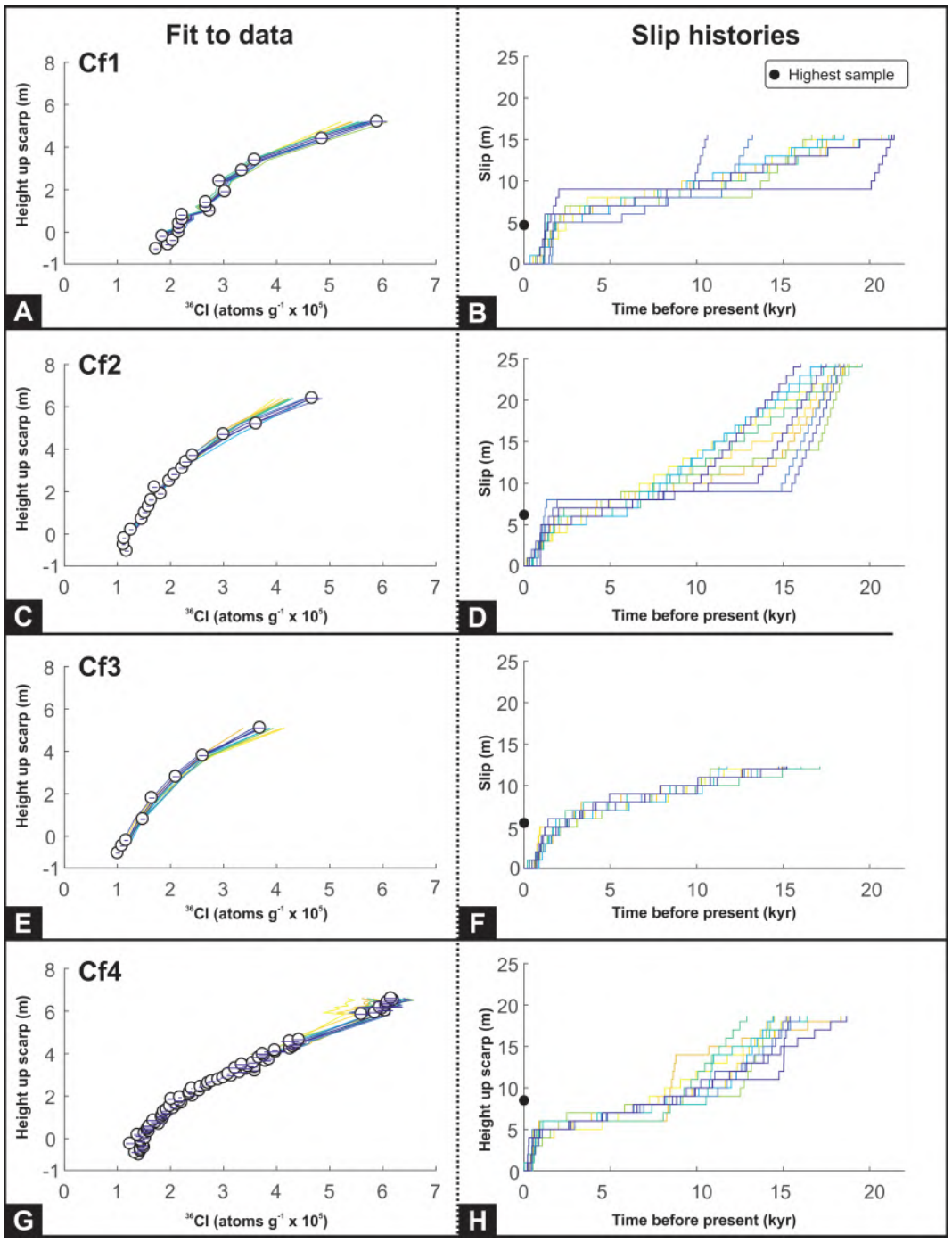

Figure 4.8: Plots A,C,E and G show fit to data of a selection of the models that have been used to calculate the average slip rate. Black circles and blue error bars represent ^{36}Cl measurement and analytical error, each colored line represents a model, with dark to light colours representing highest likelihood to lowest likelihood models. I present 10 models for each site ranging from the highest likelihood likely to lowest likelihood of the models at equal intervals through the distribution. Plots B,D,F and H represent the corresponding model slip histories. Full distributions from the inversion can be found in Supplementary Materials.

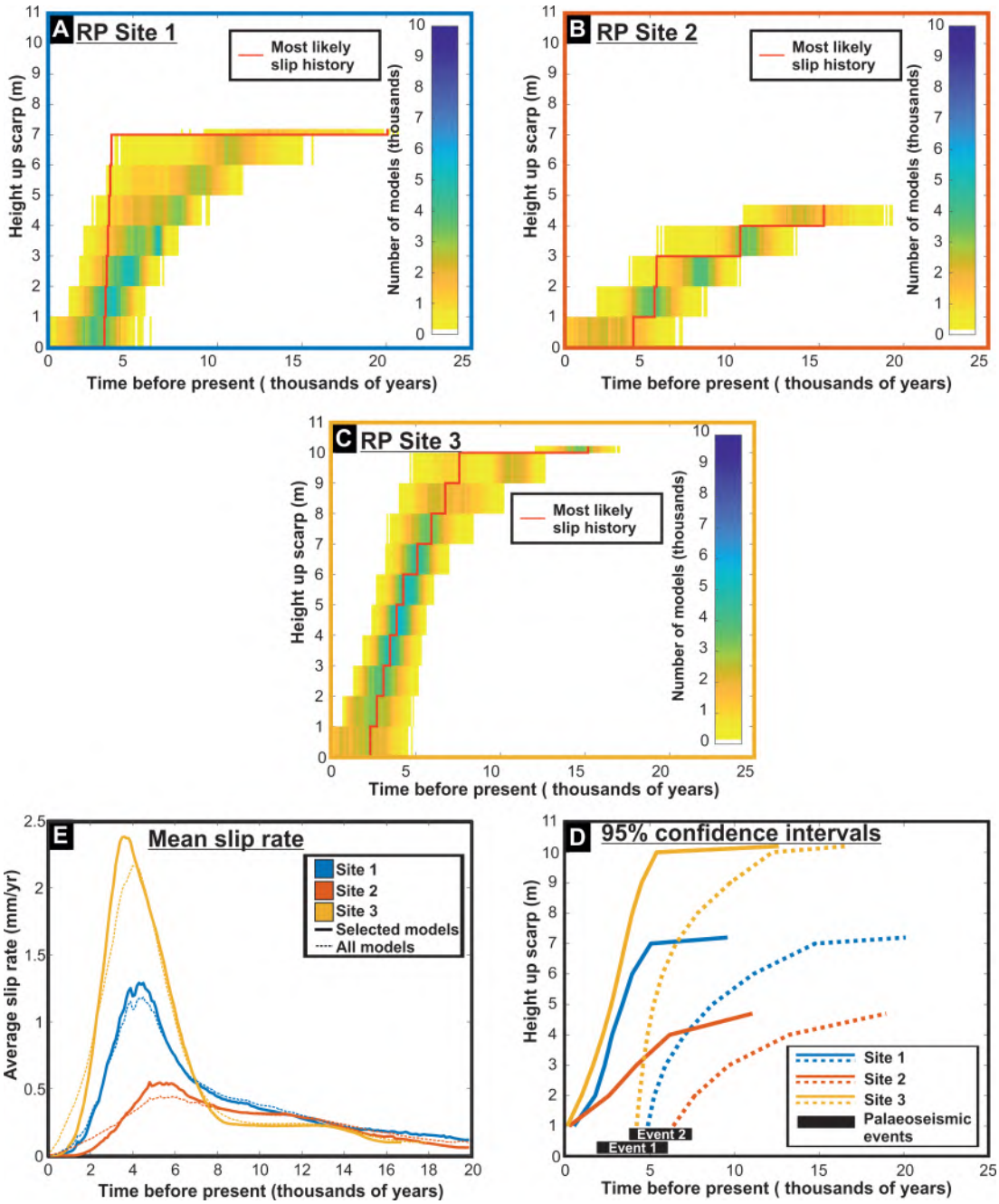

Figure 4.9: Results from the modeling of the Roccapreturo ^{36}Cl data. Plots show 10^5 iterations, minus the burn in of 10,000 iterations. Plots A-C) Distribution of slip histories, with the ages in 100 year bins. D) shows the 95% confidence intervals of plots A-C. E) Average incremental slip rate of models that fit the data to within 3 standard deviations.

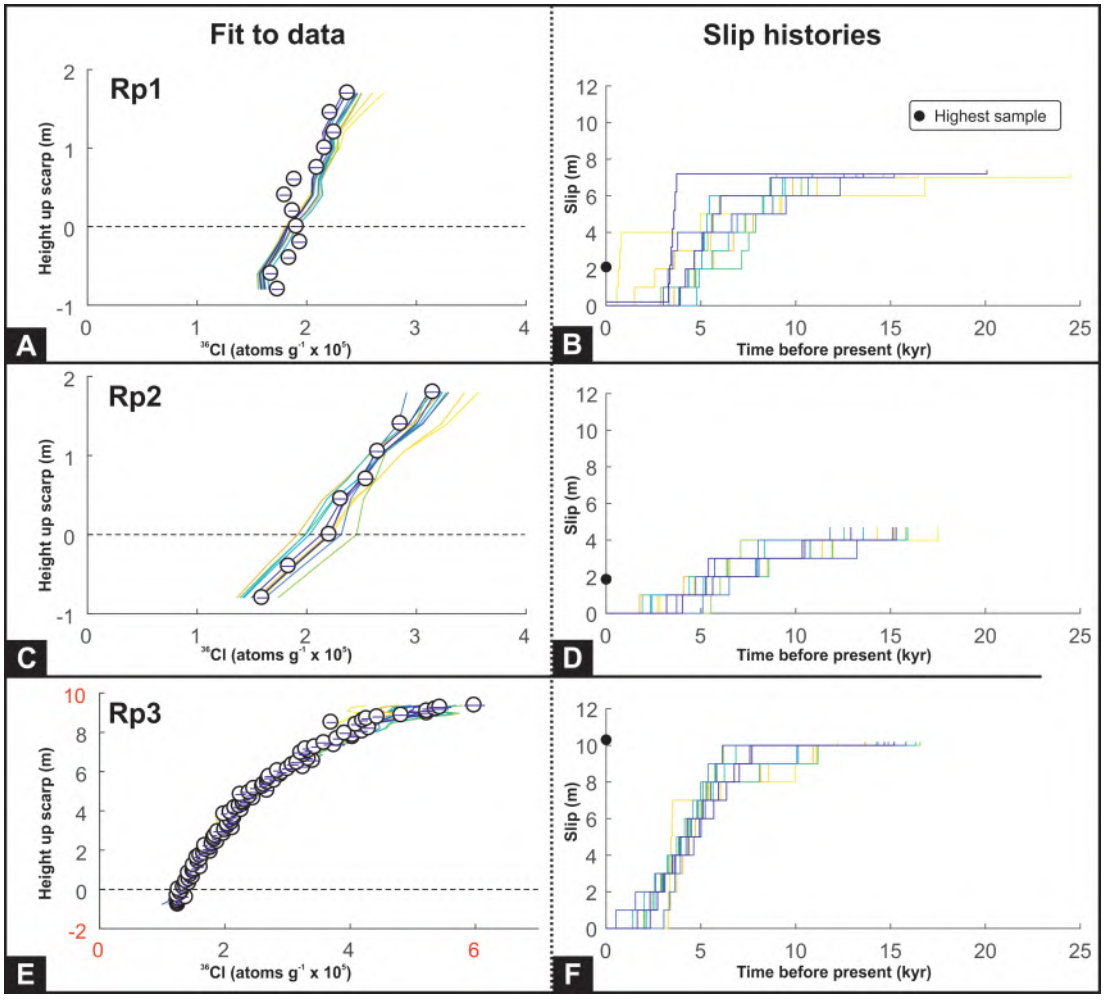

Figure 4.10: Plots A,C and E show fit to data of the of models that have been used to calculate the average slip rate. Black circles and blue error bars represent 36Cl measurement and analytical error, each colored line represents a model, with dark to light colours representing highest likelihood to lowest likelihood models. I present 10 models for each site ranging from the highest likelihood likely to lowest likelihood of the models I use to calculate average slip rate, at equal intervals. Plots B,D and F represent the corresponding model slip histories. Full distributions from the inversion can be found in the Supplementary Materials.

4.6 Discussion

4.6.1 Consistency in the method through along-strike comparison

Accurate fault slip rates derived from cosmogenic isotopes measured on bedrock fault scarps are key for understanding fault behavior over multiple earthquake cycles and for estimating seismic hazard, but it has not previously been demonstrated that repeat measurements of fault slip rate are consistent along strike on the same fault. Here I show that similar slip histories are resolved along strike, but there are discrepancies between sites due to multiple factors, which I highlight below. I discuss these results in the context of the assumptions and limitations of the ^{36}Cl method, and outline

how results from good sites can be used to infer that spatial and temporal slip rate variability is a consistently resolvable feature over millennial timescales. I also compare our results with paleoseismological studies, the agreement of which further supports the ability of cosmogenic isotopes measured on bedrock fault scarps to provide consistent, reliable constraints on fault activity. I put our results into the wider context of slip rate variation and fault complexity, and discuss the implications for Quaternary slip rate studies, and considerations that must be made when determining fault behaviour.

A common feature of modelling ^{36}Cl data on normal faults, in both this study and others, is that parts of the slip history older than ∼10 ka are poorly resolved (*Schlagenhauf et al.*, 2011, *Benedetti et al.*, 2013, *Mechernich et al.*, 2018) due to increased analytical uncertainty of the ^{36}Cl measurements at higher concentrations, and the lack of samples taken from higher up the scarp becasue of erosion of the fault surface (Figure 4.7). One challenge in interpreting the output of our Bayesian modeling is that whilst there is a single best fitting model, there are commonly hundreds or thousands of models that fit the data almost as well (Figures 4.8,4.10). This means I should consider all models that fit the data to a reasonable degree when calculating slip rates. Identifying higher frequency variations or individual slip events (earthquakes) is difficult because the data can be fit with a range of models, and is not possible using the data and modeling methods in this study. However, first order variations in slip rate, which may represent temporal clustering of earthquakes, are consistent features of the modeling.

The lack of models at all sites fitting to within 1 standard deviation suggests deficiency in the modeling. Uncertainty in the scarp age and the resulting range of possible scarp ages (typically 10-20 ka) is a major source of uncertainty as well as the fixed increments of 1 m at which the fault scarp is exhumed. The density and moisture content of the soil and colluvium likely vary both in space and time, including this spatial variation is beyond the scope of this study but likely also contributes to the uncertainty of modelled results.

At some sites no models fit the data to within 2 standard deviations because they have outliers or noisy data that are not fit by any model. Applying site averaged Ca values reduces the ability of models to fit the data because of the effect that the concentration of calcium has on the production rate of ^{36}Cl. Sampling bias is also a challenge in calculating slip rates from these models, as a greater density of samples is collected from the bottom of the scarp due to erosion higher up the scarp surface. The trans-dimensional nature of the Bayesian inversion favours simple slip histories with the lowest number of changes in slip rate and I do not apply any weighting to the data other than the standard deviation of the analytical errors. Consequently, the inversion favors simple slip histories that fit the data well in the bottom section of the scarp where there is a higher density of data, and fits less densely sampled data further up the scarp poorly. Models can fit the data with a more simple slip history by not fitting higher data points. To represent the available data and generate slip histories based

on the full dataset, in the next section I interpret a subset of the models that fit all the data well. Different subsets of models (models that fit within 2 standard deviations, 3 standard deviations etc.) can be used to do this, but they result in different average slip rates as the standard deviation primarily depends on the fit of the model to the sparse data at the top of the scarp. At sites where sampling is more dense near the top of the scarp (CF4 and RP3) the inversions favour more complex slip histories independent of the standard deviation cut-off, producing similar average slip rates. (Supplementary Materials Section B).

Results from the Campo Felice Fault demonstrate that ^{36}Cl data from multiple sites spaced $\leq$1 km on one fault can be modeled successfully with similar slip histories, showing resolvable slip rate variation on 3-5 ka timescales. A period of faster slip between 7 ka and 15 ka that was only observed at the 2 southern most sites (sites CF2 and CF4) may suggest that the fault does not always rupture completely, which matches modern observations of faults in the region (*Walters et al.*, 2018). *Benedetti et al.* (2013) determined broadly the same slip history at CF4, but given the arbitrary pre-exposure values in their modeling it is coincidence that the timing of the change in slip rate is similar to our models. The slip rate variation of *Benedetti et al.* (2013) is, however, real and independent of the pre-exposure values they assigned. Our findings agree with those of *Beck et al.* (2018), who also find that continuous sampling up the fault scarp (e.g. site CF4) does not resolve better constraint on absolute slip rates and the timing of change in slip rate compared to discrete sampling every 25-50 cm up the scarp (Figure 4.7).

There is a greater discrepancy between slip histories from sites on the Roccapreturo fault than at Campo Felice. I propose that the difference in scarp height between sites RP3, sampled by *Schlagenhauf* (2009) and sites RP1 and RP2 is likely due to site RP3 being located on the edge of a gully that crosses the hangingwall and footwall of the fault (figure 4.5). As a result, the fault scarp has been subject to active net erosive slope processes that removed material from the hangingwall slope exposing the fault surface in the gully, resulting in a higher scarp and slip rate than other sites on the fault. I propose the slower average incremental slip rate and shorter scarp height at site RP2 compared to site RP1 occurs because strain has been accommodated by the fault strand located 1 km west and across strike of the sampled fault strand. This hypothesis is further supported by the topography, between the two fault strands elevation reduces parallel to the strike of the faults towards the southeast, and there is a step in elevation across each of the fault segments, perpendicular to fault strike (Figure 4.2). This is classic relay ramp morphology, where the length of the relay ramp is $\sim$ 3 times the width (*Fossen and Rotevatn*, 2016; Figure 4.2). The difference in timing of peak slip at site RP2 suggests site RP1 experienced a more recent or significantly larger slip event, implying that the fault does not always rupture fully or that there is a significant variation in surface slip in a single event along the fault. Paleoseismic trenching of

the Roccapreturo fault suggests that the most recent event was between 2-6 ka, with another large event occurring between 3.8-7.5 ka (*Falcucci et al.*, 2015). These dates agree with the rapid slip rate between 2-7 ka at site RP2, which is located approximately 500 m from the paleoseismic trenches (Figures 4.2,4.9). This is the first time there has been agreement between paleoseismologic data and ^{36}Cl slip histories on the same fault strand (*Benedetti et al.*, 2003, *Kokkalas et al.*, 2007) and this provides further evidence for the reliability of slip histories derived from modeling of ^{36}Cl fault plane datasets.

Based on the results and the time and monetary costs associated with sample processing and ^{36}Cl measurement, I recommend that by sampling multiple sites with a discrete sampling pattern vs continuously at one sample site, ^{36}Cl studies can have greater confidence in the determined slip rates. The multi-site sampling approach also allows information to be gained on along strike variability of slip rates. The geomorphology of each sample site should be carefully examined to provide confidence in the tectonic origin of any fault plane exhumation, to provide certainty that any variation in slip rate is a function of tectonic processes, rather than other geomorphic processes. One limiting factor in studies attempting to sample multiple ^{36}Cl sites on a single fault is identifying multiple suitable sites on faults. I also suggest that sampling at regular intervals up the scarp limits sampling bias and can reduce the complexity of interpreting modeled slip rates, allowing the whole distribution of models to be considered. Whilst the prior assumption that scarps are preserved only since the demise of the LGM is strongly supported in the Central Italian Apennines (*Galadini et al.*, 2003, *Tucker et al.*, 2011), application of the method to other regions will require equally robust evidence to define the scarp age prior distribution. Combining other data sources with the ^{36}Cl data, such as historical records and estimates from other dating techniques, would aid in reducing the uncertainty in modeling and help cross validate methods.

4.6.2 Slip rate variation in the wider context

Time average slip rates are not always representative of fault behavior as slip rates are observed to be variable over millennial timescales, both in the Italian Apennines and elsewhere (*Schlagenhauf et al.*, 2011, *Benedetti et al.*, 2013, *Cowie et al.*, 2017, *Mechernich et al.*, 2018). I also find that time variable fault slip rates are a consistent feature of the data presented here. An estimate of the recurrence interval for a given earthquake magnitude is commonly used to represent the hazard posed by a particular fault (*Pace et al.*, 2006), but these estimates do not incorporate the time varying nature of seismic hazard and this should be considered in developing future seismic hazard methodologies. Calculated recurrence intervals for the fast and slow periods of each fault can be found in the Supplementary materials.

The majority of existing ^{36}Cl studies are from the central Italian Apennines, where fault scarps are only preserved since the demise of the LGM at the end of the Holocene (10-20 ka). This relatively short record usually captures $\leq$2 changes in slip rate, and

as a result it is difficult to draw conclusions about the longer term cyclicity of slip rate variability using these data alone. Slip rate variability may also be captured by quantifying slip rates using alternative methods with different spatial and temporal coverage and resolution. *Faure-Walker et al.* (2012) show that slip rates averaged over the Holocene (based on fault scarp heights) match the geodetic deformation rates, when averaged over large spatial scales (10^2 km). *Cowie et al.* (2013) suggest that the 10^4 year strain rates are representative of long-term geological rates based on the correlation between high strain and high topography, and the implications that the correlation has on the localization of shear zones in the lower crust.

A discrepancy between geodetic and geologic slip rates is well described on many faults in various tectonic settings (*Papanikolaou et al.*, 2005, *Faure-Walker et al.*, 2012, *Schlagenhauf et al.*, 2011, *Dolan et al.*, 2016, *Zinke et al.*, 2017, *Cowie et al.*, 2017), with several mechanisms invoked to explain this variability. In the Italian Apennines, *Cowie et al.* (2017) suggest that time variable slip rates are primarily caused by large scale migration of activity across the whole fault network, in order to minimize the work done by the faults. In this geodynamic model, different regions of faults are active at different times as a result of the change in gravitational potential energy acting on the uplifted footwall, inducing flexural bending of the normal fault footwall and time varying fault strength. Coulomb stress changes due to earthquakes have also been shown to play a role in causing clustering of earthquakes and variable slip rates (*Dolan et al.*, 2016, *Wedmore et al.*, 2017). *Dolan and Meade* (2017) indicate that there is not yet a single mechanism that can explain this behavior across different faults, and suggest it is caused by the complex interaction of processes that may be controlled by properties of a particular fault as well as the fault system as a whole. In order to understand the behavior of a single fault, I must also constrain the activity of faults in the rest of the network using observations over multiple timescales. Probabilistic seismic hazard models currently use time averaged constant slip rates on faults (*Valentini et al.*, 2017), and have limited temporal and spatial data coverage due to the sparsity of paleoseismic data sets (*Dolan et al.*, 2016). ^{36}Cl derived slip histories have the potential to fill some of these spatial and temporal gaps and assist in elucidating the timing and mechanisms responsible for earthquake clustering and fault interaction.

4.6.3 Fault complexity

Interaction between closely spaced fault segments can reduce the total displacement across individual faults due to strain partitioning(*McLeod et al.*, 2000, *Cowie and Roberts*, 2001, *Manighetti et al.*, 2015). Our analyses at Roccapreturo suggests that over millennial time scales the overlapping fault segments do not become completely inactive, but instead overlapping segments have slower average slip rates (or less slip per event) relative to the center of the main fault segment. Quaternary slip rate variation along strike has not been previously observed at this scale and temporal resolution,

demonstrating that ^{36}Cl provides a unique ability to investigate fault segment interaction and strain partitioning over ka timescales. The young age of the Central Italian Apennine normal fault network (2.3-3.3 Ma; *Roberts et al.*, 2002) and low extension rates across the region (2.7 mm yr^{-1} *D'Agostino et al.*, 2011) means the fault system is relatively immature, with a complex network of 20-40 km along-strike faults in the region. If extension continues across the region then Roccapreturo western splay will likely become linked at the surface and may increase in slip rate over 100's of ka.

Earthquake surface ruptures are complex, and have significant variation along strike (e.g. *Walters et al.*, 2018). Some of this complexity will average out over multiple earthquake cycles and can therefore be considered noise when determining offsets to calculate slip rates. The effect of this noise means that whilst offsets from individual events can provide the magnitude of slip at that point on the fault, they are not necessarily representative of either the fault rupture as a whole during that event, or that particular site over multiple earthquake cycles. In our results some variation in slip is consistent over multiple earthquakes cycles, such as between sites RP1 and RP2, and CF2 and CF4, which results in higher relief and lager Holocene fault scarps. If studies sample only one site on a fault using a method that covers multiple earthquake cycles, the results may not be representative of slip rates/earthquake offsets on the entire fault, if for example the sample site experiences consistently higher or lower slip than other sites along strike, or if there are multiple shallow structures accommodating deformation. Persistent patterns of high or low slip are vital to consider when analysing Quaternary slip rate datasets. By comparing ruptures from individual events with offsets accumulated over longer timescales incorporating multiple earthquakes, I can identify consistent patterns of fault rupture. Uncertainty in the significance of along strike slip rate variation can be reduced by sampling multiple sites along a fault.

4.7 Conclusions

The results of this study show that careful sample site identification for ^{36}Cl measurements on normal faults results in robust and repeatable slip history models. Paleoseismological studies from the Roccapreturo fault agree with ^{36}Cl derived slip histories, further increasing confidence in this method. Whilst sampling faults multiple times along strike is not always feasible, it can improve confidence in results by elucidating the range in slip rate and better resolving the timing of changes in slip rate. Multiple along-strike sample sites allow us to observe variation in slip rate along a single fault and can provide a powerful tool to investigate fault interaction over millennial timescales.

Chapter 5

Slip histories of the major faults in the Muğla-Yatağan basin

"The most important questions of life are, for the most part, really only problems of probability" Pierre-Simon Laplace

5.1 Summary

The objective of this chapter is to determine slip rates on the major faults in the Muğla-Yatağan basin, western Turkey. I chose this region because there are no Quaternary rates available for the 3 major faults, and the city of Muğla lies within the basin, so is likely to be affected by a large earthquake on these faults. I use ^{36}Cl analyses of limestone bedrock fault scarps and the footwall slopes, and find slip rates of 0.6, 0.5 and 0.3 mm/yr for the Muğla, Yatağan and Yilanli faults over the last ≈15 kyr. My findings show that the Yilanli fault, previously thought not to have been inactive in the Holocene, has infact been active.

5.2 Introduction

5.2.1 Regional tectonic regime

Western Anatolia is currently extending, with total N-S extension rates across the region at latitude 27° E of around 20 mm/yr (*McClusky et al.*, 2000, *Reilinger et al.*, 2006, *Aktug et al.*, 2009; Figure 5.1). Current topography in the region is dominated by a series of primarily east-west striking grabens, the largest of which are 100-150 km long and 5-15 km wide, with smaller grabens striking northeast-southwest and northwest-southeast (*Yilmaz et al.*, 2000; Figure 5.1).

Yilmaz et al. (2000) suggest a 5 stage history of extension in Western Anatolia (Figure 5.1) based on extensive field mapping, which is summarised below. Before extension began there was continental collision between the Pontide and Tauride Terrains

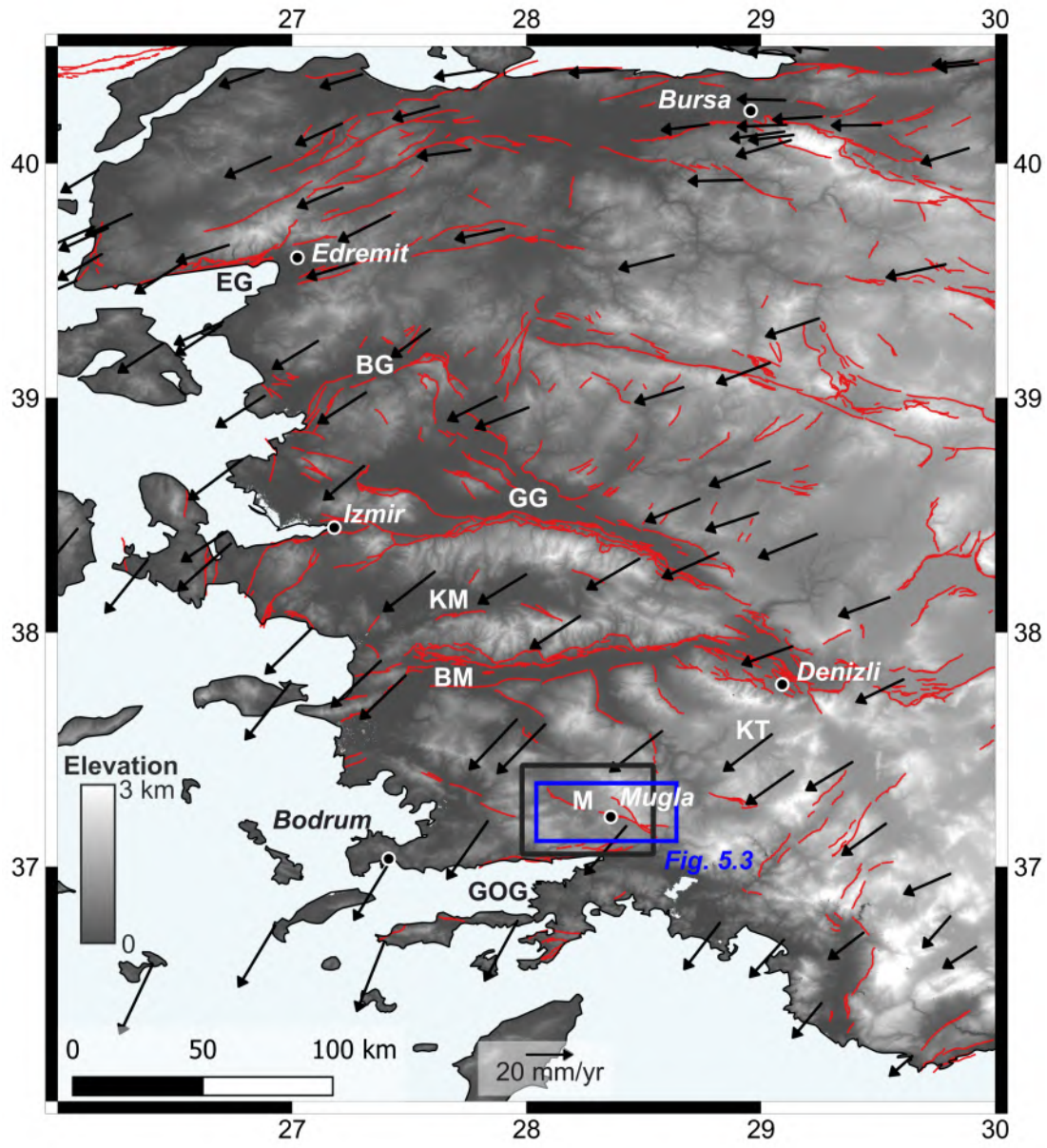

Figure 5.1: Topography of western Turkey, showing the locations of active faults (red), GNSS data (black arrows), location of Figure 5.5 (black box), and the major basins in the region. These basins are, from north to south: **EG** Edremit Graben, **BG** Bergama Graben, **GG** Gediz Graben, **KM** Kucuk Menderes Graben, **BM** Büyük Menderes Graben, **KT** Kale-Tavas Basin, **M** Muğla-Yatağan basin, **GOG** Gulf of Gökova. GNSS data are from *Aktug et al.* (2009) shown in a stable eurasia reference frame. The active fault map is from *Emre et al.* (2018) and the topography is from SRTM (*Jarvis et al.*, 2008).

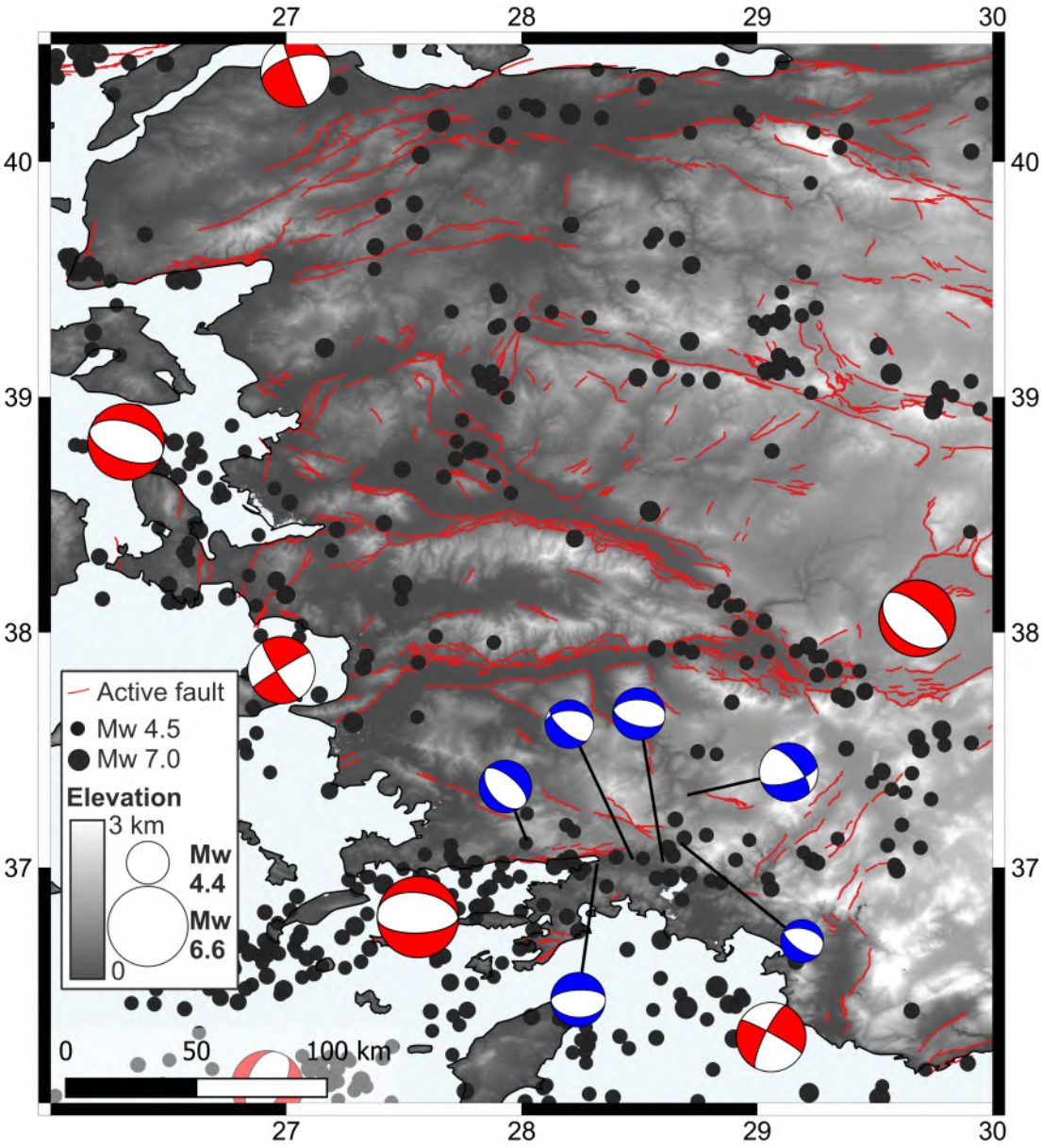

Figure 5.2: A map of seismicity in western Anatolia. The red focal mechanisms show events since 1974 with a magnitude ≥6 M_w, and the blue focal mechanisms show events ≥4.5 M_w in the vicinity of the Muğla basin, both using data from www.cmtglobalcmt.org. Black dots are all events since 1900 ≥4.5 M_w, using data from the USGS, earthquake.usgs.gov/earthquakes/search/. The active fault map is from *Emre et al.* (2018).

in the Late Cretaceous-Early Eocene interval that continued post suture to produce compressional tectonics, with thrusting ending in the Late Eocene-Oligocene in the north-western Anatolia and the Late Miocene in south-western Anatolia. A period of east-west extension resulted in formation of north-south trending grabens during the Early and Late Miocene, and the Oligocene. During the Late Miocene north-south extension began, in some cases causing reactivation of existing faults, producing east-west striking grabens. This extension appears to have been interrupted at the end of the Late Miocene, evidenced by a regional erosional surface dated using palynology (*İnci*, 1984) and by dating of basalt capped river terraces of the Gediz river using K-Ar and Ar-Ar dating (*Westaway et al.*, 2004), before restarting and continuing to the present-day. Rapid extension is evidenced by two particular geological styles: rapidly exhumed metamorphic core complexes associated with low angle shear zones/faults, such as the one found either side of the Büyük Menderes Graben (*Bozkurt and Park*, 1994), and high angle normal faults that bound the numerous basins in Western Anatolia (*Westaway*, 1993, *Bozkurt and Park*, 1994, *Bozkurt and Mittwede*, 2005; & references therein).

There are two major points of disagreement in the literature surrounding extension in Western Turkey. The first is whether currently low angle shear zones of the metamorphic shear zones were low angle (*Hetzel et al.*, 1995) or dipping more steeply than present when they were active (*Bozkurt and Mittwede*, 2005; & references therein). It is also unknown whether these geological phenomena represent one continuous extensional regime or two separate periods of extension, or in other words, are the low angle shear zones associated with the metamorphic core complexes from the same episode of extension as the currently active high angle basin bounding normal faults, mapped in Figure 5.1. Proponents of the continuous regime argue that the change in extension style is a function of crustal thinning and that the currently active high angle normal faults merge with the low angle faults at depth (*Seyitoğlu et al.*, 2002). Proponents of the two phase extension suggest offset of the shear zones of up to 2 km by steep brittle normal faults indicate there must be two phases of extension (*Bozkurt and Sözbilir*, 2004).

Finally, there are multiple competing models for the cause of extension in Western Turkey (*Bozkurt and Mittwede*, 2005). These include back-arc extension due to slab roll-back (*McKenzie*, 1978), and tectonic escape westwards of the Anatolia block due to the convergence of Arabia and Asia, with the majority of motion being accommodated on the North and East Anatolian Faults (*Şengör et al.*, 1985). Constraints on the age of these two major faults have since shown tectonic escape cannot account for the whole period of extension in Western Turkey (*Bozkurt*, 2001, *Bozkurt and Mittwede*, 2005; & references therein). Another model in contention is the orogenic collapse model, which proposes that crust that became overthickened due to collision in the Palaeogene between the Taurides in the South and the Sakarya continent in the north, immediately

collapsed, resulting in extension (*Dewey*, 1988, *Seyitoğlu and Scott*, 1991). Modern age constraints have meant proponents of this model believe collapse was delayed and began not immediately post collision, but in the Oligocene-early Miocene (*Işik et al.*, 2004, *Ring and Collins*, 2005). *Doglioni et al.* (2002) propose that the extension in Western Turkey and in the Aegean is due to differential convergence rates across the subduction zone between Greece and Western Anatolia. Present day GPS derived velocity fields indicate that Western Turkey is undergoing extension at a rate that increases westward (*Aktug et al.*, 2009; Figure 5.1), and these rates can be modelled as a continuously deforming medium (*England*, 2003, *Aktug et al.*, 2009, *England et al.*, 2016). The gravitational potential energy gradient from the high elevation of the Anatolian Plateau in the east to the low of the Helenic trench in the west drives an extensional strain rate field, best demonstrated by *England et al.* (2016). Compared with block models, where deformation occurs on the edge of small rigid undeforming blocks (*Nyst and Thatcher*, 2004, *Reilinger et al.*, 2006), modelling the lithosphere as a continuously deforming medium fits the geodetic data better, with a model requiring fewer parameters (*Aktug et al.*, 2009, *Walters et al.*, 2014, *England et al.*, 2016). The subducted slab under the western Anatolia is proposed to control the extent of rapid extension in western Turkey. *Berk Biryol et al.* (2011) use evidence from seismic tomography to propose that tears in the underlying subducted slab, and subsequent upwelling of hot material, has caused crustal weakening and thinning in western Anatolia, and therefore is partially responsible for the relatively rapid extension of the region.

5.2.2 Geology of the Muğla-Yatağan basin

In this chapter I focus on the Muğla-Yatağan basin, which is located in south-western Turkey, between the two east-west striking grabens; the Büyük Menderes Graben to the North and the Gulf of Gökova to the south (Figure 5.1). There are three main fault segments; from west to east these are: the Yatağan fault, which strikes ≈130°, dips 70-85° northeast and is ≈20 km long (*Gürer et al.*, 2013, *Emre et al.*, 2018), the Muğla fault, which has a similar strike of ≈120°, is reported to dip 70-85° (*Gürer et al.*, 2013) southwest and is ≈30 km in length, and the Yilanli fault (also known as the Aksivri fault (*Gürer et al.*, 2013), which splays off the Muğla fault and strikes ≈140° dipping to the southwest for a distance of ≈15 km (Figure 5.3).

The Yatağan fault was initially mapped as an active strike slip fault (*Şaroğlu et al.*, 1987), however it has since been mapped as a normal fault (*Barka et al.*, 1996). Striation on the fault planes of the Yatağan fault indicate normal slip, with a small dextral strike-slip component (*Gürer et al.*, 2013). The same study indicates strike slip striations overprinted by dip-slip striations on the Muğla fault. The Yatağan fault has produced micro-seismic activity (*Eyidogan et al.*, 1996) and the archeoseismological studies of the ancient site at Lagina indicate that a large normal faulting earthquake occurred in the 4th century C.E., with a dextral strike-slip component (*Karabacak*, 2016). The same

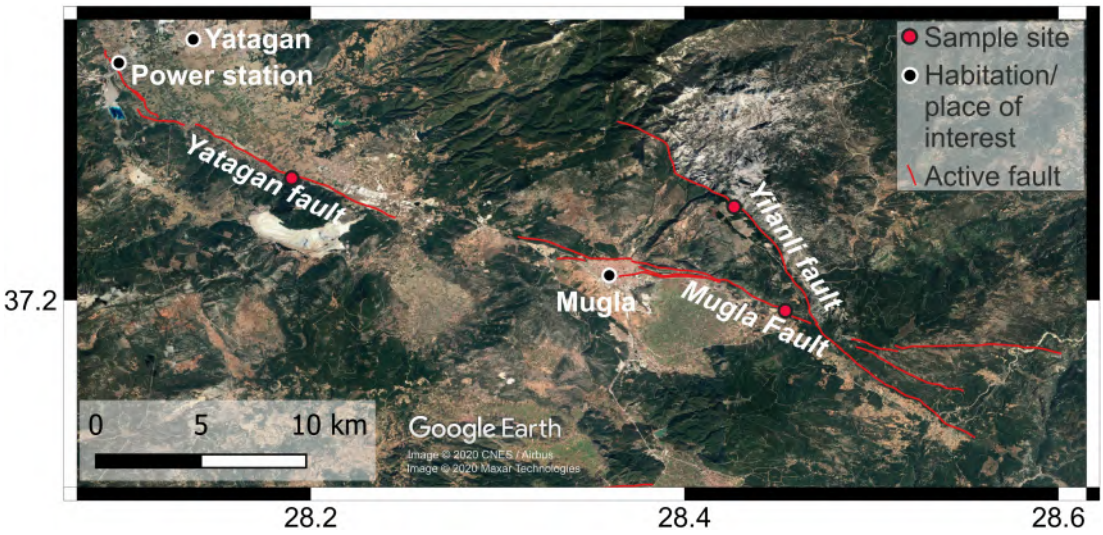

Figure 5.3: Satellite imagery of the Muğla-Yatağan basin, showing the location of mapped active faults (from *Emre et al.* (2018)), and the sample sites in this study. Higher resolution imagery of the three sample sites can be seen in Figures 5.6, 5.7 and 5.8.

study considered the Muğla and Yatağan faults as one fault, but do not offer a physical model for how this is a single fault given the Muğla and Yatağan sections dip in opposing directions. The earthquake catalogue records 2 events >M_s5 in 1941, west of and directly below Muğla, as well as a number of events of >M_s4 (www.cmtglobalcmt.org, Figure 5.2). These events provide further evidence that the Muğla and Yatağan faults are active. Seismic hazard studies have been undertaken in the region (*Demircioğlu et al.*, 2007, *Bayrak et al.*, 2008, *Sayil and Osmanşahin*, 2008, *Bayrak and Bayrak*, 2012, *Bayrak and Türker*, 2016), however the sub-regions containing Muğla encompassed a much greater area than the area considered in these studies so no detailed local results are available.

The recent dip-slip action of these faults has produced a NW-SE trending basin, separated by an intra-basinal high just NW of the city of Muğla. Stratigraphic and geological studies reveal that the Muğla-Yatağan basin is set on top of a series of older basins (*Becker-Platen*, 1970, *Atalay*, 1980, *Querol et al.*, 1999, *Alçiçek*, 2010, *Gürer et al.*, 2013). The basement rock is unconformably overlain by a series of alluvial and lacustrine deposits associated with the opening of the graben during the successive periods of east-west and north-south regional extension beginning in the Early Miocene and continuing until the present day (*Gürer et al.*, 2013; Figure 5.4). The uplifted blocks that bound the Muğla basin are composed of Jurassic to Cretaceous-aged marble, and the footwall of the Yatağan fault is composed of a mixture of the same marble and Upper Paleozoic schist (Figure 5.5). Basins in the region have been exploited for coal since 1979 from the Pliocene beds of the Yatağan formation (Figure 5.4) and extraction is ongoing at several opencast mines, with most of the coal feeding a powerplant located 12 km northwest of the town of Yatağan (*Querol et al.*, 1999, *Inaner et al.*, 2008; Figure

5.3).

5.3 Method

I apply two methods to determine slip rates on the three major normal faults in the Muğla and Yatağan basins using ^{36}Cl. The first is based on samples from the footwall slopes of the fault. By determining an exposure age for the footwall slope which represents how long the slope has been stabilised and preserved, and the total offset across the fault scarp, I can determine an average slip rate since the time that the footwall slope was preserved. This method was suggested for use in Central Italy and Greece (*Tucker et al.*, 2011), and it has not been applied to any normal faults in western Turkey. This method will therefore provide insight into the timing of preservation of limestone fault scarps in Western Turkey. Previous scarp preservation ages are based on ^{36}Cl data from the exhumed fault plane (*Akar et al.*, 2012, *Mozafari et al.*, 2019a,b), rather than exposure age of the footwall slope.

The second method is modelling the exhumation history of the fault plane, using ^{36}Cl samples from the preserved fault plane, as described in Chapters 2 and 3. The fault scarp age from the exposure dating of the footwall slope can be incorporated into the MCMC inversion code of *Cowie et al.* (2017) as a prior distribution of the scarp age parameter.

I selected sample sites for ^{36}Cl dating of the fault plane using the same methodology and criteria as those laid out in Chapter 3. There is a higher population density in the Muğla and Yatağan basins than in the Campo Felice basin (Chapter 3), which meant that it was harder to avoid areas that had been anthropologically modified. I selected one fault scarp sample site (i.e. location where I took multiple samples at different elevations up the fault plane) on each fault, because I only found one appropriate site on each fault. Whilst sampling multiple sites is ideal (Chapter 3), my work in Italy suggests that a representative measurement of fault slip rate can be obtained using a single site, as long as it is close to the center of the fault and away from any interaction with other faults. Scouting of the faults in the Muğla basin is generally more time consuming than working on the Campo Felice and Rocaprettura faults in Italy, because the faults commonly have vegetation growing up to and above the faults making access and observation difficult. As a result, characterising the geomorphology of the scarp and hangingwall and footwall slopes is challenging, and there is greater uncertainty in the quality of sample sites in Turkey compared to the sites I sampled in Italy. Individual sites are described in detail in section 5.3.1.

In addition to the ^{36}Cl samples on the fault plane I also took two samples of the footwall slope for ^{36}Cl exposure dating at each sample site. I did this because whilst there are multiple apparent footwall slope exposure ages for Italy (*Tucker et al.*, 2011; Gregory, personal comms.) that support the hypothesis that the fault scarps have

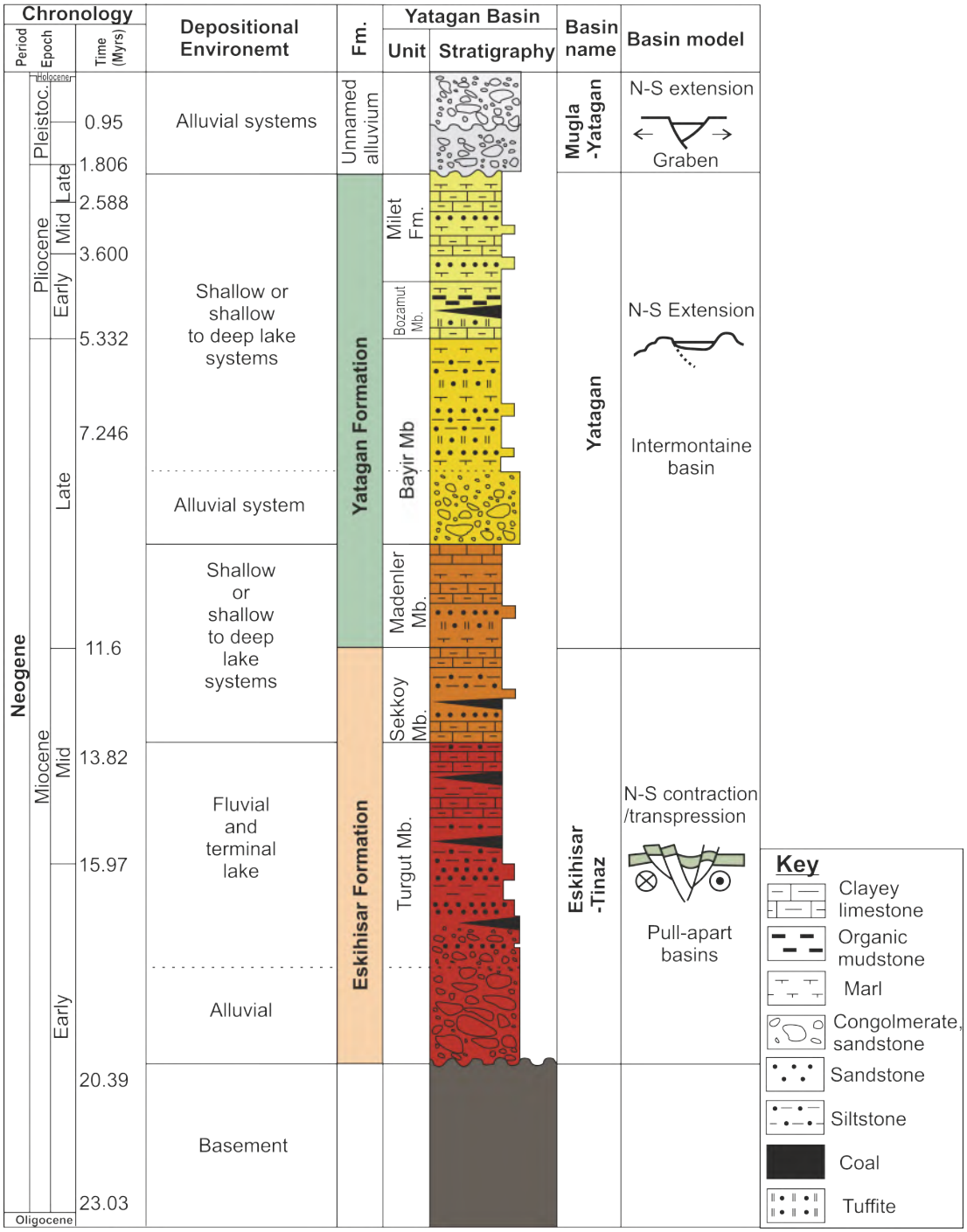

Figure 5.4: Stratigraphy of the Yatağan-Muğlas basin, after *Alçiçek* (2010), *Querol et al.* (1999) and *Gürer et al.* (2013).

.

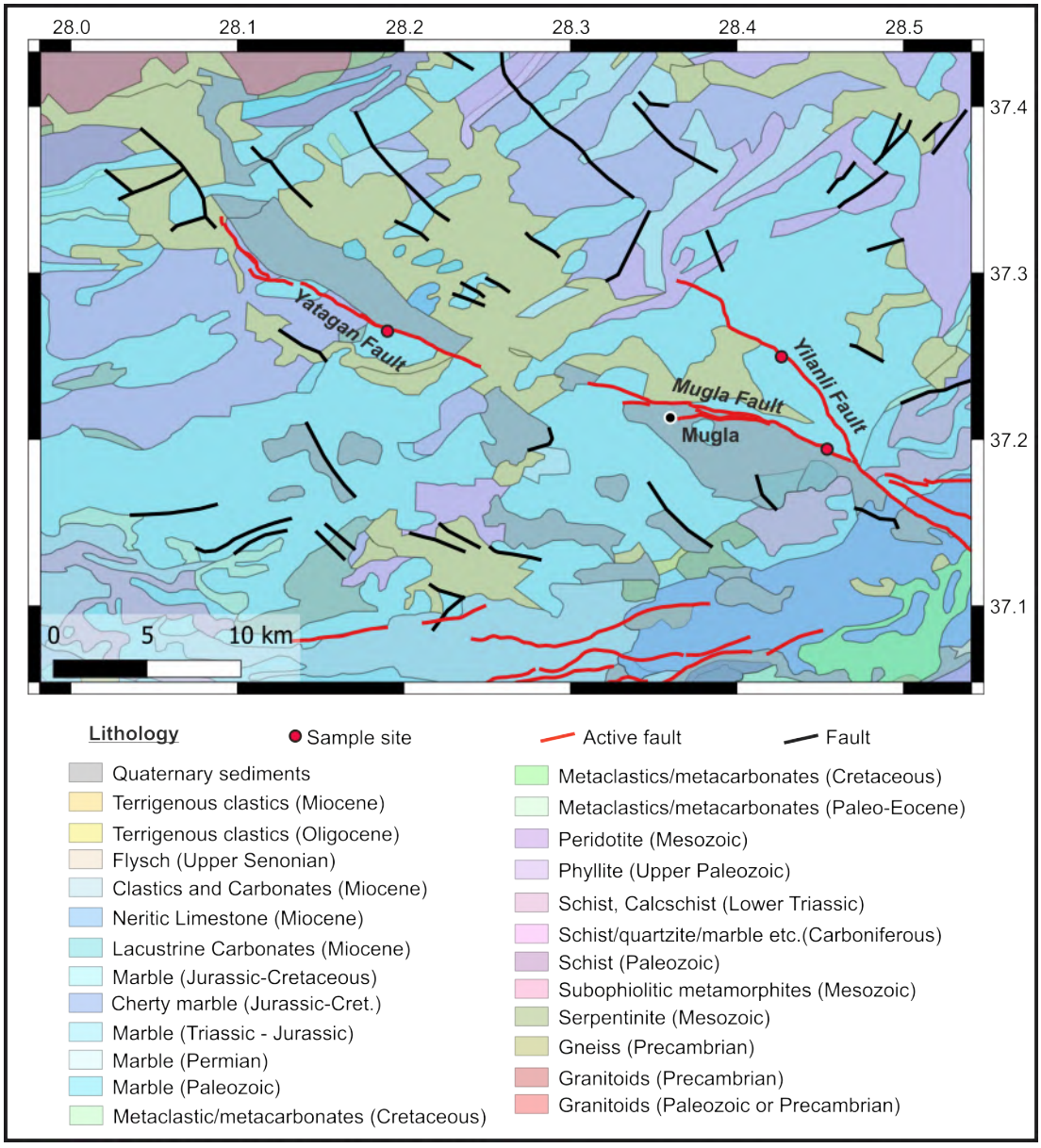

Figure 5.5: Geological map of the Muğla basin and surrounds, sample sites are shown by red dots on the three major faults. After *Akbaş et al.* (2011), location shown in Figure 5.1.

only been preserved since the decrease in erosion rates at the end of the LGM, there are no ages to support this hypothesis in western Turkey. I collected footwall slope samples from areas away from the foot of cliffs and from low outcrop aligned with the surface of the footwall slope (Figures 5.6, 5.7 and 5.8). The total offset of the scarp profile was determined using terresterial laser scanning (TLS) data (Figures C4,C5 and C10), which I collected as part of the fault scarp sampling method, and offsets were calculated using the Matlab® code crossint, developed by *Wilkinson et al.* (2015) and *Cowie et al.* (2017), as in Chapters 4 and 5. I collected all ^{36}Cl samples using an angle grinder, hammer and chisel, before preparing them in the Leeds Cosmogenic Isotope lab using the same methods described in Chapter 3 for all other ^{36}Cl samples. Sample measurement on the AMS was undertaken at SUERC by Richard Shanks and bulk rock chemistry was determined using inductively coupled plasma optical emission spectroscopy (ICP-OES) at the University of Leeds by Stephen Reid.

5.3.1 Sample site selection

Here I present photographs and descriptions of each of the ^{36}Cl sample sites investigated in this chapter.

Muğla

The sample site on the Muğla fault is located close to the centre of the fault (Figure 5.3) in Jurassic-Cretaceous marble (Figure 5.5). It is 20 m up slope from an olive grove, which is on a planar slope composed of coarse clastics. An ephemeral stream is located northwest along strike, which emerges from the gully and cuts through the slope giving insight into the hangingwall composition (Figure 5.6). The bedrock fault scarp is relatively low angled, with a dip of $\approx 40°$ (Figure C4). The tallest section of preserved fault plane is $\approx$ 2 m tall (Figure C2), however the geomorphology indicates that there has been erosion of the hangingwall at this point. The footwall-scarp and scarp hangingwall contacts are horizontal for 10 m. The footwall is relatively vegetation free for 8-10 m before more dense vegetation is found. Once in the vegetation, the footwall becomes more planar (Figures C3 and C4). The geometry of the sample site in profile can be found in Table 5.1.

Yatağan

The Yatağan sample site is located 5 km from the southeastern tip of the mapped Yatağan fault, offset southeast of the center by $\approx$4 km (Figure 5.3). The footwall at the sample site is composed of Cretaceous-Jurassic marbles (Figure 5.5). The bedrock fault scarp is exposed discontinuously for several hundred meters, from 50 m away from the road to the north-west, to around 100 m south-east of the sample site. The scarp is in forest on a steep slope above farmland in the flat valley bottom (Figure 5.7).

Site	Lat. (°)	Lon. (°)	Elev. (m)	P(z) (pa)	α (°)	β (°)	γ (°)	Scarp height (cm)	Trench Depth (cm)	El-f (avg)	Mu-f
Yl	37.2498	28.4266	1230	876	21	43	19	425	75	2.5312	1.5149
Mu	37.1943	28.4540	823	920	23	74	35	928	125	1.8299	1.2276
Ya	37.2652	28.1899	437	963	24	57	27	915	75	1.3075	1.0041

Table 5.1: Parameters of the sample sites for modelling, alpha is the hangingwall slope, beta is the fault scarp dip and gamma is the footwall dip, all determined from Terrestrial Laser Scanning data. Values in shown in this table are calculated by taking the mean of 10 separate interpretations of the scarp geometry, and the original values can be found in Tables C1, C2 and C3 in the appendices.Pressure at the site elevation (P(z)), El-f (spallation production rate factor) and Mu-f (muon production rate factor) are calculated using CRONUS calc, using the Lifton/Sato flux time dependent scaling (*Marrero et al.*, 2016, *Lifton et al.*, 2014). All sites use a production rate of 48.8, from *Stone et al.* (1996).

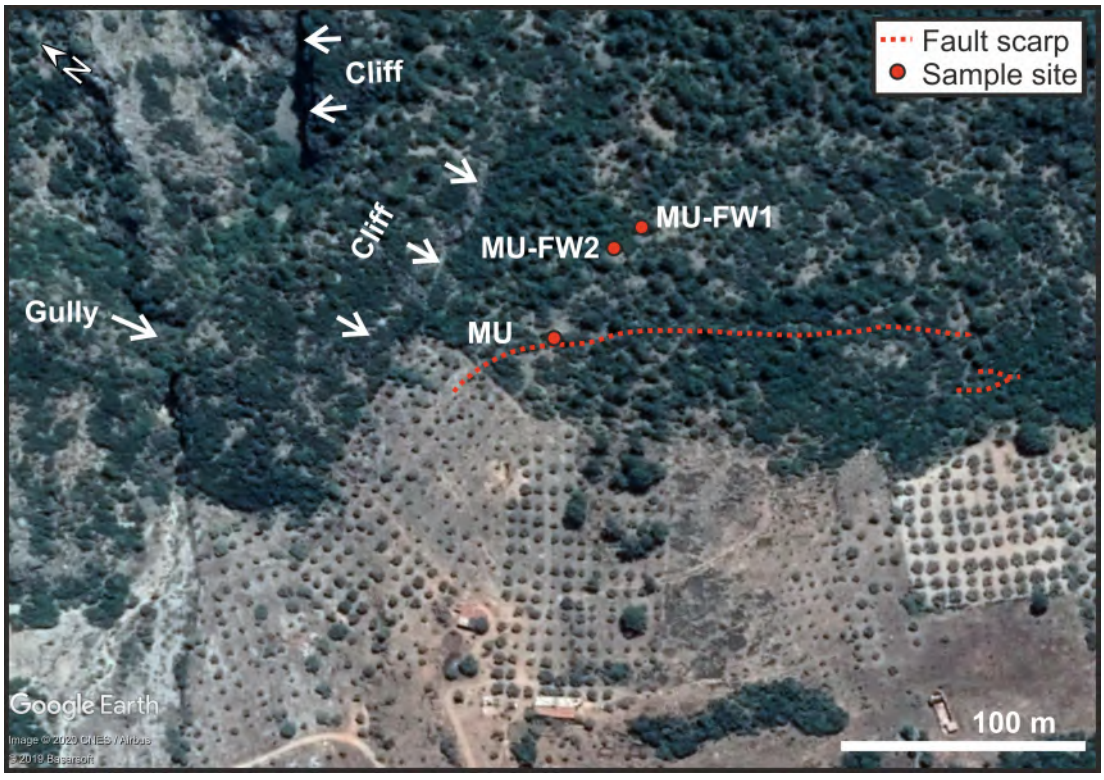

Figure 5.6: Satellite imagery of the sample site on the Muğla fault. MU is the location of the sample site on the scarp, MU-FW1 and MU-FW2 are the locations of the two footwall samples I took from the Mugla fault. Location of site within the basin can be seen in Figure 5.3.

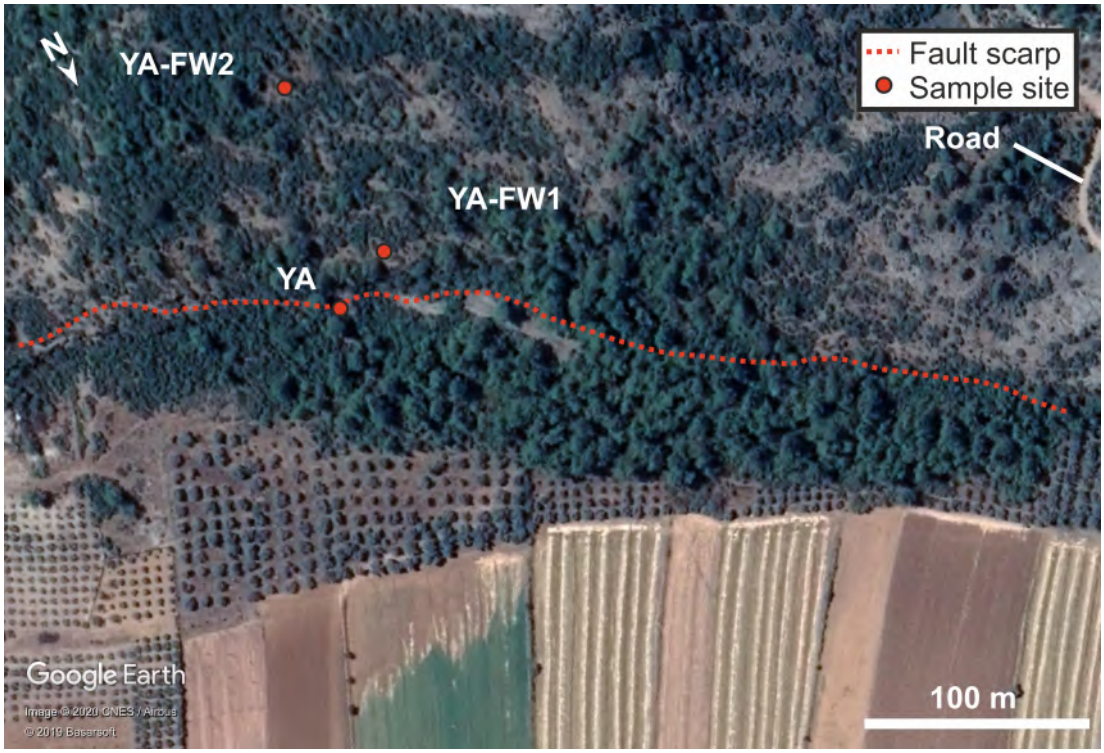

Figure 5.7: Imagery of the Yatağan sample sites. Location of site within the basin can be seen in Figure 5.3.

The scarp increases in elevation from northwest to southeast, with the road following a valley which runs perpendicular to the fault and crosses it approximately perpendicular to fault strike (Figure C8). The geometry of the sample site in profile can be found in Table 5.1.

The hangingwall of the Yatağan fault is a steep vegetated scree slope. Figure C5c provides a view of the hangingwall slope after vegetation removal, and large boulders (> 1 m) are present, and boulders up to 0.5 m were present in the trench (Figure C6b). The hangingwall-faultscarp contact is horizontal for 15 m, running into a fan/rockfall southeast along strike, and starting to slope uphill northwest along strike. The preserved fault plane dips at $\approx 70°$ and in places is well preserved for 2-3 m height. There is some banding in the lichen patterns on the fault plane that may indicate past earthquakes, and there are also rust coloured concretions on the fault plane, both above and below the current ground level (Figure C5d), which I assume are iron oxides based on the color. These concretions are commonly, but not always, associated with fractures on the fault plane. The eroded scarp is heavily vegetated and has erorded into a cliff-like morphology above the smooth planar fault plane, with 4-5 m high vertical cliffs in places. The footwall slope is relatively planar above the fault scarp, but has small discontinuous escarpments < 0.5 m tall. Footwall samples were taken from the top of these discontinuous escarpments (Figure C7). The hangingwall is rocky, with very little soil and thin gravel covering. The footwall vegetation is much less dense than in the

hangingwall slope. Both footwall sites (YL-FW1 and YL-FW2) are on sub-horizontal outcrops in line with the slope, and the site of YL-FW2 stands proud of the slope by ≈1 m and YL-FW1 stands proud ≈0.5 m. The site in profile can be found in Table 5.1.

Yilanli

The Yilanli sample site is located 8 km from where the Yilanli fault splays off from the Muğla fault (Figure 5.3). The footwall is composed of Cretaceous-Jurassic marbles. The hangingwall is naturally forested immediately underneath the fault, and ≈ 250 m downslope from the sample site on the hangingwall is managed forest, which has recently been felled (Figure 5.8). The section of sampled scarp runs discontinuously for around 350 m before terminating into a gully in both directions along strike. The scarp can be traced for a further 800 m northwest before terminating into another gully, and likely continues along strike to the southwest. The preserved bedrock fault scarp has a dip of 55-60° and is preserved to a height of 2.4 m at the sample site (Figures C9). The face itself is more weathered compared to the other sites, with some cracks that have experienced further weathering (Figure C11). The hangingwall-scarp contact is sloping by ≈ 10° at the site, however this was the best combination of preserved scarp and slope morphology that I found along the fault. There is more potential for appropriate scarp to sample along strike, however fieldwork time constraints combined with the time consuming nature of scouting sites in the terrain, made this the best feasible location. The location of the footwall samples can be seen in Figure C12.

5.3.2 Modelling

To model the footwall slope ^{36}Cl data and determine an exposure age for each sample I used CRONUS calc (*Marrero et al.*, 2016), which is an online cosmogenic exposure age calculator. It uses the cosmogenic isotope concentration, location and bulk rock chemistry to calculate the cosmogenic exposure age for a sample. I assumed that there is no erosion and no inherited ^{36}Cl.

I modelled the ^{36}Cl measurements from the fault scarp initially using the constant slip rate code of *Cowie et al.* (2017), which assumes a constant slip rate between the present and the age that offset was first preserved, and is described in detail in Chapter 2. I used exhumation increments of 0.5 m for each site and searched scarp ages at 1000 year increments between 10 kyr and 40 kyr years for each site in the first instance, and between 5 kyr and 40 kyr for Yilanli.

I then modelled the ^{36}Cl bedrock fault scarp data using the Flexible change point code, again from *Cowie et al.* (2017), described in Section 2.2.3. This code allows any number of changes in slip rate, and I used an exhumation step size of 0.5 m. I used the average values of the chemistry of all samples from the sites Yatağan, Muğla

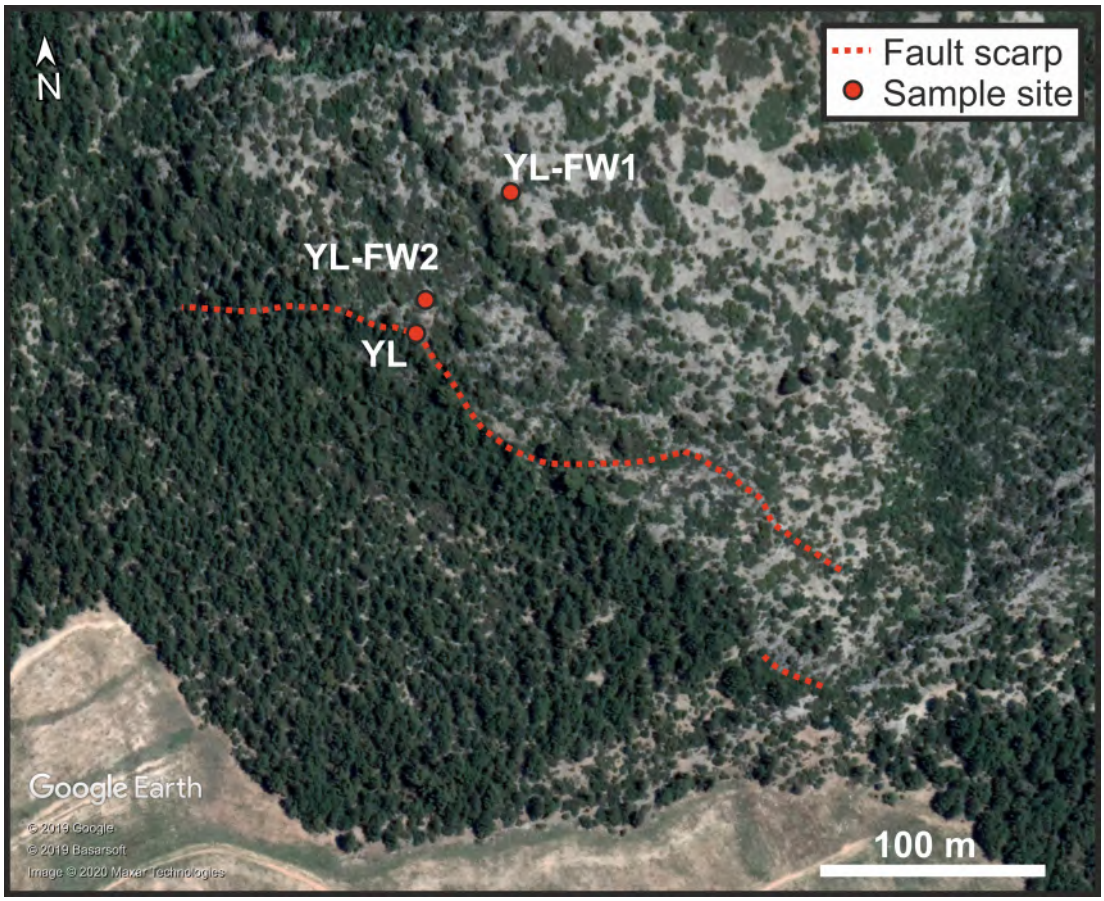

Figure 5.8: Satellite imagery of the Yilanli site. Location of site within the basin can be seen in Figure 5.3.

Site	Scarp age prior (years)	Elapsed time prior (years)	Offset (cm)
Muğla	uniform 10000-50000	uniform 0-15000	50
Yilanli	uniform 10000-50000	uniform 0-15000	50
Yatağan all	uniform 10000-50000	uniform 0-15000	50
Yatağan w/o top	uniform 10000-50000	uniform 0-15000	50
Muğla	normal 17300+/-4600	uniform 0-15000	50
Yilanli	normal 17300+/-4600	uniform 0-15000	50
Yatağan all	normal 17300+/-4600	uniform 0-15000	50
Yatağan w/o top	normal 17300+/-4600	uniform 0-15000	50

Table 5.2: A summary of MCMC models run. All sites models were run for 100k iterations. Yatağan all is all samples modelled, Yatağan w/o top is without the highest sample.

and Yilanli as representative of the chemistry of the colluvium. I ran two suites of inversions to investigate the effect of using a scarp age prior defined by ^{36}Cl dating of the footwall slope. One suite of inversions have a uniform scarp age prior, with equal likelihood between 10 k and 50 k years. The second suite of inversions has a normally distributed prior determined by using the mean exposure age of the footwall ^{36}Cl, and standard deviation of all footwall samples determined in the footwall slope age modelling (17.3±4.6 kyr, discussed in the following section).

I ran an extra suite of inversions on the Yatağan fault, because the model is strongly affected by a single sample ^{36}Cl value (as discussed below). In these extra inversions, I removed the top data point to gauge its effect on the model output. Table 5.2 provides a summary of all MCMC models run.

Whilst Bayesian modelling is a useful tool for determining slip histories from ^{36}Cl dating of bedrock fault scarps, deciding which slip rate value, or slip history to interpret from the inversion is complex. Given that the full distribution of slip histories is the solution to the inversion, deciding what value to use to calculate fault slip rate is worth careful consideration. In my work I have considered the maximum likelihood, which is the model which best fits the data, and the mean, mode and standard deviation values. All of these options can provide insight into the modelled process, and in some cases are similar values. The maximum likelihood provides the best fit to the data, however it can lead to over-fitting the data in trans-dimensional inversions, because although a model with a greater number of parameters may be able to fit the data best, the increase in number of parameters may not be justified by the increase in fit (*Bolstad*, 2009). More importantly, this value does not properly represent the whole distribution. The mean, mode and standard deviation of the posterior probability distribution do represent the entire solution distribution, are commonly presented when using a Bayesian approach (*Bendle et al.*, 2017, *Amey et al.*, 2018, *Zhao et al.*, 2018) and, therefore, are the values that I will use going forward. The footwall data are a useful addition and should be incorporated as prior information on the scarp age parameter, to maximise the available

Sample	Age (kyr)	Scarp Height (cm)	Slip rate (Individual) (mm/yr)	Slip rate (Mean) (mm/yr)
YA-FW1	14.2 ±1.1	916	0.65 ±0.05	0.53 ±0.04
YA-FW2	13.0 ±1	916	0.7 ±0.05	0.53 ±0.04
YL-FW2	19.3 ±1.4	425	0.22 ±0.01	0.25 ±0.02
YL-FW2	15.2 ±1.1	425	0.28 ±0.02	0.25 ±0.02
MU-FW1	25.5 ±1.9	928	0.36 ±0.03	0.54 ±0.04
MU-FW2	16.7 ±1.4	928	0.56 ±0.04	0.54 ±0.04

Table 5.3: Table of average slip rates determined from footwall samples. Slip rate individual is calculated by using the scarp height (Figure 2.2) and apparent exposure age for each sample and column 7 is determined using the scarp height and the mean exposure apparent age of all 6 samples. I used the time varying scaling factor of *Lifton et al.* (2014). The input data for the models can be found in Figures C17 and C18.

data. I will also present the results of using a uniform scarp age prior, to demonstrate the effect of this prior.

5.3.3 Results

Footwall slope ages and average slip rates

Data used in the CRONUS calculator (*Marrero et al.*, 2016) are shown in Figures C15 and C16 in the appendices. Notably I assume no erosion since they reached the surface and no inherited ^{36}Cl, because there is no constraint on either process. Apparent exposure ages vary between 13.0-25.5 kyr across all sites. Yatağan has the lowest ages and range, and Muğla has the highest age and range (Figure 5.9). The mean apparent scarp age from dating the footwall ages is 17.3 kyr, with a standard deviation of 4.6 kyr. There is no correlation between elevation and apparent age, which indicates the climate has had similar effects on the slopes in the Mugla basin, across a the range of elevations. Using the mean and standard deviation of ages from all sites in conjunction with the TLS derived scarp height in the plane of the fault at each site (Figure 2.2) results in average slip rates between the present day and the footwall age dates ranging from 0.2-0.7 mm/yr (Table 5.3). I do not calculate site specific rates because it is better to have more data in this calculation, and the close proximity of the sample sites should produce the same apparent age. If I assume that the age of the footwall is equal to the mean age of all the samples, then Yatağan and Muğla are both slipping at a rate of 0.5 mm/yr, and Yilanli at a rate of 0.25 mm/yr (Table 5.3). I also assume that climate has affected all of the slopes in the same way, though slip rate can effect the erosion rate (*Tucker et al.*, 2011).

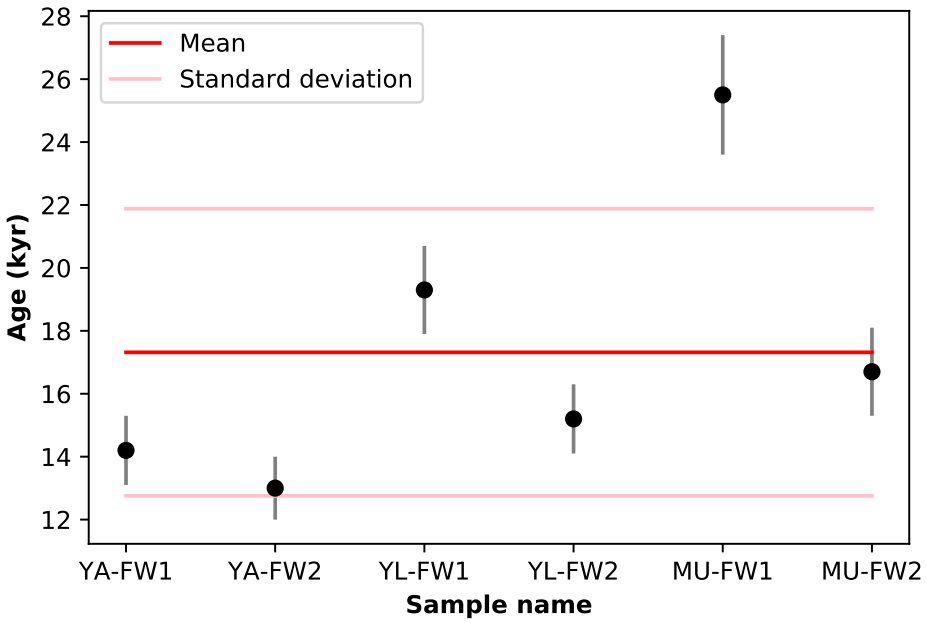

Figure 5.9: Ages for each footwall sample assuming 0 erosion, with two each from Yatağan (YA), Yilanli (YL) and Muğla (MU). Black dots show calculated ages, grey lines are 1σ uncertainties based on the analytical error and parameter uncertainties (*Marrero et al.*, 2016). Red and pink lines show the mean and standard deviation of all the ages. Ages were calculated using the online CRONUS calculator (*Marrero et al.*, 2016), using values shown in Figures C15 and C16 in the Appendices.

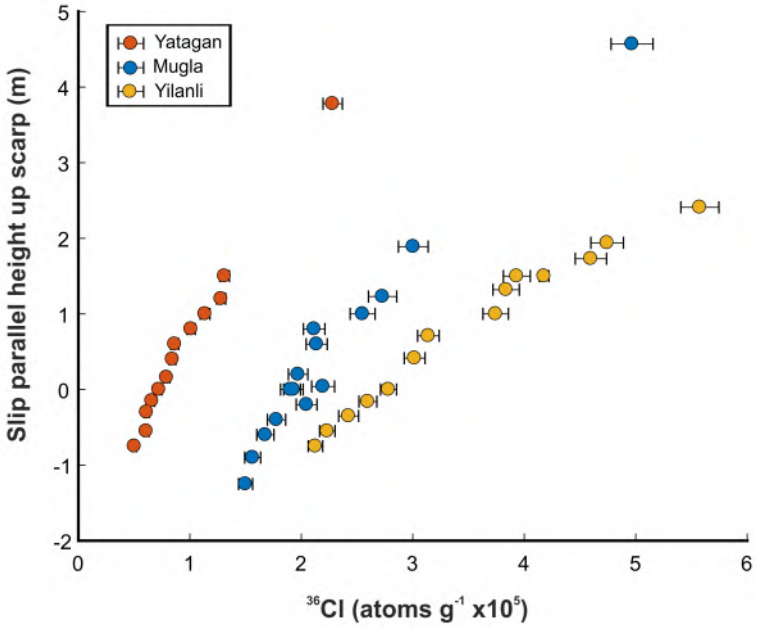

Figure 5.10: Concentration of ^{36}Cl vs height in the plane of slip for the three sites I sampled in western Turkey. 1 sigma analytical uncertainties are plotted, and for some data they are smaller than the plotted points.

Data and constant slip rate modelling

^{36}Cl vs height profiles increase in concentration with height above the footwall slope-fault scarp contact, at all sites (Figures 2.2 and 5.10). Yilanli has the greatest ^{36}Cl concentration at a given height, followed by Muğla and then Yatağan. There is a change in gradient at around 0.6 m at Yatağan, a less clear change in gradient at Muğla at a similar height, and there is a subtle change in gradient at Yilanli at around 1.5 m. Yilanli has a lower gradient than Muğla and Yatağan, which indicates that it is slipping at a slower average rate (*Cowie et al.*, 2017). Yilanli also has higher ^{36}Cl value at 0 height on the scarp than the other sites, which also supports a slower slip rate, though a long elapsed time since the last earthquake would also produce a greater concentration at 0 height. The measured geometry for each site used to model the exhumation of the fault scarp, which was calculated from the TLS data, is found in Table (5.1). Muğla can be modelled reasonably well with a constant slip rate, using a scarp age of 14 kyr (Figure 5.11). Using the same constant slip rate method, Yatağan is modelled to within analytical error until 3 m height, above which misfit increases with height, and Yilanli has a significant misfit throughout (Figure 5.11). Models of Yatağan are influenced by a single data point, highest on the scarp.

Muğla MCMC modelling

A summary of all MCMC models run for the Muğla site is found in Table 5.2, and these were run using the site geometry from Table 5.1. The distribution of the slip histories

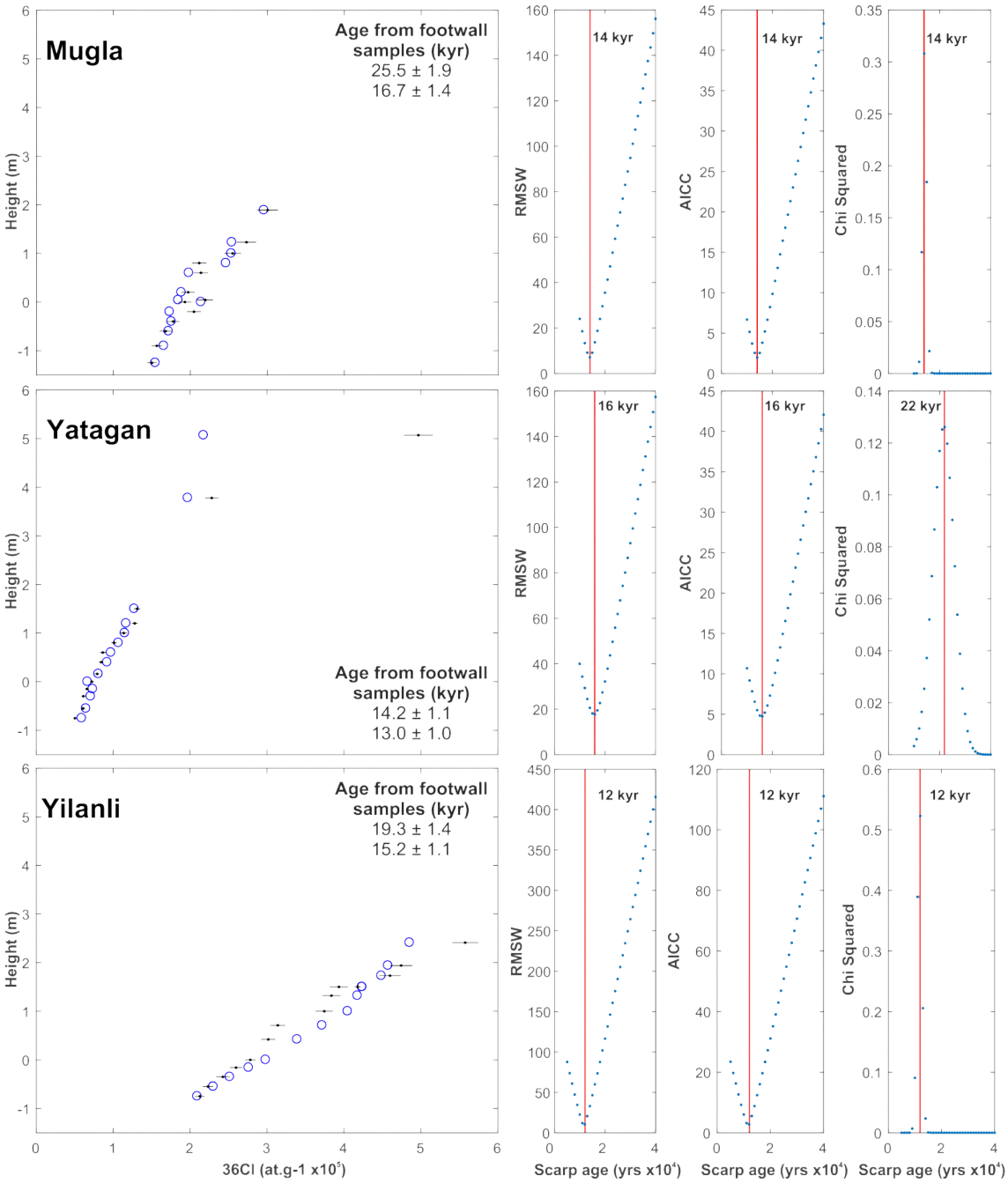

Figure 5.11: Results of constant rate modelling for the Muğla, Yatağan and Yilanli faults. Plots on the left show the lowest RMSw model (blue) fit to data (black). Plots on the right show the misfit in the form of, weighted root mean square (RMSw), modified Akaike information criterion (AICc) and Chi Squared values of the searched scarp ages, with red lines highlighting the best fitting model.

Muğla	Scarp Age Uniform (yrs)	Scap age Normal (yrs)	Elapsed time Uniform (yrs)	Elapsed time Normal (yrs)
Mean	17470	15986	2196	2153
Mode	14133	15322	112	1577
ML	12427	10859	2896	3530
95% Interval	11523 - 28244	10586 - 20840	118 - 5174	107 - 5416

Table 5.4: Statistics for the distribution of scarp age and elapsed time parameters from the MCMC inversion of the Muğla fault, the full distributions are shown in Figure 5.12. ML is maximum likelihood.

Yilanli	Scarp Age Uniform (yrs)	Scap age Normal (yrs)	Elapsed time Uniform (yrs)	Elapsed time Normal (yrs)
Mean	15031	15630	2580	2517
Mode	12407	12469	10	2040
ML	22321	23127	2532	2794
95% Interval	11749 - 19524	11785 - 20708	132 - 6096	101 - 6136

Table 5.5: Statistics for the distribution of scarp age and elapsed time parameters from the MCMC inversion of the Yilanli fault, the full distributions are plotted in Figure 5.12. ML is maximum likelihood.

indicates that a constant slip rate model fits the data well, in both the uniform and normal scarp age prior cases (Figures 5.13), though in the uniform scarp age case, a change in slip rate does occur in some models at ≈8 m height up the scarp. Note that constant slip rate models in the MCMC inversion can vary the elapsed time, unlike the constant rate modeling shown in the previous section, which presumes a constant rate until the present day. For both the normal and uniform scarp age prior cases the highest likelihood model has a variable slip rate, with a period of rapid slip at ≈4 kyr, followed by a period of quiescence, with a second period of fast slip starting at ≈10 kyr (red lines, Figure 5.13). In the normal scarp age prior case there is a slowing of slip rate at 8.5 m height. In both the normal and uniform scarp age prior cases, many of the displayed models fit the data reasonably well via a wide range of slip histories (Figures 5.14 and 5.15).

Modeling of the Muğla fault using footwall ages to inform the scarp age produces ≈10 k models which fit the data to within 2 standard deviations (Table 5.9). Using a uniform scarp age prior instead results in fewer models which fit the data within 2 standard deviations, however the number of models that fit the data in 3,4 and 5 standard deviations is similar between uniform and normal scarp age priors (Table 5.10). This is primarily due to the wider uniform prior resulting in a larger parameter space meaning convergence requires a greater number of iterations.

At all sites the number of parameters increases with the number of slip rate changes, and the number of changes in slip rate is determined by the inversion. At Muğla both

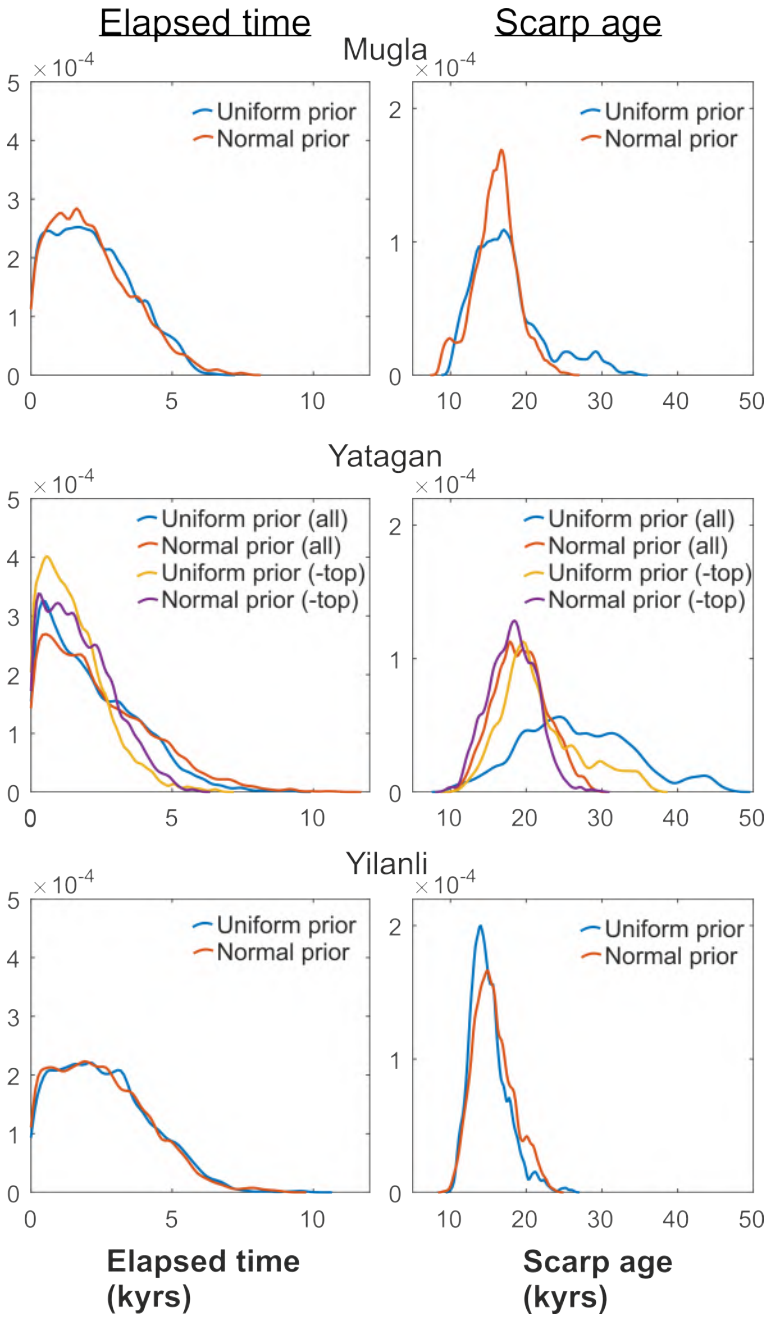

Figure 5.12: Histograms of the elapsed time and scarp age parameters from the MCMC modelling of each site. Results are shown for both the normal and uniform scarp age prior cases for all sites, as well as with and without the highest sample up the scarp for the Yatağan site.

Yatağan (All samples)	Scarp Age Uniform (yrs)	Scap age Normal (yrs)	Elapsed time Uniform (yrs)	Elapsed time Normal (yrs)
Mean	26788	19295	2149	2402
Mode	20341	20694	101	18
ML	37875	26316	1201	2216
95% Interval	15272 - 41332	13737 - 25263	79 - 5893	81 - 6871

Table 5.6: Statistics for the distribution of scarp age and elapsed time parameters from the MCMC inversion of the Yatağan fault using all samples, the full distributions are in Figure 5.12.

Yatağan (- top sample)	Scarp Age Uniform (yrs)	Scap age Normal (yrs)	Elapsed time Uniform (yrs)	Elapsed time Normal (yrs)
Mean	21694	18194	1522	1738
Mode	23675	19936	35	54
ML	15084	15354	489	968
95% Interval	14715 - 32786	12940 - 23201	54 - 4270	69 - 4412

Table 5.7: Statistics for the distribution of scarp age and elapsed time parameters from the MCMC inversion of the Yatağan fault omitting the highest sample on the scarp, the full distributions are in Figure 5.12.

the uniform and normal scarp age prior models show a higher frequency of models with 0 changes in slip rate, and this is true regardless of the ranking of likelihood (Figures C14 and C13). Using the uniform scarp age prior results in a greater proportion of variable slip rate models, apart from in the case of the best fitting models (fitting within 2 standard deviations) where proportions are similar.

Using the uniform or normal scarp age prior produces similar posterior distributions of elapsed time, which is time since the most recent slip, and scarp age, which is the time from when slope offset is preserved (Figure 5.12, Table 5.4). Using a uniform scarp age distribution produces a posterior scarp age distribution which is more skewed towards higher ages and has a higher mean and larger range (Table 5.4). The average slip rates over the period modelled are similar between the two cases, where the slip rate is determined using the equation:

$$\text{Average slip rate} = \frac{\text{scarp age}}{\text{scarp height}} \tag{5.1}$$

Modal and mean scarp age values of the normal scarp age prior case equate to an average slip rate over the period modelled of ≈0.6 mm/yr, with the most likely model (ML) at a higher value of 0.85 mm/yr and a standard deviation of 0.09 mm/yr (Table 5.8).

Calculating the mean slip rate using a moving non-overlapping 100 year window results in similar slip rates across all fits to the data, with a slight peak in rate between

Muğla	Scarp age Normal (yrs)	Scarp height (cm)	Slip rate (mm/yr)
Mean	15986	928	0.58
Mode	15322	928	0.61
ML	10859	928	0.85
St. dev.	2876	-	0.09

Table 5.8: Average Holocene calculated using Equation 5.1 and the output of the MCMC inversion using a normal scarp age prior, for the Muğla fault.St. dev. is the standard deviation of the posterior scarp age distribution

Site	SD2	SD3	SD4	SD5
Muğla	10148	79886	88712	89965
Yatağan	0	0	1115	14702
Yatağan W	2503	23927	43883	59515
Yilanli	9738	37033	58460	72294

Table 5.9: Table of fit to data of MCMC flexible change point modelling using a normally distributed scarp age prior of 17.3 ka +/- 4.6ka . Each model run produced 90 k models once the burn-in was removed, and the values in this table represent how many models fit the data to within 2, 3, 4 or 5 standard deviations.

3-10 kyr, apart from in models that fit withing 2sd where there is a plateau between 3 and 15 kyr at ≈0.6 mm/yr in the normal scarp age prior case (Figure 5.16). In the uniform scarp age prior case, the plateau is similar in magnitude but drops off at ≈12 kyr; this is because the number of models reduces (Figure 5.17).

Yilanli MCMC modelling

A summary of all MCMC inversions I ran for the Yilanli site site is found in Table 5.2, and these were run using the site geometry from Table 5.1. On the Yilanli fault, the histogram of accepted slip histories can be fit with a constant rate, but the change in gradient of the range of accepted models indicates a variable slip rate is likely (Figure 5.13). The highest likelihood slip history is variable, with one change in slip rate at around 4 m and 4 kyr (Figure 5.13). Modelling the Yilanli fault with the normal scarp

Site	SD2	SD3	SD4	SD5
Muğla	8488	7974	88738	89930
Yatağan	0	18	1971	8321
Yatağan W	2881	23078	43634	58772
Yilanli	7828	35560	57613	72722

Table 5.10: Table of fit to data of MCMC flexible change point modeling using a uniformly distributed scarp age prior between 10 ka and 50 ka. Each model run produced 90 k models once burn-in was removed, values in this table represent how many models fit the data to within 2, 3, 4 or 5 standard deviations.

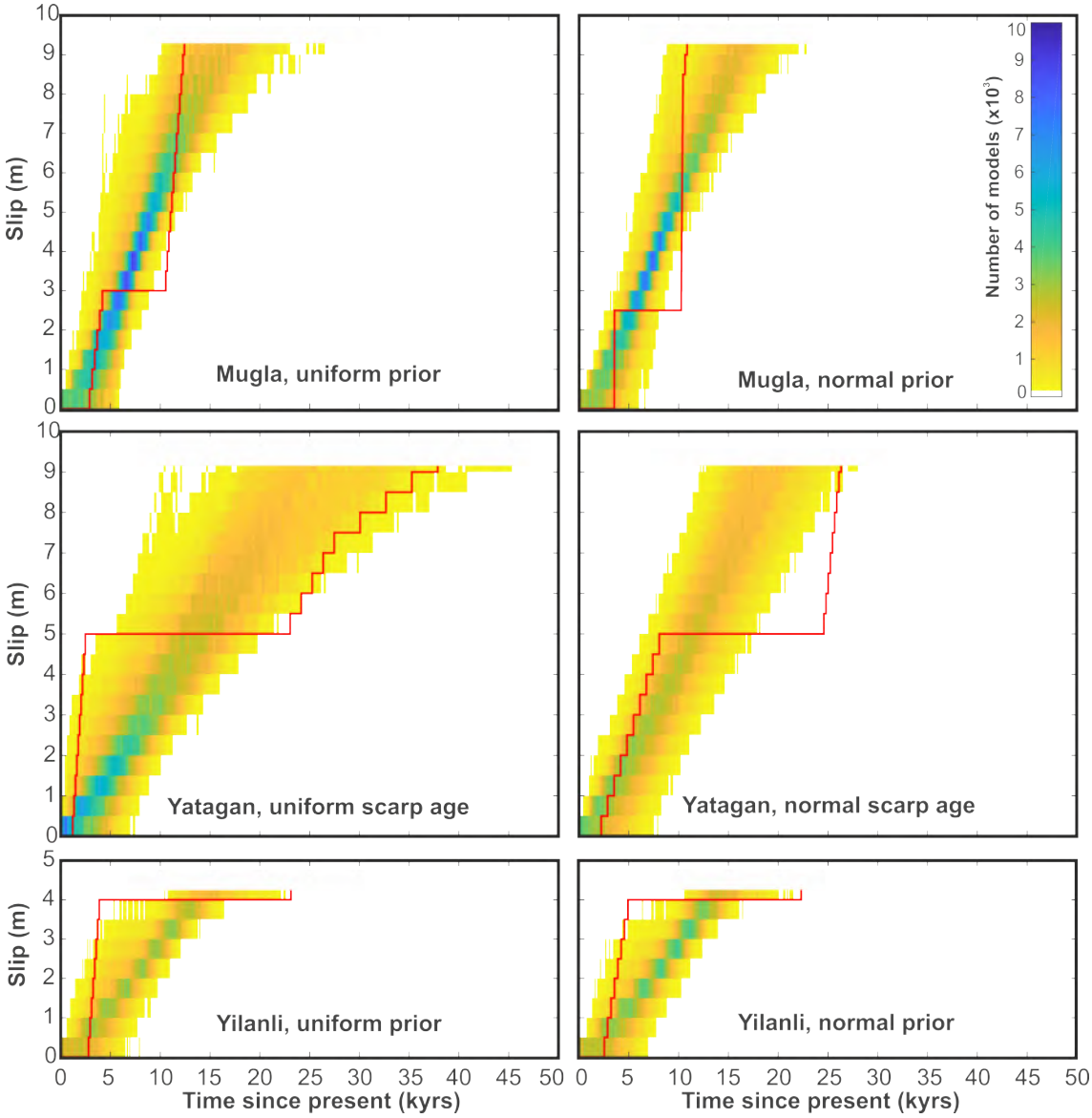

Figure 5.13: All plots show a histogram of the distribution of slip histories, in 200 year bins. A burn-in of 10 k has been removed. The plots on the left have a uniform scarp age prior between 10 kyr and 50 kyr, and the plots on the right use a normally distributed scarp age of 17.3±4.6 kyr. The red line is the most likely slip history.

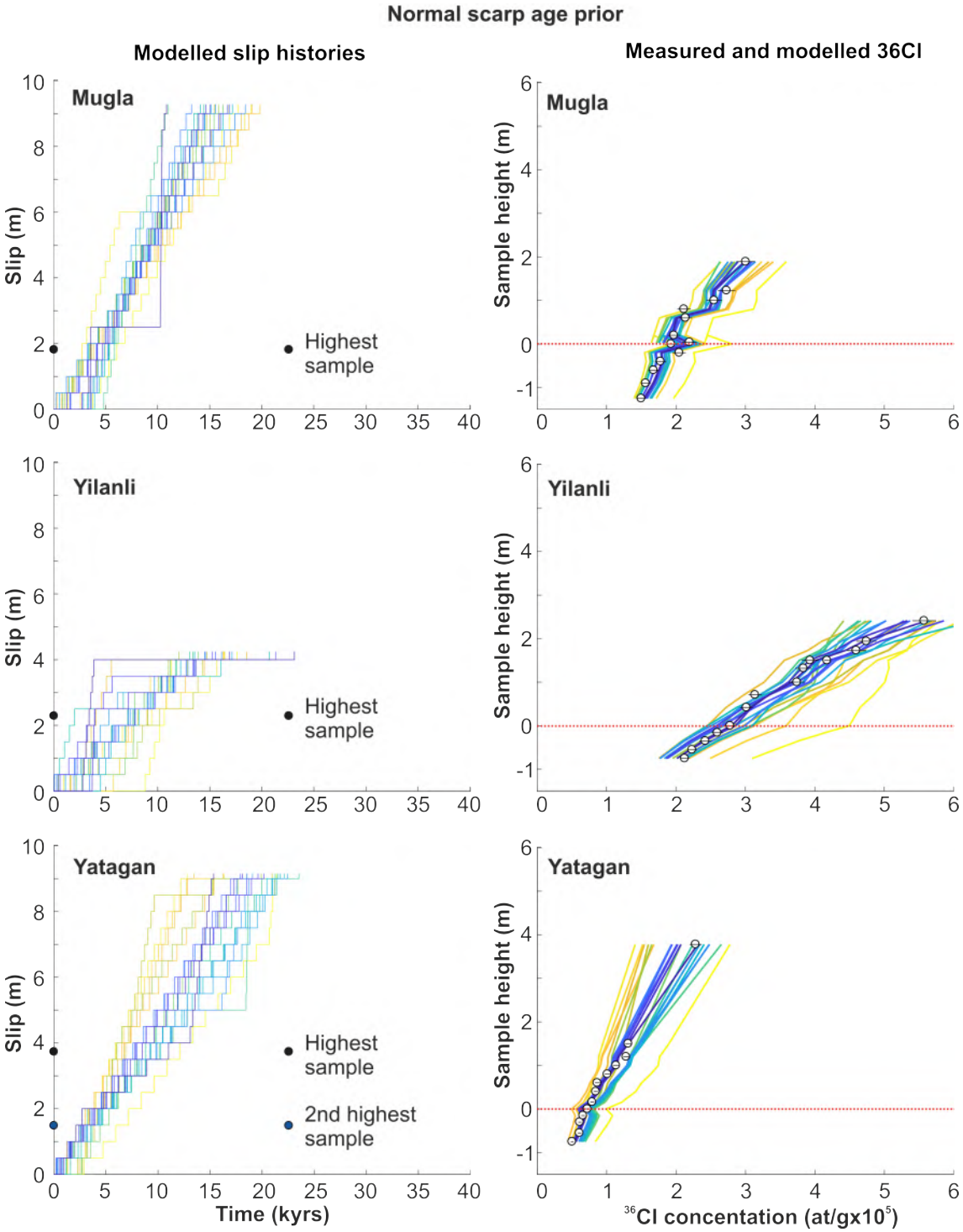

Figure 5.14: Plots on the left show every 4500th slip history, with the burn-in models removed. Dark colors show higher likelihood, and lighter colours show lower likelihood. Plots on the right show the fit to the data for each of these models, with corresponding colours. These were all modelled with a normally distributed scarp age prior, and the results for Yatağan do not include the highest sample up the scarp.

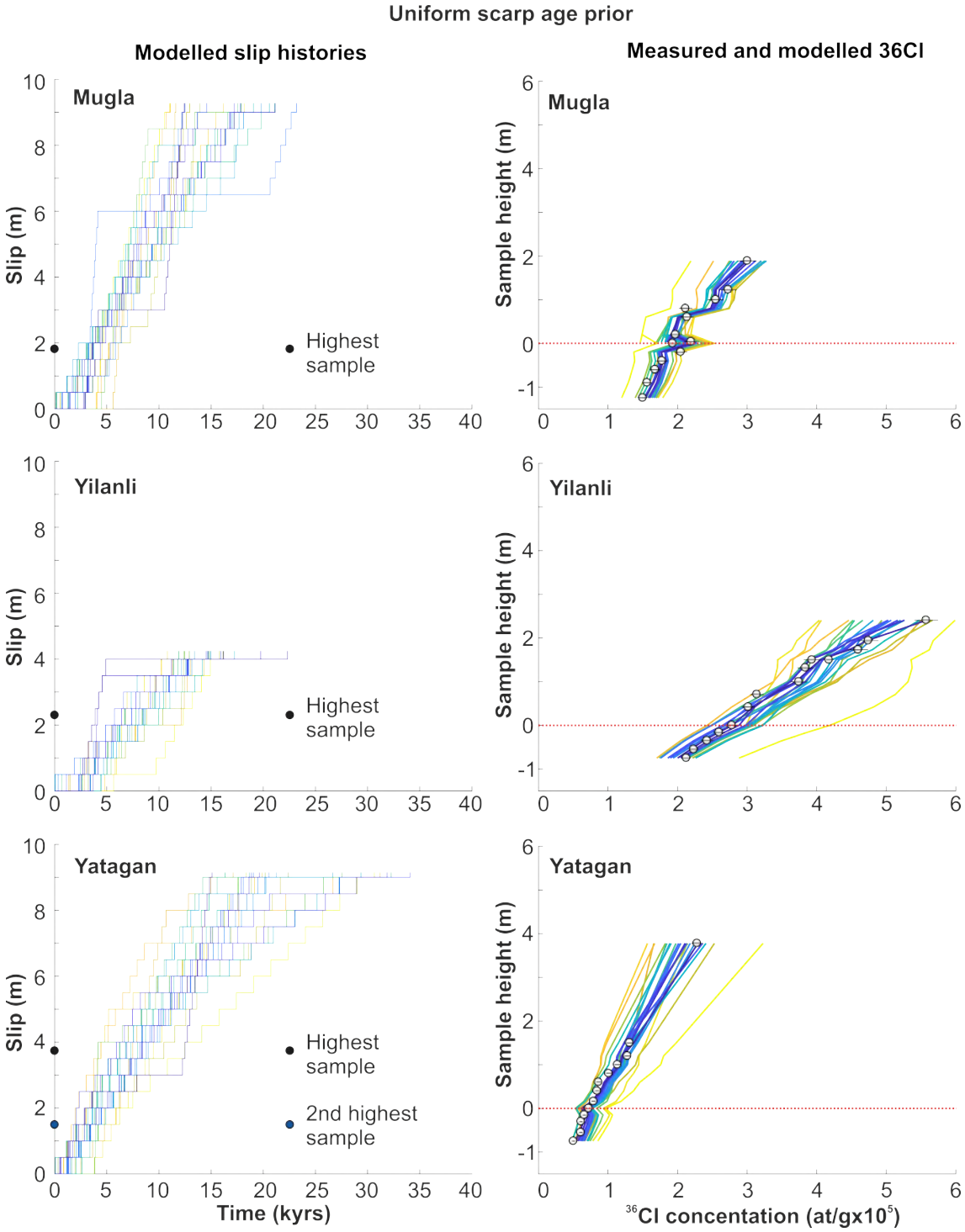

Figure 5.15: Plots on the left show every 4500th slip history, with the burn-in models removed. Dark colors show higher likelihood, and lighter colours show lower likelihood. Plots on the right show the fit to the data for each of these models, with corresponding colours. These were all modelled with a uniformly distributed scarp age prior, and the results for Yatağan do not include the highest sample up the scarp.

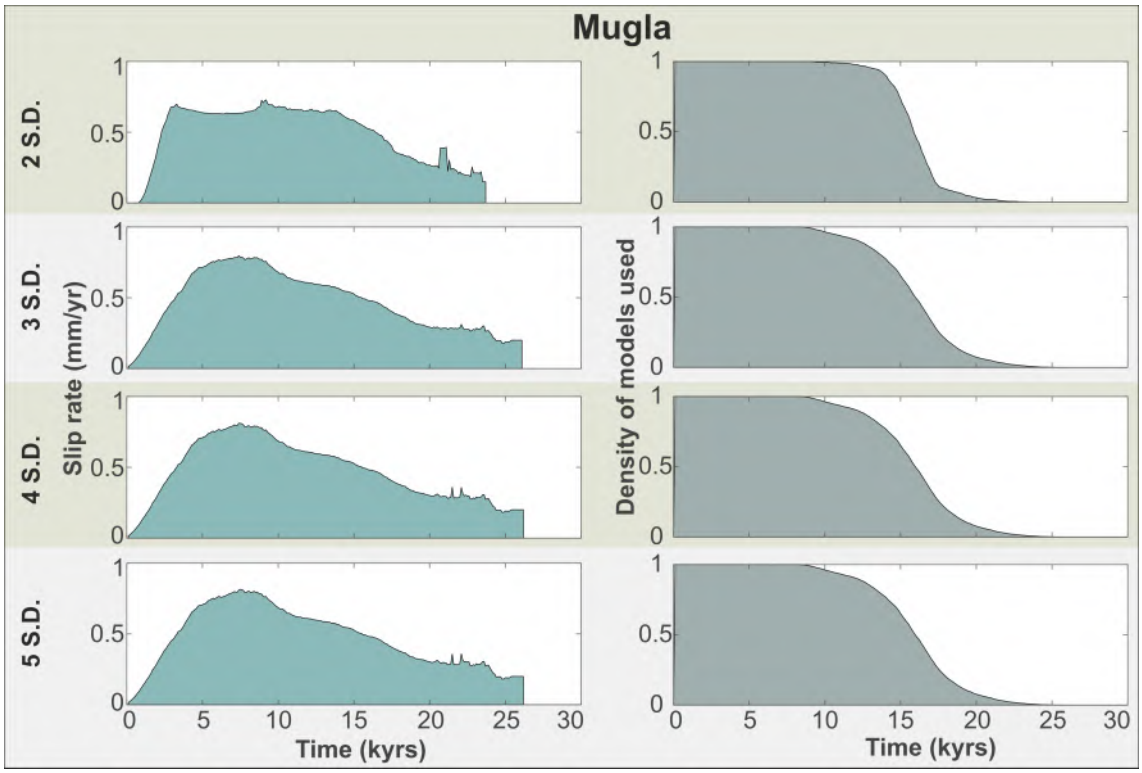

Figure 5.16: Slip rate derived from the normally distributed scarp age prior inversion of the Muğla fault. Plots on left show the mean slip rate calculated in 100 year windows, for models that fit within 2, 3, 4 and 5 standard deviations. Plots on the right show how many models are used, 1 being all the models, and 0 none of the models. When number of models drops below 1, the average slip rates will not be representative.

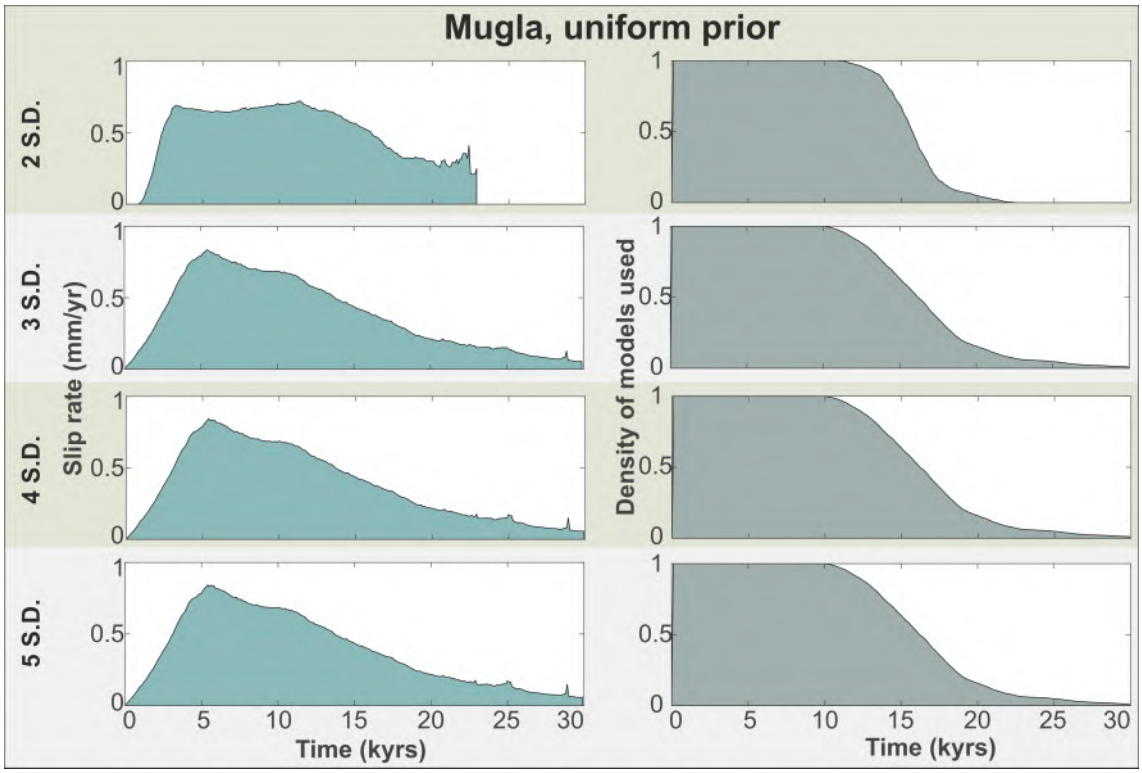

Figure 5.17: Results from the uniformly distributed scarp age prior inversion of the Muğla fault. Plots on left show the mean slip rate calculated in 100 year windows, for models that fit within 2, 3, 4 and 5 standard deviations. Plots on the right show how many models are used, 1 being all the models, and 0 none of the models. When number of models drops below 1, the average slip rates will not be representative.

Yilanli	Scap age Normal (yrs)	Scarp height (cm)	Slip rate (mm/yr)
Mean	15630	425	0.27
Mode	12469	425	0.34
ML	23127	425	0.18
St. dev.	2616	425	0.04

Table 5.11: Average Holocene calculated using Equation 5.1 and the output of the MCMC inversion using a normal scarp age prior, for the Yilanli fault.

age prior results in 10 k models which fit the data within 2 standard deviations, and using the uniform scarp age prior results in 8000 models that fit within 2 standard deviations (Tables 5.9 and 5.10). The number of models that fit the data within 3 and 4 standard deviations is 1-2 thousand less in the case of uniform scarp age prior relative to the normal scarp age prior case, and 5 standard deviations is similar in both cases.

The models fit the data well, producing a similar range of fits to the data between the normal and uniform scarp age prior cases (Figures 5.14 and 5.15). Using a normal scarp age prior results in a modal value of one change in slip rate, particularly in the best fitting (2sd) models (Figure C14). In the case of the uniform scarp age prior, only the best fitting (2sd) models preferred one change in slip rate, all other subsets had modes of 0 changes in slip (Figure C13).

The uniform scarp age prior and normal scarp age prior cases produce similar scarp age and elapsed time distributions, and therefore similar average slip rates over the period of the model (Figures 5.12 and Table 5.5). In the normal scarp age prior case, mean, modal and most likely posterior scarp age values equate to average slip rates of 0.27, 0.34 and 0.18 mm/yr (Table 5.5).

Both scarp age prior cases also produce similar mean slip rate distributions, with peak slip rates between 3-5 kyr of 0.5-0.7 mm/yr, falling to around 0.2-0.3 mm/yr earlier than 5 kyr. This is true except that models with a normal scarp age prior fitting within 5 standard deviations have a higher slip rate (0.5 mm/yr) for a longer period than the uniform scarp age prior case (Figures 5.18 and 5.19).

Yatağan MCMC modelling

A summary of all MCMC models I ran for the Yatağan site is found in Table 5.2. These models used site geometry from Table 5.1. I initially modelled the Yatağan site using all available ^{36}Cl measurements, running two different inversions, one with the normal scarp age prior and one with a uniform scarp age prior (Figure 5.20). Both of these inversions produced relatively poor fits to the data compared to the other sites discussed in this chapter (Tables 5.9 and 5.10). Plots of the fit to data show that the all models do not fit the highest sample up the fault scarp (Figures 5.22 and 5.21). To

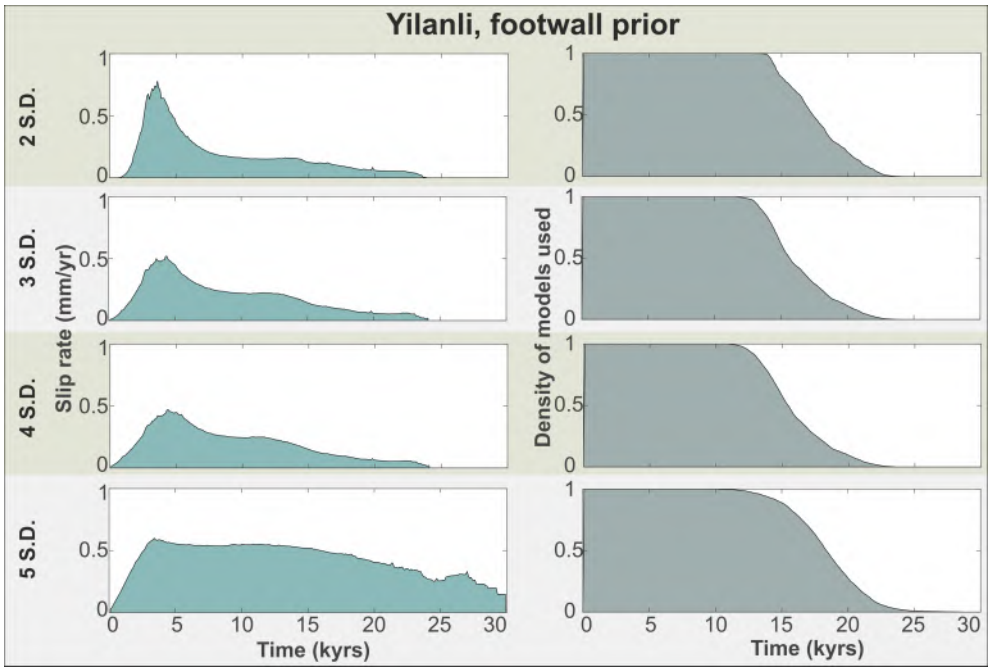

Figure 5.18: Results from the normally distributed scarp age prior inversion of the Yilanli fault. Plots on left show the mean slip rate calculated in 100 year windows, for models that fit within 2, 3, 4 and 5 standard deviations. Plots on the right show how many models are used in calculating the mean, 1 being all the models, and 0 none of the models.

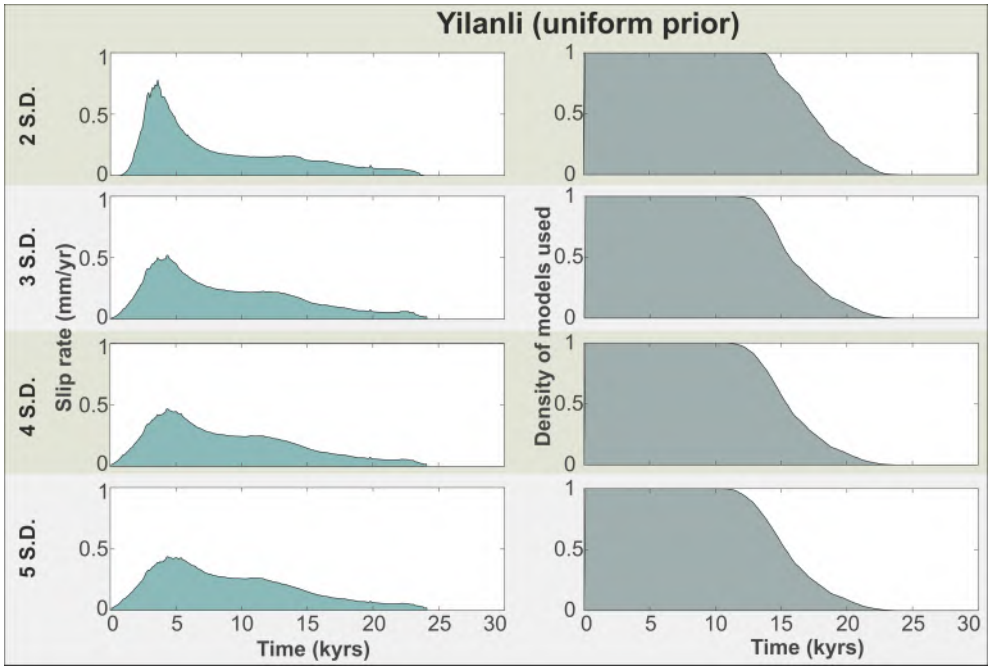

Figure 5.19: Results from the uniformly distributed scarp age prior inversion of the Yilanli fault. Plots on left show the mean slip rate calculated in 100 year windows, for models that fit within 2, 3, 4 and 5 standard deviations. Plots on the right show how many models are used in calculating the mean, 1 being all the models, and 0 none of the models.

determine if the highest sample is an outlier, I ran a two additional inversions, both of them omitting the highest ^{36}Cl sample up the fault scarp, one for each case of the scarp age prior, as above. In both cases this reduced the range of likely slip histories (Figure 5.20) and resulted in a better model fit to the data (Tables 5.9 and 5.10, Figures 5.22 and 5.21). All four cases produced similar elapsed time distributions. Using a normal scarp age prior results in similar scarp age distributions either with or without the top sample (Figure 5.12, Tables 5.6 and 5.7). Using a uniform scarp age prior results in wider range of scarp age distribuition in both cases, with a larger effect when the top sample is included. When the top sample is included and a uniform scarp age prior used, the modal value is 6 kyr older than when it is omitted (Figure 5.12, Tables 5.6 and 5.7) .

The poor fit to the top sample may be because the modelling does not consider an active physical process such as weathering, or it could be a function of how the model is trying to fit the data. It may be that to better fit the data a large number of changes in slip rate are required, but because the model uses the standard deviation of the whole data set rather than the analytical uncertainty of each sample to fit the data, the optimum fit is allowed to deviate significantly from the analytical uncertainty of a single or a a few samples, as is apparent in Figures 5.22 and 5.21. One physical mechanism that could be responsible for an elevated ^{36}Cl concentration in the highest sample is inheritance of ^{36}Cl due to exposure during the LGM, however this is unlikely to be an issue because the sample was at ≈5 m depth at this time. Interaction with meteoric water can enrich limestones in ^{36}Cl because atmospheric comsogenic ^{36}Cl is abundant in meteoric water(*Dunai*, 2010), and is a more likely scenario, however there is no evidence to support or disprove this mechanism.

The best fitting model when including the highest sample has a scarp age of ≈27 kyr with a long period of inactivity between 8-25 kyr (Figure 5.22), however this model does not fit the lowest data well. This suggests that if the concentration in the highest sample is accurate, then the fault likely experienced significant variation in slip rate, however this conclusion is only supported by a single data point, and is therefore not robust. To determine if the slip variation higher on the scarp is real requires more samples to be taken at a similar height. As a result, going forward I will only consider inversions undertaken omitting the highest ^{36}Cl up the fault scarp at the Yatağan site as I have greater confidence in the results of this inversion due to it's ability to fit all the data, and both the uniform and normal scarp age priors favour 0 changes in slip rate (Figures C14 and C13). Similar posterior scarp age distributions for both cases result in similar average slip rates. In the normal prior case, the mean, modal and most likely scarp age posterior values equate to slip rates of 0.5, 0.46 and 0.60 mm/yr (Table 5.12).

Yatağan	Scap age Normal (yrs)	Scarp height (cm)	Slip rate (mm/yr)
Mean	18194	916	0.50
Mode	19936	916	0.46
ML	15354	916	0.60
St. dev.	3161	916	0.07

Table 5.12: Average Holocene calculated using Equation 5.1 and the output of the MCMC inversion using a normal scarp age prior, for the Yatağan fault.

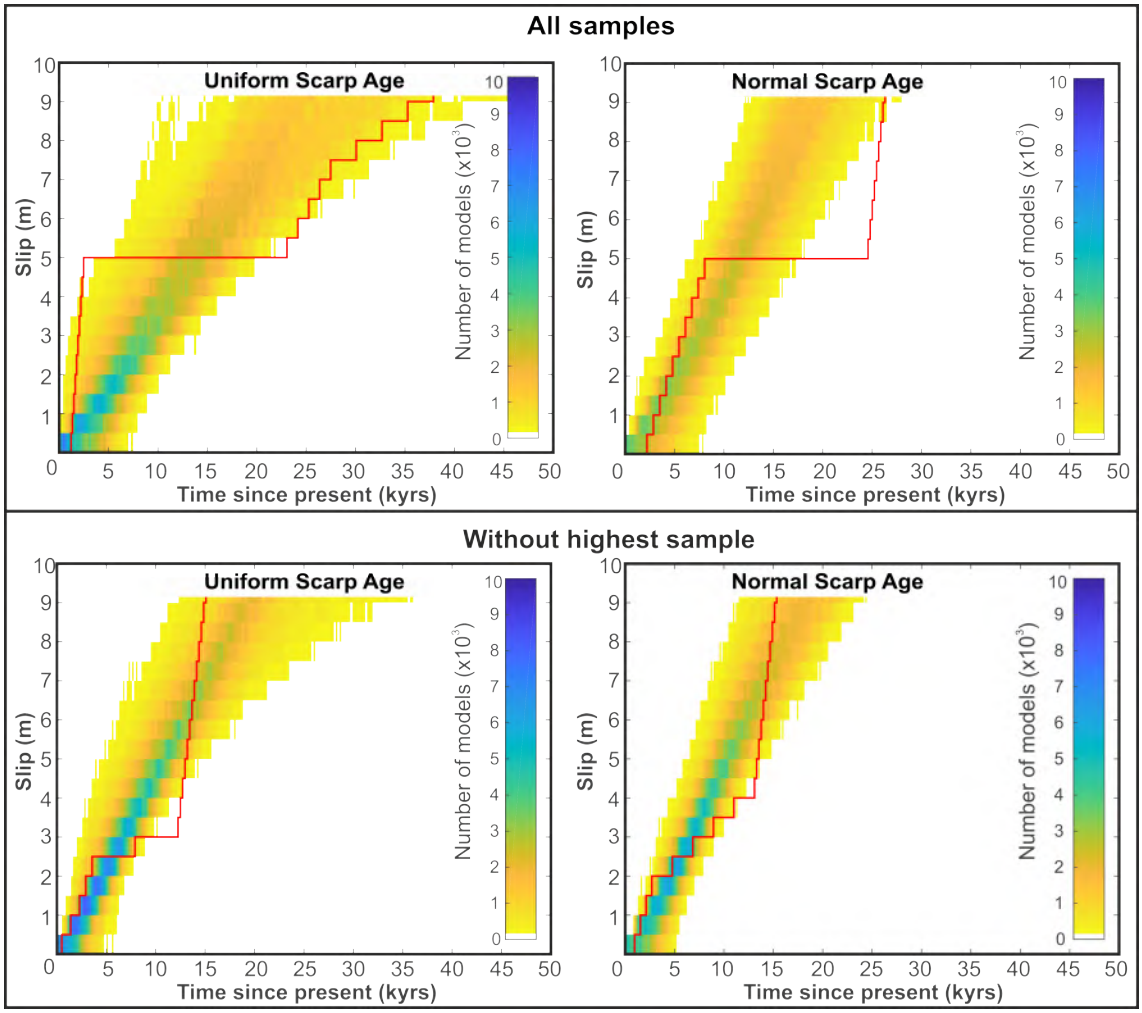

Figure 5.20: All plots show distribution of slip histories for the Yatağan fault, binned into 200 year bins. The red line is the most likely slip history. A burn-in of 10 k iterations has been removed. Plots on the left have a uniform scarp age prior scarp age between 10 kyr and 50 kyr, and plots on the right use a normally distributed scarp age of 17.3±4.6 kyr. The top row plots include the highest sample up the scarp, and the bottom plots do not.

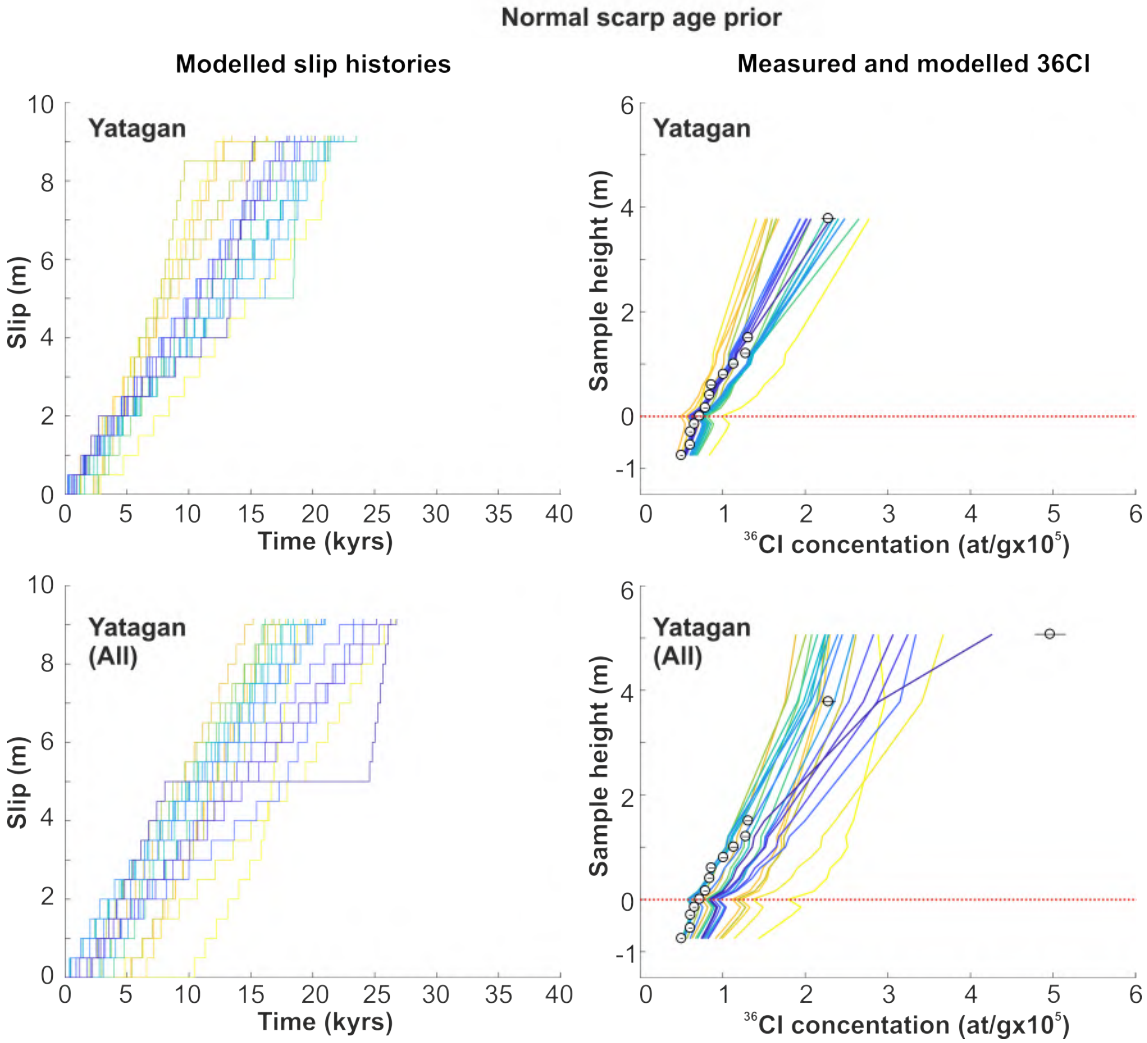

Figure 5.21: Plots on the left show every 4500th slip history, with the burn-in models removed. Dark colors show higher likelihood, and lighter colours show lower likelihood. Plots on the right show the fit to the data for each of these models, with corresponding colours. All models use a normally distributed scarp age prior, the top row is without the highest sample at 5 m, and the bottom row with the highest sample.

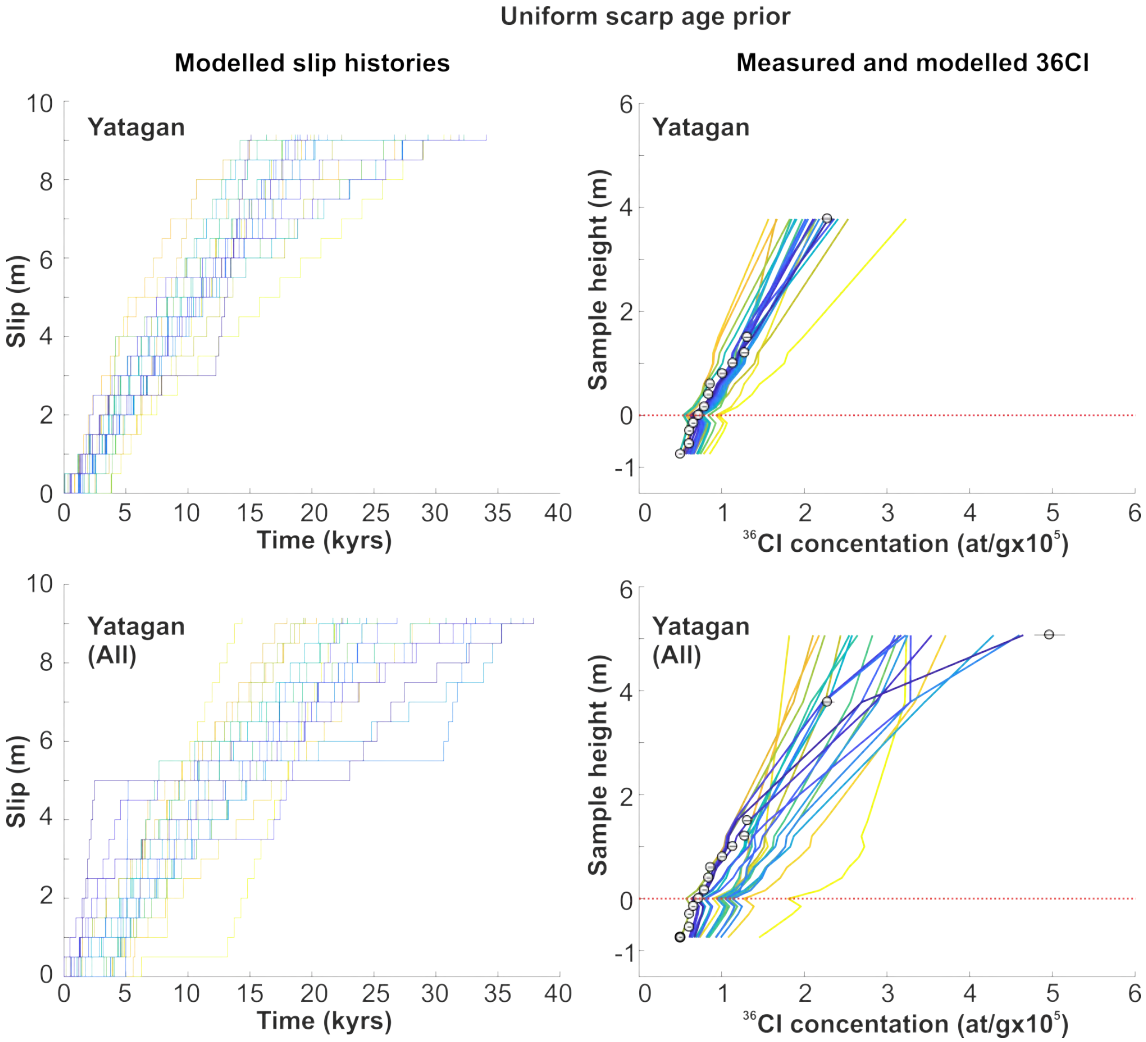

Figure 5.22: Plots on the left show every 4500th slip history, with the burn-in models removed. Dark colors show higher likelihood, and lighter colours show lower likelihood. Plots on the right show the fit to the data for each of these models, with corresponding colours. All models use a uniformly distributed scarp age prior, the top row is without the highest sample at 5 m, and the bottom row with the highest sample.

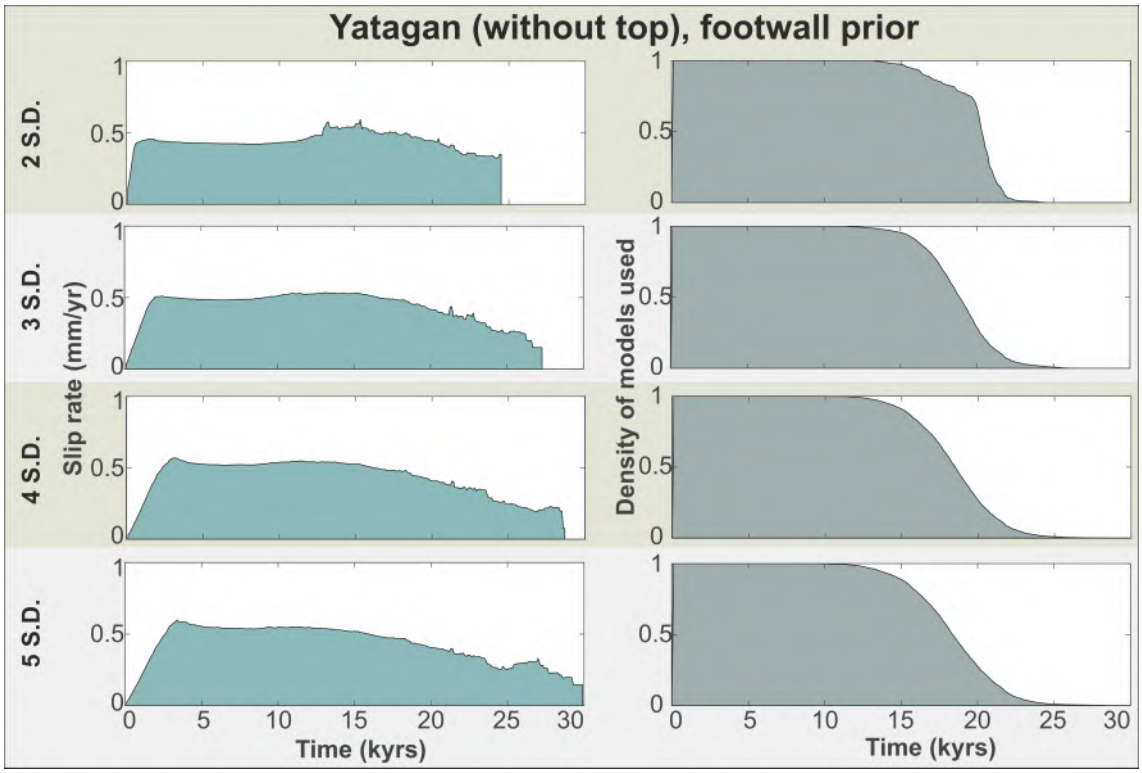

Figure 5.23: Results from the normally distributed scarp age prior inversion of the Yatağan fault, omitting the highest sample. Plots on left show the mean slip rate calculated in 100 year windows, for models that fit within 2, 3, 4 and 5 standard deviations. Plots on the right show how many models are used in calculating the mean, 1 being all the models, and 0 none of the models.

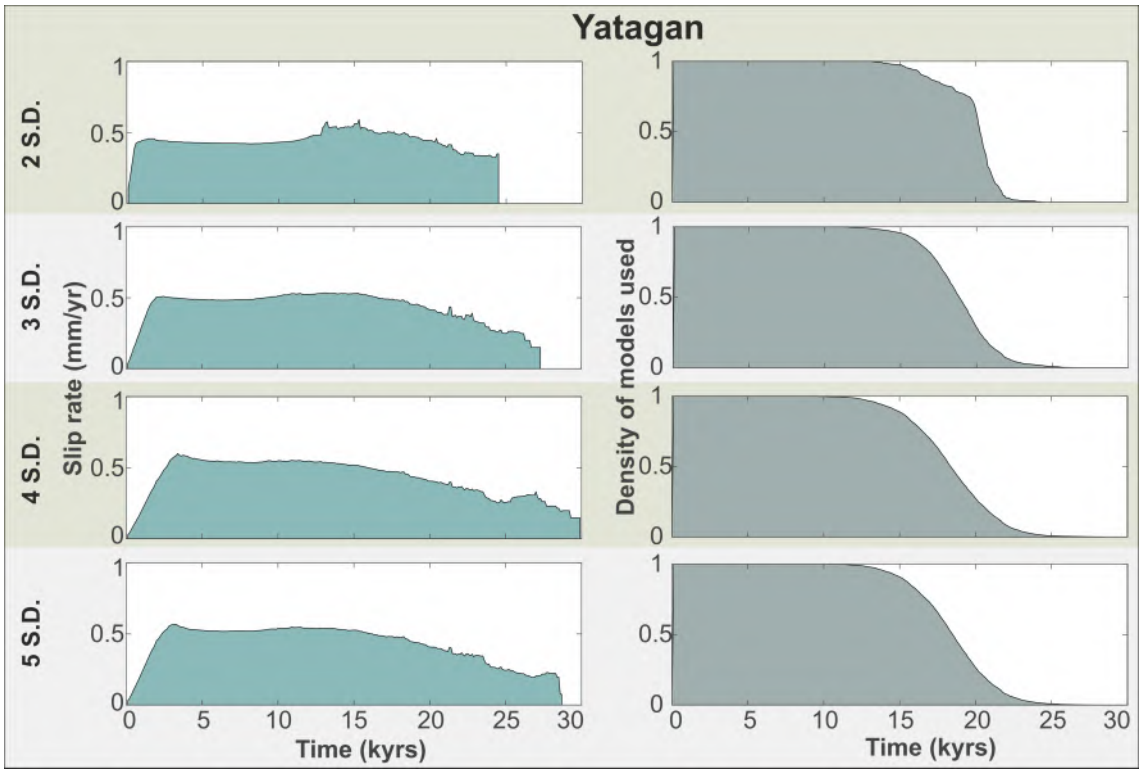

Figure 5.24: Results from the uniformly distributed scarp age prior inversion of the Yatağan fault, omitting the highest sample. Plots on left show the mean slip rate calculated in 100 year windows, for models that fit within 2, 3, 4 and 5 standard deviations. Plots on the right show how many models are used in calculating the mean, 1 being all the models, and 0 none of the models.

5.3.4 Discussion of ^{36}Cl data and modelling

The exposure ages determined the ^{36}Cl dating of the footwall slopes in south western Turkey (13.0 kyr to 25.5 kyr) are similar to those measured in similar settings in Italy (8-31 ka, Laura Gregory, personal comms.) and Greece (19-37 ka, Mechernich, pers. comms.). There is a large range in ages on both individual faults and over different faults, likely because sample locations on footwall slopes may have experienced erosion, or contain inherited nuclides because it has a more complex exposure history than the fault plane. The modelling to calculate these ages, and the ages from Gregory and Mechernich, does not incorporate erosion as the erosion rates are unknown and complex. This means that the real age of the transition in erosion rates is possibly different to the calculated ages. The local LGM ended around 20 kyr B.P., and the climate in western Turkey became warmer and drier as a result (*Sarıkaya et al.*, 2008). This likely resulted in a transition to reduced erosion rates, allowing preservation of fault scarps, similar to the situation in the Italian Apennines (*Tucker et al.*, 2011). Whilst this apparent surface age does not represent the onset of slip, it does provide a loose constraint on the time period that slip is likely to have been preserved in the landscape. This constraint is independent of the fault scarp ^{36}Cl data and can therefore act as a prior on the scarp age in the inversion. Conversely if a uniform prior is used for scarp age, then agreement between fault scarp data modelling scarp ages and the footwall derived scarp ages presented in Table 5.3 provides greater confidence in both methods.

Using the mean of all six footwall samples taken from different sites does result in different slip rates than using a site average of the two samples from each site, however this only results in a relatively small discrepency, which is largest at Yatağan. Using just the data from Yatağan results in an average slip rate of 0.68 mm/yr, and using data from all sites equates to an average rate of 0.53 mm/yr (Table 5.3). Given the small number of samples at each site it is more robust to use the mean of all six samples. In future sampling campaigns, collecting more footwall samples at each sample site would increase the confidence in footwall ages, and may provide more accurate post LGM slip rates. The spread of ages between sites does suggest that the timing and/or nature of slope stability is not just a function of elevation as may be expected. Data from other footwall slopes in the region would assist in determining if there is a systematic variation.

Whilst I ran inversions both using a scarp age prior based on the apparent footwall ages and with a uniform prior to explore it's effect, the ages I determined by dating the footwall slope are similar to footwall slope ages in central Italy and Greece (Gregory and Mechernich, personal comms.), which provides confidence in my results. The inversions with a uniformly distributed scarp age prior produce modal and mean scarp age values that lie within the 17.3±4.6 kyr (the mean footwall age, Figure 5.12), which provides

further confidence in the footwall slope ages I have determined. I will therefore use the results of my inversions that incorporate a normally distributed scarp age prior in further discussion, because they exploit all of the available information.

The Muğla fault ML solution is a variable slip rate (Figure 5.13), however, the inversion suggests that there are many other more simple models that fit the data almost as well (Figures 5.14 and C14). The modal and mean slip rate are ≈0.6 mm/yr during the Holocene. Whilst a variable slip rate cannot be discounted, the additional complexity is not required to model the data.

Inversion of the ^{36}Cl data from the Yilanli fault scarp results in an mean, mode and most likely average slip rate over the period of the model of 0.27, 0.35 and 0.18 mm/yr, with a standard deviation of 0.04 mm/yr (Table 5.11). However the inversion indicates that a variable slip rate is more likely, with stronger evidence for variation in slip rate in the normal scarp age prior case, though the same is only true for the best fitting models (2sd) in the uniform scarp age prior case (Figures C14 and C13). The fault slip rate during the fast and slow periods is more difficult to estimate. The method I use to calculate the average slip rate through time calculates the mean slip rate for models in 100 year intervals. Using only the best fitting models (models that fit within 2sd), the peak mean slip rate is 0.7 mm/yr, between ≈3-5 kyr dropping to around 0.2 mm/yr before 5 kyr (Figure 5.18). Inclusion of more poorly fitting models results in a decreasingly varied constant average slip rate, i.e. reduced peak value and increased background value. 3 and 4 sd show peaks of up to 0.50 mm/yr, with background rates closer to 0.25 mm/yr (Figure 5.18). Whilst the magnitude of this change in slip rate is poorly constrained, the period of fast slip is reasonably well constrained in models that fit within 2-4 sd to between 3 and 5 kyr. Interestingly this fits with period of fast slip in the most likely solutions at all sample sites, which hints at synchronisation between the faults (Figure 5.13).

At the Yatağan fault site the highest sample cannot be modelled well because it has a higher ^{36}Cl concentration relative to other samples at the site. The inversion has best modelled this with a long period of no activity between 8-25 kyr, which is plausible (Figure 5.21). The highest sample was more eroded than the other samples at the site, but an eroded sample would be expected to have a lower ^{36}Cl concentration because it has been exposed more recently. Another explanation could be pre-exposure, i.e. the long term accumulation of ^{36}Cl before the Holocene, however this sample would have been at around 4 m below the pre-Holocene ground level, so significant accumulation is not expected. Interaction with meteoric water may have enriched the sample in ^{36}Cl (*Dunai*, 2010), which is the most plausible explanation. It could be that the slope has not been stable since the demise of the LGM, and therefore the sample site has undergone a more complex exhumation and re-burial history, however the site geomorphology does not indicate this is the case because the footwall and hangingwall slopes are relatively planar and the scarp-slope contacts are horizontal and

perpendicular. Finally, it could have been a measurement error, with the samples being contaminated at some point in the processing or measurement. There is no reason to think this is the case, as there were no problems with the blanks processed and measured alongside. The accuracy of the this single data point is critical to the interpretation of slip rate on this fault, and it highlights a common problem in ^{36}Cl dating of fault scarps. Degradation of scarp increases with height, meaning there are commonly fewer appropriate sampling locations up the scarp, leading to a biased sampling strategy, with a greater density of samples in the lower portion of the scarp. Some studies take continuous ladders to combat this bias (*Benedetti et al.*, 2003, *Schlagenhauf et al.*, 2011), however another source of error with unknown magnitude is introduced by these samples with unknown erosion histories. In the case of the site on Yatağan, taking another sample close to the top sample would significantly improve confidence in a more variable slip history, as it stands I argue the data better support a constant slip rate.

When the highest sample on the fault scarp is omitted, the inversion for Yatagan prefers a constant slip rate (Figure C14), but similar to Muğla, the ML slip history has more changes in slip rate, with a faster period occuring between 3-5 kyr (Figure 5.13). The Holocene-averaged fault slip rate at the Yatağan site is 0.5 mm/yr, with agreement between the mean and modal solutions. The agreement with slip rates based on footwall ages, which have a mean rate of 0.53 mm/yr, further supports my choice to omit the highest data. The elapsed time (time since last event) has a mean of 1738 years, a modal value of 54 years, a highest likelihood of 968 years and a standard deviation of 1195 yrs. Archeo-seismological evidence indicates an elapsed time of $\approx$ 1600-1700 years (*Karabacak*, 2016) at the ancient settlement of Lagina which is 20 km northwest along strike. This similarity provides further confidence in the inversion results. The modal value being particularly low may be due to the discretisation of slip (in this case 0.5m), and the most recent event which occurred was between these 0.5 m increments. This demonstrates that it is important to use a number of metrics when analysing the posterior probability distributions.

The elapsed time distributions overlap between sites, and the choice of a uniformly or normally distributed scarp age prior has little effect on the elapsed time of any site posterior distribution (Figure 5.12, Table 5.13). The mean and modal elapsed time suggest that Yilanli likely has the longest elapsed time, followed by Muğla, and then Yatağan (Table 5.13).

The slip rate estimates based on ^{36}Cl data suggest that the Muğla and Yatağan faults are slipping at the fastest rate, and the Yilanli fault is slipping at a rate around 50 % less than either. The active fault network is more complex than currently mapped, and the two major basins (Muğla to the southeast and Yatağan to the northwest) have a zone of more complex topography between them that is $\approx$ 8 km wide, over which there is a drop in elevation of $\approx$200 m going from the Muğla to the Yatağan basin. This

	Muğla Elapsed time Normal (yrs)	**Yilanli** Elapsed time Normal (yrs)	**Yatağan** Elapsed time Normal (yrs)
Mean	2153	2517	1738
Mode	1577	2040	54
ML	3530	2794	968
St. dev.	1437	1667	1195

Table 5.13: Statistics of the elapsed time posterior distributions for the normal scarp age prior inversion case.

suggests there are active faults within this zone of complex topography. The similar slip rates between the Yatağan and Muğla faults indicate that they have similar Holocene slip histories (Figure 5.25).

Whilst the two faults are almost along strike from each other at the surface, assuming they have typical normal fault dips of ≈60°, they will become increasingly distant from each other at depth. In a structural sense they are two separate structures. The Yilanli fault may or may not link with the Muğla fault at depth. Normal faults are commonly thought to migrate basinward over geological time-scales (*Gawthorpe and Leeder*, 2008) and become increasingly localised (*Ackermann et al.*, 2001, *Gawthorpe et al.*, 2003, *Cowie et al.*, 2008). The Yilanli fault was a basin bounding fault of the Miocene-Pliocene age Yatağan basin (*Yilmaz et al.*, 2000), the Muğla and Yatağan faults have been active only since the Pliocene-Quaternary (*Gürer et al.*, 2013). This indicates that primary fault accomodating extension has moved basinward, with slip presently primarily accommodated on the Muğla and Yatağan faults, similar to observations in other similar extensional settings (*Goldsworthy and Jackson*, 2001, *Gawthorpe and Leeder*, 2008). The change in strike fits with the counter-clockwise rotation that has been occurring (*Howell et al.*, 2017), particularly if the Yilanli fault extends further northwest than was previously mapped (Figure 5.26). The Muğla and Yatağan faults likely accommodate more extension because they are oriented more optimally to accommodate strain in the current stress field 5.1 and 5.2. Both changing relative stress fields and heterogeneity have been shown to affect fault orientation (*Morley*, 2017), so either could cause the Yilanli and Muğla faults to have different strikes. More simply the faults may be orientated as they are because the deformation imposed by the overall strain-rate field cannot be accommodated on the Muğla and Yatağan faults.

Whilst the Muğla and Yatağan faults slip at a constant rate during the last 10 kyr, the Yilanli has a variable slip rate (Figure 5.25). *Cowie et al.* (2012) find that faults with higher mean slip rates have a more constant slip rate, and that younger faults typically have a more variable slip rate. My results suggest that as fault networks mature and the primary active faults migrate basinward, older faults will again increase in slip rate variability. This model is in alignment with the conclusion of *Cowie et al.* (2012) that

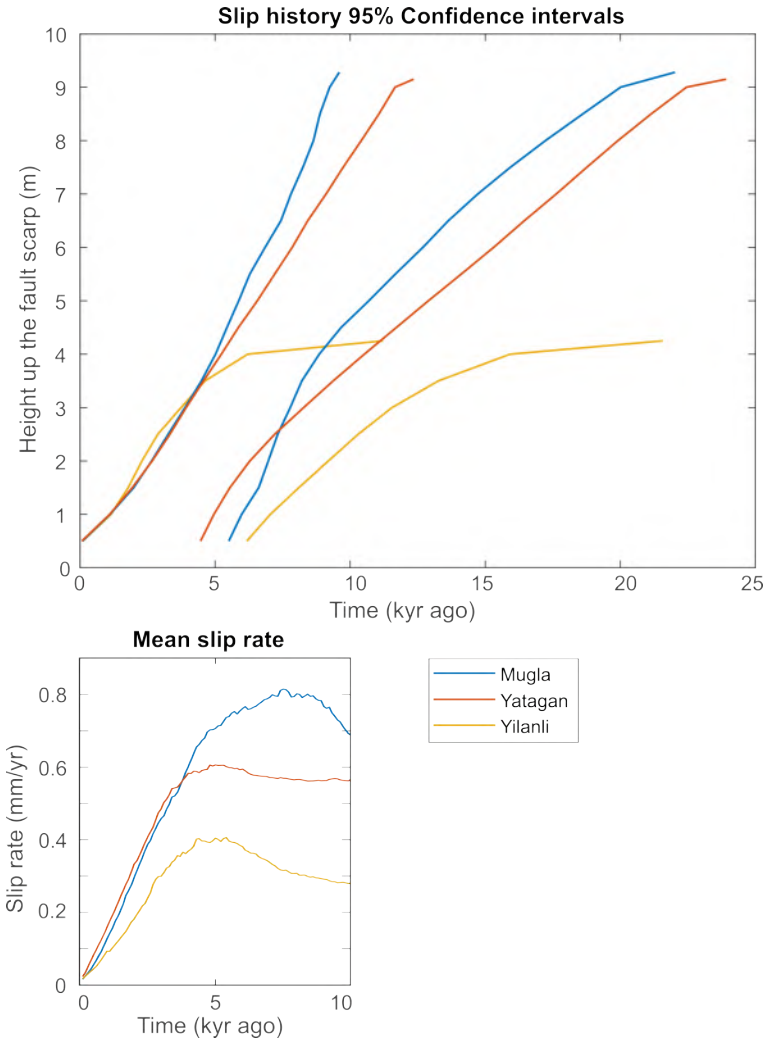

Figure 5.25: The top panel is a plot of the 95% confidence intervals of the slip histories resulting from the MCMC inversions of the ^{36}Cl fault scarp data using a normally distributed scarp age prior (Figure 5.13). The bottom panel is the mean slip rate through time, cut off at 10 kyr because this is when the number of models in the slip rate calculation drops below 100% (Figures 5.16, 5.23 and 5.18).

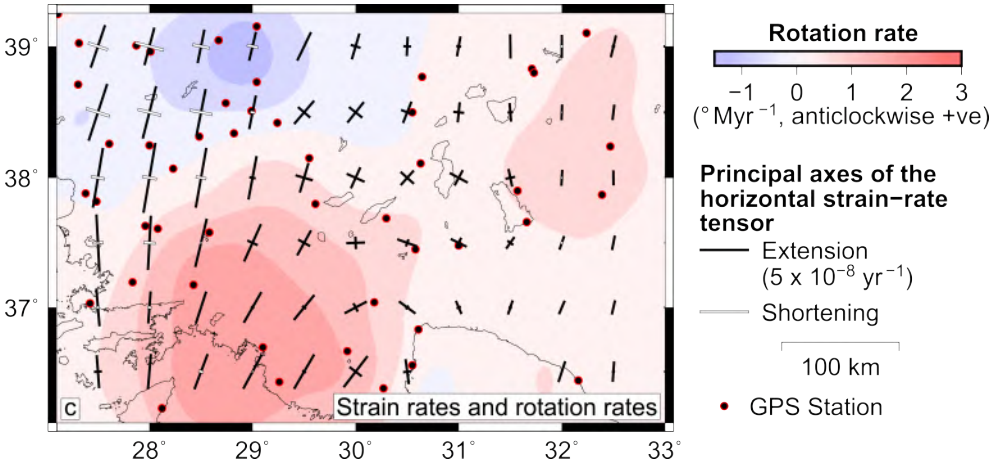

Figure 5.26: Strain and rotation rates for southwest Turkey from *Howell et al.* (2017), derived from GPS data of *Aktug et al.* (2009) and *Tiryakioğlu et al.* (2013).

slower faults have higher slip rate variability. This shows that ^{36}Cl analysis of fault scarps is a valuable tool, because it can provide a measure of slip rate variability over millennial time-scales, which informs our understanding of the evolutionary stage of an individual fault within a network.

5.4 Conclusion

I have determined Holocene slip rates for the three major fault in the Muğla, Yatağan and Yilanli faults, which make up the three major active faults in the Muğla-Yatağan basin. They are slipping at 0.6, 0.5 and 0.3 respectively, and only they Yilanli fault shows evidence of variable slip rate. My results also indicate that the faults have been preserved since the demise of the LGM, similar to the limestone fault scarps found in the central Italian Apennines. The Yilanli fault was previously not known to be active during the Holocene, and in the next chapter I will determine what hazard these three faults pose to local populations. I will also compare my findings to strain rates from geodetic data, and undertake local fault mapping to determine how these three faults fit into the wider fault network.

Chapter 6

Muğla-Yatağan basin seismic hazard

"Those who have knowledge don't predict. Those who predict, don't have knowledge. "

Lao Tzu

6.1 Summary

This chapter has two objectives. Firstly, to better understand the seismic hazard in the Muğla-Yatağan basin and surrounding faults. To achieve this I have two primary objectives. The first objective is to determine if the strain rate in the Muğla-Yatağan basin derived from geodetic measurements is equal to the Holocene strain rate derived from ^{36}Cl scarp and footwall data presented in the previous chapter. I find they are equal, which suggests that Holocene fault slip rates can be determined using geodesy and knowledge of the fault locations, both in western Turkey and globally. A greater number of Holocene slip rates derived from non-geodetic methods will be required to test this theory.

The second objective of this chapter is to determine the hazard the major faults of the Muğla-Yatağan basin pose to local populations. To achieve this I first present an updated active fault map of the region I created using a mixture of remote sensing and field work, before using this as the foundation for a deterministic seismic hazard model. I find that each fault is capable of producing PGA of 0.7g in populated areas, and that my estimated PGA is likely lower than the true value.

6.2 Background

Inter-seismic strain rate, measured using geodetic data, has been shown to both be equal to and vary from the Holocene/Quaternary slip rates on faults (*Cowgill et al.*, 2009,

Dolan and Meade, 2017, *Lifton et al.*, 2020). A discrepancy between the Holocene slip rates and the geodetic rate has implications for the mechanics and the spatio-temporal distribution of strain in the lithosphere (*Dolan and Meade*, 2017). Quantifying the long term strain budget, represented by interseismic deformation captured using geodetic data, and determining how much the faults I have determined Holocene slip rates for contribute towards this, provides insight into the relative importance of structures in the region for accommodating deformation.

The configuration of the Muğla and Yatağan faults as they are currently mapped creates a space problem between the two, because they dip in the opposite directions yet are almost along strike. Identifying how this space problem is accommodated requires mapping of the other active tectonic structures between and surrounding the faults. As well as providing insight into the mechanics of the faulting, this will identify the seismic hazard in the area. I present two outputs; first a map of all surface expressions of active structures, second, a map defining plausible seismic sources for seismic hazard characterisation based on the geomorphological mapping and existing geological maps (*Akbaş et al.*, 2017). I then present the spatial distribution of the resulting peak ground acceleration (PGA) if each fault were to host an earthquake at the maximum possible magnitude.

6.3 Method

6.3.1 Geodetic strain rate

The geodetic strain rate across the Muğla-Yatağan basin is determined using GNSS measurements from *Aktug et al.* (2009) and *Tiryakioğlu et al.* (2013), Figure 6.1. All GNSS data are in the Anatolia-fixed reference frame of *Tiryakioğlu et al.* (2013), as in *Howell et al.* (2017), and the data were provided in this format when I contacted Howell (personal comms, 2020). I then used trigonometry to calculate the magnitude of the velocity for all GNSS sites in a fault perpendicular and fault parallel directions, using an approximate dip direction of 030° and 210° for the Yatağan and Muğla faults, and did the same for the GNSS errors. Whilst the Yilanli fault has a dip direction closer to 240°, it is moving at a slower rate than Yatağan or Muğla, so I assume the basin is generally extending perpendicular to the Yatağan and Muğla faults. I then applied a spatial filter to the GNSS data, creating a rectangle 100 km by 400 km centred on the centre of my study area (Lat: 37.2322° N, Lon: 028.2722° E), with the long axis perpendicular to the fault strike (Figure 6.1). The width of the filter (50 km either side of the profile) is chosen to optimize the trade-off between the number of available GNSS sites and the noise in the profile.

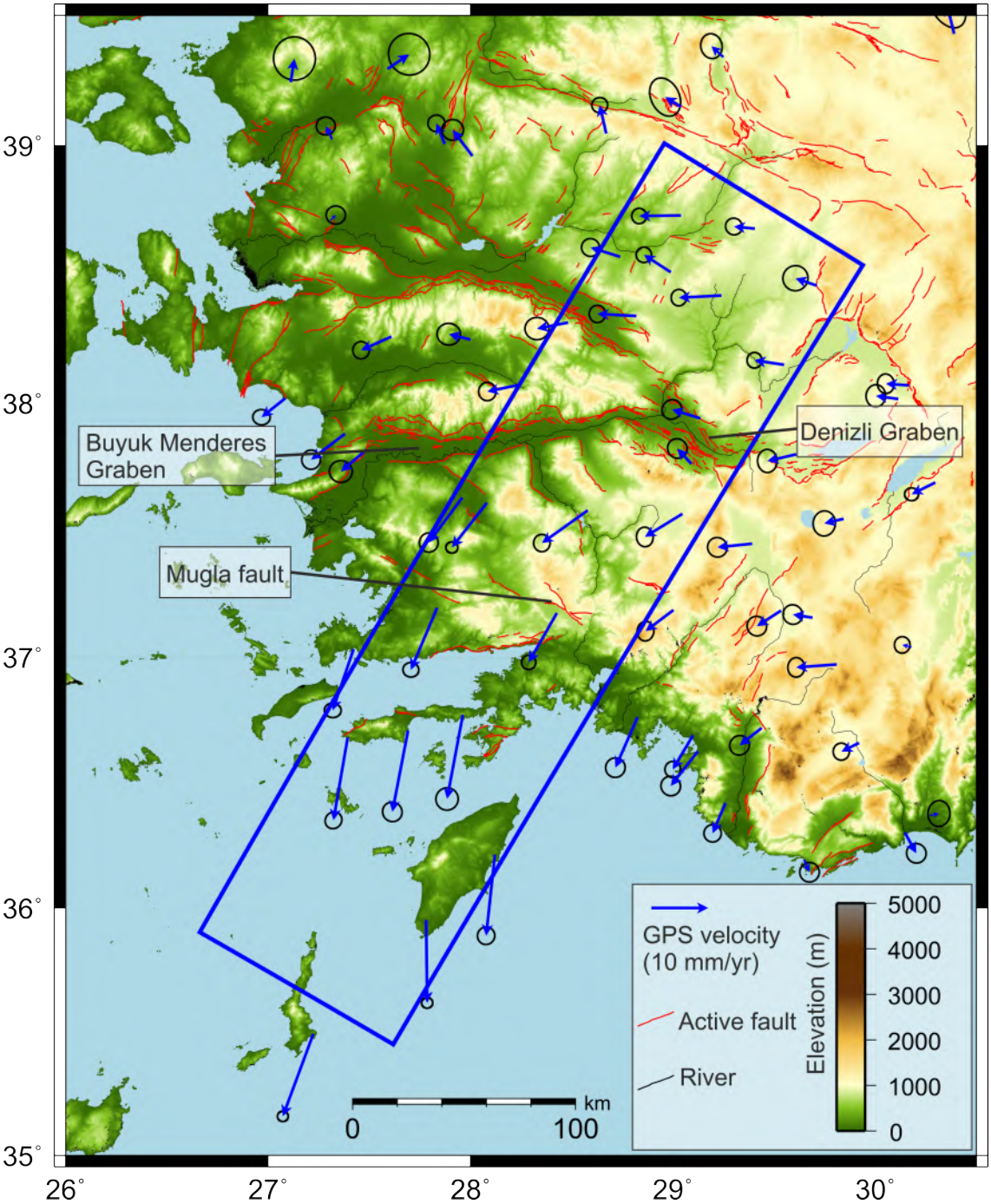

Figure 6.1: GPS velocities from *Aktug et al.* (2009) and *Tiryakioğlu et al.* (2013) in the Anatolia fixed reference frame of *Tiryakioğlu et al.* (2013). The data from *Aktug et al.* (2009) were rotated into the reference frame by *Howell et al.* (2017). The blue box indicates the area in which GPS velocities were used to construct a fault perpendicular profile across the Muğla and Yatağan faults. Active faults are from *MTA* (2016).

6.3.2 Geomorphological mapping and seismic hazard

The most efficient way to map active faults over large areas is using satellite and aerial data and existing geological maps (*Akbaş et al.*, 2017), then ground truth this data in the field where possible. I use satellite imagery as well as high resolution digital elevation models (DEMs) from TanDEMx (*Wessel et al.*, 2018) and SRTM (*Jarvis et al.*, 2008), and derivatives of these DEMs such as slope maps and topographic profiles. I also use existing active fault maps, geological maps and field observations to assist in identifying active structures. I have identified active faults using a number of geomorphic criteria from *Taylor and Yin* (2009): Linearity of topographic features such as fault scarps, triangular facets, change in slope and variations in drainage. I classify faults with a clear geomorphic signal as confident, and faults with ambiguous geomorphic signal as possible.

When producing a seismic hazard map, seismic sources should not follow the surface expression of the fault, but the character of the fault at depth (*Litchfield et al.*, 2013). As such I join some along-strike segments and simplified the geometry of the mapped surface expression of the faults to produce a reasonable representation of the fault at depth. I assume a fault dip of 60° as the surface dip may not represent the structure at depth, and active normal faults typically have an average dip of 30-60° (*Jackson and McKenzie*, 1983). I use an elastic layer with a thickness of 15 km (*Ergin et al.*, 2009, *Tan*, 2013) and assume pure normal slip. I use the length/magnitude relationship from *Wells and Coppersmith* (1994) to determine that each fault can host earthquakes up to a magnitude of M_w 6.7 (all faults are a similar length). To undertake seismic hazard modelling, I use the global earthquake models (GEM) openquake engine (*Pagani et al.*, 2014), which uses ground motion prediction equations (GMPE) to calculate ground motion fields, e.g. PGA as a function of distance from the source. I use the GMPE of *Abrahamson et al.* (2014), because it can be applied to earthquakes between magnitude 3-8.5 and distances of 0-300 km. A required input for the GMPE is the site conditions, as different material produces different accelerations. This effect is captured in the shear wave velocity in the top 30 m, known as the Vs30. I use a value of 700 m/s as this is similar to the Vs30 at the Yatağan seismic station (*AFAD*, 2017; 696 m/s). I did not use the Vs30 value of 466 m/s from the seismic station in Muğla (*AFAD*, 2017) because I want the PGA to provide a minimum PGA value, and lower Vs30 produce a higher PGA all else being equal (*Abrahamson et al.*, 2014). The large difference in Vs30 is likely because the Yatağan site is on bedrock, and the Muğla site is located on quaternary sediments (*AFAD*, 2017). I assume that the ground motion fields are spatially correlated (*Jayaram and Baker*, 2009), and present the mean of 1000 samples of the ground motion field. This is done to account for uncertainties associated with the GMPE. I run 3 scenarios, one for each of the faults rupturing in it's entirety (Table 6.1).

Scenario	Magnitude (Mw)	Dip (°)	Top depth (km)	Bottom depth (km)
Muğla	6.7	60	0	15
Yatağan	6.7	60	0	15
Yilanli	6.7	60	0	15

Table 6.1: Parameters for the PGA modelling, with each event having pure normal slip.

6.4 Results

6.4.1 Geodetic strain rate

Twenty-two GNSS fault perpendicular velocities are within the area of interest and are plotted along with the position of the Yatağan and Muğla faults, the Ören fault and the Denizli Graben (Figure 6.2). The Ören fault and Denizli Graben cover a large area of the plot compared to the Muğla basin faults because they are not perpendicular to the profile. The velocities show a correlation with distance along the profile, and there is more scatter around the Denizli Graben. The gradient of the profile is equal to the strain rate, and I fit the profile with straight line using the best linear unbiased estimator (BLUE) which produces a strain rate of $5\text{x}10^{-8}$ year^{-1}. This is equal to a change in velocity of 15 mm/yr over 300 km.

6.4.2 Geomorphological mapping and seismic hazard

Figure 6.4 is an updated fault map for the Muğla-Yatağan basin and surrounding area based on geomorphological mapping, and I have characterised these faults as 3 seismic sources. There are more faults than previously identified, and faults are longer than previously mapped, particularly the Yilanli fault (Figure 5.5). The resultant spatial distribution of PGA for each seismic hazard scenario, i.e. the case of each fault rupturing individually, is plotted in Figure 6.6. The maximum PGA in all cases is between 0.6-0.7g and the spatial distribution is similar at all sites primarily because the Vs30 used is uniform. Muğla will produce 0.6-0.7 g in the town of Muğla, as does the Yilanli fault. Yatağan only produces 0.2-0.3 g at Muğla, but does result in 0.6-0.7 g in the town of Yatağan, the local power plant, and at the ancient site of Lagina.

6.5 Discussion

Comparison of geodetic strain rate

The strain rates I obtained are of the same magnitude ($5\text{x}10^{-8}$ year^{-1}) as those calculated by *Howell et al.* (2017), however *Howell et al.* (2017) calculated average strain rates for a regular grid, rather than a profile. One assumption I have made is that the Muğla-Yatağan basin has formed perpendicular to the maximum strain direction,

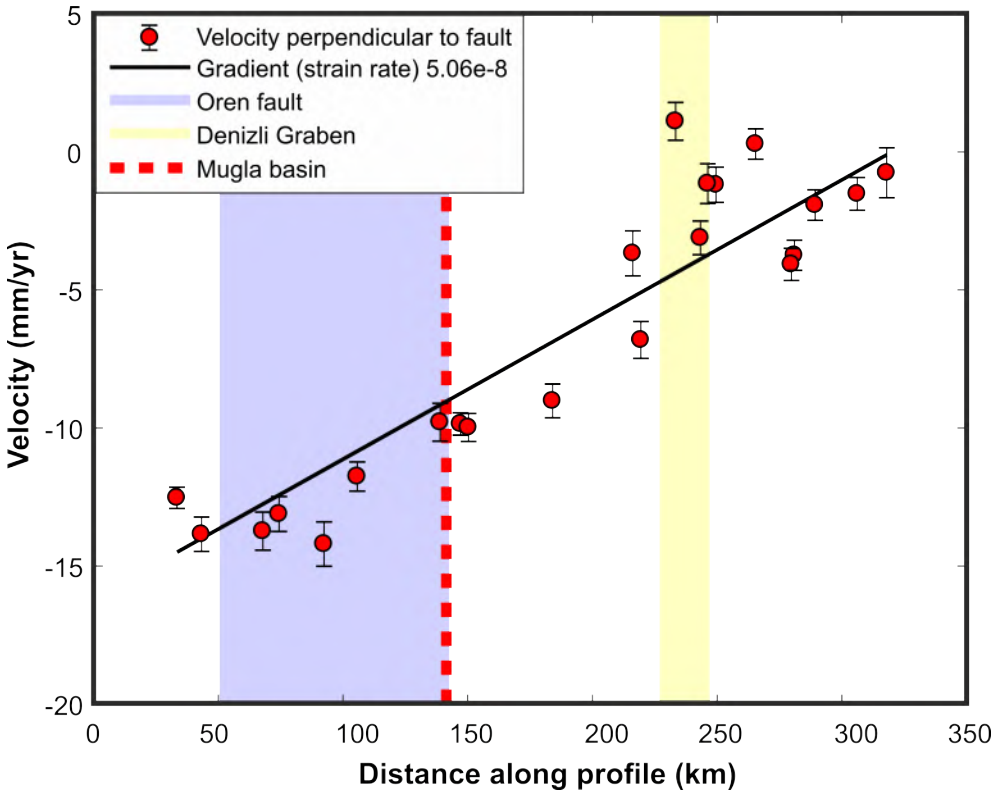

Figure 6.2: Profile of GPS velocity component in the direction 030° along the profile shown in Figure 6.1. The black line is the best linear fit and is found using the best linear unbiased estimator (BLUE). Locations of the Muğla, Yatağan and Yilanli faults are shown by red dashed line. The locations of the Ören and Denizili graben are wider as they are not parallel to the Muğla basin, and therefore not perpendicular to the profile. The GPS data are from *Aktug et al.* (2009) and *Tiryakioğlu et al.* (2013).

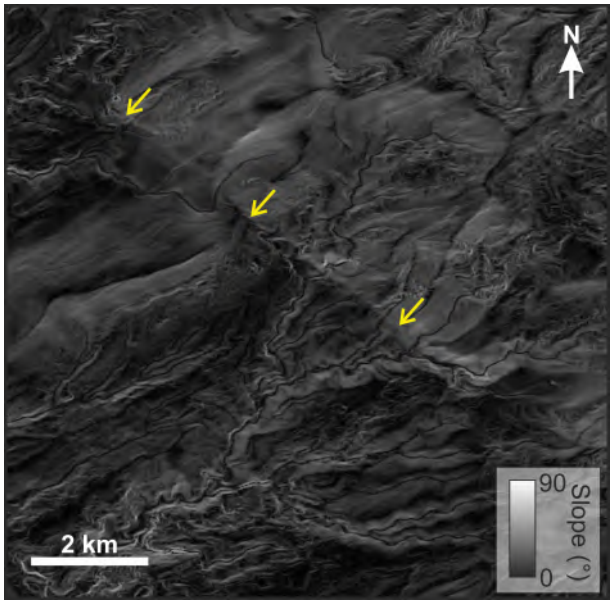

Figure 6.3: An example of a previosuly unmapped portion of fault, 90 degrees indicates a vertical slope, 0 a horizontal surface. Image centred on lat:37.3817°, lon: 28.2912°, location shown by black box in Figure 6.4. A change in slope is not associated with a change in lithology, suggesting an active fault. This location is along strike from the mapped Yilanli fault, and the slope map was derived from TanDEMx data (*Wessel et al.*, 2018).

meaning that the maximum strain direction is oriented ≈030°-≈210°. Howell et al. calculated the principal extensional axis of the horizontal strain rate tensor in the region of the Muğla and Yatağan faults to be ≈015°-≈195°. They also calculated rotation rates for the region, and the Muğla and Yatağan basins are rotating at rates of 2.0-2.5° Myr $^{-1}$. This rate of rotation decreases to the north-west (Figure 6.7).

Comparing the geodetic and Holocene extension rates across the Muğla will improve the understanding of how strain is being partitioned in the surrounding lithosphere. To compare geodetic deformation rates to Quaternary slip rates determined on faults I have to make a number of assumptions. The primary assumption is that away from recent earthquakes, geodetic deformation rates represent the long term deformation rate (*Cowgill et al.*, 2009). If I assume that deformation occurs on a narrow ductile fault zone at below the frictional-viscous transition zone, I can determine the land surface area that will be affected by deformation of a single shear zone by using a simple elastic dislocation model (*Okada*, 1985). In this model I assume that the fault is infinitely long and infinitely deep, with a rake of -90° (pure normal). I vary the top depth of the dislocation, to represent the bottom of the seismogenic zone, and I vary the dip of the dislocation between 40 to 80 degrees. I assume a constant horizontal displacement (heave) of 1 m, and vary the slip on the fault using the equation 6.1 to account for the geometry.

$$Heave = slip \times cos(dip) \tag{6.1}$$

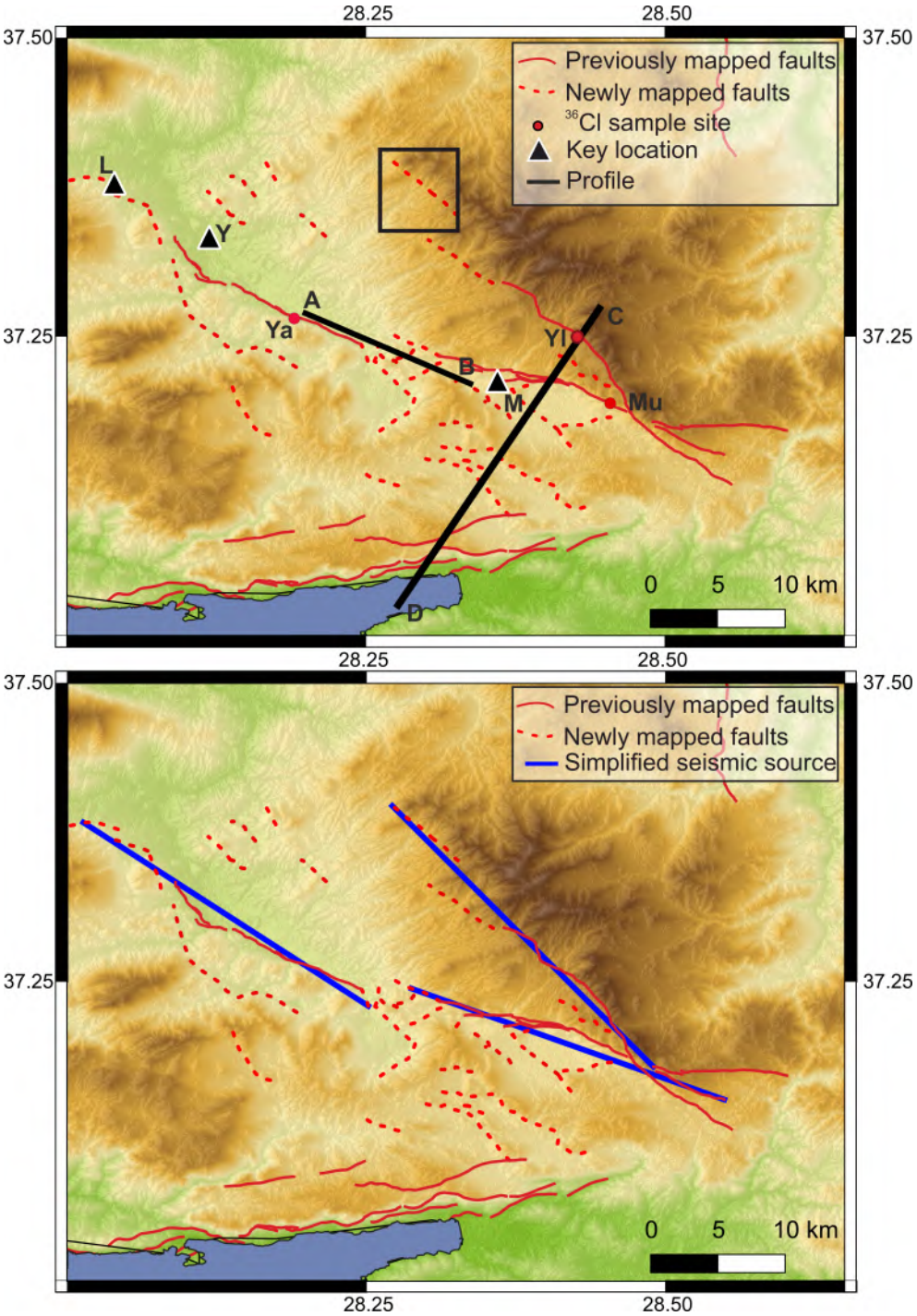

Figure 6.4: Top panel, an updated active fault map for the Muğla basin region, showing key locations in black trangles. L = Lagina an ancient settlement, Y = the town of Yatağan, M = the town of Muğla. Black box shows location of Figure 6.3. Profile A-B is the location of the profile in Figure 6.5, profile C-D shows the location of the profile in Figure 6.9 . The lower panel shows the simplified fault network used to model potential seismic sources in the seismic hazard modelling, compared to the mapped surface traces of the three faults.

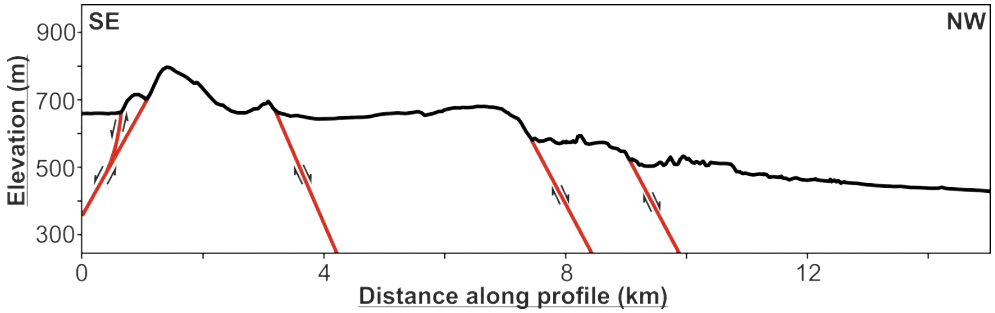

Figure 6.5: An interpreted topographic profile across the area of complex faulting between the Muğla and Yatağan faults. The Profile is approximately parallel to the Yatağan fault and the location of profile is shown by line A-B in Figure 6.4

.

Plots of the horizontal displacement in a profile perpendicular to the fault of a suite of these models show that the magnitude of horizontal displacement is controlled by the dip of the fault, and the distribution of displacement is controlled by the depth to the top of the dislocation, or the seismogenic thickness (Figure 6.8). They also show that the majority of deformation occurs within 50 km of the fault, independent of the fault dip and depth in the ranges modelled.

To compare geodetic rates to fault slip rates I convert slip rates to horizontal extension in the direction of the principle extension. This requires accounting for the dip of the fault, and the dip of the fault at the sample sites varies from this value, (43°, 74° and 57° for Muğla, Yatağan and Yilanli, Table 5.1). *Gürer et al.* (2013) report dips of 70-85° on the Yatağan fault, and 75-85° on the Muğla fault, indicating that fault dip varies significantly along strike. Seismology also suggests that fault dips at depth vary between faults (*Howell et al.*, 2017). For these reasons I do not use the dip measured at the site as it is likely to be unrepresentative of the larger scale structure, but use a value of 60° at all sites, which falls within the typical range of a normal fault.

The Yilanli fault strikes approximately 150°, which is a deviation of 30° from the assumed principal extension direction, so I also account for this. Using Holocene time-averaged slip rates of 0.6, 0.5 and 0.25 mm/yr for Muğla, Yatağan and Yilanli respectively, corresponds to extension rates of 0.30, 0.25 and 0.11 mm/yr. Compared with the extension rates across the region (Figure 6.2), it is clear that the Muğla basin is accomodating only a small fraction of the total strain. There are two large steps in the velocity profile, each on the order of 5 mm/yr, and the most well defined is in the region of the Ören fault (Figures 6.1 and 6.2), where there is a step of ≈4 mm/yr. The second is in the region of the Denizli Graben (Figures 6.1 and 6.2), but there is greater scatter in the data at this point. This scatter is likely due to the distribution of GNSS sites around a complex region of faulting. The Ören fault is within 20 km of the Muğla basin along the profle (Figure 6.2), so the effect of both the Ören fault and the Muğla-Yatağan basin faults are likely combining to produce the step observed in GPS,

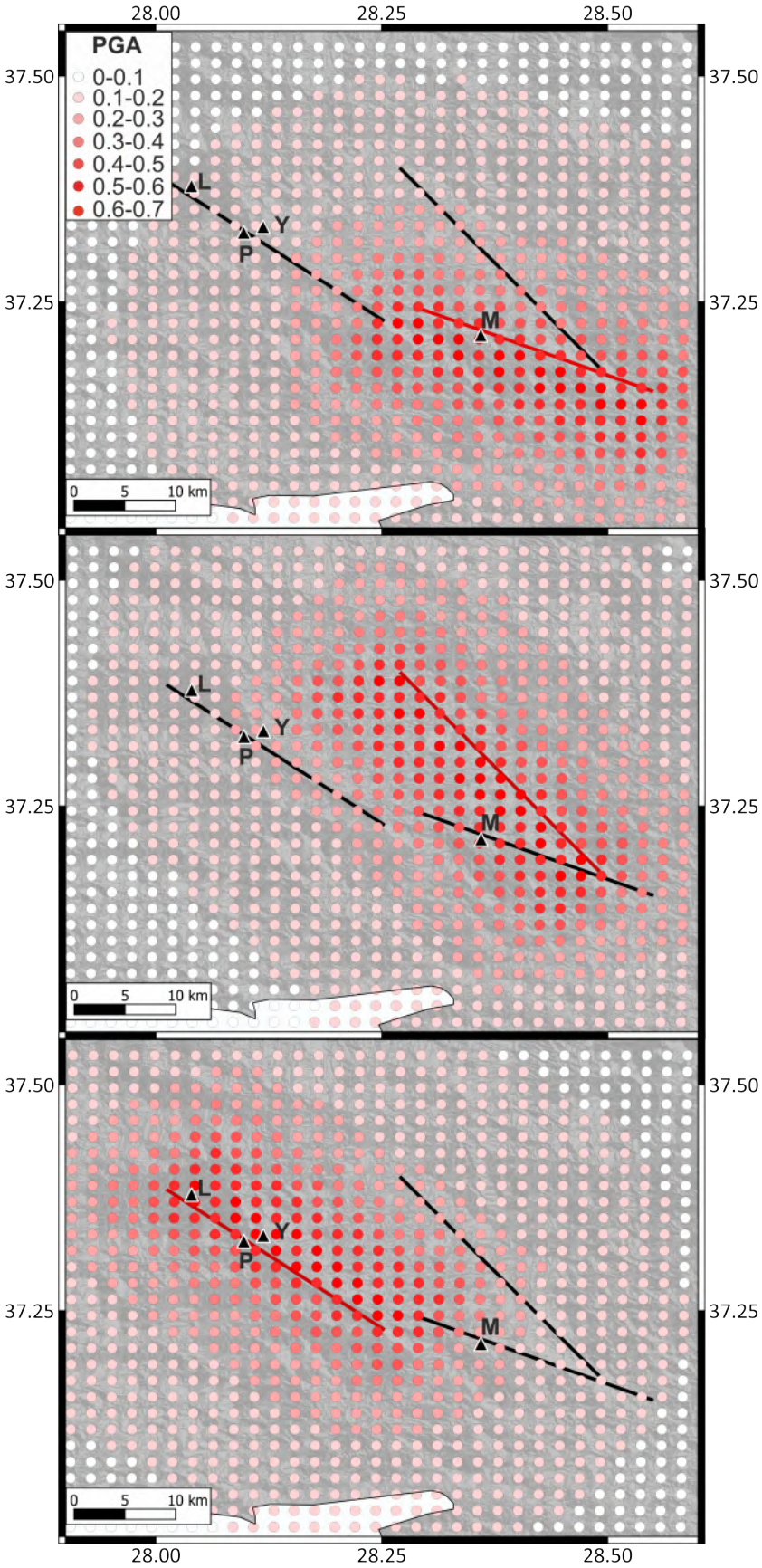

Figure 6.6: Mean of the modelled PGA, for the Muğla, Yilanli and Yatağan earthquake source events, with each fault rupturing in a M_w6.7 earthquake from the surface to a depth of 15 km and a fault dip of 60°. Black triangles show the location of: M the town of Muğla, Y the town of Yatağan, L the ancient site of Lagina, and P. the Yatağan power plant.

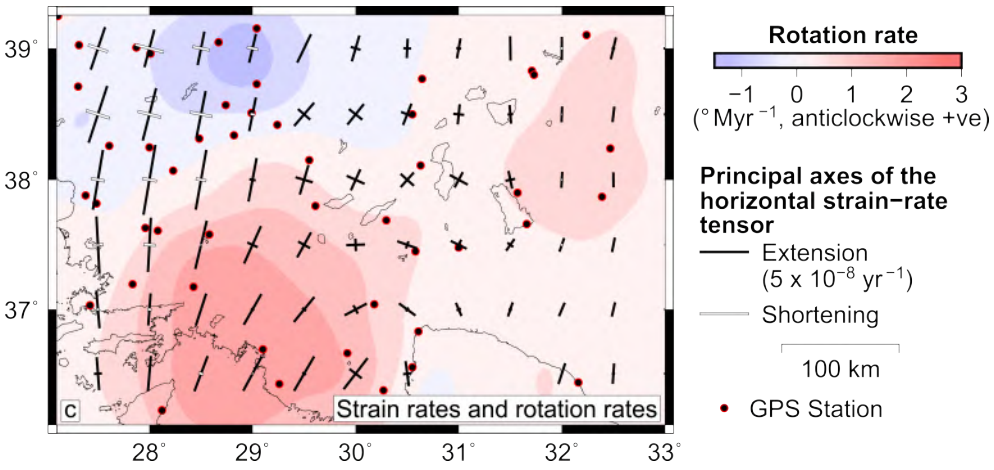

Figure 6.7: Strain and rotation rates for southwest Turkey from *Howell et al.* (2017), derived from GPS data of *Aktug et al.* (2009) and *Tiryakioğlu et al.* (2013).

based on the width over which the deformation is active over (Figure 6.8). The Ören fault network is significantly longer than the Muğla-Yatağan basin (Figure 6.2) and it has a more M≥5 events recorded (*Howell et al.*, 2017; and references therein), which suggest the Oren fault is currently more active and accommodates a greater amount of strain than the Muğla-Yatağan basin faults. Assuming a fault dip of 60°, a strain rate of $5x10^{-8}$ and a combined extension rate of 0.66 mm/yr across the Muğla, Yatağan and Yilanli faults, faults would be spaced at intervals of 13.2 km, if equally spaced and accommodating the same slip rate on fault. Mapping of the current active fault network surrounding the Muğla-Yatağan basin will provide greater insight into whether the strain is distributed as modelled in this simple calculation.

6.5.1 Geomorphological mapping and seismic hazard

The mapping of active faults using DEM data shows that the fault network is much more complex than previously mapped (*Emre et al.*, 2018). One of the key new faults is the northwest extension of the Yilanli and Yatağan faults. This increase in length increases the size of earthquake that could occur on the fault, and is important in terms of seismic hazard.

The location of previously unidentified fault surface traces may also be important when planning resilience in infrastructure. Fieldwork and further investigation of the DEM data may allow identification of even more fault surface traces, particularly creation of more profiles through areas of complex topography. This may be especially useful around the power plant close to Yatağan (Figure 6.6) and the associated infrastructure. This study shows that whilst the current active fault map (*Emre et al.*, 2018) has captured the major faults throughout Turkey, in areas away from recent earthquakes many of the more minor active faults are likely to have been missed, and that detailed studies using high resolution DEMs can be used to further improve the active

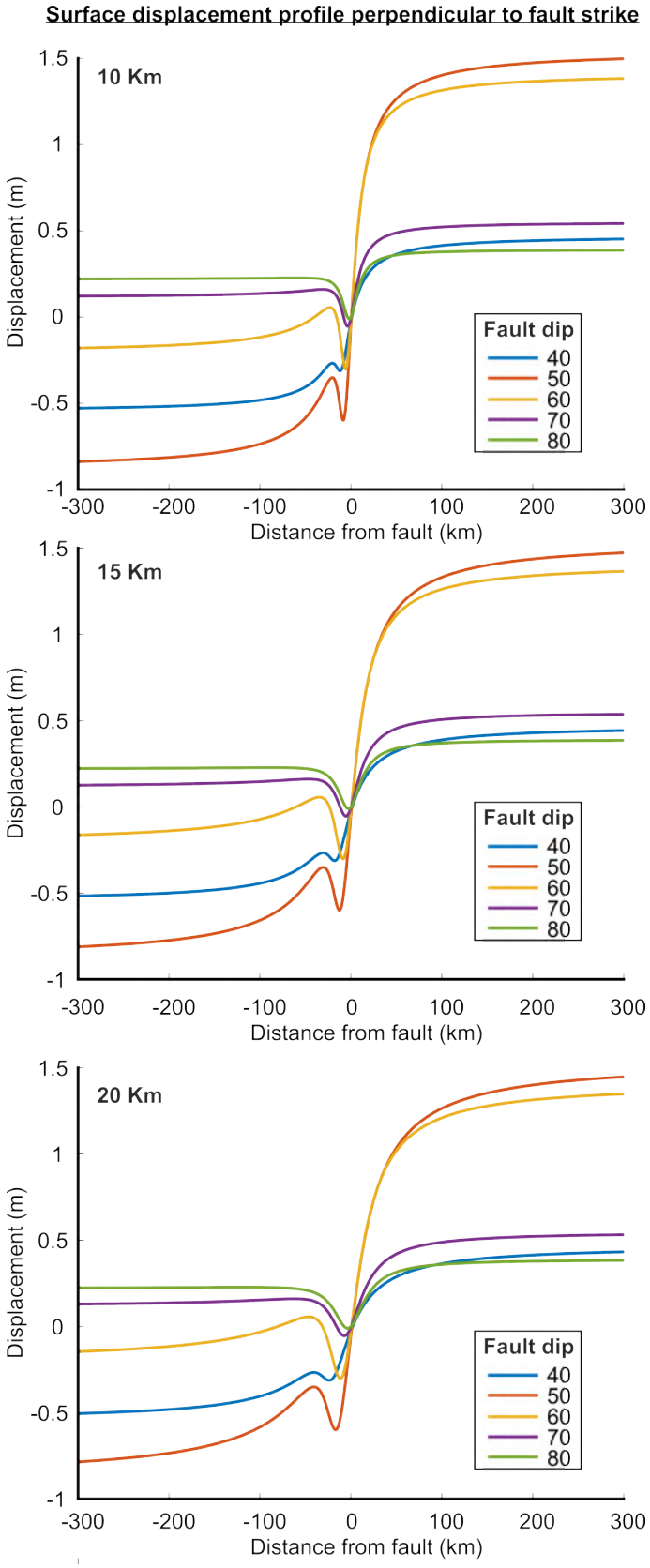

Figure 6.8: Results for a simple dislocation model in an elastic half space, based on the equations of *Okada* (1985). Top panel shows displacement profile perendicular to fault strike, for various fault dips, assuming a locking depth of 10 km. The middle and bottom plot show the same but for 15 km and 20 km locking depths respectively.

fault maps.

The results of the seismic hazard modelling show that each of the 3 major faults identified can produce significant PGA that are likely to cause damage to structures in the area. These PGAs provide minimum values, as I chose a low Vs30 value from the local data available. In the real world, the Vs30 varies spatially, particularly between the basins and the uplifted bedrock. In areas where the surface is composed of sediments, such as Muğla, the PGA is likely higher than modelled, and the hazard is currently under-estimated in the modelling presented here. Future work to improve the hazard model should incorporate spatial variation of Vs30 in areas of interest, such as the Yatağan power plant, and the Muğla and Yatağan population centres. This could be based on the topography using the global Vs30 model from *Allen and Wald* (2007), or use regional Vs30 data from *AFAD* (2017) and geological mapping to produce a Vs30 distribution based on outcropping lithology. One of the key assumptions I have made is that the whole fault ruptures at once, and that the faults do not rupture simultaneously. Either one of these scenarios will have an effect on the resultant PGA. I also assume that the faults dip at 60°, as there is no information on the fault dips at depth for any of the faults. Waveform inversion of events in the gulf of Gokova indicate dips are likely closer to 40-50° (*Yolsal-Çevikbilen et al.*, 2014) if the structural style is similar. Uncertainty in the dip could also be incorporated into future models.

Whilst there are many improvements that can be made on the seismic hazard assessment of the 3 main faults in this study, it demonstrates that all 3 faults are locally important seismic sources. Whilst there have been many seismic hazard studies undertaken in Turkey for almost 100 years (*Akkar et al.*, 2018), these commonly use a probabilistic approach. This means it is difficult to compare between the results of my deterministic approach taken in this study, and the existing work. However, a recent probabilistic seismic hazard assesment (PSHA) map for the whole of Turkey, indicates that the Muğla-Yatağan basin is located in an area of high seismic hazard (*Sesetyan et al.*, 2018), which my results also indicate.

To make the seismic hazard study more useful for emergency planning future work should include fragility, vulnerability and exposure data. This would allow modelling of the number of deaths and losses in the region and would allow the social and economic impact of different earthquake scenarios to be modelled. Whilst some of this data is available for Turkey (Vitor Silva, personal comms), it is currently at a regional scale, which is too broad to be useful using my current approach.

6.6 Implications of all results in this chapter for the Muğla-Yatağan basin

One important implication of my work in Chapter 5 is that the Yilanli fault is an active and capable fault that has slipped during the Holocene, contrary to the active

fault map of *Emre et al.* (2018). Fault mapping based on the geomorphology also suggests the Yatağan and Yilanli faults are longer than shown on the current active fault map (Figure 6.4). This means that the seismic hazard, if based on the maximum magnitude that these faults could produce, is underestimated. It is difficult to draw conclusions on whether faults in the basin are likely to rupture at the same time using the ^{36}Cl and other available data. ^{36}Cl fault scarp data on the Yatağan and Muğla faults indicate a constant slip rate, so the data can neither confirm nor reject that the faults are synchronized. Elapsed time distributions have a large amount of overlap (Figure 5.12), suggesting they may rupture in the same event, or within a short time frame similar to earthquake clusters observed in the Italian Apennines (*Walters et al.*, 2018). The Yilanli fault does have a variable slip rate, which suggests it does not rupture at the same time as the Muğla and Yatağan faults every time. It could be that some times it ruptures during the same event, and other times does not. *DuRoss et al.* (2011) present a method which essentially combines PDFs of earthquake event times from multiple paleoseismic trenches along a single fault segment to correlate rupture event times, however this method still requires qualitative analysis, notably a decision as to which events are correlated. A similar approach could be taken with elapsed time PDFs from ^{36}Cl data, and either other ^{36}Cl fault scarp sampling locations, or earthquake dates from new paleoseismic studies on the Muğla-Yatağan basin faults. It would be inappropriate to apply this method to the elapsed time from each fault, as this requires the assumption that they rupture simultaneously, for which there is no compelling evidence.

How the Muğla and Yatağan fault work in a mechanical sense is partially explained by my mapping. My mapping reveals a complex zone of faulting between the two fault tips, with faults primarily perpendicular to the strike of the Muğla and Yatağan faults. This is contrary to experimental data and observations of transfer zones between normal faults with opposing dip, which indicate that faults in these transfer zone settings should be closer in strike to the main basin bounding faults (*Bose and Mitra*, 2010, *Childs et al.*, 2019). There are a number of mapped inactive faults in the surrounding area with orientations similar those I have mapped between the Muğla and Yatağan fault (*Gürer et al.*, 2013, *Akbaş et al.*, 2017), which suggests that the faults within the transfer zone between the Muğla and Yatağan fault are re-activating old structures or existing fabrics (Figures 5.5 and 6.4). This indicates that pre-existing crustal heterogeneities have strong controls over the geometry of faults in this transfer zone, in line with observations in other basins and fault models (*Morley et al.*, 2004, *Bellahsen and Daniel*, 2005, *Bezerra et al.*, 2014). The orientation of faults in this transfer zone suggests that they have a large strike slip component, and field investigation of these transfer faults may provide a better control on their dip and the sense of movement.

The exact surface trace of the fault can be difficult to identify, however the steps in topography not associated with a change in lithology indicates multiple active faults

are present (Figures 6.4 and 6.5). These faults are relatively short and therefore do not need to be accounted for when defining sources for seismic hazard mapping, but their identification may be useful in safeguarding any vital infrastructure crossing them. The Yatağan and Muğla fault have previously been considered as a single fault (*Karabacak*, 2016), and this is not the case because the faults dip in opposite directions. However, these faults may form above the same zone of localised deformation within the ductily deforming lithosphere, and earthquakes ruptures are known to jump across gaps larger than that between the Muğla and Yatağan faults (*Biasi and Wesnousky*, 2016) and dynamically trigger earthquakes on nearby faults (*Fan and Shearer*, 2016, *Nissen et al.*, 2016). I have found no examples of opposing dipping faults along strike rupturing in the same event, however there is a case of opposing dipping normal faults rupturing within one month of each other (*Payne et al.*, 2004), though these were essentially aftershocks of the M_s7.3 Borah Peak earthquake.

How the faults of the Muğla-Yatağan basin are related at depth to the surrounding faults is an interesting question that remains open. I have produced a cross section of the Muğla basin (Figure 6.9), in which there are two major faults, the Muğla fault and the Ören fault, and these link to multiple faults in the surface. There are also some faults between the two which have smaller topographic expression (Figure 6.9). The GPS data suggest that there is around 4 mm/yr extension over the profile length, and given that the Muğla and Yilanli fault are taking up ≈0.7 mm/yr, the majority of the rest of this extension is likely occurring on the Ören faults, and other structures in the Gulf of Gokova. The large topographic step across the northern boundary faults of the Gulf of Gokova supports this hypothesis that the Gulf of Gokova is currently dominating extension in the region (Figure 6.9). The three major groups of faults are located at intervals of ≈10 km, which is in line with the prediction of fault spacing from the GPS derived strain rate, and slip rates from ^{36}Cl data. This suggests that the Muğla-Yatağan basin faults are extending at a rate compatible with spatially averaged regional GPS derived strain rates, but that the Gulf of Gokova is currently slipping at a higher rate than the regional strain rate. Globally, previous studies comparing geodetic rates to Quaternary rates have generally found agreement between the two methods (*Cowgill et al.*, 2009, *Mohadjer et al.*, 2017, *Middleton et al.*, 2017), however examples of discrepancies have been observed, tending to be due to Quaternary rates being greater than geodetic rates (*Thatcher*, 2009, *Mohadjer et al.*, 2017).

The extension rate across the Yatağan fault is slower than the summed extension rate of the Muğla and Yilanli faults. This suggests there is either more rapid extension in the south-east, or that deformation is occurring on other structures across-strike from Yatagan as well. My geomorphological mapping shows there are other active structures across strike from both the Yatağan and the Muğla faults. A step in topography indicates that there is an active structure in the Yatağan basin, south west of the Yatağan fault, as well as faults to the north-east (Figure 6.4). The Yilanli fault may

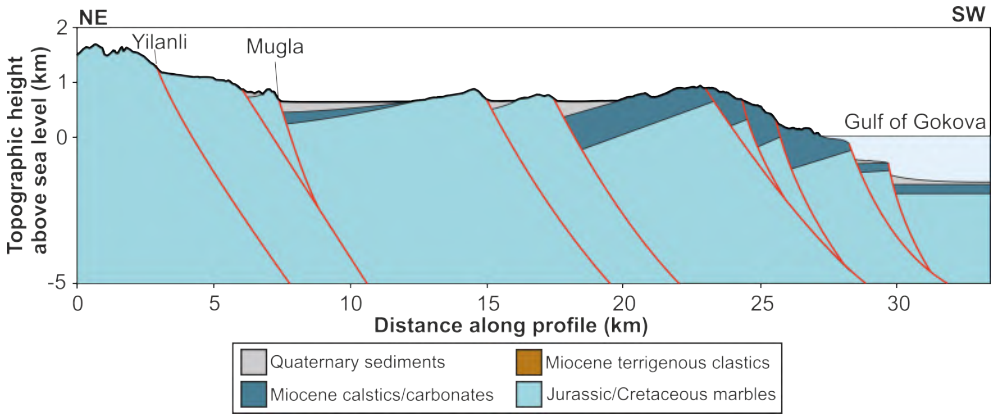

Figure 6.9: A geological cross section based on the geological map of *Akbaş et al.* (2017), the active fault map of *Emre et al.* (2018) and my updated active fault map (Figure 6.4). Location is shown by line C-D in Figure 6.4. The topography is derived from the TanDEMx data (*Wessel et al.*, 2018). The dips of bedding are not based on any data, as none was available. As a result no restoration and calculation of total throw was possible. Bathymetry data is not available near-shore, however bathymetry and seismic reflection data has been interpreted to generally show late quaternary active faults off shore (e.g. *Uluğ et al.* (2005)), and this section shows a possible configuration.

extend significantly further than in current active fault maps (*Gürer et al.*, 2013, *Emre et al.*, 2018; Figures 5.5 and 6.4), which may explain the difference in summed rates in the NW and SE Muğla-Yatağan basin. Further field investigation of both these structures will determine which, if any, is currently accommodating strain in the NW of the Muğla-Yatağan basin. More simply it could be the case that the fault dip varies between the faults and so horizontal strain rate estimates in this study are incorrect because of this, and future events in the basin that are large enough for waveform inversion may provide better insight into the fault at depth (*Howell et al.*, 2017).

6.7 Conclusion

In this chapter have updated the active fault map of the Muğla-Yatağan basin and immediate surrounds, and using this and existing geodetic data I have determined that the Holocene slip rate across the three major faults in the basin is equal to the geodetic strain rate. If this is true for all of western Turkey, then using only an accurate active fault map and the geodetic strain rate, slip rates could be determined far all faults. To determine this requires more Quaternary fault slip rate data. I have also demonstrated that the Muğla, Yatağan and Yilanli faults are capable of producing PGA in of 0.7g in populated areas, which is particularly important for the Yilanli fault, which was previously considered inactive during the Holocene.

Chapter 7

Discussion

"There is no real ending. It's just the place where you stop the story."
Frank Herbert

7.1 Thesis summary

I began this thesis by providing a background in extensional tectonics, and cosmogenic isotope analysis of fault scarps. In Chapter 2 I present a review of previous ^{36}Cl fault scarp studies and the evolution of modelling used in these studies. In this review I find that there has been little published evidence demonstrating that ^{36}Cl analysis of a fault scarp results in a reliable slip history. A previous study by *Schlagenhauf et al.* (2011) has shown agreement between 4 sites on the same fault, and therefore suggested ^{36}Cl fault scarp analysis resulting in reliable slip histories. However, *Schlagenhauf et al.* (2011) varied a parameter in their modelling (pre-exposure), with no justification of why it would vary between sample sites, to suggest correlation between sites. In chapter 3 I modelled the data from *Schlagenhauf et al.* (2011) treating each site the same, to determine how similar slip histories are if all sites are treated identically. My results showed that the sites produced very different slip histories, and investigation of sample site geomorphology indicates this is likely due to non-tectonic exhumation of the fault scarp at sample sites.

As a result of my findings in Chapter 3, in Chapter 4 I tested the hypothesis that if ^{35}Cl dating of fault scarps is a reliable tool, then it should produce similar slip histories at sites closely spaced along strike. I present a new study with multiple sample sites across two different faults in the central Italian Apennines. On the first fault, the Campo Felice fault, I used 4 sample sites, including data from a site published by *Benedetti et al.* (2013). I found the slip histories were similar between sites, leading me to conclude that ^{36}Cl analysis of fault scarps can provide repeatable and therefor reliable measurements of slip history, provided sample sites with appropriate geomorphology are chosen. The second fault in the chapter was the Rocapretturo fault, here I sampled

two sites and used data from a site sampled by *Schlagenhauf* (2009). On this fault I found a discrepency in slip histories between sites. This was the result of non-tectonic exhumation of the fault scarp at the site from *Schlagenhauf* (2009), and the discrepancy between the two sites I sampled was due to strain partitioning between overlapping fault strands. This result demonstrates the ability of ^{36}Cl fault scarp analysis to observe along strike variation in slip rate over millennial time scales.

In my final study, I applied ^{36}Cl analysis of fault scarps to three faults in western Turkey: the Muğla, Yatağan and Yılanlı faults, which form the Muğla-Yatağan basin. I determined slip histories for these faults, concluding that Muğla and Yatağan were slipping at constant rates, and Yılanlı was slipping at approximately half the rate of these more dominant structures, and had a variable slip rate. I found the rates were similar to those calculated using geodetic strain rates, given the fault spacing in the region. Using deterministic earthquake hazard mapping, I demonstrated that all three faults pose a hazard to local populations, and I complemented this finding with an updated surface map of the faults, based on field and satellite mapping. In this chapter I will discuss how this thesis fits in and adds to current understanding of both ^{36}Cl analysis of limestone fault scarps and the wider context of extensional tectonics. Finally I will discuss future research opportunities arising from my research.

7.2 How this thesis adds to our understanding of ^{36}Cl analysis of fault scarps

Previous studies using ^{36}Cl dating of limestone bedrock fault scarps have often attempted to identify the timing of individual earthquakes on normal faults (*Zreda and Noller*, 1998, *Benedetti et al.*, 2002, 2003, *Palumbo et al.*, 2004, *Schlagenhauf et al.*, 2010, 2011, *Mouslopoulou et al.*, 2014, *Tesson et al.*, 2016). I have shown that a previous study that stated individual earthquakes can be identified using ^{36}Cl by *Schlagenhauf et al.* (2011) relied on arbitrarily varying parameters between sites (Chapter 2). *Mitchell et al.* (2001) were the first to suggest that only periods of rapid motion and periods of slower motion can be determined using ^{36}Cl dating of limestone bedrock fault scarps and *Cowie et al.* (2017) continued in this line of research, developing a modelling method which does not try to identify single events, but periods of fast and slow slip. *Tesson and Benedetti* (2019) and *Beck et al.* (2018) use modelling methods which solve for event size and individual earthquakes and displacement, however results from both studies show that only periods of relatively fast or slow slip can be determined, not the timing of events, and require significantly more parameters to do so. My work on the Campo Felice and Rocaprettura faults (Chapter 4) shows that changes in slip rate are consistently resolvable at multiple sample sites on the same fault, as long as the sample site has been chosen using the guidelines laid out by *Bubeck et al.* (2015) and further discussed in this thesis.

In chapter two I identify studies based on data from sample sites where the fault scarp has been buried and/or exhumed by non-seismic processes (*Zreda and Noller*, 1998, *Benedetti et al.*, 2003, *Schlagenhauf*, 2009, *Schlagenhauf et al.*, 2011, *Mozafari et al.*, 2019a). As the community's understanding of the importance of geomorphology increases, the community should select and document more appropriate samples sites in future studies. The results of existing studies which have inappropriate geomorphology should be viewed sceptically. Ideal sample site geomorphology likely does not exist on most faults, and one can never be certain that a slope has not been modified. The quality of available sample site will vary between faults and all reasonable efforts should be made to determine and document this along a fault. Determining the most appropriate sample site on a fault commonly comes down to qualitative assessment, however it is essential for authors to provide as much information on the sample site characteristics as possible, be that in descriptions, photographs, or providing digital models of the site (e.g. LiDAR, Structure from motion etc.), so readers can form their own opinions. Simple checks, such as if all the faults in a region have Holocene slip rates that sum to orders of magnitude greater than the total extension rate, would indicate that there is likely a problem with material being removed from the hangingwall, exposing the fault scarp more rapidly than seismic slip. I propose a systematic review of all published ^{36}Cl sample sites by the ^{36}Cl community, which would allow groups who use ^{36}Cl derived slip rates to form a better judgement on the model results from these studies. This may require visiting sample sites, given that key features of the geomorphology are commonly not recorded in publications, e.g. in *Mozafari et al.* (2019a) where the presence of a road three meters from the fault scarp was not mentioned. I have begun a systematic review in Chapter 2, however there are many sites that I have not visited, and where there is limited site information. The large amounts of both time and money that go into each ^{36}Cl fault scarp study means that coming to a consensus on whether a sampled site is suitable may be difficult, however I think it is important for increasing trust of ^{36}Cl fault scarp studies going forward. This systematic review could involve re-modelling the data, so that output is comparable between studies, though again different groups commonly advocate different modelling approaches, so coming a consensus may be difficult. A useful community resource would be an online repository for ^{36}Cl fault scarp data. Similar databases exist, such as one for cosmogenic and luminescence dating of fluvial sediments (*Codilean et al.*, 2018). This database should contain all the information needed to model the data, in a standardised format. This would mean; ^{36}Cl measurements, geochemical data, site geometry including shielding measurements, site location, and photos and/or high resolution DEMs of the sample sites and surroundings. As modelling techniques develop, all existing sample sites could then be re-modelled more easily, making sure that the full potential of all legacy ^{36}Cl data is explored and exploited. It would also mean the community could develop best practices for sampling fault scarps, and share these practices easily.

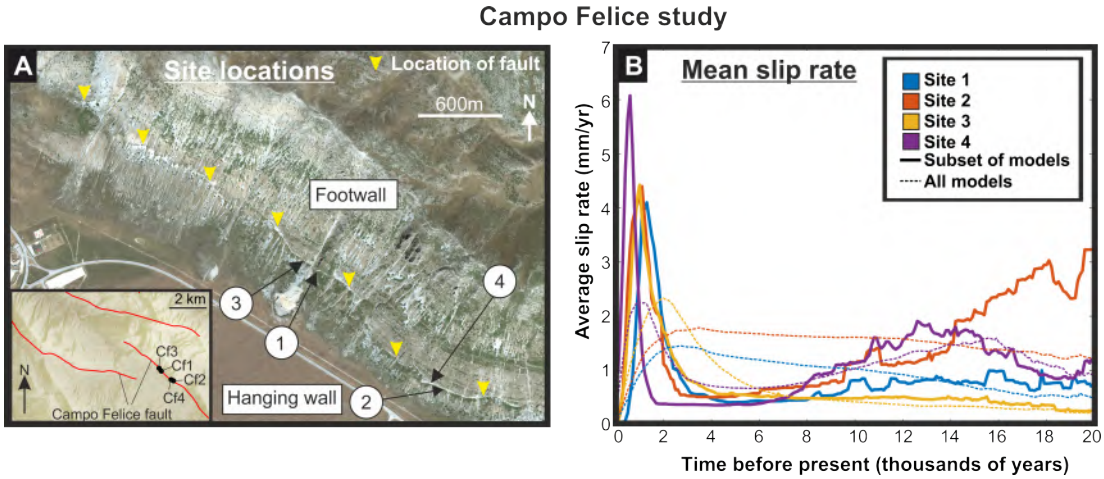

Figure 7.1: A, shows the locations of the 4 sites from which I analysed samples on my study of the Campo Felice fault in the Italian Apennines, and B shows the mean slip rates derived from the ^{36}Cl data taken from the sample sites. Solid lines show the mean of the best fitting models and the dotted line shows mean of the entire distribution. Details of this plot can be found in Figure 4.7 and associated text.

In future studies, if there are particular faults of interest for ^{36}Cl study, but all possible sites do not have ideal geomorphology there are two ways that confidence in ^{36}Cl data can be increased. The first is by taking multiple sample sites closely spaced along strike as I did in the Italian Apenines. If sites along the fault result in similar modelled slip histories as at the Campo Felice fault (Figure 7.1), then it provides confidence that the fault scarp exhumation is due to seismic events, rather than other shorter wavelength geomorphic processes. Secondly, corroboration or disagreement between ^{36}Cl data and other Quaternary or paleoseismic dating techniques can also provide confidence in modelled slip histories, such as my work on the Rocaprettura fault, which corroborates with results from paleoseismic trenches 400 m along strike (Chapter 4). Disagreement between other sources and ^{36}Cl scarp data can also reduce confidence in ^{36}Cl sample sites, as is the case on the Kaparelli fault where ^{36}Cl derived slip histories (*Benedetti et al.*, 2003), disagree with paleoseismic data (*Kokkalas et al.*, 2007). Disagreement in the case of the Kaparelli fault may be due to problems with the modelling method, though the geomorphology has been affected by human influence (Chapter 2).

Modelling ^{36}Cl data to produce a slip history of a fault is a key part to using ^{36}Cl fault scarp data, and modeling methods have evolved over the 20 years of ^{36}Cl fault scarp studies. I undertake a systematic review of modelling methods in Chapter 2, however one useful addition would be a comparative test between all published modelling methods using the same ^{36}Cl data set. A comparative test performed on a synthetic data set would allow the relative strengths and weaknesses of each model to be assessed. It may also be worthwhile testing the models on the same real data set. I propose that data from the 4 sites from Campo Felice (Chapter 4) would be a good test

case, because uniquely there are multiple sites on the same fault that can be modelled with similar slip histories. Future modelling codes could then be better compared to the existing codes. Again, a central updatable repository would be useful, with links to all existing codes and future codes as they are developed. The advances in modelling mean that some of the early studies have been modelled in a way that is now thought flawed, or possibly too simplistic (*Mitchell et al.*, 2001). Now better modeling methods are available, it may be useful to re-model old data sets, particularly those where parameter space was not explored in a systematic way e.g. *Benedetti et al.* (2002). The afore mentioned modeling code comparison study would assist in deciding which code to use. I currently favour the MCMC flexible change point code from *Cowie et al.* (2017), due to the low number of parameters used and it's trans-dimensional nature.

The most recent ^{36}Cl fault scarp inversions (*Cowie et al.*, 2017, *Beck et al.*, 2018, *Tesson and Benedetti*, 2019) use Bayesian Markov Chain Monte Carlo algorithms, but there are difficulties in interpretation of output of these models. The output of these algorithms is a probability distribution for each parameter, and as a result there is not a single correct solution, but a distribution of solutions with varying probability, known as the posterior distribution. Relying on the highest probability solution, or some other single measure of the distribution over simplifies the solution, and can misrepresent the data. For example, there is commonly covariance in the modelled slip histories. The same ^{36}Cl profile can result from either a slip history that is fast then slow, or slow then fast, because the slip history is non-unique when the model allows a variable slip rate. This may lead to a bi-modal distribution, and, therefore, the mean result is a constant rate, but in fact the inversion is really indicating that a variable slip rate is the most probable solution (Figure 7.2). Investigating model outputs such as the number of change points can indicate if this kind of trade-off is occurring. It is only through careful consideration of these posterior distributions that a conclusion regarding the likely slip history of a fault can be derived from ^{36}Cl. I think there is commonly a danger of over-interpreting the data, as studies often interpret a very detailed single or narrow range of slip histories, with the aim of resolving individual earthquakes or properties of the fault slip that cannot be resolved by the data (e.g. timing of earthquakes or slip in individual earthquakes).

Aside from difficulties in interpreting models of ^{36}Cl data, one of the major issues with ^{36}Cl analysis of fault scarps is that it is very limited to where it can be applied. Currently it has only once been applied on bedrock fault with a non-carbonate lithology (*Webber et al.*, 2018), however, the limited information provided on the geomorphology of the site in *Webber et al.* (2018) suggests material has been removed from on top of the fault plane, possibly by landslide, and this is not in the paper. Exploring the possibility of fault scarps in other lithologies would greatly increase the applicability of cosmogenic dating of fault scarps, however I am yet to see a convincing example of a normal bedrock fault scarp that is well-preserved on an active fault in a lithology

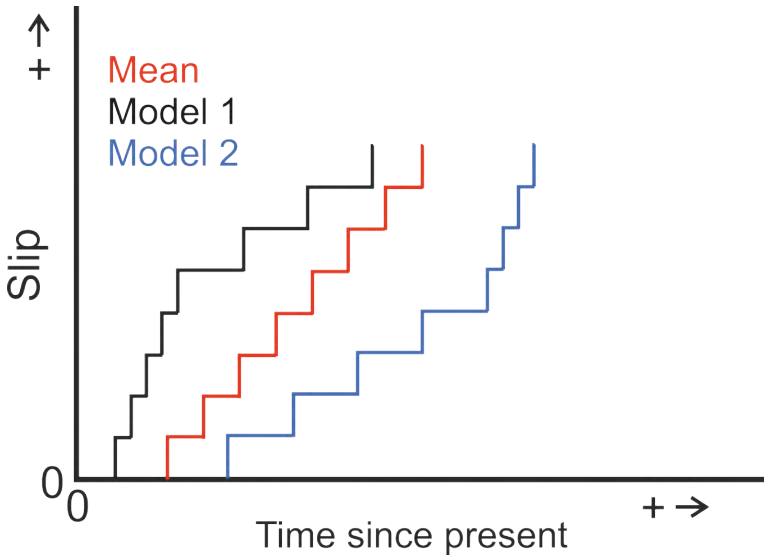

Figure 7.2: If a posterior slip history distribution was bimodally distributed around model 1 and model 2, then the mean would not be an appropriate representation of the model to draw conclusions on variable slip rate from.

other than carbonates. The combination of appropriate lithology, slip rates greater than erosion rates and appropriate geomorphology makes a reasonable ^{36}Cl fault scarp sample site a rarity, however this reliance on goldilocks conditions is a common problem in Quaternary dating. As a result multiple dating techniques may be needed to asses a fault network in heterogenous lithology.

7.2.1 Limestone fault scarp footwalls

During the LGM erosion rates in the Italian Apennines were greater than at present (*Tucker et al.*, 2011). This change from faster to the present slower rates is recorded in the cosmogenic exposure age of the slopes offset by limestone normal fault scarp. During the LGM erosion rates were greater than exhumation rates, so no slope offset was preserved, but since erosion rates reduced to lower than the exhumation rate, fault offset of the slope has been preserved (Figure 7.3). I use dating of footwall slopes using ^{36}Cl to determine the timing of this change in slip rate in western Turkey (Chapter 5). Whilst footwall dating does not have the same potential as dating of the fault scarp directly in terms of observing variable slip rates, it can provide an estimate of average slip rates over the Holocene. I determine the first footwall ages for normal faults in western Turkey (Chapter 5). The ages I modelled suggest that the faults scarps are preserved from around the demise of the last glacial maximum (LGM), similar to limestone bedrock normal fault scarps in the Italian Apennines (*Tucker et al.*, 2011, *Cowie et al.*, 2017; Gregory, personal communication).

I was provided with ^{36}Cl concentrations and required supplementary data for eight samples from two ^{36}Cl footwall sites in bedrock limestone by S. Mechernich (personal

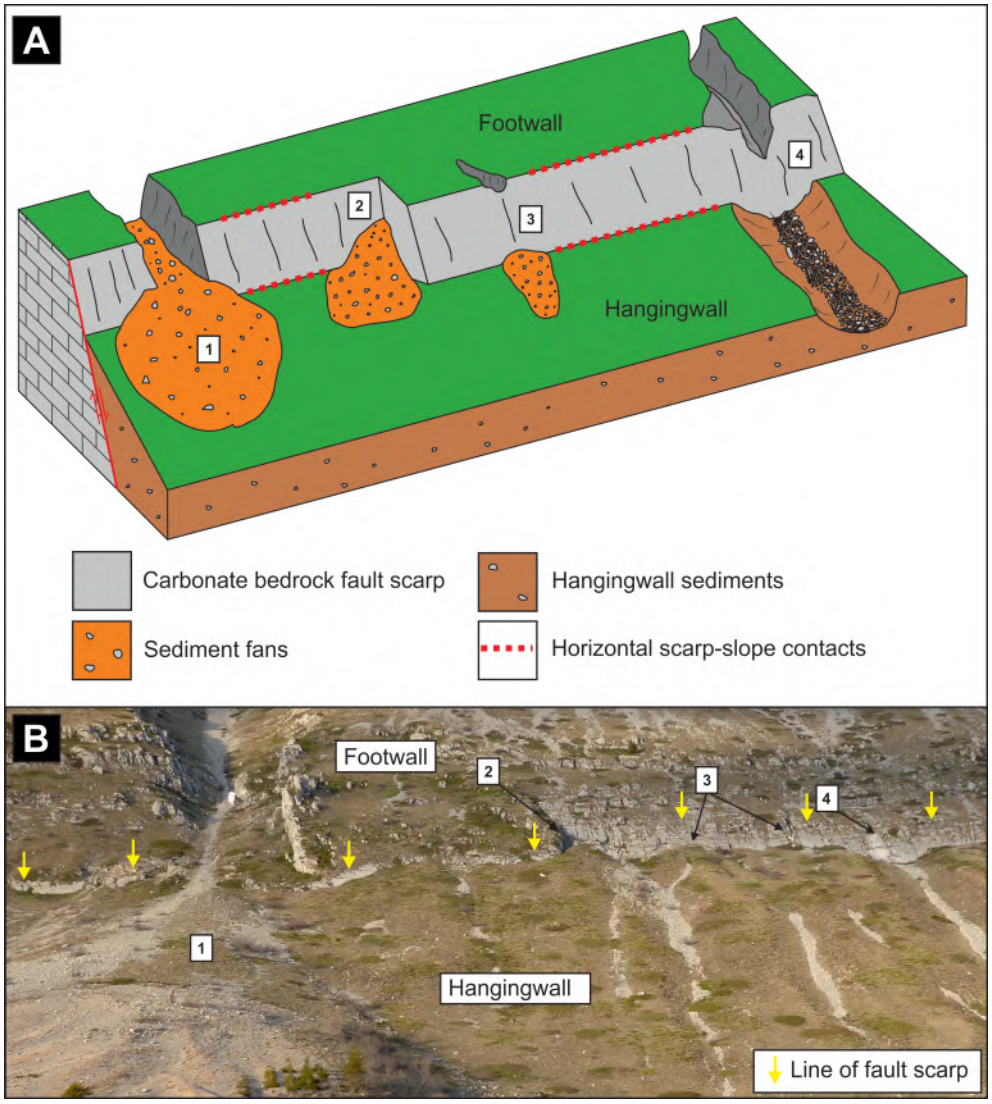

Figure 7.3: A) A schematic diagram of slope processes that can produce non tectonic exhumation and burial of active limestone fault scarps. Labels 1-4 indicate areas of hangingwall erosion or deposition that would be inappropriate to sample. Ideal sample sites are located away from areas affected by depositional and erosional slope processes, where the scarp-slope contacts are horizontal, after *Bubeck et al.* (2015). B) The Campo Felice fault with features from A indicated. Photo taken from (42.2308° N, 13.4343° E) looking northeast. Horizontal scale is approximately 320 m across image at height of scarp.

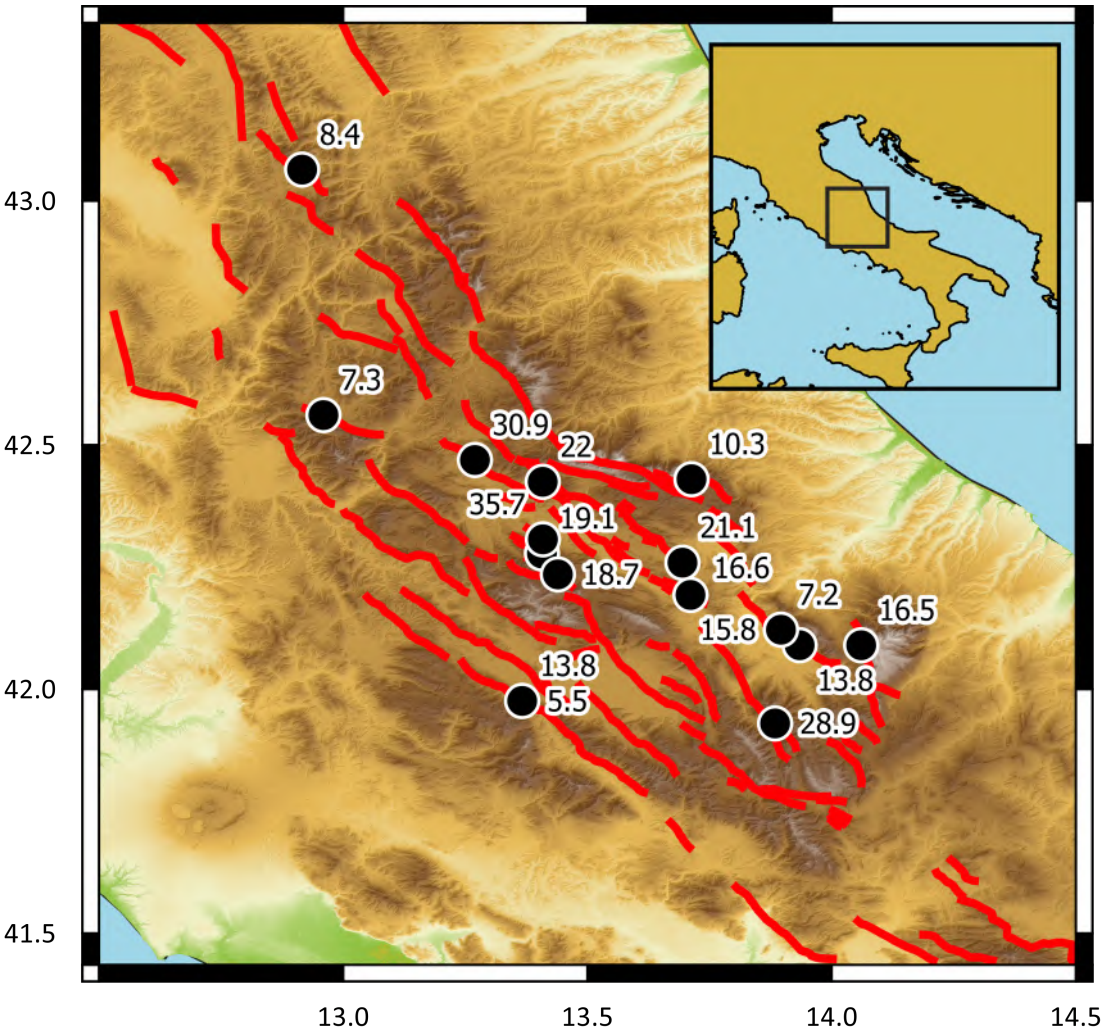

Figure 7.4: A map of ^{36}Cl footwall ages in the central Italian Apennines, location of sample sites are shown by black circles, and ages are in kyr. Data are currently unpublished from Gregory (personal communication).

Fault	Apparent age (kyr)
Spili	21.7±5.1
	22.3±2.7
	22.3±2.1
	23.4±2.1
Lastros	31.3±2.8
	19.3±1.6
	37.2±3.2
	27.2±2.3

Table 7.1: Apparent footwall exposure ages for samples from the Spili and Lastros faults in Greece, calculated using the method in Chapter 5.

comm.s), on the Spili and Lastros faults in Greece. I used the same method as set out in Chapter 4 to calculate exposure ages, which resulted in a range of ≈ 19-37 kyr (Table 7.1). When collated, the data shows an age range of ≈40 kyr, with Italy having the largest range in values (Figure 7.5). This is likely due to the greater number of separate faults sampled, as well as the greater number of individual samples. Greece has an older mean apparent age of 26.6 kyr, whereas Italy and Turkey have similar means of 17.3 kyr and 17.9 kyr. Due to the low number of faults sampled in Greece and Turkey (2 and 3 respectively), the ages may not be representative of footwall slopes in the region. There is no correlation between age and elevation (Figure 7.5), and within the Italy data, there is no correlation with latitude or footwall slope dip (Gregory, personal comms.), suggesting there is no physical process controlling the variability in footwall age.

Dating footwall slopes is problematic because the surface being sampled has been eroded at an unknown rate, and the exposure age can be influenced by erosion and inheritance (*Tucker et al.*, 2011). Selection of sample location is important because if, for example, a sample is taken that recently had several meters of rock removed (e.g. due to rockfall or cliff collapse), then the modelled exposure age will be younger than the time of slope stabilisation, and not be representative of the footwall slope. To counter this a large number of samples should be collected. Footwall slope ages for individual faults (Figure 7.4) in Italy are currently based on one or two samples at each fault and four per site in Greece. Given the uncertainty in the footwall slope preservation, a greater number of samples gives greater confidence in the values, so using a regional average allows incorporation of many samples to determine a regional footwall age. A better approach for determining a fault specific footwall age would be to take a greater number of samples at each sample site. I have also modelled the footwall ages without any erosion or inheritance, for ease of comparison with other footwall ages, however this results in an apparent footwall age. In future work, exposure modelling of footwall samples should take into account the erosion rate of the footwall and inherited ^{36}Cl to

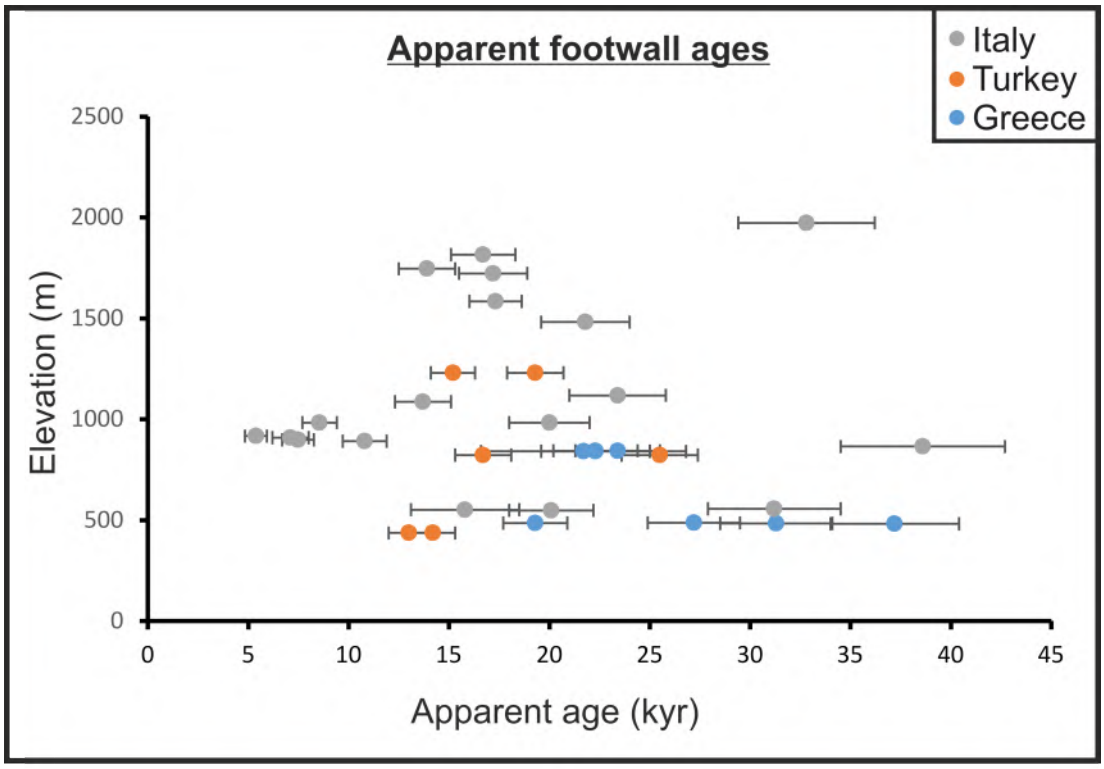

Figure 7.5: Plot of footwall ages vs elevation above sea level, from normal faults in the Mediterranean. Ages for Turkey are from this thesis, Italy from Gregory (personal comms) and Greece from Mechernich (personal comms.), and ages and 1σ uncertainties were all calculated using the online Cronus calculator (*Marrero et al.*, 2016) and using the same parameters described in Chapter 4.

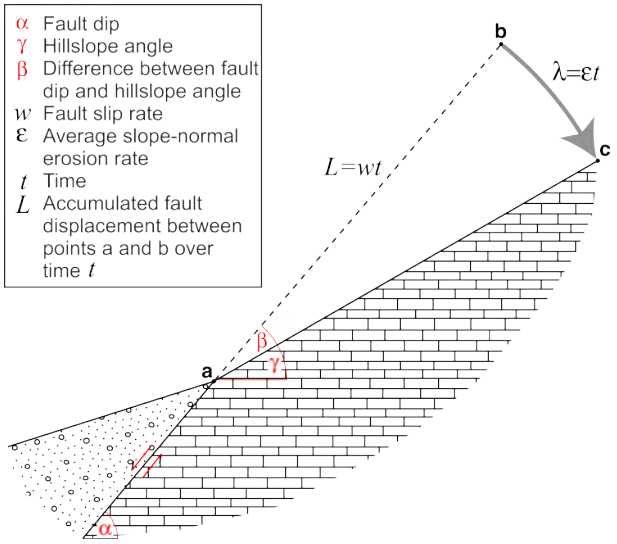

Figure 7.6: A geometric model of limestone bedrock normal fault, after *Tucker et al.* (2011).

provide a better estimation of the age the footwall slope stabilised.

The geometry of normal limestone bedrock fault scarps can be used in conjunction with the slip rate to determine the average erosion rates of the footwall during the LGM. Similarly, if the the erosion rate is known, a slip rate on the fault can be determined. This relationship was derived by *Tucker et al.* (2011) and is based on a schematic model (Figure 7.6).

Based on the model in Figure 7.6, the distance between point b and point c is the cumulative slope-normal erosion depth at point c, and can be expressed as:

$$\lambda = (\alpha - \gamma)L \tag{7.1}$$

when angles are expressed in radians. The average erosion rate is

$$\epsilon = \frac{\lambda}{t} \tag{7.2}$$

If the slip rate ($w = \frac{L}{t}$) is known, the erosion rate is

$$\epsilon = (\alpha - \gamma)w \tag{7.3}$$

and inversley if the erosion rate is known, slip rate is

$$w = \frac{\epsilon}{(\alpha - \gamma)} \tag{7.4}$$

Tucker et al. (2011) state that this model is only applicable to normal faults with planar footwall slopes with little to no regolith cover, which have a relatively stable footwall (i.e. no bedrock landsliding). These criteria are commonly met in both western

Site	Scarp dip α (°)	F.w. dip γ (°)	Slip rate w (mm/yr)	Erosion rate ϵ (mm/yr)	Elev. (m)
Campo Felice 1	51	35	1.1	0.31	1674
Campo Felice 2	54	33	1.6	0.59	1603
Campo Felice 3	57	36	0.9	0.33	1667
Campo Felice 4	54	35	1.2	0.40	1595
			Mean	0.40	
			St. dev.	0.13	
Rocaprettura 1	49	31	0.5	0.16	839
Rocaprettura 2	66	27	0.3	0.20	923
			Mean	0.18	
			St. dev.	0.30	
Muğla	43	19	0.6	0.25	823
Yılanlı	57	27	0.25	0.13	1230
Yatağan	74	35	0.5	0.34	437
			St. dev.	0.11	

Table 7.2: LGM erosion rates calculated from fault geometry and ^{36}Cl slip rate, using equation 7.3 from *Tucker et al.* (2011). Parameters are defined in Figure 7.6. Slip rate is calculated using the mean posterior scarp age from the ^{36}Cl fault scarp data analysis undertaken in Chapters 4 and 5.

Turkey and central Italy, and my study provides slip rates for a number of faults as well as the scarp dip and footwall dip angles.

I calculate footwall erosion rates for each sample sites I investigated in Chapters 4 and 5 using the geometry from TLS measurements and the average slip rate based on mean posterior scarp age ^{36}Cl fault scarp surface MCMC inversion. The values used for modelling and resulting erosion rates can be found in Table 7.2.

The Campo Felice fault has higher LGM erosion rates than the Rocaprettura fault, and the range of erosion rates is larger along the Campo Felice fault, however the three faults have similar standard deviations (Table 7.2) indicating this difference in range is mostly due to differing numbers of samples. Erosion rates in Turkey lie between Rocaprettura and Campo Felice, but again, the significance cannot be gauged due to the low number of measurements.

The difference in rates between the Campo Felice and Rocaprettura faults may be becayse they are situated at ≈1600 m altitude and ≈900m respectively. It has also been proposed that the footwall lithology can effect erosion rates and therefor slope morphology(*Zuchiewicz and McCALPIN*, 2000, *Hurst et al.*, 2013), so it may be that the footwall is more competent at Rocaprettura. *Menges* (1990) suggest that lithology is only of secondary importance, and that fault dip and slip rate are the most important factors, in line with more recent studies (*Tucker et al.*, 2011, 2020). A study by in *Kent et al.* (2016) in south central Turkey found a relationship between long term (10^5-10^6 yrs) throw rate and topography, which also suggest that fault slip rate and dip

are the two key factors controlling footwall morphology. Based on numerical models *Densmore et al.* (1998) suggest that scarp footwall slope angle is a result of the angle of failure planes that produce landslides, however my field observations in Italy, Greece and Turkey, along with observations of others (*Petit et al.*, 2009, *Tucker et al.*, 2020), provide little evidence that landslides are a major active process on footwall slopes.

Tucker et al. (2011), who derived the relationship between fault geometry, slip rate and erosion rate, calculated erosion rates of the footwall of the Magnola fault in Central Italy of 0.22-0.40 mm/yr based on the average Holocene slip rates determined from ^{36}Cl fault scarp study of *Schlagenhauf et al.* (2010). While these erosion rates are similar to all the footwall erosion rates calculated from sites in Turkey and Italy (Table 7.2), the slip rates they are based on are flawed, due to problems with both the modelling method and the sample site selection, which I explored in Chapter 2.

One key assumption which both I and *Tucker et al.* (2011) rely on when using equation 7.3 to model erosion rates, is that the slip rate calculated from ^{36}Cl fault scarp modelling is representative of the average slip rate over the entire formation of the planar footwall slope, so over a period longer than that recorded by ^{36}Cl data, and that the fault is moving at a constant rate. If the fault had a variable slip rate, this may be recorded in the topography as subtle changes in slope (*Hamblin*, 1976). Another key assumption is the planar nature of normal faults. This model assumes that the fault is a completely planar feature and can therefore be projected as a straight line. Whether the current fault scarp has a dip representative of the projected fault scarp (vector a-b in Figure 7.3) is unknown. A more representative fault scarp dip (γ in Figure 7.2) may be obtained by taking the average value of multiple dips taken along strike along the scarp. I also assume that the erosion rate is constant over the LGM/exhumation of the footwall slope, which may not be the case.

Whilst the effect of the assumptions above need testing, more studies of erosion rate using this method could assist in quantifying the effect of normal faulting on hill slope morphology. For example, if the erosion rate is known, then the hill slope angle and fault scarp may be used to calculate the slip rate of a fault, with the aid of additional information (*Tucker et al.*, 2020). Currently there are not enough data to make statistically valid statements, however this analysis can easily be applied to any ^{36}Cl fault scarp sample site which fullfills the site selection criteria I have used in my studies, which were set out by *Bubeck et al.* (2015). Future ^{36}Cl fault scarp studies should make use of the footwall slope exposure age method, as it adds little extra work in the field and lab and provides an independent data set. *Tucker et al.* (2020) have produced a more complex model which builds on *Tucker et al.* (2011), and predicts a non-linear relation between erosion rate and gradient when slip rate is normalised, and suggest that this relationship could be tested using cosmogenic footwall data like that I have collected. Testing of this and similar hypotheses are the next stage in developing our understanding of normal fault facet evolution, and, importantly for the tectonic

and seismic hazard community, may provide further insight into quantifying slip rates using normal fault facet geometries.

7.2.2 Consideration for future ^{36}Cl studies

The primary conclusion from my work in Central Italy is that the most important component of any future ^{36}Cl fault scarp study is in picking a sample site with good geomorphology. As long as the geomorphology of the site has been stable over the Holocene, the sample site will produce a reliable slip rate and estimate of slip rate variability. Whilst there will likely always be disagreement on the best way to model the data, and modelling methods and analyses of ^{36}Cl data will likely advance, good data can always be re-modelled and new reliable conclusions drawn. ^{36}Cl fault scarp dating has been plagued by studies with poor geomorphology (Chapter 2), and going forward a real effort must be made by all researchers in the field to combat this and document the characteristics at every site. A second key message is that interpretation of ^{36}Cl fault scarp data is not straight forward and the community does not currently have a good method for quantifying all the uncertainties. Two resultant pitfalls are overfitting the data, and over interpretation of the data, and both should be avoided. Deciding whether to take multiple sites on a fault depends on the scope of the study. On the one hand, multiple sites on a single fault can provide information on along strike slip rate variation over the Holocene and provide greater confidence in the determined slip rate. On the other hand, spreading sample sites across multiple faults can provide slip rates on multiple faults, giving insight into fault network behaviour over Holocene time frames, all be it with reduced confidence in the determined rates. Both approaches are valid and can be used to answer slightly different questions. Going forward, utilising both approaches will increase scientific understanding of faults at the single fault and fault network scales.

7.2.3 Interpretation of Quaternary slip rates

Interpreting Quaternary slip rate measurements is difficult because slip varies spatially in one earthquake and probably over multiple earthquake cycles (*Barka et al.*, 2002, *Haeussler et al.*, 2004, *Wesnousky*, 2008, *Walters et al.*, 2018, *Wedmore et al.*, 2019) as my results from Chapters 3 and 4 also demonstrate. Methods for determining Quaternary slip rates typically only record the deformation occurring at a single point on the fault. Furthermore this point is always at the intersection of the fault plane and the earth's surface. Therefore a single Quaternary slip rate measurement may not be representative of either the fault slip along strike at the surface, or the fault activity at depth. Coneceptual surface slip models typically have a smooth slip distribution along strike (*Wesnousky*, 2008, *Rotevatn et al.*, 2018), however slip distributions deviate from these idealised models (*Akyuz et al.*, 2002, *Barka et al.*, 2002, *Wedmore et al.*, 2019;

Figure 1.4). A study on the Mt. Vettore-Mt. Bove fault system in Central Italy shows correlation in slip between the geological throw, the Holocene throw and the coseismic offset, indicating that larger scale variation in coseismic surface slip distribution may be representative of longer timescale slip variations, and therefore processes at depth (*Brozzetti et al.*, 2019). My work on the Campo Felice and Rocaprettura faults shows that changes in slip rate occur at a similar time along strike (Chapter 4), independent of the average Holocene slip rate at each site. The same work shows that the shorter wavelength coseismic slip variation is smoothed out over multiple earthquake cycles, at least in the resolution of ^{36}Cl fault scarp data, in line with the findings of *Walsh and Watterson* (1987). This gives cosmogenic fault scarp analyses an advantage over techniques that are more susceptible to short wavelength variation in displacement, such as paleoseismic trenching, when considering a single sample site or trench on a fault. One possibility for reducing uncertainties in slip rates and slip histories is to jointly invert multiple closely spaced sites, as *Gold et al.* (2017) did, when determining slip rates using multiple faulted river terrace risers situated close to one another. Faults are 3 dimensional objects and subsurface slip can deviate from idealised distributions (*Walters et al.*, 2018), therefore extrapolating moment magnitude or slip at depth from a single point measurement of displacement will always have uncertainties. Variable slip rate along strike has been observed in other studies that have used Quaternary dating techniques at multiple points along a fault. Data sets that cover both temporal and spatial distribution of slip rate on a single fault provide can provide insight into how faults are segmented, and therefore the likely magnitude of ruptures. *Frankel et al.* (2007) and *Farbod et al.* (2016) used cosmogenic dating of offset fans to determine along strike slip rates variations on a strike slip faults. Studies of topography and geomorphology have also revealed along strike slip rate variation on normal faults (*Boulton and Whittaker*, 2009, *Brozzetti et al.*, 2019). Combining novel observations, such as geodetic information with high resolution surface rupture mapping, has demonstrated the complexity of the relationship between slip at the surface, slip at depth and moment magnitude (*Dolan and Haravitch*, 2014, *Anderson et al.*, 2017, *Walters et al.*, 2018, *Brozzetti et al.*, 2019), and perhaps with similar data from a greater number of events these relationships can be better quantified.

Slip rates also vary temporally (*Friedrich et al.*, 2003, *Dolan et al.*, 2016, *Biemiller and Lavier*, 2017, *Khajavi et al.*, 2018). I have observed variable slip rates over thousand year time scales using ^{36}Cl fault scarp data, as have other similar studies (*Cowie et al.*, 2017), however, this method typically only captures one or two changes in slip rate. As a result we cannot tell if the slip rate variation is a regular pattern or more chaotic. Variable slip rates also mean that the slip rate calculated at a given point in time cannot necessarily be used to determine the slip rate in the future, for example just because a fault has been in a period of relatively fast slip for the last 5 kyr, does not mean it is currently slipping rapidly. This is a problem for probabilistic seismic hazard modelling,

and studies have tried to quantify this variation using the coefficient of variation (CV) which is defined as

$$CV = \frac{\sigma}{T_{mean}} \tag{7.5}$$

in *Cowie et al.* (2012) and references therein, where σ is the standard deviation of the inter-event time, and T_{mean} is the long term average recurrence interval. Input for Equation 7.5 is typically palseoseismic trench data and resultantly CV is generally poorly constrained due to the limited timeframe covered (*Ellsworth et al.*, 1999). Modelling of fault networks shows that CV generally is generally higher when strain is partitioned on multiple faults, and the relationship between CV and the mean long term slip rate is poorly constrained (*Cowie et al.*, 2012). *Cowie et al.* (2012) define a new term, slip rate variation (SRV)

$$SRV = \frac{\sigma_{SR}}{SR_{mean}} \tag{7.6}$$

where σ_{SR} is the standard deviation of a short term slip rate over a sliding time window of fixed length, and SR_{mean} is the long term average slip rate. Through modelling the evolution of normal fault networks *Cowie et al.* (2012) demonstrate that slower faults have higher slip rate variation, and that slip rate variation increases with increased fault spacing. They also find that earthquake recurrence varies systematically as a function of fault geometry. SRV is useful in the case of modelling ^{36}Cl fault scarp data, as it does not require timing of individual events and incorporates displacement.

Whilst all the Italian ^{36}Cl sites I have sampled demonstrate some variation in slip rate, in the Muğla basin, western Turkey, only the Yılanlı fault showed clear variable slip rate. I used the MCMC flexible change point code of *Cowie et al.* (2017) to model the ^{36}Cl fault scarp data. *Cowie et al.* (2017) show in their sensitivity testing of the MCMC flexible change point model, that only SRV > 0.2 can be resolved with confidence. It would be useful and interesting to determine the SRV value for sites on the Campo Felice and Rocaprettura faults and see if SRV varies along strike on the fault. Implementation of SRV on output from the MCMC flexible change point code is not straightforward, as SRV should be calculated for each accepted slip history, and then the resulting distribution of time varying SRV should be analysed. This is likely to be computationally expensive.

The ^{36}Cl fault scarp data I modelled in Turkey showed a variable slip rate only on the Yılanlı fault. This suggest that SRV < 0.2 on the Yatağan and Muğla faults, which have higher long term slip rates. This is in line with the observation *Cowie et al.* (2012) made that SRV is inversely proportional to mean slip rate, implying that major faults in the Apennines have more stable slip rates. It is also possible that the ^{36}Cl site on the Yılanlı fault is not representative of the rest of the fault because of the interaction with the Muğla fault, however my results from the Rocaprettura fault suggest that variable slip rate occurs at similar times along strike, even when there is interaction with other

faults. This in turn suggests that the SRV I observe in my modelling of the ^{36}Cl data at Yılanlı is representative. *Kent et al.* (2016) find that there is reduced Quaternary slip rates towards segment tips of normal graben bounding faults in Turkey and this has has been observed in normal faults more widely (*McLeod et al.*, 2000, *Cowie and Roberts*, 2001), which suggests that whilst the SRV may be representative at the Yılanlı site, the slip rate may currently be underestimated.

7.3 Future work

My work in the Muğla basin shows that there are likely many unmapped active faults in western Turkey. Whilst the largest active faults appear to be mapped (*Emre et al.*, 2018), many smaller faults up to 5 km long have not. Understanding the behaviour of a single fault requires understanding the behaviour of the surrounding fault network (*Cowie et al.*, 2012), and the first step in doing this is identifying those surrounding structures. As I have shown, this can be undertaken in the field, or using high resolution DEMs and satellite imagery, at relatively low cost. Whilst it is likely impossible to identify all structures, as faults can be blind, or produce small surface offsets which are not preserved, high resolution active fault mapping is key and can be produced from existing data.

To understand why variable slip rate occurs requires information on fault slip rates from as many faults in a network as possible. A project in Italy has determined Holocene slip rates on a number of faults in the Italian Apennines (*Cowie et al.*, 2017), and further work is under way, aiming to sample the most of the major faults in the region. Analysis of the resultant data set will provide insight into where and how variable slip rate occurs in the Apennines at the whole network scale. Whilst conceptually, taking the same approach in western Turkey would provide a wealth of information and allow detailed comparison between two extending regions, the variable lithology of western Turkey means this blanket approach can not be taken, as many of the faults, including many major faults, are not in carbonate rocks so can't be sampled for ^{36}Cl dating. This means that in order to create a similar study in western Turkey, other Quaternary dating techniques and morphological analyses are required. Combining multiple techniques, such as: paleoseismic trenching and geomorphological dating (*DuRoss et al.*, 2020), stream network analyses, long profile analyses of streams and geological mapping (*Boulton and Whittaker*, 2009), and using mutliple different cosmogenic isotopes and radiocarbon to date offeset features (*Rizza et al.*, 2019), can reduce uncertainty in slip rate estimates as well as provide an indication of slip rate variability through time. Regarding the Muğla-Yatağan basin in particular, it would be useful to undertake paleoseismic trenching to determine if the three major faults rupture synchronously, because if they do it would result in a much larger earthquake than modelled in my seismic hazard analysis. It would also be useful to assess the Quatenary slip rate using the

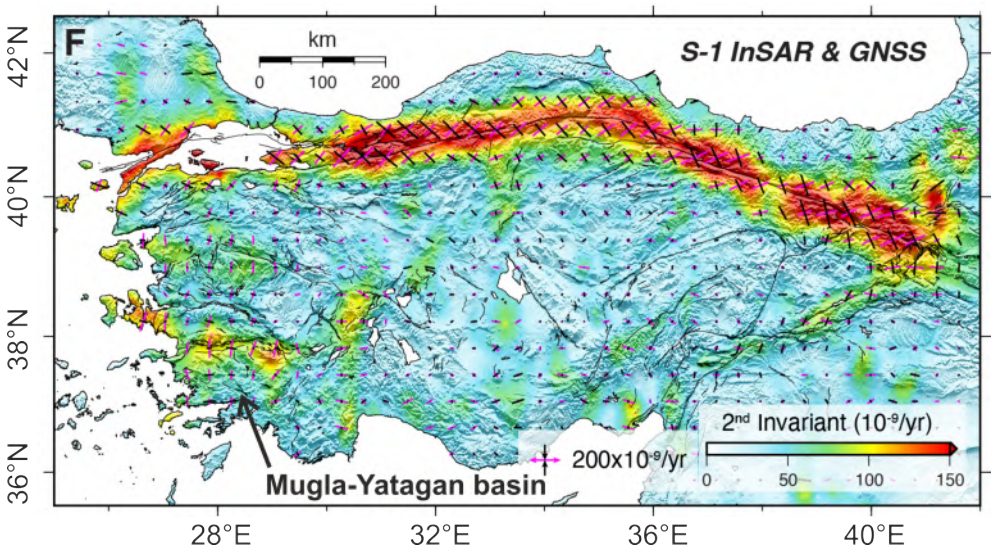

Figure 7.7: Map of second invariant of the strain rate tensor, essentially the magnitude of strain. Black and magenta bars represent contractional and extensional principal strain rates, respectively. Figure after *Weiss et al.* (2020).

topography as a proxy for uplift as *Kent et al.* (2016) did in the Gediz Graben to the north. *Akyüz et al.* (2018) have trenched and analysed the topography of the Yatağan fault, however results have not yet been published. The combination of trench ages (*Akyüz et al.*, 2018), archeoseismological ages (*Karabacak*, 2016) and elapsed time ages (Chapter 4) should result in a well defined estimate of the timing of the most recent earthquake on the Yatağan fault. The ages from the trench could be used as prior information when inverting the ^{36}Cl fault scarp data, which may reduce uncertainties in the posterior slip history distribution.

Comparison of geodetic and Quaternary slip rates could be much improved in the grabens of western Turkey. Velocity models from joint inversion of InSAR and GNSS models by *Weiss et al.* (2020) provide a more accurate model with greater spatial coverage than the inverting for GNSS data alone, or producing simple profiles through GNSS data as I did in Chapter 5. Comparison between Quaternary slip rates and this novel high resolution velocity map from *Weiss et al.* (2020), shown in Figure 7.7, may provide greater insight into spatio-temporal variation in strain accommodation across western Turkey, though locally anthropogenic subsidence due to water extraction and the large topographic steps can be an issue (*Weiss et al.*, 2020).

Another added complexity in western Turkey is that some of the major extensional faults are offshore, such as those in the Gulf of Gokova (*Uluğ et al.*, 2005, *Tur et al.*, 2015), making many methods for determining Quaternary slip rate impossible, however the opportunity to use and collect high resolution seismic imagery of an actively extending fault network, which also has an onshore expression, presents numerous exciting opportunities to combine geophysical, geological, Quaternary and geodetic techniques.

The Gulf of Corinth, Greece, is a similar larger extending region where this multi-disciplinary approach can be taken, as shown with the wealth of data and studies in the area, including cosmogenic fault scarp analysis (*Benedetti et al.*, 2002, 2003, *Mechernich et al.*, 2018) as well as geophysical, geological and other Quaternary studies (*Jackson et al.*, 1982, *Zygouri et al.*, 2008, *Bell et al.*, 2008, *Gawthorpe and Leeder*, 2008, *Robertson et al.*, 2020).

An opposing but equally valid approach that would provide insight into how faults are working is by conducting a much more intense study of a single fault. On all the faults I have worked on, there is no information on their geometry at depth. The geometry could be determined either via geophysical surveys, or by the use of seismology if that fault has been recently active. Reflection seismology combined with dated core from the basin sediments could provide information on along strike variation in slip rates over much longer time scales.

7.4 Wider implications of thesis findings

One clear implication of my work is that to truly understand fault behaviour, either in terms of geodynamics or seismic hazard, multi-disciplinary studies which use data covering different time frames are required. Further more, faults must be considered as entities that are part of a larger network of faults, which are forming in a heterogeneous medium. Whilst this complexity may appear daunting, my work suggests that the solution is more data. In Chapter 6, my comparison of geodetic and Quaternary deformation rates clearly shows a lack of Quaternary slip rates within the relatively small region I focus on, though the same is true globally. This is partly down to the relatively time and labour intensive work which is generally required to produce Quaternary slip rates, however if geodetic and Quaternary rates are similar as I found in Chapter 6, then Quaternary slip rates can be estimated with confidence from geodetic data, which is less labour intensive to cover a large area. Another implication of my work on ^{36}Cl fault scarp and footwall analysis is that if all limestone bedrock fault scarps have been preserved from a similar time, then an average Holocene slip rate can be determined using only the geometry of the fault scarp and the footwall and hangingwall slopes. This therefore means that Quaternary slip rates could be quickly determined for any limestone fault scarp at significantly reduced costs, and on faults that may otherwise inappropriate to sample. Whilst this kind of study has been undertaken in central Italy (*Roberts and Michetti*, 2004), I have now shown that this could also be applied to western Turkey, and possibly any other similar setting. If a concerted effort was made to do this on all possible faults in western Turkey, the resultant map of Quaternary fault slip rates could provide insight into the geodynamics and seismic hazard of the region.

My work on the reliability of ^{36}Cl fault scarp analysis has wider implications for

how new Quaternary dating methods are developed. ^{36}Cl fault scarp analysis has been in use since *Zreda and Noller* (1998), however it wasn't until *Schlagenhauf et al.* (2011) that a reasonable attempt was made to determine if the method was reliable, and until this thesis that a statistically rigorous comparison was done. Slip rates from ^{36}Cl have previously been challenged (*Kastelic et al.*, 2017), and whist this study was flawed because measurement sites were located in clearly unstable areas, and it did not account for the interaction of the authors of the study with the slope they were measuring, it is hard to refute similar arguments without studies such as the one I undertook in Chapter 4. For developing new Quaternary methods, it would seem that by undertaking rigorous testing, including checking the repeatability of measurements similar to Chapter 4, at a significantly earlier stage, the method could be better utilised from the start.

7.5 Conclusion

In this thesis I have improved ^{36}Cl fault scarp analysis methodology, and determined that slip rates calculated using this method are robust. I have determined Holocene slip rates for two faults in the Italian Apennines, and determined the first Quaternary slip rates for the three major faults in the Muğla-Yatağan basin, western Turkey. Finally, I have highlighted opportunities for future research based on the work of myself and others.

References

Abrahamson, N. A., W. J. Silva, and R. Kamai (2014), Summary of the ASK14 ground motion relation for active crustal regions, *Earthquake Spectra*, *30*(3), 1025–1055. 6.3.2

Ackermann, R. V., R. W. Schlische, and M. O. Withjack (2001), The geometric and statistical evolution of normal fault systems: an experimental study of the effects of mechanical layer thickness on scaling laws, *Journal of Structural Geology*, *23*(11), 1803–1819. 5.3.4

AFAD (2017), Report of 21/07/2017 Mw=6.5 Bodrum Offshore Earthquake., *Disaster and Emergency Management Authority Presidential of Earthquake Department of Turkey, https://deprem.afad.gov.tr/downloadDocument?id=1549.* 6.3.2, 6.5.1

Akaike, H. (1974), A new look at the statistical identification model, *IEEE Transactions on Automatic Control*, *19*, 716. 2.2.3

Akar, N., D. Tikhomirov, a. zkaymak, S. Ivy-Ochs, V. Alfimov, H. Szbilir, B. Uzel, and C. Schlchter (2012), 36cl exposure dating of paleoearthquakes in the Eastern Mediterranean: First results from the western Anatolian extensional province, Manisa fault zone, Turkey, *Geological Society of America Bulletin*, *124*(11-12), 1724–1735. 2.2.1, 2.1, 2.2.2, 2.7, 4.2, 4.3, 5.3

Akbaş, B., N. Akdeniz, A. Aksay, İ. Altun, V. Balcı, E. Bilginer, T. Bilgiç, M. Duru, T. Ercan, İ. Gedik, et al. (2011), diğerleri, Türkiye Jeoloji Haritası, *Maden Tetkik ve Arama Genel Müdürlüğü Yayını, Ankara, Türkiye.* 5.5

Akbaş, B., N. Akdeniz, A. Aksay, İ. Altun, V. Balcı, E. Bilginer, T. Bilgiç, M. Duru, T. Ercan, İ. Gedik, et al. (2017), Geological map of Turkey, *MTA (General Directorate of Mineral Research and Exploration of Turkey) Publications, Ankara.* 6.2, 6.3.2, 6.6, 6.9

Akkar, S., T. Azak, T. Çan, U. Çeken, M. D. Tümsa, T. Duman, M. Erdik, S. Ergintav, F. Kadirioğlu, D. Kalafat, et al. (2018), Evolution of seismic hazard maps in Turkey, *Bulletin of Earthquake Engineering*, *16*(8), 3197–3228. 6.5.1

Aktug, B., J. Nocquet, A. Cingöz, B. Parsons, Y. Erkan, P. England, O. Lenk,

M. Gürdal, A. Kilicoglu, H. Akdeniz, et al. (2009), Deformation of western Turkey from a combination of permanent and campaign GPS data: Limits to block-like behavior, *Journal of Geophysical Research: Solid Earth*, *114*(B10). 1.3.2, 5.2.1, 5.1, 5.2.1, 5.26, 6.3.1, 6.1, 6.2, 6.7

Akyuz, H., R. Hartleb, A. Barka, E. Altunel, G. Sunal, B. Meyer, and v. R. Armijo (2002), Surface rupture and slip distribution of the 12 November 1999 Duzce earthquake (m 7.1), North Anatolian fault, Bolu, Turkey, *Bulletin of the Seismological Society of America*, *92*(1), 61–66. 1.4, 7.2.3

Akyüz, H. S., E. Kırkan, M. Basmenji, E. Aksoy, A. D. Akyüz, G. Uçarkuş, N. Yakupoğlu, C. Zabcı, et al. (2018), Paleoseismological and Morphotectonical Characteristics of Active Faults in the Vicinity of Muğla Area (SW Turkey), in *Conference of the Arabian Journal of Geosciences*, pp. 253–256, Springer. 7.3

Alçiçek, H. (2010), Stratigraphic correlation of the Neogene basins in southwestern Anatolia: regional palaeogeographical, palaeoclimatic and tectonic implications, *Palaeogeography, Palaeoclimatology, Palaeoecology*, *291*(3-4), 297–318. 5.2.2, 5.4

Allen, T. I., and D. J. Wald (2007), Topographic slope as a proxy for seismic site-conditions (VS30) and amplification around the globe, *Tech. rep.*, Geological Survey (US). 6.5.1

Altunel, E., M. Meghraoui, V. Karabacak, S. H. Akyüz, M. Ferry, Ç. Yalçıner, and M. Munschy (2009), Archaeological sites (tell and road) offset by the dead sea fault in the Amik Basin, southern Turkey, *Geophysical Journal International*, *179*(3), 1313–1329. 1.1.5

Ambraseys, N. (2009), *Earthquakes in the Mediterranean and Middle East: a multidisciplinary study of seismicity up to 1900*, Cambridge University Press. 1.1.1, 1.1.5, 1.3.2

Amey, R., A. Hooper, and R. Walters (2018), A Bayesian method for incorporating self-similarity into earthquake slip inversions, *Journal of Geophysical Research: Solid Earth*, *123*(7), 6052–6071. 1.1.4, 5.3.2

Amey, R., A. Hooper, and Y. Moshishita (2019), Going to any lengths: solving for fault size and fractal slip for the 2016, Mw 6.2 Central Tottori Earthquake, Japan,

using a trans-dimensional inversion scheme, *Journal of Geophysical Research: Solid Earth*. 1.1.4

Anderson, H., and J. Jackson (1987), Active tectonics of the Adriatic region, *Geophysical Journal International*, *91*(3), 937–983. 1.3.1

Anderson, J. G., G. P. Biasi, and S. G. Wesnousky (2017), Fault-scaling relationships depend on the average fault-slip rate, *Bulletin of the Seismological Society of America*, *107*(6), 2561–2577. 7.2.3

Atalay, Z. (1980), Muğla-yatağan ve yakın dolayı karasal Neojen'inin stratigrafi araştırması, *TJK Bülteni*, *23*(1), 93–99. 5.2.2

Balco, G. (2017), Production rate calculations for cosmic-ray-muon-produced 10Be and 26Al benchmarked against geological calibration data, *Quaternary Geochronology*, *39*, 150–173. 2.2.3

Bao, H., J.-P. Ampuero, L. Meng, E. J. Fielding, C. Liang, C. W. Milliner, T. Feng, and H. Huang (2019), Early and persistent supershear rupture of the 2018 magnitude 7.5 Palu earthquake, *Nature Geoscience DOI*, *10*. 1.1.3

Barbot, S., Y. Hamiel, and Y. Fialko (2008), Space geodetic investigation of the coseismic and postseismic deformation due to the 2003 Mw7. 2 Altai earthquake: Implications for the local lithospheric rheology, *Journal of Geophysical Research: Solid Earth*, *113*(B3). 1.1.5

Barka, A., H. Akyuz, and K. I. Saroglu F, Emre O (1996), Güneybat anadolunun aktif faylar ve kireçta fay evlerinin incelenmesi (Investigations of active faults and limestone scarps in SW anatolia), *TUBITAK*, *YDABCAG-237/G*. 5.2.2

Barka, A., H. Akyuz, E. Altunel, G. Sunal, Z. Cakir, A. Dikbas, B. Yerli, R. Armijo, B. Meyer, J. De Chabalier, et al. (2002), The surface rupture and slip distribution of the 17 August 1999 Izmit earthquake (M 7.4), North Anatolian fault, *Bulletin of the Seismological Society of America*, *92*(1), 43–60. 1.1.3, 1.4, 7.2.3

Baumont, D., F. Courboulex, O. Scotti, N. S. Melis, and G. Stavrakakis (2002), Slip distribution of the Mw 5.9, 1999 Athens earthquake inverted from regional seismological data, *Geophysical research letters*, *29*(15), 15–1. 1.1.4

Bayrak, Y., and E. Bayrak (2012), An evaluation of earthquake hazard potential

for different regions in Western Anatolia using the historical and instrumental earthquake data, *Pure and applied geophysics*, *169*(10), 1859–1873. 5.2.2

Bayrak, Y., and T. Türker (2016), The determination of earthquake hazard parameters deduced from Bayesian approach for different seismic source regions of Western Anatolia, *Pure and Applied Geophysics*, *173*(1), 205–220. 5.2.2

Bayrak, Y., S. Öztürk, G. C. Koravos, G. Leventakis, and T. Tsapanos (2008), Seismicity assessment for the different regions in and around Turkey based on instrumental data: Gumbel first asymptotic distribution and Gutenberg-Richter cumulative frequency law, *Natural Hazards and Earth System Sciences*, *8*(1), 109–122. 5.2.2

Beck, J., S. Wolfers, and G. P. Roberts (2018), Bayesian earthquake dating and seismic hazard assessment using chlorine-36 measurements (BED v1). 2.2.3, 2.14, 3.3, 4.2, 4.6.1, 7.2, 7.2

Becker-Platen, J. D. (1970), Lithostratigraphische Untersuchungen im Känozoikom-südwest-Anatoliens (Türkei).-(Känozoikum und Braunkohlen der Türkei. 2.). 5.2.2

Bell, R. E., L. C. McNeill, J. M. Bull, and T. J. Henstock (2008), Evolution of the offshore western Gulf of Corinth, *Geological Society of America Bulletin*, *120*(1-2), 156–178. 7.3

Bellahsen, N., and J. M. Daniel (2005), Fault reactivation control on normal fault growth: an experimental study, *Journal of Structural Geology*, *27*(4), 769–780. 6.6

Bendle, J. M., A. P. Palmer, V. R. Thorndycraft, and I. P. Matthews (2017), High-resolution chronology for deglaciation of the Patagonian Ice Sheet at Lago Buenos Aires (46.5 S) revealed through varve chronology and Bayesian age modelling, *Quaternary Science Reviews*, *177*, 314–339. 5.3.2

Benedetti, L., R. Finkel, D. Papanastassiou, G. King, R. Armijo, F. Ryerson, D. Farber, and F. Flerit (2002), Post-glacial slip history of the Sparta fault (Greece) determined by ^{36}Cl cosmogenic dating: evidence for non-periodic earthquakes, *Geophysical Research Letters*, *29*(8). 1.2.2, 2.2.1, 2.1, 2.2.3, 2.2.3, 2.8, 2.2.3, 2.2.3, 2.2.3, 3.2, 4.2, 7.2, 7.2, 7.3

Benedetti, L., R. Finkel, G. King, R. Armijo, D. Papanastassiou, F. Ryerson, F. Flerit, D. Farber, and G. Stavrakakis (2003), Motion on the Kaparelli fault (Greece) prior to the 1981 earthquake sequence determined from 36cl cosmogenic dating, *Terra Nova*, *15*(2), 118–124. 2.2.1, 2.1, 2.2.2, 2.5, 2.2.3, 2.9, 2.2.3, 2.2.3, 3.2, 4.6.1, 5.3.4, 7.2, 7.3

Benedetti, L., I. Manighetti, Y. Gaudemer, R. Finkel, J. Malavieille, K. Pou, M. Arnold, G. Aumatre, D. Bourls, and K. Keddadouche (2013), Earthquake synchrony and clustering on Fucino faults (Central Italy) as revealed from in situ ^{36}Cl exposure dating, *Journal of Geophysical Research: Solid Earth*, *118*(9), 4948–4974. 2.2.1, 2.1, 2.2.3, 4.2, 4.2, 4.1, 4.3, 4.5, 4.5.1, 4.6, 4.6.1, 4.6.2, 7.1

Berk Biryol, C., S. L. Beck, G. Zandt, and A. A. Özacar (2011), Segmented African lithosphere beneath the Anatolian region inferred from teleseismic p-wave tomography, *Geophysical Journal International*, *184*(3), 1037–1057. 5.2.1

Bezerra, F., D. Rossetti, R. Oliveira, W. Medeiros, B. B. Neves, F. Balsamo, F. Nogueira, E. Dantas, C. Andrades Filho, and A. Góes (2014), Neotectonic reactivation of shear zones and implications for faulting style and geometry in the continental margin of NE Brazil, *Tectonophysics*, *614*, 78–90. 6.6

Biasi, G. P., and S. G. Wesnousky (2016), Steps and gaps in ground ruptures: Empirical bounds on rupture propagation, *Bulletin of the Seismological Society of America*, *106*(3), 1110–1124. 6.6

Biemiller, J., and L. Lavier (2017), Earthquake supercycles as part of a spectrum of normal fault slip styles, *Journal of Geophysical Research: Solid Earth*, *122*(4), 3221–3240. 7.2.3

Biggs, J., R. Burgmann, J. T. Freymueller, Z. Lu, B. Parsons, I. Ryder, G. Schmalzle, and T. Wright (2009), The postseismic response to the 2002 M 7.9 Denali Fault earthquake: constraints from InSAR 2003–2005, *Geophysical Journal International*, *176*(2), 353–367. 1.1.5

Bodin, T., and M. Sambridge (2009), Seismic tomography with the reversible jump algorithm, *Geophysical Journal International*, *178*(3), 1411–1436. 2.2.3

Bolstad, W. M. (2009), *Understanding computational Bayesian statistics*, vol. 644,

John Wiley & Sons. 5.3.2

Bose, S., and S. Mitra (2010), Analog modeling of divergent and convergent transfer zones in listric normal fault systems, *AAPG bulletin*, *94*(9), 1425–1452. 6.6

Boulton, S. J., and A. C. Whittaker (2009), Quantifying the slip rates, spatial distribution and evolution of active normal faults from geomorphic analysis: Field examples from an oblique-extensional graben, southern Turkey, *Geomorphology*, *104*(3-4), 299–316. 1.1.5, 7.2.3, 7.3

Bozkurt, E. (2001), Neotectonics of Turkey–a synthesis, *Geodinamica acta*, *14*(1-3), 3–30. 5.2.1

Bozkurt, E., and S. K. Mittwede (2005), Introduction: evolution of continental extensional tectonics of western Turkey, *Geodinamica Acta*, *18*(3-4), 153–165. 5.2.1

Bozkurt, E., and L. R. Park (1994), Southern Menderes Massif: an incipient metamorphic core complex in western Anatolia, Turkey, *Journal of the Geological Society*, *151*(2), 213–216. 5.2.1

Bozkurt, E., and H. Sözbilir (2004), Tectonic evolution of the Gediz Graben: field evidence for an episodic, two-stage extension in western Turkey, *Geological Magazine*, *141*(1), 63–79. 5.2.1

Briggs, R. W., S. G. Wesnousky, J. N. Brune, M. D. Purvance, and S. A. Mahan (2013), Low footwall accelerations and variable surface rupture behavior on the Fort Sage Mountains fault, northeast California, *Bulletin of the Seismological Society of America*, *103*(1), 157–168. 1.1.5

Brodsky, E. E. (2019), The importance of studying small earthquakes, *Science*, *364*(6442), 736–737. 1.1.5

Brozzetti, F., P. Boncio, D. Cirillo, F. Ferrarini, R. de Nardis, A. Testa, F. Liberi, and G. Lavecchia (2019), High-resolution field mapping and analysis of the August–October 2016 coseismic surface faulting (central Italy earthquakes): Slip distribution, parameterization, and comparison with global earthquakes, *Tectonics*. 1.1.3, 3.4.1, 7.2.3

Bubeck, A., M. Wilkinson, G. P. Roberts, P. Cowie, K. McCaffrey, R. Phillips, and P. Sammonds (2015), The tectonic geomorphology of bedrock scarps on active

normal faults in the Italian Apennines mapped using combined ground penetrating radar and terrestrial laser scanning, *Geomorphology*, *237*, 38–51. 1.1.5, 2.2.1, 4.2, 4.3, 4.4.1, 4.3, 7.2, 7.3, 7.2.1

Budzikiewicz, H., and R. D. Grigsby (2006), Mass spectrometry and isotopes: a century of research and discussion, *Mass spectrometry reviews*, *25*(1), 146–157. 1.2.1

Bürgmann, R., and G. Dresen (2008), Rheology of the lower crust and upper mantle: Evidence from rock mechanics, geodesy, and field observations, *Annu. Rev. Earth Planet. Sci.*, *36*, 531–567. 1.1.2, 1.1

Burnham, K., and D. Anderson (2002), Model selection and multimodel inference: a practical information-theoretic approach, *Carroll, RJ & Ruppert, D.(1981). Prediction and the Power Transformation Family*. 2.2.3

Cakir, Z., A. M. Akoglu, S. Belabbes, S. Ergintav, and M. Meghraoui (2005), Creeping along the Ismetpasa section of the North Anatolian fault (Western Turkey): Rate and extent from InSAR, *Earth and Planetary Science Letters*, *238*(1-2), 225–234. 1.1.2

Carcaillet, J., I. Manighetti, C. Chauvel, A. Schlagenhauf, and J.-M. Nicole (2008), Identifying past earthquakes on an active normal fault (Magnola, Italy) from the chemical analysis of its exhumed carbonate fault plane, *Earth and Planetary Science Letters*, *271*(1-4), 145–158. 1.1.5

Cavalié, O., C. Lasserre, M.-P. Doin, G. Peltzer, J. Sun, X. Xu, and Z.-K. Shen (2008), Measurement of interseismic strain across the Haiyuan fault (Gansu, China), by InSAR, *Earth and Planetary Science Letters*, *275*(3-4), 246–257. 1.1.5

Chevalier, M.-L., J. Van der Woerd, P. Tapponnier, H. Li, F. J. Ryerson, and R. C. Finkel (2016), Late Quaternary slip-rate along the central Bangong-Chaxikang segment of the Karakorum fault, western Tibet, *Bulletin*, *128*(1-2), 284–314. 1.1.5

Chiaraluce, L., R. Di Stefano, E. Tinti, L. Scognamiglio, M. Michele, E. Casarotti, M. Cattaneo, P. De Gori, C. Chiarabba, G. Monachesi, et al. (2017), The 2016 central Italy seismic sequence: A first look at the mainshocks, aftershocks, and source models, *Seismological Research Letters*, *88*(3), 757–771. 1.1.5

Childs, C., R. P. Worthington, J. J. Walsh, and V. Roche (2019), Conjugate relay zones: geometry of displacement transfer between opposed-dipping normal faults, *Journal of Structural Geology*, *118*, 377–390. 6.6

Choi, J.-H., P. Edwards, K. Ko, and Y.-S. Kim (2016), Definition and classification of fault damage zones: A review and a new methodological approach, *Earth-Science Reviews*, *152*, 70–87. 1.7, 1.1.4

Civico, R., S. Pucci, F. Villani, L. Pizzimenti, P. M. De Martini, R. Nappi, and O. E. W. Group (2018), Surface ruptures following the 30 October 2016 M w 6.5 Norcia earthquake, central Italy, *Journal of Maps*, *14*(2), 151–160. 1.1.3

Codilean, A. T., H. Munack, T. J. Cohen, W. Saktura, A. G. Gray, and S. M. Mudd (2018), OCTOPUS: an open cosmogenic isotope and luminescence database. 7.2

Contreras, J., M. H. Anders, and C. H. Scholz (2000), Growth of a normal fault system: observations from the Lake Malawi basin of the east African rift, *Journal of Structural Geology*, *22*(2), 159–168. 1.1.5

Cooper, F. J., G. P. Roberts, and C. J. Underwood (2007), A comparison of 103–105 year uplift rates on the South Alkyonides Fault, central Greece: Holocene climate stability and the formation of coastal notches, *Geophysical Research Letters*, *34*(14). 1.1.5

Cowgill, E., R. D. Gold, C. Xuanhua, W. Xiao-Feng, J. R. Arrowsmith, and J. Southon (2009), Low Quaternary slip rate reconciles geodetic and geologic rates along the Altyn Tagh fault, northwestern Tibet, *Geology*, *37*(7), 647–650. 6.2, 6.5, 6.6

Cowie, P., S. Gupta, and N. Dawers (2008), Implications of fault array evolution for synrift depocentre development: insights from a numerical fault growth model, *Basin Research*, *12*(3-4), 241–261. 5.3.4

Cowie, P., C. Scholz, G. P. Roberts, J. F. Walker, and P. Steer (2013), Viscous roots of active seismogenic faults revealed by geologic slip rate variations, *Nature Geoscience*, *6*(12), 1036. 4.6.2

Cowie, P., R. Phillips, G. Roberts, K. McCaffrey, L. Zijerveld, L. Gregory, J. Faure Walker, L. Wedmore, T. Dunai, S. Binnie, et al. (2017), Orogen-scale uplift

drives episodic behaviour of earthquake faults, *Scientific Reports*. (document), 1.1.5, 2.2.3, 2.2.3, 2.12, 2.2.3, 2.13, 2.14, 2.2.3, 3.3, 3.1, 3.3.1, 3.4, 3.4, 3.6, 4.2, 4.1, 4.3, 4.4.2, 4.4.3, 4.6.2, 5.3, 5.3.2, 5.3.3, 7.2, 7.2, 7.2.1, 7.2.3, 7.2.3, 7.3, C4

Cowie, P. A., and G. P. Roberts (2001), Constraining slip rates and spacings for active normal faults, *Journal of Structural Geology*, *23*(12), 1901–1915. 4.6.3, 7.2.3

Cowie, P. A., G. P. Roberts, J. M. Bull, and F. Visini (2012), Relationships between fault geometry, slip rate variability and earthquake recurrence in extensional settings, *Geophysical Journal International*, *189*(1), 143–160. 5.3.4, 7.2.3, 7.2.3, 7.3

Daëron, M., L. Benedetti, P. Tapponnier, A. Sursock, and R. C. Finkel (2004), Constraints on the post 25-ka slip rate of the Yammoûneh fault (lebanon) using in situ cosmogenic 36cl dating of offset limestone-clast fans, *Earth and Planetary Science Letters*, *227*(1-2), 105–119. 1.2.1

D'agostino, N., R. Giuliani, M. Mattone, and L. Bonci (2001), Active crustal extension in the central Apennines (Italy) inferred from GPS measurements in the interval 19941999, *Geophysical Research Letters*, *28*(10), 2121–2124. 1.3.1

D'Agostino, N., S. Mantenuto, E. D'Anastasio, R. Giuliani, M. Mattone, S. Calcaterra, P. Gambino, and L. Bonci (2011), Evidence for localized active extension in the central Apennines (Italy) from global positioning system observations, *Geology*, *39*(4), 291–294. 1.3.1, 4.1, 4.3, 4.6.3

Davis, R., and O. A. Schaeffer (1955), Chlorine-36 in nature, *Annals of the New York Academy of Sciences*, *62*(5), 107–121, doi:10.1111/j.1749-6632.1955.tb35368.x. 1.2.1

De Martini, P. M., D. Pantosti, N. Palyvos, F. Lemeille, L. McNeill, and R. Collier (2004), Slip rates of the Aigion and Eliki faults from uplifted marine terraces, Corinth Gulf, Greece, *Comptes Rendus Geoscience*, *336*(4-5), 325–334. 1.1.5

Demircioğlu, M. B., K. Sesetyan, E. Durukal, and M. Erdik (2007), Assessment of earthquake hazard in Turkey, in *Proceedings of the 4th international conference on earthquake geotechnical engineering, Thessaloniki, Greece*. 5.2.2

Densmore, A. L., M. A. Ellis, and R. S. Anderson (1998), Landsliding and the evolution of normal-fault-bounded mountains, *Journal of geophysical research: solid*

earth, *103*(B7), 15,203–15,219. 7.2.1

Deschamps, A., Y. Gaudemer, and A. Cisternas (1982), The El Asnam, Algeria, earthquake of 10 october 1980: multiple-source mechanism determined from long-period records, *Bulletin of the Seismological Society of America*, *72*(4), 1111–1128. 1.1.5

Dewey, J. (1988), Extensional collapse of orogens, *Tectonics*, *7*(6), 1123–1139. 5.2.1

Doglioni, C., S. Agostini, M. Crespi, F. Innocenti, P. Manetti, F. Riguzzi, and Y. Savascin (2002), On the extension in western Anatolia and the Aegean Sea, *Journal of the Virtual Explorer*, *8*, 169–183. 1.3.2, 5.2.1

Dolan, J. F., and B. D. Haravitch (2014), How well do surface slip measurements track slip at depth in large strike-slip earthquakes? The importance of fault structural maturity in controlling on-fault slip versus off-fault surface deformation, *Earth and Planetary Science Letters*, *388*, 38–47. 7.2.3

Dolan, J. F., and B. J. Meade (2017), A comparison of geodetic and geologic rates prior to large strike-slip earthquakes: A diversity of earthquake-cycle behaviors?, *Geochemistry, Geophysics, Geosystems*, *18*(12), 4426–4436. 4.6.2, 6.2

Dolan, J. F., L. J. McAuliffe, E. J. Rhodes, S. F. McGill, and R. Zinke (2016), Extreme multi-millennial slip rate variations on the Garlock fault, California: Strain super-cycles, potentially time-variable fault strength, and implications for system-level earthquake occurrence, *Earth and Planetary Science Letters*, *446*, 123–136. 4.6.2, 7.2.3

Dunai, T. J. (2010), *Cosmogenic nuclides: principles, concepts and applications in the earth surface sciences*, Cambridge University Press. 1.2.1, 1.9, 1.2.1, 4.4.1, 5.3.3, 5.3.4

DuRoss, C. B., S. F. Personius, A. J. Crone, S. S. Olig, and W. R. Lund (2011), Integration of paleoseismic data from multiple sites to develop an objective earthquake chronology: Application to the Weber segment of the Wasatch Fault Zone, Utah, *Bulletin of the Seismological Society of America*, *101*(6), 2765–2781. 6.6

DuRoss, C. B., R. D. Gold, R. W. Briggs, J. E. Delano, D. A. Ostenaa, M. S.

Zellman, N. Cholewinski, S. J. Wittke, and S. A. Mahan (2020), Holocene earthquake history and slip rate of the southern Teton fault, Wyoming, USA, *Bulletin*, *132*(7-8), 1566–1586. 7.3

Elliott, J., R. Walters, and T. Wright (2016), The role of space-based observation in understanding and responding to active tectonics and earthquakes, *Nature communications*, *7*, 13,844. 1.1.4

Ellsworth, W. L., M. V. Matthews, R. M. Nadeau, S. P. Nishenko, P. A. Reasenberg, and R. W. Simpson (1999), A physically-based earthquake recurrence model for estimation of long-term earthquake probabilities, *US Geol. Surv. Open-File Rept. 99*, *522*, 23. 7.2.3

Emre, Ö., T. Y. Duman, S. Özalp, F. Şaroğlu, Ş. Olgun, H. Elmacı, and T. Can (2018), Active fault database of Turkey, *Bulletin of Earthquake Engineering*, *16*(8), 3229–3275. 1.14, 5.1, 5.2, 5.2.2, 5.3, 6.5.1, 6.6, 6.9, 7.3

England, P. (2003), The alignment of earthquake T-axes with the principal axes of geodetic strain in the Aegean region, *Turkish Journal of Earth Sciences*, *12*(1), 47–53. 5.2.1

England, P., and J. Jackson (2011), Uncharted seismic risk, *Nature Geoscience*, *4*(6), 348. 1.1.1

England, P., G. Houseman, and J.-M. Nocquet (2016), Constraints from GPS measurements on the dynamics of deformation in Anatolia and the Aegean, *Journal of Geophysical Research: Solid Earth*, *121*(12), 8888–8916. 1.3.2, 5.2.1

Ergin, M., M. Aktar, S. Özalaybey, M. C. Tapirdamaz, O. Selvi, and A. Tarancioglu (2009), A high-resolution aftershock seismicity image of the 2002 Sultandağı-çay earthquake (Mw= 6.2), Turkey, *Journal of seismology*, *13*(4), 633–646. 6.3.2

Eyidogan, H., Akıncı, O. Gundogdu, O. Polat, and B. Kaypak (1996), Investigation of recent seismicity of Gokova Basin), *TUBITAK, YDABAG-238/G*. 5.2.2

Faccenna, C., T. W. Becker, F. P. Lucente, L. Jolivet, and F. Rossetti (2001), History of subduction and back arc extension in the Central Mediterranean, *Geophysical Journal International*, *145*(3), 809–820. 1.12

Falcucci, E., S. Gori, M. Moro, G. Fubelli, M. Saroli, C. Chiarabba, and

F. Galadini (2015), Deep reaching versus vertically restricted quaternary normal faults: Implications on seismic potential assessment in tectonically active regions: Lessons from the middle Aterno valley fault system, central Italy, *Tectonophysics*, *651*, 186–198. 4.3, 4.2, 4.6.1

Fan, W., and P. M. Shearer (2016), Local near instantaneously dynamically triggered aftershocks of large earthquakes, *Science*, *353*(6304), 1133–1136. 6.6

Farbod, Y., E. Shabanian, O. Bellier, M. R. Abbassi, R. Braucher, L. Benedetti, D. Bourlès, and K. Hessami (2016), Spatial variations in late Quaternary slip rates along the Doruneh Fault System (Central Iran), *Tectonics*, *35*(2), 386–406. 7.2.3

Farolfi, G., and C. Del Ventisette (2017), Strain rates in the Alpine Mediterranean region: Insights from advanced techniques of data processing, *GPS solutions*, *21*(3), 1027–1036. 1.3.1

Faulkner, D., C. Jackson, R. Lunn, R. Schlische, Z. Shipton, C. Wibberley, and M. Withjack (2010), A review of recent developments concerning the structure, mechanics and fluid flow properties of fault zones, *Journal of Structural Geology*, *32*(11), 1557–1575. 1.1.4

Faure-Walker, J., G. P. Roberts, P. Cowie, I. Papanikolaou, A. Michetti, P. Sammonds, M. Wilkinson, K. McCaffrey, and R. Phillips (2012), Relationship between topography, rates of extension and mantle dynamics in the actively-extending Italian Apennines, *Earth and Planetary Science Letters*, *325*, 76–84. 1.3.1, 4.3, 4.6.2

Fisher, R. A. (1992), Statistical methods for research workers, in *Breakthroughs in statistics*, pp. 66–70, Springer. 3.3.1

Fossen, H., and A. Rotevatn (2016), Fault linkage and relay structures in extensional settings, a review, *Earth-Science Reviews*, *154*, 14–28. 4.6.1

Frankel, K. L., K. S. Brantley, J. F. Dolan, R. C. Finkel, R. E. Klinger, J. R. Knott, M. N. Machette, L. A. Owen, F. M. Phillips, J. L. Slate, et al. (2007), Cosmogenic 10Be and 36Cl geochronology of offset alluvial fans along the northern Death Valley fault zone: Implications for transient strain in the eastern California shear zone, *Journal of Geophysical Research: Solid Earth*, *112*(B6). 1.2.1, 7.2.3

Friedrich, A. M., B. P. Wernicke, N. A. Niemi, R. A. Bennett, and J. L. Davis (2003), Comparison of geodetic and geologic data from the Wasatch region, Utah, and implications for the spectral character of earth deformation at periods of 10 to 10 million years, *Journal of Geophysical Research: Solid Earth*, *108*(B4). 7.2.3

Galadini, F., and P. Galli (2000), Active tectonics in the central Apennines (Italy)–input data for seismic hazard assessment, *Natural Hazards*, *22*(3), 225–268. 4.3

Galadini, F., P. Messina, B. Giaccio, and A. Sposato (2003), Early uplift history of the Abruzzi Apennines (central Italy): available geomorphological constraints, *Quaternary International*, *101*, 125–135. 4.6.1

Galli, P., F. Galadini, and D. Pantosti (2008), Twenty years of paleoseismology in Italy, *Earth-Science Reviews*, *88*(1-2), 89–117. 1.1.5

Gawthorpe, R., and M. Leeder (2008), Tectono-sedimentary evolution of active extensional basins, *Basin Research*, *12*(3-4), 195–218. 5.3.4, 7.3

Gawthorpe, R. L., C. A.-L. Jackson, M. J. Young, I. R. Sharp, A. R. Moustafa, and C. W. Leppard (2003), Normal fault growth, displacement localisation and the evolution of normal fault populations: the Hammam Faraun fault block, suez rift, egypt, *Journal of Structural Geology*, *25*(6), 883–895. 5.3.4

Giaccio, B., F. Galadini, A. Sposato, P. Messina, M. Moro, M. Zreda, A. Cittadini, S. Salvi, and A. Todero (2003), Image processing and roughness analysis of exposed bedrock fault planes as a tool for paleoseismological analysis: results from the Campo Felice fault (central Apennines, Italy), *Geomorphology*, *49*(3-4), 281–301. 1.1.5, 4.3

Giraudi, C. (2012), The Campo Felice late Pleistocene glaciation (Apennines, central Italy), *Journal of Quaternary Science*, *27*(4), 432–440. 4.3

Giraudi, C., G. Bodrato, M. R. Lucchi, N. Cipriani, I. M. Villa, B. Giaccio, and G. M. Zuppi (2011), Middle and late Pleistocene glaciations in the Campo Felice Basin (central Apennines, Italy), *Quaternary Research*, *75*(1), 219–230. 4.3

Gold, R. D., R. W. Briggs, A. J. Crone, and C. B. DuRoss (2017), Refining fault slip rates using multiple displaced terrace risersAn example from the Honey Lake

fault, NE California, USA, *Earth and Planetary Science Letters*, *477*, 134–146. 1.1.5, 7.2.3

Goldsworthy, M., and J. Jackson (2000), Active normal fault evolution in Greece revealed by geomorphology and drainage patterns, *Journal of the Geological Society*, *157*(5), 967–981. 1.1.3, 1.6, 4.3

Goldsworthy, M., and J. Jackson (2001), Migration of activity within normal fault systems: examples from the Quaternary of mainland Greece, *Journal of Structural Geology*, *23*(2-3), 489–506. 5.3.4

Gosse, J. C., and F. M. Phillips (2001), Terrestrial in situ cosmogenic nuclides: theory and application, *Quaternary Science Reviews*, *20*(14), 1475–1560. 1.2.1, 1.2.1, 1.2.2

Green, P. J. (1995), Reversible jump Markov chain Monte Carlo computation and Bayesian model determination, *Biometrika*, *82*(4), 711–732. 2.2.3

Gürer, Ö. F., E. Sanğu, M. Özburan, A. Gürbüz, and N. Sarica-Filoreau (2013), Complex basin evolution in the Gökova gulf region: implications on the Late Cenozoic tectonics of southwest Turkey, *International Journal of Earth Sciences*, *102*(8), 2199–2221. 5.2.2, 5.2.2, 5.4, 5.3.4, 6.5, 6.6

Haeussler, P. J., D. P. Schwartz, T. E. Dawson, H. D. Stenner, J. J. Lienkaemper, B. Sherrod, F. R. Cinti, P. Montone, P. A. Craw, A. J. Crone, et al. (2004), Surface rupture and slip distribution of the Denali and Totschunda faults in the 3 November 2002 M 7.9 earthquake, Alaska, *Bulletin of the Seismological Society of America*, *94*(6B), S23–S52. 1.1.3, 7.2.3

Hamblin, W. (1976), Patterns of displacement along the Wasatch fault, *Geology*, *4*(10), 619–622. 7.2.1

Hamling, I. J., S. Hreinsdóttir, K. Clark, J. Elliott, C. Liang, E. Fielding, N. Litchfield, P. Villamor, L. Wallace, T. J. Wright, et al. (2017), Complex multifault rupture during the 2016 Mw 7.8 Kaikōura earthquake, New Zealand, *Science*, *356*(6334), eaam7194. 1.1.3

Hastings, W. K. (1970), Monte Carlo sampling methods using Markov chains and their applications. 2.2.3

He, H., Z. Wei, and A. Densmore (2016), Quantitative morphology of bedrock fault surfaces and identification of paleo-earthquakes, *Tectonophysics*, *693*, 22–31. 1.1.5

Hetzel, R., U. Ring, C. Akal, and M. Troesch (1995), Miocene NNE-directed extensional unroofing in the Menderes Massif, southwestern Turkey, *Journal of the Geological Society*, *152*(4), 639–654. 5.2.1

Hirth, G., and D. Kohlstedt (2003), Rheology of the upper mantle and the mantle wedge: A view from the experimentalists, *Inside the subduction Factory*, pp. 83–105. 1.1.2

Howell, A., J. Jackson, A. Copley, D. McKenzie, and E. Nissen (2017), Subduction and vertical coastal motions in the eastern Mediterranean, *Geophysical Journal International*, *211*(1), 593–620. (document), 5.3.4, 5.26, 6.3.1, 6.1, 6.5, 6.5, 6.7, 6.6

Hurst, M. D., S. M. Mudd, K. Yoo, M. Attal, and R. Walcott (2013), Influence of lithology on hillslope morphology and response to tectonic forcing in the northern Sierra Nevada of California, *Journal of Geophysical Research: Earth Surface*, *118*(2), 832–851. 7.2.1

Hussain, E., A. Hooper, T. J. Wright, R. J. Walters, and D. P. Bekaert (2016), Interseismic strain accumulation across the central North Anatolian Fault from iteratively unwrapped InSAR measurements, *Journal of Geophysical Research: Solid Earth*, *121*(12), 9000–9019. 1.1.5

Inaner, H., E. Nakoman, and A. Karayigit (2008), Coal resource estimation in the Bayir field, Yatagan-Mugla, SW Turkey, *Energy Sources, Part A*, *30*(11), 1005–1015. 5.2.2

İnci, U. (1984), Demirci ve Burhaniye bitümlü şeyllerinin stratigrafisi ve organik özellikleri, *Geological Society of Turkey Bulletin*, *5*, 27–40. 1.3.2, 5.2.1

Isik, V., O. Tekeli, and G. Seyitoglu (2004), The 40Ar/39Ar age of extensional ductile deformation and granitoid intrusion in the northern Menderes core complex: implications for the initiation of extensional tectonics in western Turkey, *Journal of Asian Earth Sciences*, *23*(4), 555–566. 5.2.1

Jackson, J. (2001), Living with earthquakes: know your faults, *Journal of Earthquake Engineering*, *5*(spec01), 5–123. 1.1.2

Jackson, J. (2002), Strength of the continental lithosphere: time to abandon the jelly sandwich?, *GSA today*, *12*, 4–10. 1.1.2

Jackson, J., and D. McKenzie (1983), The geometrical evolution of normal fault systems, *Journal of Structural Geology*, *5*(5), 471–482. 6.3.2

Jackson, J., J. Gagnepain, G. Houseman, G. King, P. Papadimitriou, C. Soufleris, and J. Virieux (1982), Seismicity, normal faulting, and the geomorphological development of the Gulf of Corinth (Greece): the Corinth earthquakes of February and March 1981, *Earth and Planetary Science Letters*, *57*(2), 377–397. 7.3

Jarvis, A., H. I. Reuter, A. Nelson, E. Guevara, et al. (2008), Hole-filled SRTM for the globe version 4, *available from the CGIAR-CSI SRTM 90m Database (http://srtm. csi. cgiar. org)*, *15*, 25–54. 5.1, 6.3.2

Jayaram, N., and J. W. Baker (2009), Correlation model for spatially distributed ground-motion intensities, *Earthquake Engineering & Structural Dynamics*, *38*(15), 1687–1708. 6.3.2

Jibson, R. W. (1996), Use of landslides for paleoseismic analysis, *Engineering geology*, *43*(4), 291–323. 1.1.5

Karabacak, V. (2016), Seismic damage in the Lagina sacred area on the Mugla Fault: a key point for the understanding of the obliquely situated faults of western Anatolia, *Journal of Seismology*, *20*(1), 277–289. 5.2.2, 5.3.4, 6.6, 7.3

Kastelic, V., P. Burrato, M. Carafa, and R. Basili (2017), Repeated surveys reveal nontectonic exposure of supposedly active normal faults in the central Apennines, Italy, *Journal of Geophysical Research: Earth Surface*. 7.4

Katsumata, A., and N. Kamaya (2003), Low-frequency continuous tremor around the Moho discontinuity away from volcanoes in the southwest Japan, *Geophysical Research Letters*, *30*(1), 20–1. 1.1.2

Kelsey, H. M., R. C. Witter, and E. Hemphill-Haley (2002), Plate-boundary earthquakes and tsunamis of the past 5500 yr, Sixes River estuary, southern Oregon, *GSA Bulletin*, *114*(3), 298–314. 1.1.5

Kent, E., S. Boulton, I. Stewart, A. Whittaker, and M. Alçiçek (2016), Geomorphic and geological constraints on the active normal faulting of the Gediz (Alaşehir)

Graben, Western Turkey, *Journal of the Geological Society*, *173*(4), 666–678. 7.2.1, 7.2.3, 7.3

Khajavi, N., A. Nicol, M. C. Quigley, and R. M. Langridge (2018), Temporal slip-rate stability and variations on the Hope Fault, New Zealand, during the late Quaternary, *Tectonophysics*, *738*, 112–123. 7.2.3

Kokkalas, S., S. Pavlides, I. Koukouvelas, A. Ganas, and L. Stamatopoulos (2007), Paleoseismicity of the Kaparelli fault (eastern Corinth Gulf): evidence for earthquake recurrence and fault behavior, *BOLLETTINO-SOCIETA GEOLOGICA ITALIANA*, *126*(2), 387. 2.2.2, 4.6.1, 7.2

Koukouvelas, I. K., V. Zygouri, G. A. Papadopoulos, and S. Verroios (2017), Holocene record of slip-predictable earthquakes on the Kenchreai Fault, Gulf of Corinth, Greece, *Journal of Structural Geology*, *94*, 258–274. 1.1.5

Kruskal, W. H., and W. A. Wallis (1952), Use of ranks in one-criterion variance analysis, *Journal of the American statistical Association*, *47*(260), 583–621. 3.3.1

Lal, D. (1991), Cosmic ray labeling of erosion surfaces: in situ nuclide production, *Earth and Planetary Science Letters*, *104*, 424–439. 2.9

Leya, I., H. Busemann, H. Baur, R. Wieler, M. Gloris, S. Neumann, R. Michel, F. Sudbrock, and U. Herpers (1998), Cross sections for the proton-induced production of He and Ne isotopes from magnesium, aluminum, and silicon, *Nuclear Instruments and Methods in Physics Research Section B: Beam Interactions with Materials and Atoms*, *145*(3), 449–458. 1.2.1

Li, S., J. Bedford, M. Moreno, W. D. Barnhart, M. Rosenau, and O. Oncken (2018), Spatiotemporal variation of mantle viscosity and the presence of cratonic mantle inferred from 8 years of postseismic deformation following the 2010 Maule, Chile, earthquake, *Geochemistry, Geophysics, Geosystems*, *19*(9), 3272–3285. 1.1.2

Lifton, N., T. Sato, and T. J. Dunai (2014), Scaling in situ cosmogenic nuclide production rates using analytical approximations to atmospheric cosmic-ray fluxes, *Earth and Planetary Science Letters*, *386*, 149–160. 2.2.3, 5.1, 5.3

Lifton, Z. M., J. Lee, K. L. Frankel, A. V. Newman, and J. M. Schroeder (2020), Quaternary slip rates on the White Mountains fault zone, eastern California:

Implications for comparing geologic to geodetic slip rates across the Walker Lane, *GSA Bulletin*. 6.2

Lindsey, E. O., R. Natsuaki, X. Xu, M. Shimada, M. Hashimoto, D. Melgar, and D. T. Sandwell (2015), Line-of-sight displacement from ALOS-2 interferometry: Mw 7.8 Gorkha Earthquake and Mw 7.3 aftershock, *Geophysical Research Letters*, *42*(16), 6655–6661. 1.1.3

Litchfield, N. J., B. Wyss, A. Christophersen, R. Thomas, K. Berryman, P. Henshaw, and P. Villamor (2013), *Guidelines for Compilation of Neotectonic Faults, Folds and Fault Sources: GEM Faulted Earth*, Institute of Geological and Nuclear Sciences Limited. 6.3.2

Malik, J. N., A. K. Sahoo, A. A. Shah, D. P. Shinde, N. Juyal, and A. K. Singhvi (2010), Paleoseismic evidence from trench investigation along Hajipur fault, Himalayan Frontal Thrust, NW Himalaya: implications of the faulting pattern on landscape evolution and seismic hazard, *Journal of structural geology*, *32*(3), 350–361. 1.1.5

Manighetti, I., E. Boucher, C. Chauvel, A. Schlagenhauf, and L. Benedetti (2010), Rare earth elements record past earthquakes on exhumed limestone fault planes, *Terra Nova*, *22*(6), 477–482. 1.1.5

Manighetti, I., C. Caulet, L. Barros, C. Perrin, F. Cappa, and Y. Gaudemer (2015), Generic along-strike segmentation of Afar normal faults, East africa: Implications on fault growth and stress heterogeneity on seismogenic fault planes, *Geochemistry, Geophysics, Geosystems*, *16*(2), 443–467. 4.6.3

Marrero, S. M., F. M. Phillips, B. Borchers, N. Lifton, R. Aumer, and G. Balco (2016), Cosmogenic nuclide systematics and the CRONUScalc program, *Quaternary Geochronology*, *31*, 160–187. 4.4.3, 5.1, 5.3.2, 5.3.3, 5.9, 7.5, C15, C16

McClusky, S., S. Balassanian, A. Barka, C. Demir, S. Ergintav, I. Georgiev, O. Gurkan, M. Hamburger, K. Hurst, H. Kahle, et al. (2000), Global Positioning System constraints on plate kinematics and dynamics in the eastern Mediterranean and Caucasus, *Journal of Geophysical Research: Solid Earth*, *105*(B3), 5695–5719. 5.2.1

McKenzie, D. (1978), Active tectonics of the Alpine-Himalayan belt: the Aegean Sea and surrounding regions, *Geophysical Journal International*, *55*(1), 217–254. 1.3.2, 5.2.1

McLeod, A. E., N. H. Dawers*, and J. R. Underhill (2000), The propagation and linkage of normal faults: insights from the Strathspey–Brent–Statfjord fault array, northern North Sea, *Basin Research*, *12*(3-4), 263–284. 1.1.3, 1.1.5, 4.6.3, 7.2.3

Mechernich, S., S. Schneiderwind, J. Mason, I. D. Papanikolaou, G. Deligiannakis, A. Pallikarakis, S. A. Binnie, T. J. Dunai, and K. Reicherter (2018), The seismic history of the Pisia fault (eastern Corinth rift, Greece) from fault plane weathering features and cosmogenic 36Cl dating, *Journal of Geophysical Research: Solid Earth*, *123*(5), 4266–4284. 2.2.1, 2.1, 2.2.3, 4.2, 4.6.1, 4.6.2, 7.3

Menges, C. M. (1990), Soils and geomorphic evolution of bedrock facets on a tectonically active mountain front, western Sangre de Cristo Mountains, New Mexico, *Geomorphology*, *3*(3-4), 301–332. 7.2.1

Metropolis, N., A. W. Rosenbluth, M. N. Rosenbluth, A. H. Teller, and E. Teller (1953), Equation of state calculations by fast computing machines, *The journal of chemical physics*, *21*(6), 1087–1092. 2.2.3

Middleton, T. A., R. T. Walker, B. Parsons, Q. Lei, Y. Zhou, and Z. Ren (2016), A major, intraplate, normal-faulting earthquake: The 1739 Yinchuan event in northern China, *Journal of Geophysical Research: Solid Earth*, *121*(1), 293–320. 1.1.2

Middleton, T. A., J. R. Elliott, E. J. Rhodes, S. Sherlock, R. T. Walker, W. Wang, J. Yu, and Y. Zhou (2017), Extension rates across the northern Shanxi Grabens, China, from Quaternary geology, seismicity and geodesy, *Geophysical Journal International*, *209*(2), 535–558. 6.6

Mitchell, S. G., A. Matmon, P. R. Bierman, Y. Enzel, M. Caffee, and D. Rizzo (2001), Displacement history of a limestone normal fault scarp, northern Israel, from cosmogenic ^{36}Cl, *Journal of Geophysical Research: Solid Earth*, *106*(B3), 4247–4264. 2.2.1, 2.1, 2.2.3, 2.2.3, 2.2.3, 7.2, 7.2

Mohadjer, S., T. A. Ehlers, R. Bendick, and S. G. Mutz (2017), Review of GPS and

Quaternary fault slip rates in the Himalaya-Tibet orogen, *Earth-Science Reviews*, *174*, 39–52. 6.6

Morley, C. (2017), The impact of multiple extension events, stress rotation and inherited fabrics on normal fault geometries and evolution in the Cenozoic rift basins of Thailand, *Geological Society, London, Special Publications*, *439*(1), 413–445. 5.3.4

Morley, C., C. Haranya, W. Phoosongsee, S. Pongwapee, A. Kornsawan, and N. Wonganan (2004), Activation of rift oblique and rift parallel pre-existing fabrics during extension and their effect on deformation style: examples from the rifts of Thailand, *Journal of Structural Geology*, *26*(10), 1803–1829. 6.6

Mörner, N.-A. (1996), Liquefaction and varve deformation as evidence of paleoseismic events and tsunamis. the autumn 10,430 BP case in Sweden, *Quaternary Science Reviews*, *15*(8-9), 939–948. 1.1.5

Mouslopoulou, V., D. Moraetis, L. Benedetti, V. Guillou, O. Bellier, and D. Hristopulos (2014), Normal faulting in the forearc of the Hellenic subduction margin: Paleoearthquake history and kinematics of the Spili Fault, Crete, Greece, *Journal of Structural Geology*, *66*, 298–308. 2.2.1, 2.2.3, 7.2

Mozafari, N., D. Tikhomirov, Ö. Sumer, Ç. Özkaymak, B. Uzel, S. Yeşilyurt, S. Ivy-Ochs, C. Vockenhuber, H. Sözbilir, and N. Akçar (2019a), Dating of active normal fault scarps in the Büyük Menderes Graben (western Anatolia) and its implications for seismic history, *Quaternary Science Reviews*, *220*, 111–123. 2.2.1, 2.2.2, 2.6, 5.3, 7.2

Mozafari, N., Ö. SÜMER, D. Tikhomirov, S. Ivy-Ochs, V. Alfimov, C. Vockenhuber, U. İNCİ, H. SÖZBİLİR, and N. Akcar (2019b), Holocene seismic activity of the Priene-Sazlı Fault revealed by cosmogenic 36 cl, Western Anatolia, Turkey, *Turkish Journal of Earth Sciences*, *28*(3). 2.2.1, 2.1, 5.3

MTA (2016), *1:500 000 Scale Geological Inventory Map Series of Turkey*, http://maps.mta.gov.tr/geological/500000-scale.php [accessed: 10/11/2016]. 6.1

Muller, R. A. (1977), Radioisotope dating with a cyclotron, *Science*, *196*(4289),

489–494. 1.2.1

Muller, R. N., and M. E. Hamilton (1992), A simple, effective method for determining the bulk density of stony soils, *Communications in soil science and plant analysis*, *23*(3-4), 313–319. 4.4.2

Myers, W. B., and W. B. Hamilton (1964), *Deformation Accompanging the Bebgen Lake Earthquake of August 17, 1959*, US Government Printing Office. 2.2.2

Nicol, A., J. Walsh, J. Watterson, and J. R. Underhill (1997), Displacement rates of normal faults, *Nature*, *390*(6656), 157. 1.1.5

Nicol, A., J. Walsh, K. Berryman, and S. Nodder (2005), Growth of a normal fault by the accumulation of slip over millions of years, *Journal of Structural Geology*, *27*(2), 327–342. 1.1.3, 1.3

Nissen, E., T. Maruyama, J. R. Arrowsmith, J. R. Elliott, A. K. Krishnan, M. E. Oskin, and S. Saripalli (2014), Coseismic fault zone deformation revealed with differential lidar: Examples from Japanese Mw 7 intraplate earthquakes, *Earth and Planetary Science Letters*, *405*, 244–256. 1.1.3

Nissen, E., J. Elliott, R. Sloan, T. Craig, G. Funning, A. Hutko, B. Parsons, and T. Wright (2016), Limitations of rupture forecasting exposed by instantaneously triggered earthquake doublet, *Nature Geoscience*, *9*(4), 330–336. 6.6

Nocquet, J.-M. (2012), Present-day kinematics of the Mediterranean: A comprehensive overview of gps results, *Tectonophysics*, *579*, 220–242. 1.12

Noda, A., T. TuZino, Y. Kanai, R. Furukawa, and J.-i. Uchida (2008), Paleoseismicity along the southern Kuril Trench deduced from submarine-fan turbidites, *Marine Geology*, *254*(1-2), 73–90. 1.1.5

Noriega, G. R., J. R. Arrowsmith, L. B. Grant, and J. J. Young (2006), Stream channel offset and late holocene slip rate of the San Andreas fault at the Van Matre ranch site, Carrizo Plain, California, *Bulletin of the Seismological Society of America*, *96*(1), 33–47. 1.1.5

Nyst, M., and W. Thatcher (2004), New constraints on the active tectonic deformation of the Aegean, *Journal of Geophysical Research: Solid Earth*, *109*(B11). 5.2.1

Okada, Y. (1985), Surface deformation due to shear and tensile faults in a half-space, *Bulletin of the seismological society of America*, *75*(4), 1135–1154. 6.5, 6.8

Pace, B., L. Peruzza, G. Lavecchia, and P. Boncio (2006), Layered seismogenic source model and probabilistic seismic-hazard analyses in central Italy, *Bulletin of the Seismological Society of America*, *96*(1), 107–132. 4.6.2

Pagani, M., D. Monelli, G. Weatherill, L. Danciu, H. Crowley, V. Silva, P. Henshaw, L. Butler, M. Nastasi, L. Panzeri, et al. (2014), OpenQuake engine: An open hazard (and risk) software for the global earthquake model, *Seismological Research Letters*, *85*(3), 692–702. 6.3.2

Palumbo, L., L. Benedetti, D. Bourles, A. Cinque, and R. Finkel (2004), Slip history of the Magnola fault (Apennines, Central Italy) from ^{36}Cl surface exposure dating: evidence for strong earthquakes over the Holocene, *Earth and Planetary Science Letters*, *225*(1), 163–176. 2.2.1, 2.1, 2.8, 2.2.3, 2.2.3, 2.2.3, 2.10, 3.3.2, 3.3, 3.4, 3.6, 4.1, 7.2

Papanikolaou, I. D., G. P. Roberts, and A. M. Michetti (2005), Fault scarps and deformation rates in Lazio–Abruzzo, Central Italy: Comparison between geological fault slip-rate and GPS data, *Tectonophysics*, *408*(1-4), 147–176. 1.1.5, 4.6.2

Patacca, E., R. Sartori, and P. Scandone (1990), Tyrrhenian basin and Apenninic arcs: kinematic relations since Late Tortonian times, *Mem. Soc. Geol. It.*, *45*, 425–451. 1.3.1

Payne, S. J., J. E. Zollweg, and D. W. Rodgers (2004), Stress triggering of conjugate normal faulting: Late aftershocks of the 1983 Ms 7.3 Borah Peak, Idaho, earthquake, *Bulletin of the Seismological Society of America*, *94*(3), 828–844. 6.6

Petit, C., B. Meyer, Y. Gunnell, M. Jolivet, V. San'Kov, V. Strak, and N. Gonga-Saholiariliva (2009), Height of faceted spurs, a proxy for determining long-term throw rates on normal faults: Evidence from the North Baikal Rift System, Siberia, *Tectonics*, *28*(6). 7.2.1

Phillips, F. M., M. G. Zreda, J. C. Gosse, J. Klein, E. B. Evenson, R. D. Hall, O. A. Chadwick, and P. Sharma (1997), Cosmogenic ^{36}Cl and ^{10}be ages of

Quaternary glacial and fluvial deposits of the Wind River Range, Wyoming, *Geological Society of America Bulletin*, *109*(11), 1453–1463. 1.2.1

Piccardi, L., Y. Gaudemer, P. Tapponnier, and M. Boccaletti (1999), Active oblique extension in the central Apennines (Italy): evidence from the Fucino region, *Geophysical Journal International*, *139*(2), 499–530. 1.1.5

Pollitz, F. F., R. Bürgmann, and P. Banerjee (2011), Geodetic slip model of the 2011 M9.0 Tohoku earthquake, *Geophysical Research Letters*, *38*(7). 1.1.4

Querol, X., A. Alastuey, F. Plana, A. Lopez-Soler, E. Tuncali, S. Toprak, F. Ocakoglu, and A. Koker (1999), Coal geology and coal quality of the Miocene Mugla basin, southwestern Anatolia, Turkey, *International Journal of Coal Geology*, *41*(4), 311–332. 5.2.2, 5.4

Ran, Y., L. Chen, J. Chen, H. Wang, G. Chen, J. Yin, X. Shi, C. Li, and X. Xu (2010), Paleoseismic evidence and repeat time of large earthquakes at three sites along the Longmenshan fault zone, *Tectonophysics*, *491*(1-4), 141–153. 1.1.5

Reid, H. F. (1910), The mechanics of the earthquake, *The California Earthquake of April 18, 1906, Report of the State Earthquake Investigation Commission*. 1.1.2

Reilinger, R., S. McClusky, P. Vernant, S. Lawrence, S. Ergintav, R. Cakmak, H. Ozener, F. Kadirov, I. Guliev, R. Stepanyan, et al. (2006), GPS constraints on continental deformation in the Africa-Arabia-Eurasia continental collision zone and implications for the dynamics of plate interactions, *Journal of Geophysical Research: Solid Earth*, *111*(B5). 5.2.1, 5.2.1

Reynolds, K., and A. Copley (2017), Seismological constraints on the down-dip shape of normal faults, *Geophysical Journal International*, *213*(1), 534–560, doi:10.1093/gji/ggx432. 1.1.4

Rhie, J., D. Dreger, R. Bürgmann, and B. Romanowicz (2007), Slip of the 2004 Sumatra–Andaman earthquake from joint inversion of long-period global seismic waveforms and GPS static offsets, *Bulletin of the Seismological Society of America*, *97*(1A), S115–S127. 1.1.4

Ring, U., and A. S. Collins (2005), U–Pb SIMS dating of synkinematic granites: timing of core-complex formation in the northern Anatolide belt of western Turkey,

Journal of the Geological Society, *162*(2), 289–298. 5.2.1

Rizza, M., K. Abdrakhmatov, R. Walker, R. Braucher, V. Guillou, A. Carr, G. Campbell, D. McKenzie, J. Jackson, G. Aumaître, et al. (2019), Rate of slip from multiple Quaternary dating methods and paleoseismic investigations along the Talas-Fergana Fault: Tectonic implications for the Tien Shan Range, *Tectonics*, *38*(7), 2477–2505. 7.3

Roberts, G. P., and A. M. Michetti (2004), Spatial and temporal variations in growth rates along active normal fault systems: an example from the Lazio–Abruzzo Apennines, central Italy, *Journal of Structural Geology*, *26*(2), 339–376. 1.1.5, 1.1.5, 1.3.1, 1.13, 3.2, 4.1, 4.3, 7.4

Roberts, G. P., A. M. Michetti, P. Cowie, N. C. Morewood, and I. Papanikolaou (2002), Fault slip-rate variations during crustal-scale strain localisation, central Italy, *Geophysical Research Letters*, *29*(8), 9–1. 4.6.3

Robertson, A., and M. Grasso (1995), Overview of the Late Tertiary–Recent tectonic and palaeo-environmental development of the Mediterranean region, *Terra Nova*, *7*(2), 114–127. 1.12

Robertson, J., G. P. Roberts, F. Iezzi, M. Meschis, D. Gheorghiu, D. Sahy, C. Bristow, and C. Sgambato (2020), Distributed normal faulting in the tip zone of the South Alkyonides Fault System, Gulf of Corinth, constrained using 36Cl exposure dating of Late-Quaternary wave-cut platforms, *Journal of Structural Geology*, p. 104063. 7.3

Rodrıguez-Pascua, M., J. Calvo, G. De Vicente, and D. Gómez-Gras (2000), Soft-sediment deformation structures interpreted as seismites in lacustrine sediments of the Prebetic Zone, SE Spain, and their potential use as indicators of earthquake magnitudes during the Late Miocene, *Sedimentary Geology*, *135*(1-4), 117–135. 1.1.5

Romano, F., A. Piatanesi, S. Lorito, and K. Hirata (2010), Slip distribution of the 2003 Tokachi-oki Mw 8.1 earthquake from joint inversion of tsunami waveforms and geodetic data, *Journal of Geophysical Research: Solid Earth*, *115*(B11). 1.1.4

Rotevatn, A., C. A.-L. Jackson, A. B. Tvedt, R. E. Bell, and I. Blækkan (2018),

How do normal faults grow?, *Journal of Structural Geology*. 1.1.3, 7.2.3

Rovida, A. N., M. Locati, R. D. CAMASSI, B. Lolli, and P. Gasperini (2016), CPTI15, the 2015 version of the Parametric Catalogue of Italian earthquakes. 4.3

Sahin, S., C. Yildirim, M. Akif Sarikaya, O. Tuysuz, S. Genc, M. Ersen Aksoy, and M. Ertekin Doksanalti (2016), Reconstruction of the earthquake history of limestone fault scarps in Knidos Fault Zone using in-situ Chlorine-36 exposure dating and "R" programming language, *18*, 13,608. 2.1

Salvi, S., F. Cinti, L. Colini, G. D'addezio, F. Doumaz, and E. Pettinelli (2003), Investigation of the active celano–l'aquila fault system, abruzzi (central apennines, italy) with combined ground-penetrating radar and palaeoseismic trenching, *Geophysical Journal International*, *155*(3), 805–818. 4.3

Sambridge, M., K. Gallagher, A. Jackson, and P. Rickwood (2006), Trans-dimensional inverse problems, model comparison and the evidence, *Geophysical Journal International*, *167*(2), 528–542. 2.2.3

Sarıkaya, M. A., M. Zreda, A. Çiner, and C. Zweck (2008), Cold and wet Last Glacial Maximum on Mount Sandıras, SW Turkey, inferred from cosmogenic dating and glacier modeling, *Quaternary Science Reviews*, *27*(7-8), 769–780. 5.3.4

Şaroğlu, F., Ö. Emre, and A. Boray (1987), Türkiyenin diri fayları ve depremsellikleri, *MTA. Rap*, *394*. 5.2.2

Sayil, N., and İ. Osmanşahin (2008), An investigation of seismicity for western Anatolia, *Natural Hazards*, *44*(1), 51–64. 5.2.2

Schimmelpfennig, I., L. Benedetti, R. Finkel, R. Pik, P.-H. Blard, D. Bourles, P. Burnard, and A. Williams (2009), Sources of in-situ 36Cl in basaltic rocks. Implications for calibration of production rates, *Quaternary Geochronology*, *4*(6), 441–461. 1.2.2

Schlagenhauf, A. (2009), Identification des forts séismes passés sur les failles normales actives de la région Lazio-Abruzzo (Italie Centrale) par'datations cosmogéniques'(^{36}Cl) de leurs escarpements, Ph.D. thesis, Grenoble 1. 2.2.1, 2.1, 4.2, 4.2, 4.1, 4.3, 4.2, 4.5, 4.6, 4.6.1, 7.1, 7.2

Schlagenhauf, A., Y. Gaudemer, L. Benedetti, I. Manighetti, L. Palumbo,

I. Schimmelpfennig, R. Finkel, and K. Pou (2010), Using in situ Chlorine-36 cosmonuclide to recover past earthquake histories on limestone normal fault scarps: a reappraisal of methodology and interpretations, *Geophysical Journal International*, *182*(1), 36, doi:10.1111/j.1365-246X.2010.04622.x. (document), 1.2.2, 2.2.1, 2.1, 2.2.3, 2.2.3, 2.2.3, 2.10, 2.2.3, 2.2.3, 3.2, 4.2, 4.4.3, 7.2, 7.2.1

Schlagenhauf, A., I. Manighetti, L. Benedetti, Y. Gaudemer, R. Finkel, J. Malavieille, and K. Pou (2011), Earthquake supercycles in central Italy, inferred from ^{36}Cl exposure dating, *Earth and Planetary Science Letters*, *307*(3), 487–500. 2.1, 2.2.1, 2.1, 2.2.3, 2.2.3, 2.2.3, 3.1, 3.2, 3.3, 3.3.2, 3.2, 3.3, 3.4, 3.6, 4.2, 4.1, 4.3, 4.6.1, 4.6.2, 5.3.4, 7.1, 7.2, 7.4

Searle, M. P., J. Elliott, R. Phillips, and S.-L. Chung (2011), Crustal–lithospheric structure and continental extrusion of Tibet, *Journal of the Geological Society*, *168*(3), 633–672. 1.1.5

Şengör, A., N. Görür, and F. Şaroğlu (1985), Strike-slip faulting and related basin formation in zones of tectonic escape: Turkey as a case study. 1.3.2, 5.2.1

Sesetyan, K., M. B. Demircioglu, T. Y. Duman, T. Can, S. Tekin, T. E. Azak, and Ö. Z. Fercan (2018), A probabilistic seismic hazard assessment for the Turkish territory part i: the area source model, *Bulletin of Earthquake Engineering*, *16*(8), 3367–3397. 6.5.1

Seyitoğlu, G., and B. Scott (1991), Late Cenozoic crustal extension and basin formation in west Turkey, *Geological Magazine*, *128*(2), 155–166. 5.2.1

Seyitoğlu, g., O. Tekeli, I. Çemen, Ş. ŞEN, and V. IŞIK (2002), The role of the flexural rotation/rolling hinge model in the tectonic evolution of the Alaşehir graben, western Turkey, *Geological Magazine*, *139*(1), 15–26. 5.2.1

Shen, Z.-K., D. D. Jackson, Y. Feng, M. Cline, M. Kim, P. Fang, and Y. Bock (1994), Postseismic deformation following the Landers earthquake, California, 28 June 1992, *Bulletin of the Seismological Society of America*, *84*(3), 780–791. 1.1.2

Shirzaei, M., and R. Bürgmann (2013), Time-dependent model of creep on the Hayward fault from joint inversion of 18 years of InSAR and surface creep data, *Journal of Geophysical Research: Solid Earth*, *118*(4), 1733–1746. 1.1.2

Simons, M., Y. Fialko, and L. Rivera (2002), Coseismic deformation from the 1999 M w 7.1 Hector Mine, California, earthquake as inferred from InSAR and GPS observations, *Bulletin of the Seismological Society of America*, *92*(4), 1390–1402. 1.1.3

Sintubin, M., and I. S. Stewart (2008), A logical methodology for archaeoseismology: A proof of concept at the archaeological site of Sagalassos, southwest Turkey, *Bulletin of the Seismological Society of America*, *98*(5), 2209–2230. 1.1.5

Sreejith, K., P. Sunil, R. Agrawal, A. P. Saji, D. Ramesh, and A. Rajawat (2016), Coseismic and early postseismic deformation due to the 25 April 2015, Mw 7.8 Gorkha, Nepal, earthquake from InSAR and GPS measurements, *Geophysical Research Letters*, *43*(7), 3160–3168. 1.1.5

Stein, R. S., and M. Lisowski (1983), The 1979 Homestead valley earthquake sequence, California: Control of aftershocks and postseismic deformation, *Journal of Geophysical Research: Solid Earth*, *88*(B8), 6477–6490. 1.1.2

Stewart, I. S., and L. Piccardi (2017), Seismic faults and sacred sanctuaries in Aegean antiquity, *Proceedings of the Geologists' Association*, *128*(5-6), 711–721. 1.1.5

Stone, J., G. Allan, L. Fifield, and R. Cresswell (1996), Cosmogenic chlorine-36 from calcium spallation, *Geochimica et Cosmochimica Acta*, *60*(4), 679–692. 5.1

Szeliga, W., T. I. Melbourne, M. M. Miller, and V. M. Santillan (2004), Southern Cascadia episodic slow earthquakes, *Geophysical Research Letters*, *31*(16). 1.1.2

Tan, O. (2013), The dense micro-earthquake activity at the boundary between the Anatolian and South Aegean microplates, *Journal of Geodynamics*, *65*, 199–217. 6.3.2

Tan, O., M. C. Tapirdamaz, and A. Yörük (2008), The earthquake catalogues for Turkey, *Turkish Journal of Earth Sciences*, *17*(2), 405–418. 1.1.5, 1.3.2

Tarquini, S., S. Vinci, M. Favalli, F. Doumaz, A. Fornaciai, and L. Nannipieri (2012), Release of a 10-m-resolution DEM for the Italian territory: Comparison with global-coverage DEMs and anaglyph-mode exploration via the web,

Computers & geosciences, *38*(1), 168–170. 4.2

Taylor, M., and A. Yin (2009), Active structures of the Himalayan-Tibetan orogen and their relationships to earthquake distribution, contemporary strain field, and Cenozoic volcanism, *Geosphere*, *5*(3), 199–214. 6.3.2

Tesson, J., and L. Benedetti (2019), Seismic history from in situ 36Cl cosmogenic nuclide data on limestone fault scarps using Bayesian reversible jump Markov chain Monte Carlo, *Quaternary Geochronology*, *52*, 1–20. 2.2.1, 2.2.3, 2.14, 3.3, 4.2, 7.2, 7.2

Tesson, J., B. Pace, L. Benedetti, F. Visini, M. Delli Rocioli, M. Arnold, G. Aumaître, D. Bourlès, and K. Keddadouche (2016), Seismic slip history of the Pizzalto fault (central Apennines, Italy) using in situ-produced 36Cl cosmic ray exposure dating and rare earth element concentrations, *Journal of Geophysical Research: Solid Earth*, *121*(3), 1983–2003. (document), 1.1.5, 2.2.1, 2.1, 2.2.3, 2.11, 2.2.3, 4.2, 4.1, 7.2

Thatcher, W. (2009), How the continents deform: The evidence from tectonic geodesy, *Annual Review of Earth and Planetary Sciences*, *37*. 6.6

Tikhomirov, D., N. M. Amiri, S. Ivy-Ochs, V. Alfimov, C. Vockenhuber, and N. Akçar (2019), Fault Scarp Dating Tool-a MATLAB code for fault scarp dating using in-situ chlorine-36 supplemented with datasets of Yavansu and Kalafat faults, *Data in Brief*, p. 104476. 2.2.3, 2.14

Tiryakioğlu, İ., M. Floyd, S. Erdoğan, E. Gülal, S. Ergintav, S. McClusky, and R. Reilinger (2013), GPS constraints on active deformation in the Isparta Angle region of SW Turkey, *Geophysical Journal International*, *195*(3), 1455–1463. 5.26, 6.3.1, 6.1, 6.2, 6.7

Tucker, G. E., S. W. McCoy, A. C. Whittaker, G. P. Roberts, S. T. Lancaster, and R. Phillips (2011), Geomorphic significance of postglacial bedrock scarps on normal-fault footwalls, *Journal of Geophysical Research: Earth Surface*, *116*(F1). (document), 2.2.1, 4.2, 4.3, 4.6.1, 5.3, 5.3.3, 5.3.4, 7.2.1, 7.2.1, 7.2.1, 7.6, 7.2.1, 7.2, 7.2.1

Tucker, G. E., D. Hobley, S. W. McCoy, and W. T. Struble (2020), Modeling the

shape and evolution of normal-fault facets, *Journal of Geophysical Research: Earth Surface*, *125*(3). 7.2.1

Tur, H., C. Yaltırak, İ. Elitez, and K. T. Sarıkavak (2015), Pliocene–Quaternary tectonic evolution of the Gulf of Gökova, southwest Turkey, *Tectonophysics*, *638*, 158–176. 7.3

Uluğ, A., M. Duman, Ş. Ersoy, E. Özel, and M. Avcı (2005), Late Quaternary sea-level change, sedimentation and neotectonics of the Gulf of gökova: Southeastern Aegean Sea, *Marine Geology*, *221*(1), 381–395. 6.9, 7.3

Valentini, A., F. Visini, and B. Pace (2017), Integrating faults and past earthquakes into a probabilistic seismic hazard model for peninsular Italy, *Natural Hazards Earth System Sciences*. 4.6.2

Vauchez, A., A. Tommasi, and G. Barruol (1998), Rheological heterogeneity, mechanical anisotropy and deformation of the continental lithosphere, *Tectonophysics*, *296*(1-2), 61–86. 1.1.2

Wallace, R. E. (1980), Degradation of the Hebgen Lake fault scarps of 1959, *Geology*, *8*(5), 225–229. 1.1.3, 1.5

Walsh, J., and J. Watterson (1987), Distributions of cumulative displacement and seismic slip on a single normal fault surface, *Journal of Structural Geology*, *9*(8), 1039–1046. 1.1.3, 7.2.3

Walters, R., J. Elliott, N. D'agostino, P. England, I. Hunstad, J. Jackson, B. Parsons, R. Phillips, and G. Roberts (2009), The 2009 L'Aquila earthquake (central Italy): A source mechanism and implications for seismic hazard, *Geophysical Research Letters*, *36*(17). 1.1.2, 1.1.4, 4.1

Walters, R., B. Parsons, and T. Wright (2014), Constraining crustal velocity fields with InSAR for Eastern Turkey: Limits to the block-like behavior of Eastern Anatolia, *Journal of Geophysical Research: Solid Earth*, *119*(6), 5215–5234. 5.2.1

Walters, R. J., L. C. Gregory, L. Wedmore, T. J. Craig, K. McCaffrey, M. Wilkinson, J. Chen, Z. Li, J. R. Elliott, H. Goodall, et al. (2018), Dual control of fault intersections on stop-start rupture in the 2016 Central Italy seismic sequence, *Earth and Planetary Science Letters*, *500*, 1–14. 1.1.3, 1.1.4, 1.3.1, 2.2.3,

4.3, 4.6.1, 4.6.3, 6.6, 7.2.3

Wang, X., S. Wei, and W. Wu (2017), Double-ramp on the Main Himalayan Thrust revealed by broadband waveform modeling of the 2015 Gorkha earthquake sequence, *Earth and Planetary Science Letters*, *473*, 83–93. 1.1.4

Ward, S. N., and G. R. Valensise (1989), Fault parameters and slip distribution of the 1915 Avezzano, Italy, earthquake derived from geodetic observations, *Bulletin of the Seismological Society of America*, *79*(3), 690–710. 1.1.2

Webber, S., K. Norton, T. Little, L. Wallace, and S. Ellis (2018), How fast can low-angle normal faults slip? Insights from cosmogenic exposure dating of the active Mailiu fault, Papua New Guinea, *Geology*, *46*(3), 227–230. 7.2

Wedmore, L., J. F. Walker, G. P. Roberts, P. Sammonds, K. McCaffrey, and P. Cowie (2017), A 667 year record of coseismic and interseismic Coulomb stress changes in central Italy reveals the role of fault interaction in controlling irregular earthquake recurrence intervals, *Journal of Geophysical Research: Solid Earth*, *122*(7), 5691–5711. 1.1.5, 1.3.1, 4.6.2

Wedmore, L., L. Gregory, K. McCaffrey, H. Goodall, and R. Walters (2019), Partitioned off-fault deformation in the 2016 Norcia earthquake captured by differential terrestrial laser scanning, *Geophysical Research Letters*. 1.1.3, 1.4, 7.2.3

Wei, M., Y. Kaneko, Y. Liu, and J. J. McGuire (2013), Episodic fault creep events in California controlled by shallow frictional heterogeneity, *Nature geoscience*, *6*(7), 566. 1.1.2

Weiss, J. R., R. J. Walters, Y. Morishita, T. J. Wright, M. Lazecky, H. Wang, E. Hussain, A. J. Hooper, J. R. Elliott, C. Rollins, et al. (2020), High-resolution surface velocities and strain for Anatolia from Sentinel-1 InSAR and GNSS data, *Geophysical Research Letters*, p. e2020GL087376. (document), 7.7, 7.3

Wells, D. L., and K. J. Coppersmith (1994), New empirical relationships among magnitude, rupture length, rupture width, rupture area, and surface displacement, *Bulletin of the seismological Society of America*, *84*(4), 974–1002. 6.3.2

Wesnousky, S. G. (2008), Displacement and geometrical characteristics of earthquake surface ruptures: Issues and implications for seismic-hazard analysis

and the process of earthquake rupture, *Bulletin of the Seismological Society of America*, *98*(4), 1609–1632. 1.1.3, 7.2.3

Wessel, B., M. Huber, C. Wohlfart, U. Marschalk, D. Kosmann, and A. Roth (2018), Accuracy assessment of the global TanDEM-X Digital Elevation Model with GPS data, *ISPRS Journal of Photogrammetry and Remote Sensing*, *139*, 171–182. 6.3.2, 6.3, 6.9

Westaway, R. (1993), Neogene evolution of the Denizli region of western Turkey, *Journal of Structural Geology*, *15*(1), 37–53. 5.2.1

Westaway, R., M. Pringle, S. Yurtmen, T. Demir, D. Bridgland, G. Rowbotham, and D. Maddy (2004), Pliocene and Quaternary regional uplift in western Turkey: the Gediz River terrace staircase and the volcanism at Kula, *Tectonophysics*, *391*(1-4), 121–169. 5.2.1

Wiatr, T., I. Papanikolaou, T. Fernández-Steeger, and K. Reicherter (2015), Reprint of: Bedrock fault scarp history: Insight from t-LiDAR backscatter behaviour and analysis of structure changes, *Geomorphology*, *237*, 119–129. 1.1.5

Wilkinson, M., G. P. Roberts, K. McCaffrey, P. A. Cowie, J. P. F. Walker, I. Papanikolaou, R. J. Phillips, A. M. Michetti, E. Vittori, L. Gregory, et al. (2015), Slip distributions on active normal faults measured from LiDAR and field mapping of geomorphic offsets: an example from L'Aquila, Italy, and implications for modelling seismic moment release, *Geomorphology*, *237*, 130–141. 1.1.5, 4.3, 4.4.2, 5.3, C4

Wilkinson, M. W., K. J. McCaffrey, R. R. Jones, G. P. Roberts, R. E. Holdsworth, L. C. Gregory, R. J. Walters, L. Wedmore, H. Goodall, and F. Iezzi (2017), Near-field fault slip of the 2016 Vettore M w 6.6 earthquake (Central Italy) measured using low-cost GNSS, *Scientific reports*, *7*(1), 4612. 1.1.3, 1.1.5

Yilmaz, Y., Ş. C. Genç, F. Gürer, M. Bozcu, K. Yilmaz, Z. Karacik, Ş. Altunkaynak, and A. Elmas (2000), When did the western Anatolian grabens begin to develop?, *Geological Society, London, Special Publications*, *173*(1), 353–384. 1.3.2, 5.2.1, 5.2.1, 5.3.4

Yin, A., and T. M. Harrison (2000), Geologic evolution of the Himalayan-Tibetan

orogen, *Annual review of earth and planetary sciences*, *28*(1), 211–280. 1.1.5

Yolsal-Çevikbilen, S., T. Taymaz, and C. Helvacı (2014), Earthquake mechanisms in the Gulfs of Gökova, Sığacık, Kuşadası, and the Simav region (western Turkey): Neotectonics, seismotectonics and geodynamic implications, *Tectonophysics*, *635*, 100–124. 6.5.1

Zhao, T., Y. Hu, and Y. Wang (2018), Statistical interpretation of spatially varying 2D geo-data from sparse measurements using Bayesian compressive sampling, *Engineering Geology*, *246*, 162–175. 5.3.2

Zinke, R., J. F. Dolan, E. J. Rhodes, R. Van Dissen, and C. P. McGuire (2017), Highly variable latest Pleistocene-Holocene incremental slip rates on the Awatere fault at Saxton River, South Island, New Zealand, revealed by lidar mapping and luminescence dating, *Geophysical Research Letters*, *44*(22). 4.6.2

Zreda, M., and J. S. Noller (1998), Ages of prehistoric earthquakes revealed by cosmogenic chlorine-36 in a bedrock fault scarp at Hebgen lake, *Science*, *282*(5391), 1097–1099. 1.2.2, 2.2.1, 2.1, 2.2.2, 2.4, 2.2.3, 7.2, 7.4

Zuchiewicz, W., and J. P. McCALPIN (2000), Geometry of faceted spurs on an active normal fault: case study of the Central Wasatch Fault, Utah, USA, in *Annales Societatis Geologorum Poloniae*, vol. 70. 7.2.1

Zygouri, V., S. Verroios, S. Kokkalas, P. Xypolias, and I. Koukouvelas (2008), Scaling properties within the Gulf of Corinth, Greece; comparison between offshore and onshore active faults, *Tectonophysics*, *453*(1-4), 193–210. 7.3

Appendix

A Sampling Records

A1 Sample collection procedure

I excavate a trench in the footwall slope. I remove material in 10-30cm thick horizontal layers. Material removed is placed into a bucket and weighed before disposal. The dimensions of each layer removed are recorded to allow the volume of material removed

and therefor the density of the removed material calculated. This allows a density profile to be calculated at a site.

To sample the fault plane, I mark out a series of discrete samples on the fault plane including on the fault scarp exposed in the trench and use as regular vertical spacing as possible, avoiding degraded, fractured or otherwise inappropriate fault plane. The samples are aligned parallel to the slip vector on the fault, I assume slip is parallel to dip away from fault tips. I occasionally sample up to 32cm along strike from the dip parallel line to avoid inappropriate areas of fault plane and I record the sample layout (supplementary materials section A2). I remove samples with an angle grinder and chisel, samples are comprised of tiles 15cm along strike, 5cm along dip and 2.5cm into the fault scarp. It is not always possible to remove tiles intact but I make efforts to capture all fragments from within the marked sample volume.

A2 Site characterisation

Site parameters

Site ID	Elevation (m)	Latitude (°N)	Longitude (°E)	α	β	γ	Scarp Height[1] (cm)	Trench Depth (cm)	HW density (g/cm^3)	Production rate[2]
CF1	1674	42.2336	13.43789	32	51	35	1560	120	1.5	48.8
CF2	1603	42.22777	13.44517	33	54	33	2440	150	1.5	48.8
CF3	1667	42.23434	13.43651	27	57	36	1230	60	1.5	48.8
RP1	839	42.19242	13.71068	30	49	31	720	120	1.5	48.8
RP2	923	42.20612	13.68602	27	66	27	470	80	1.5	48.8

(1) Calculated in the plane of the fault

(2) Spallation production rate from ^{40}Ca used in modelling (Stone et al., 1996). Other spallation production rates (K, Ti, Fe) and slow muon stopping rates are the same as in Schlagenhauf et al., 2001.

Figure A1: Sample site parameters

Table S2: Datarock files including whole rock chemistry

SITE ALL ALL DATA		Ba	Sr	Al2O3 (Al)	Fe2O3 (Fe)	MnO (Mn)	MgO (Mg)	CaO (Ca)	Na2O(Na)	K2O(K)	P2O5(P)	B	Li	H2Otot (H)
sample name	LU code	ppm	ppm	%	%	%	%	%	%	%	%	ppm	ppm	%
CF1														
CF-120	LU270	0.00000	132.36	0.01351387	0.01382139	0.003183963	0.46703583	61.7178161	0.02055978	0	0.01324488	0.00	0.00	0.219
CF-100	LU271	0.00000	131.73	0.0126022	0.01216198	0.001809884	0.45383594	62.0508592	0.02058829	0	0.01188614	0.00	0.00	0.219
CF-80	LU272	0.00000	129.44	0.01248996	0.01399144	0.001527247	0.45335255	60.1565363	0.01895775	0	0.0132157	0.00	0.00	0.219
CF-60	LU273	0.00000	144.09	0.01357977	0.015779	0.001429482	0.43460983	62.1607329	0.01749448	0	0.01295559	0.00	0.00	0.219
CF-40	LU276	1.64322	136.40	0.02464924	0.01230946	0.00135784	0.31324236	56.4693572	0.01351073	0	0.01091742	0.00	0.00	0.219
CF-20	LU277	1.04612	147.51	0.0137217	0.00978502	0.001408575	0.31268586	57.5846325	0.01381853	0	0.00855955	0.00	0.00	0.219
CF0	LU278	1.61556	138.16	0.02042181	0.01536923	0.001725612	0.38256067	58.358663	0.01674761	0	0.0131899	0.00	0.00	0.219
CF+20	LU279	1.34342	142.16	0.01742788	0.01463877	0.001445449	0.37620552	57.0011923	0.0175444	0	0.01278989	0.00	0.00	0.219
CF+40	LU280	1.09698	187.63	0.00668364	0.00584163	0.001327822	0.25606041	57.1836014	0.0130486	0	0.00521483	0.00	0.00	0.219
CF+60	LU281	6.69036	125.90	0.02851277	0.03158497	0.006327959	0.4881192	57.3423259	0.0283118	0	0.01903478	0.00	0.00	0.219
CF+80	LU282	6.56363	127.19	0.04655731	0.03288416	0.005335106	0.54269875	55.0704593	0.02139368	0.007331223	0.02419637	0.00	0.00	0.219
CF+100	LU283	6.01826	128.03	0.05591671	0.03520874	0.004622389	0.53022857	56.999288	0.0205918	0.006951893	0.02573733	0.00	0.00	0.219
CF+150	LU284	3.81179	198.09	0.0209394	0.01173694	0.002801493	0.27845007	58.8472133	0.03556976	0	0.01115115	0.00	0.00	0.219
CF+200	LU285	6.17582	139.00	0.04171877	0.02377339	0.005640025	0.44031728	57.8064454	0.0199377	0.00660446	0.01794485	0.00	0.00	0.219
CF+250	LU286	0.00000	119.07	0.01221217	0.01072132	0.00111415	0.38388418	56.5592382	0.02059779	0	0.00963318	0.00	0.00	0.219
CF+300	LU287	0.00000	127.41	0.00979042	0.00936537	0.000967871	0.31920608	57.7558907	0.01871458	0	0.00769096	0.00	0.00	0.219
CF+400	LU360	2.82697	128.19	0.03038328	0.03605826	0.001966943	0.64140957	60.5267299	0.02675764	0	0.0220204	0.00	0.00	0.219
CF+480	LU289	3.48797	124.26	0.02689756	0.03875763	0.002435954	0.51389561	57.0263334	0.030388	0	0.01692628	0.00	0.00	0.219
CF2														
CF2-150	LU373	0.00000	0.00	0.00195101	0.0010589	9.20592E-05	0.02740279	62.5202154	0.001306	0.000613904	0.00068768	0.00	0.00	0.219
CF2-120	LU374	0.00000	0.00	0.0019598	0.00099331	0.000260323	0.0297167	65.9825186	0.00143464	0	0.00070698	0.00	0.00	0.219
CF2-90	LU375	0.00000	0.00	0.00360234	0.001597	0.000330759	0.02897804	65.7200994	0.00138315	0	0.00099217	0.00	0.00	0.219
CF2-50	LU376	0.00000	0.00	0.00232578	0.0012958	0.000263434	0.03010288	64.5136085	0.00139933	0	0.00076212	0.00	0.00	0.219
CF2-0	LU377	0.00000	0.00	0.00300533	0.00146562	9.71643E-05	0.03014869	65.314641	0.00133882	0.00043411	0.00074738	0.00	0.00	0.219
CF2+30	LU378	0.00000	0.00	0.00267598	0.00125568	0.000121179	0.02868556	64.7622377	0.00128087	0	0.00069308	0.00	0.00	0.219
CF2+60	LU379	0.00000	0.00	0.00296262	0.00128608	0.000108565	0.02904308	65.8841506	0.00132205	0	0.0007439	0.00	0.00	0.219
CF2+90	LU380	0.00000	0.00	0.00281471	0.00128105	0.000246173	0.02853957	65.7380516	0.00121521	0	0.00080055	0.00	0.00	0.219
CF2+120	LU381	0.00000	0.00	0.00259657	0.00129158	0.000206048	0.02899382	65.0986238	0.00128345	0.000420538	0.00084373	0.00	0.00	0.219
CF2+150	LU382	0.00000	0.00	0.00257449	0.00124299	0.000146357	0.03161366	65.6436877	0.00149553	0.000428808	0.00070083	0.00	0.00	0.219
CF2+180	LU383	0.00000	0.00	0.00276293	0.00112916	0.000139284	0.03021995	64.901085	0.00141808	0.000447776	0.00067537	0.00	0.00	0.219
CF2+210	LU384	0.00000	0.00	0.00185631	0.00090095	0.000120554	0.02907449	60.9947931	0.00139332	0	0.00051643	0.00	0.00	0.219

Figure A2: Elements with 0 concentration not recorded.

SITE ALL ALL DATA		Ba	Sr	Al2O3 (Al)	Fe2O3 (Fe)	MnO (Mn)	MgO (Mg)	CaO (Ca)	Na2O(Na)	K2O(K)	P2O5(P)	B	Li	H2Otot (H)
sample name	LU code	ppm	ppm	%	%	%	%	%	%	%	%	ppm	ppm	%
CF1														
CF2+270	LU386	0.00000	0.00	0.00219658	0.00111194	0.000156678	0.02952872	61.0934971	0.00132939	0	0.00060299	0.00	0.00	0.219
CF2+300	LU389	0.00000	0.00	0.00247214	0.00121396	8.33548E-05	0.03151655	57.0667726	0.00156699	0	0.00058529	0.00	0.00	0.219
CF2+400	LU390	0.00000	0.00	0.00194245	0.00096358	0.000092212	0.02971839	60.9291584	0.00156275	0	0.00046772	0.00	0.00	0.219
CF2+450	LU391	0.00000	0.00	0.00169785	0.0009283	9.14965E-05	0.03374892	61.8493422	0.00185233	0	0.00049058	0.00	0.00	0.219
CF2+570	LU392	0.00000	0.00	0.00182645	0.00106767	5.86246E-05	0.02937765	62.3100516	0.00164495	0.000486818	0.00038651	0.00	0.00	0.219
CF3														
CF3-60	LU393	0.00000	0.00	0.00156565	0.00099135	0.000110305	0.03470838	62.1909498	0.00080243	0	0.00410913	0.00	0.00	0.219
CF3-25	LU394	0.00000	0.00	0.00158341	0.00094179	6.89402E-05	0.03643136	61.0475793	0.00084221	0	0.00470767	0.00	0.00	0.219
CF3-0	LU395	0.00000	0.00	0.00143776	0.00101395	6.41772E-05	0.03619709	61.99793	0.00078872	0	0.00353139	0.00	0.00	0.219
CF3+100	LU396	0.00000	0.00	0.00106131	0.0008459	8.90946E-05	0.0408043	62.1068461	0.00074083	0	0.003144	0.00	0.00	0.219
CF3+200	LU397	0.00000	0.00	0.0017337	0.00156657	0.000270681	0.02900152	61.4208368	0.000953	0	0.00140516	0.00	0.00	0.219
CF3+300	LU398	0.00000	0.00	0.0017254	0.00145418	0.000196826	0.02659466	65.2792099	0.00106693	0	0.00111972	0.00	0.00	0.219
CF3+400	LU399	0.00000	0.00	0.00158336	0.00148684	0.000298782	0.02724159	60.500694	0.00117657	0	0.00091711	0.00	0.00	0.219
CF3+530	LU400	0.00000	0.00	0.00165645	0.00142182	9.40317E-05	0.02480105	52.8597688	0.00102823	0	0.00079417	0.00	0.00	0.219
RP1														
RP-100	LU195	6.31632	363.47	0.03434385	0.01493211	0.008314359	0.20538818	53.3484324	0.05515198	0.003600039	0.07687125	0	0	0.219
RP-80	LU196	6.57897	371.01	0.03569422	0.01654354	0.007971618	0.20762015	58.0318965	0.05184188	0.003047962	0.08494673	0	0	0.219
RP-60	LU197	6.42923	346.62	0.03726851	0.01475067	0.008017558	0.20154106	56.5279501	0.05114967	0.003853275	0.09620797	0	0	0.219
RP-40	LU198	6.25313	379.37	0.02962989	0.02875104	0.008204561	0.19404262	56.0486443	0.0520744	0.002524307	0.07317839	0	0	0.219
RP-20	LU199	6.29617	350.03	0.03675542	0.01534659	0.007966627	0.18714986	56.9676666	0.04905201	0.00288194	0.08517691	0	0	0.219
RP0	LU200	6.20147	348.49	0.03407694	0.01390624	0.007972621	0.18867333	57.384812	0.05168162	0.00305202	0.08488011	0	0	0.219
RP+20	LU201	6.06912	348.22	0.0331116	0.01371286	0.00791251	0.1874759	56.9938112	0.05207568	0.003387821	0.08369753	0	0	0.219
RP+40	LU202	5.96513	340.21	0.03415538	0.01410347	0.007435192	0.18086638	57.6739949	0.04651005	0	0.08483509	0	0	0.219
RP+55	LU203	0	271.18	0	0	0	0.16309253	57.7015989	0	0	0	0	0	0.219
RP+80	LU204	6.6062	364.39	0.05901573	0.02684834	0.010072928	0.23888384	57.2848999	0.03621116	0.003334569	0.1129345	0	0	0.219
RP+100	LU205	6.43766	416.19	0.06431167	0.02783407	0.009933724	0.27246792	57.1276943	0.03699457	0.002345258	0.11309727	0	0	0.219
RP+125	LU206	6.67725	328.92	0.0545352	0.0286861	0.010743384	0.22570202	57.6492571	0.03212363	0.003010999	0.11359441	0	0	0.219
RP+150	LU207	6.01692	356.64	0.04925866	0.02155208	0.008545525	0.25016166	57.581944	0.0362702	0.003060131	0.09863771	0	0	0.219

Figure A3: Elements with 0 concentration not recorded.

SITE ALL ALL DATA		Ba	Sr	Al2O3 (Al)	Fe2O3 (Fe)	MnO (Mn)	MgO (Mg)	CaO (Ca)	Na2O(Na)	K2O(K)	P2O5(P)	B	Li	H2Otot (H)
sample name	LU code	ppm	ppm	%	%	%	%	%	%	%	%	ppm	ppm	%
RP2														
RP2-80	LU401	0	0	0.00131225	0.00073777	0.000137768	0.02433289	50.0227205	0.00127653	0	0.00873668	0	0	0.219
RP2-40	LU402	0	0	0.00152777	0.00080651	0.000126774	0.02625937	60.2472922	0.00138868	0	0.00959206	0	0	0.219
RP2-0	LU405	0	0	0.00132432	0.00077342	0.000133377	0.02613802	63.6446539	0.00139451	0	0.00982719	0	0	0.219
RP2+45	LU406	0	0	0.00136125	0.00092594	0.00017546	0.02387577	63.2377384	0.00131543	0	0.01050098	0	0	0.219
RP2+70	LU407	0	0	0.00136256	0.00079058	0.000139788	0.02659403	63.3638667	0.00141775	0	0.01101375	0	0	0.219
RP2+105	LU408	0	0	0.0013153	0.00086042	0.000144905	0.02221125	63.9401193	0.0012409	0	0.01155451	0	0	0.219
RP2+140	LU409	0	0	0.00119756	0.00065135	0.000104391	0.02656062	61.7150548	0.00135599	0	0.00863559	0	0	0.219
RP2+180	LU410	0	0	0.00191137	0.00108734	0.000159993	0.02631207	63.3792085	0.00150409	0	0.01476813	0	0	0.219

Figure A4: Elements with 0 concentration not recorded.

	CO2 tot (C)	O,rock	O,water	Cl nat AMS	Ca ICP	Z (position on the scarp)	Sample Thickness	[36Cl] AMS	uncertainty	Z(HEIGHT)	*Z (position with z<0 for the buried samples)*
sample name	%			ppm	ppm	cm	cm	at/g.rock			
CF1											
CF-120	43	16.21	0.19	20.23	413371	0	2.5	1.73E+05	4.55E+03	0	-120
CF-100	43	16.21	0.19	19.49	413371	20	2.5	1.96E+05	5.80E+03	20	-100
CF-80	43	16.21	0.19	21.30	413371	40	2.5	2.05E+05	6.02E+03	40	-80
CF-60	43	16.21	0.19	19.73	413371	60	2.5	1.85E+05	5.87E+03	60	-60
CF-40	43	16.21	0.19	18.87	385322	80	2.5	2.16E+05	6.56E+03	80	-40
CF-20	43	16.21	0.19	16.18	427064	100	2.5	2.17E+05	6.70E+03	100	-20
CF0	43	16.21	0.19	17.32	411824	120	2.5	2.16E+05	6.55E+03	120	0
CF+20	43	16.21	0.19	20.33	420556	140	2.5	2.23E+05	4.67E+03	140	20
CF+40	43	16.21	0.19	12.72	417992	160	2.5	2.22E+05	6.89E+03	160	40
CF+60	43	16.21	0.19	41.20	419491	180	2.5	2.74E+05	6.47E+03	180	60
CF+80	43	16.21	0.19	24.37	410071	200	2.5	2.67E+05	8.41E+03	200	80
CF+100	43	16.21	0.19	21.72	430201	220	2.5	2.67E+05	7.19E+03	220	100
CF+150	43	16.21	0.19	31.63	420662	270	2.5	3.03E+05	8.31E+03	270	150
CF+200	43	16.21	0.19	25.69	400191	320	2.5	2.92E+05	8.92E+03	320	200
CF+250	43	16.21	0.19	22.81	415074	370	2.5	3.35E+05	1.01E+04	370	250
CF+300	43	16.21	0.19	22.61	408852	420	2.5	3.59E+05	1.48E+04	420	300
CF+400	43	16.21	0.19	48.90	404251	520	2.5	4.86E+05	1.46E+04	520	400
CF+480	43	16.21	0.19	46.02	415644	600	2.5	5.89E+05	1.81E+04	600	480
CF2											
CF2-150	43	16.21	0.19	18.42	375011	0	2.5	1.18E+05	3.84E+03	0	-150
CF2-120	43	16.21	0.19	16.91	376470	30	2.5	1.12E+05	3.30E+03	30	-120
CF2-90	43	16.21	0.19	14.70	369890	60	2.5	1.13E+05	3.30E+03	60	-90
CF2-50	43	16.21	0.19	17.28	372881	100	2.5	1.26E+05	4.12E+03	100	-50
CF2-0	43	16.21	0.19	15.14	376578	150	2.5	1.46E+05	3.90E+03	150	0
CF2+30	43	16.21	0.19	12.60	374606	180	2.5	1.52E+05	4.37E+03	180	30
CF2+60	43	16.21	0.19	15.66	377183	210	2.5	1.59E+05	4.28E+03	210	60
CF2+90	43	16.21	0.19	14.36	376588	240	2.5	1.64E+05	4.74E+03	240	90
CF2+120	43	16.21	0.19	15.85	371569	270	2.5	1.82E+05	5.27E+03	270	120
CF2+150	43	16.21	0.19	15.47	376552	300	2.5	1.70E+05	4.90E+03	300	150
CF2+180	43	16.21	0.19	16.59	374971	330	2.5	1.98E+05	5.71E+03	330	180
CF2+210	43	16.21	0.19	17.49	372230	360	2.5	2.08E+05	5.99E+03	360	210

Figure A5: Elements with 0 concentration not recorded.

	CO2 tot (C)	O,rock	O,water	Cl nat AMS	Ca ICP	Z (position on the scarp)	Sample Thickness	[36Cl] AMS	uncertainty	Z(HEIGHT)	*Z (position with z<0 for the buried samples)*
sample name	%			ppm	ppm	cm	cm	at/g.rock			
CF1											
CF2+270	43	16.21	0.19	16.38	370888	420	2.5	2.30E+05	7.49E+03	420	270
CF2+300	43	16.21	0.19	19.76	371048	450	2.5	2.42E+05	8.03E+03	450	300
CF2+400	43	16.21	0.19	20.16	377404	550	2.5	3.00E+05	9.12E+03	550	400
CF2+450	43	16.21	0.19	22.59	377537	600	2.5	3.62E+05	1.08E+04	600	450
CF2+570	43	16.21	0.19	22.70	388728	720	2.5	4.67E+05	1.39E+04	720	570
CF3											
CF3-60	43	16.21	0.19	8.86	398270	0	2.5	1.01E+05	3.68E+03	0	-60
CF3-25	43	16.21	0.19	8.85	409438	35	2.5	1.09E+05	3.88E+03	35	-25
CF3-0	43	16.21	0.19	10.59	400240	60	2.5	1.17E+05	3.84E+03	60	0
CF3+100	43	16.21	0.19	8.73	403301	160	2.5	1.48E+05	5.10E+03	160	100
CF3+200	43	16.21	0.19	21.71	399360	260	2.5	1.65E+05	5.26E+03	260	200
CF3+300	43	16.21	0.19	25.12	393246	360	2.5	2.10E+05	6.56E+03	360	300
CF3+400	43	16.21	0.19	24.86	388045	460	2.5	2.61E+05	7.87E+03	460	400
CF3+530	43	16.21	0.19	25.95	402979	590	2.5	3.69E+05	1.11E+04	590	530
RP1											
RP-100	43	16.21	0.19	14.1	384559	0	2.5	1.74E+05	5561.197	0	-100
RP-80	43	16.21	0.19	12.01	366927	20	2.5	1.67E+05	5026.748	20	-80
RP-60	43	16.21	0.19	11.75	369781	40	2.5	1.84E+05	5503.992	40	-60
RP-40	43	16.21	0.19	10.4	372367	60	2.5	1.94E+05	5839.178	60	-40
RP-20	43	16.21	0.19	10.02	368565	80	2.5	1.91E+05	5721.548	80	-20
RP0	43	16.21	0.19	11.07	375013	100	2.5	1.87E+05	4102.36	100	0
RP+20	43	16.21	0.19	11.01	374969	120	2.5	1.80E+05	5364.873	120	20
RP+40	43	16.21	0.19	9.68	370118	140	2.5	1.89E+05	5676.51	140	40
RP+55	43	16.21	0.19	6.44	376704	155	2.5	2.10E+05	6302.579	155	55
RP+80	43	16.21	0.19	9.07	377468	180	2.5	2.16E+05	4737.376	180	80
RP+100	43	16.21	0.19	9.39	365863	200	2.5	2.25E+05	6795.613	200	100
RP+125	43	16.21	0.19	8.57	373395	225	2.5	2.22E+05	5795.359	225	125
RP+150	43	16.21	0.19	9.23	378891	250	2.5	2.37E+05	7088.874	250	150

Figure A6: Elements with 0 concentration not recorded.

	CO2 tot (C)	O,rock	O,water	Cl nat AMS	Ca ICP	Z (position on the scarp)	Sample Thickness	[36Cl] AMS	uncertainty	Z(HEIGHT)	*Z (position with z<0 for the buried samples)*
sample name	%			ppm	ppm	cm	cm	at/g.rock			
RP2											
RP2-80	43	16.21	0.19	14.01317661	403500	0	2.5	159317.3821	4826.080652	0	-80
RP2-40	43	16.21	0.19	13.89600543	411222	40	2.5	183544.6771	6281.990146	40	-40
RP2-0	43	16.21	0.19	14.12270707	407675	80	2.5	220692.4327	6440.287636	80	0
RP2+45	43	16.21	0.19	12.14526236	397425	125	2.5	231137.8256	6973.301901	125	45
RP2+70	43	16.21	0.19	12.93858491	399156	150	2.5	254276.3668	7557.375365	150	70
RP2+105	43	16.21	0.19	10.30838142	395448	185	2.5	264902.6269	7884.781741	185	105
RP2+140	43	16.21	0.19	14.46002098	406291	220	2.5	285503.5451	8379.057262	220	140
RP2+180	43	16.21	0.19	11.34255226	399554	260	2.5	315217.5787	7653.101729	260	180

Figure A7: Elements with 0 concentration not recorded.

AMS Analytical data for CF1

Sample ID	Leeds University Code	AMS ID	m sample	m_cl spike[a]	36Cl/Cl[b] ± 1 sigma uncertainty				37Cl/35Cl	Clnat AMS	N_Cl36,rock	
		SUERC-	[g]	[mg]	derived from 36Cl/35Cl		derived from 36Cl/37Cl			[ppm]	36Cl [atoms/g]	s36Cl [atoms/g]
CF1												
CF-120	LU270	c3650	30.2404	1.0683	1.568E-13	3.981E-15	3.726E-13	9.459E-15	0.1235	20.23	1.729E+05	4.55E+03
CF-100	LU271	c3657	30.1214	1.0392	1.830E-13	5.192E-15	4.354E-13	1.236E-14	0.1228	19.49	1.958E+05	5.80E+03
CF-80	LU272	c3658	30.4736	1.0468	1.864E-13	5.277E-15	4.266E-13	1.208E-14	0.1277	21.30	2.047E+05	6.02E+03
CF-60	LU273	c3659	30.1111	1.0120	1.751E-13	5.266E-15	4.098E-13	1.232E-14	0.1248	19.73	1.848E+05	5.87E+03
CF-40	LU276	c3660	30.2742	1.0829	1.995E-13	5.835E-15	4.893E-13	1.431E-14	0.1191	18.87	2.160E+05	6.56E+03
CF-20	LU277	c3661	30.6831	1.0183	2.208E-13	6.292E-15	5.601E-13	1.597E-14	0.1152	16.18	2.168E+05	6.70E+03
CF0	LU278	c3667	30.0288	1.0519	2.090E-13	5.964E-15	5.207E-13	1.486E-14	0.1159	17.32	2.162E+05	6.55E+03
CF+20	LU279	c3668	30.0085	1.0658	2.032E-13	3.735E-15	4.760E-13	8.750E-15	0.1233	20.33	2.228E+05	4.67E+03
CF+40	LU280	c3669	31.5020	1.0322	2.442E-13	7.042E-15	6.739E-13	1.943E-14	0.1047	12.72	2.219E+05	6.89E+03
CF+60	LU281	c3670	30.2343	1.0405	1.919E-13	4.044E-15	3.346E-13	7.053E-15	0.1657	41.20	2.740E+05	6.47E+03
CF+80	LU282	c3671	30.1429	1.0094	2.382E-13	6.917E-15	5.050E-13	1.467E-14	0.1363	24.37	2.675E+05	8.41E+03
CF+100	LU283	c3677	29.7383	1.0658	2.368E-13	5.958E-15	5.414E-13	1.362E-14	0.1263	21.72	2.669E+05	7.19E+03
CF+150	LU284	c3678	30.3233	1.0227	2.420E-13	6.071E-15	4.631E-13	1.162E-14	0.151	31.63	3.029E+05	8.31E+03
CF+200	LU285	c3679	29.9467	1.0278	2.513E-13	7.142E-15	5.264E-13	1.496E-14	0.1379	25.69	2.923E+05	8.92E+03
CF+250	LU286	c3680	30.1740	1.0563	2.968E-13	8.464E-15	6.582E-13	1.877E-14	0.1302	22.81	3.350E+05	1.01E+04
CF+300	LU287	c3681	30.3438	1.0259	3.261E-13	1.289E-14	7.160E-13	2.831E-14	0.1316	22.61	3.589E+05	1.48E+04
CF+400	LU360	c3826	30.0251	1.0355	3.086E-13	8.737E-15	5.120E-13	1.449E-14	0.1714	48.90	4.856E+05	1.46E+04
CF+480	LU289	c3656	29.9568	1.0430	3.854E-13	1.111E-14	6.560E-13	1.891E-14	0.1717	46.02	5.892E+05	1.81E+04

[a]Mass of $^{35/37}$Cl spike added to sample prior to dissolution. Spike concentration on next page.
[b]36Cl/Cl is based on either the measured ^{36}Cl/^{35}Cl or ^{36}Cl/^{37}Cl ratios assuming natural ^{35}Cl/^{37}Cl ratios.

Figure A8: CF1 AMS measurements

AMS Analytical data for CF2 and CF3

Sample ID	Leeds University	AMS ID SUERC-	m sample [g]	m_cl spike[a] [mg]	36Cl/Cl[b] ± 1 sigma uncertainty derived from 36Cl/35Cl		derived from 36Cl/37Cl		37Cl/35Cl	Clnat AMS [ppm]	N_Cl36,rock 36Cl [atoms/g]	s36Cl [atoms/g]
CF2												
CF2-150	LU373	c3942	29.6847	1.1085	1.067E-13	3.424E-15	2.676E-13	8.575E-15	0.1156	18.42	1.177E+05	3.84E+03
CF2-120	LU374	c3943	29.5816	1.0589	1.070E-13	2.983E-15	2.733E-13	7.602E-15	0.1135	16.91	1.118E+05	3.30E+03
CF2-90	LU375	c3944	29.6509	1.0583	1.123E-13	3.101E-15	3.036E-13	8.369E-15	0.1072	14.70	1.129E+05	3.30E+03
CF2-50	LU376	c3945	29.8090	1.0506	1.208E-13	3.760E-15	3.039E-13	9.446E-15	0.1153	17.28	1.258E+05	4.12E+03
CF2-0	LU377	c3951	29.5884	1.0564	1.437E-13	3.596E-15	3.842E-13	9.591E-15	0.1085	15.14	1.460E+05	3.90E+03
CF2+30	LU378	c3952	30.4311	1.0602	1.590E-13	4.333E-15	4.536E-13	1.234E-14	0.1016	12.60	1.518E+05	4.37E+03
CF2+60	LU379	c3953	29.5555	1.0493	1.557E-13	3.915E-15	4.091E-13	1.027E-14	0.1103	15.66	1.590E+05	4.28E+03
CF2+90	LU380	c3954	30.1019	1.0544	1.655E-13	4.524E-15	4.487E-13	1.224E-14	0.1070	14.36	1.638E+05	4.74E+03
CF2+120	LU381	c3955	29.9212	1.0480	1.789E-13	4.889E-15	4.657E-13	1.270E-14	0.1115	15.85	1.818E+05	5.27E+03
CF2+150	LU382	c3960	29.9306	1.0686	1.663E-13	4.567E-15	4.404E-13	1.207E-14	0.1095	15.47	1.701E+05	4.90E+03
CF2+180	LU383	c3961	29.9556	1.0525	1.919E-13	5.235E-15	4.904E-13	1.336E-14	0.1135	16.59	1.979E+05	5.71E+03
CF2+210	LU384	c3962	30.4921	1.0506	2.014E-13	5.490E-15	4.971E-13	1.353E-14	0.1170	17.49	2.075E+05	5.99E+03
CF2+240	LU385	c3963	29.8493	1.0576	2.042E-13	5.572E-15	4.879E-13	1.329E-14	0.1213	19.61	2.224E+05	6.40E+03
CF2+270	LU386	c3964	29.4960	1.0493	2.212E-13	6.884E-15	5.713E-13	1.776E-14	0.1123	16.38	2.296E+05	7.49E+03
CF2+300	LU389	c3995	29.3696	1.0892	2.159E-13	6.629E-15	5.216E-13	1.592E-14	0.1197	19.76	2.419E+05	8.03E+03
CF2+400	LU390	c3996	29.6322	1.0486	2.747E-13	7.375E-15	6.454E-13	1.719E-14	0.1231	20.16	3.002E+05	9.12E+03
CF2+450	LU391	c3997	29.9558	1.0847	3.138E-13	8.433E-15	7.097E-13	1.892E-14	0.1279	22.59	3.616E+05	1.08E+04
CF2+570	LU392	c3998	29.9453	1.0654	4.089E-13	1.086E-14	9.159E-13	2.412E-14	0.1291	22.70	4.667E+05	1.39E+04
CF3												
CF3-60	LU393	c4005	30.6172	1.0750	1.135E-13	3.811E-15	3.718E-13	1.242E-14	0.0883	8.86	1.006E+05	3.68E+03
CF3-25	LU394	c4006	30.2112	1.0692	1.221E-13	3.957E-15	4.011E-13	1.293E-14	0.0880	8.85	1.089E+05	3.88E+03
CF3-0	LU395	c4007	30.0468	1.0506	1.276E-13	3.705E-15	3.893E-13	1.123E-14	0.0948	10.59	1.167E+05	3.84E+03
CF3+100	LU396	c4008	30.1884	1.0795	1.644E-13	5.188E-15	5.455E-13	1.712E-14	0.0872	8.73	1.481E+05	5.10E+03
CF3+200	LU397	c4014	29.8400	1.0325	1.499E-13	4.199E-15	3.382E-13	9.408E-15	0.1282	21.71	1.648E+05	5.26E+03
CF3+300	LU398	c4015	29.4951	1.0885	1.741E-13	4.925E-15	3.797E-13	1.066E-14	0.1326	25.12	2.102E+05	6.56E+03
CF3+400	LU399	c4016	29.9966	1.0493	2.242E-13	5.947E-15	4.803E-13	1.264E-14	0.1350	24.86	2.609E+05	7.87E+03
CF3+530	LU400	c4017	29.6499	1.0847	3.029E-13	8.193E-15	6.493E-13	1.742E-14	0.1349	25.95	3.687E+05	1.11E+04

[a]Mass of $^{35/37}$Cl spike added to sample prior to dissolution. Spike concentration on next page.
[b]36Cl/Cl is based on either the measured ^{36}Cl/^{35}Cl or ^{36}Cl/^{37}Cl ratios assuming natural ^{35}Cl/^{37}Cl ratios.

Figure A9: CF2 and CF3 AMS measurements

AMS Analytical data for RP1, and RP2

Sample ID	Leeds University	AMS ID SUERC-	m sample [g]	m_cl spike[a] [mg]	36Cl/Cl[b] ± 1 sigma uncertainty derived from 36Cl/35Cl		derived from 36Cl/37Cl		37Cl/35Cl	Clnat AMS [ppm]	N_Cl36,rock 36Cl [atoms/g]	s36Cl [atoms/g]
RP1												
RP-100	LU195	c3405	29.4587	1.0212	1.777E-13	5.492E-15	4.793E-13	1.483E-14	0.1070	14.08	1.734E+05	5.64E+03
RP-80	LU196	c3406	29.6373	1.0306	1.788E-13	5.153E-15	5.152E-13	1.487E-14	0.1001	12.00	1.684E+05	5.12E+03
RP-60	LU197	c3407	29.5279	1.0244	1.969E-13	5.658E-15	5.719E-13	1.646E-14	0.0993	11.73	1.843E+05	5.61E+03
RP-40	LU198	c3408	29.8841	1.0231	2.148E-13	6.213E-15	6.511E-13	1.886E-14	0.0951	10.38	1.940E+05	5.94E+03
RP-20	LU199	c3409	30.0763	1.0306	2.138E-13	6.158E-15	6.583E-13	1.899E-14	0.0937	10.00	1.920E+05	5.83E+03
RP0	LU200	c3415	29.4896	1.0281	2.025E-13	4.171E-15	6.035E-13	1.247E-14	0.0968	11.06	1.880E+05	4.28E+03
RP+20	LU201	c3416	29.8327	1.0288	1.968E-13	5.630E-15	5.852E-13	1.677E-14	0.0970	10.99	1.809E+05	5.47E+03
RP+40	LU202	c3417	29.3778	1.0288	2.091E-13	6.028E-15	6.580E-13	1.900E-14	0.0917	9.67	1.899E+05	5.78E+03
RP+55	LU203	c3418	29.3142	1.0288	2.467E-13	7.097E-15	9.001E-13	2.594E-14	0.0791	6.43	2.106E+05	6.42E+03
RP+80	LU204	c3419	28.7354	1.0294	2.380E-13	4.880E-15	7.736E-13	1.591E-14	0.0887	9.06	2.177E+05	4.94E+03
RP+100	LU205	c3424	28.9617	1.0037	2.476E-13	7.187E-15	7.850E-13	2.282E-14	0.0910	9.38	2.219E+05	6.92E+03
RP+125	LU206	c3425	29.1356	1.0288	2.487E-13	6.194E-15	8.219E-13	2.051E-14	0.0873	8.56	2.227E+05	5.96E+03
RP+150	LU207	c3426	29.1787	1.0294	2.633E-13	7.557E-15	8.459E-13	2.431E-14	0.0898	9.22	2.387E+05	7.22E+03
RP+180	LU317	c3751	29.6225	1.0354	2.990E-13	8.553E-15	1.031E-12	2.950E-14	0.0839	8.03	2.659E+05	8.08E+03
RP+205	LU318	c3752	29.7885	1.0335	2.918E-13	7.155E-15	9.525E-13	2.335E-14	0.0887	9.23	2.640E+05	7.00E+03
RP2												
RP2-80	LU401	c4018	29.9682	1.0583	1.621E-13	4.324E-15	4.432E-13	1.172E-14	0.1058	14.01	1.593E+05	4.83E+03
RP2-40	LU402	c4019	29.9204	1.0795	1.839E-13	5.804E-15	5.094E-13	1.598E-14	0.1045	13.90	1.835E+05	6.28E+03
RP2-0	LU405	c3970	29.9579	1.0879	2.191E-13	5.946E-15	6.085E-13	1.648E-14	0.1048	14.12	2.207E+05	6.44E+03
RP2+45	LU406	c3971	29.9752	1.0737	2.404E-13	6.689E-15	7.029E-13	1.968E-14	0.0991	12.15	2.311E+05	6.97E+03
RP2+70	LU407	c3972	29.9558	1.0776	2.595E-13	7.167E-15	7.422E-13	2.047E-14	0.1015	12.94	2.543E+05	7.56E+03
RP2+105	LU408	c3973	30.0982	1.0622	2.876E-13	7.859E-15	8.940E-13	2.439E-14	0.0934	10.31	2.649E+05	7.88E+03
RP2+140	LU409	c3974	30.0729	1.0705	2.860E-13	7.776E-15	7.768E-13	2.108E-14	0.1067	14.46	2.855E+05	8.38E+03
RP2+180	LU410	c3975	29.8615	1.0403	3.389E-13	7.156E-15	1.008E-12	2.123E-14	0.0975	11.34	3.152E+05	7.65E+03

[a]Mass of $^{35/37}$Cl spike added to sample prior to dissolution. Spike concentration on next page.
[b]36Cl/Cl is based on either the measured ^{36}Cl/^{35}Cl or ^{36}Cl/^{37}Cl ratios assuming natural ^{35}Cl/^{37}Cl ratios.

Figure A10: RP1 and RP2 AMS measurements

Processed blanks: run alongside each batch of samples to correct for contamination during sample processing

Corresponding Sample Ids[a]	Leeds University Code	AMS ID SUERC-	m_cl spike[a] [mg]	36Cl/Cl[b] ± 1 sigma uncertainty derived from 36Cl/35Cl		derived from 36Cl/37Cl		37Cl/35Cl
LU195-LU207	LU211	c3404	1.0281	1.803E-15	3.138E-16	1.074E-14	1.873E-15	0.0485
LU195-LU207	LU212	c3414	1.0193	9.752E-16	2.238E-16	5.709E-15	1.310E-15	0.0493
LU317-LU318	LU322	c3736	1.0481	1.155E-16	6.666E-17	7.034E-16	4.061E-16	0.0480
LU317-LU318	LU323	c3747	1.0474	2.210E-16	1.105E-16	1.369E-15	6.845E-16	0.0467
LU270-LU273	LU274	c3634	1.0360	3.949E-16	1.974E-16	2.368E-15	1.184E-15	0.0482
LU276-LU289	LU290	c3666	1.0278	6.443E-16	2.278E-16	3.876E-15	1.370E-15	0.0480
LU276-LU289	LU291	c3683	1.0424	1.279E-15	2.418E-16	7.758E-15	1.466E-15	0.0476
LU360	LU371	c3822	1.0229	1.457E-15	2.403E-16	9.024E-15	1.491E-15	0.0459
LU360	LU372	c3833	1.0323	9.929E-16	2.994E-16	6.001E-15	1.810E-15	0.0471
LU373-LU386	LU387	c3941	1.0551	1.787E-15	2.317E-16	1.083E-14	1.404E-15	0.0479
LU373-LU386	LU388	c3950	1.0583	1.690E-15	2.247E-16	1.006E-14	1.338E-15	0.0487
LU389-LU402	LU403	c4004	1.0673	7.842E-16	1.458E-16	4.754E-15	8.837E-16	0.0477
LU389-LU402	LU404	c3994	1.0525	1.922E-15	2.646E-16	1.141E-14	1.570E-15	0.0487
LU405-LU410	LU416	c3969	1.0570	4.344E-15	7.743E-16	2.550E-14	4.564E-15	0.0494
LU405-LU410	LU417	c3980	1.0686	2.103E-15	3.769E-16	1.281E-14	2.295E-15	0.0476

(a) Each processed blank corresponds to a batch of samples (listed below) and the 36Cl concentrations are propagated as errors through the calcutation of 36Cl in at/g. from raw AMS data.

Analytical blanks: no processing has been applied, these blanks are used for correcting AMS-specific results

BATCH NO.	13	Samples associated:								
DATE RUN	OCT 2015	LU195-LU207								
NAT	Sample ID	Material type	36Cl/35Cl	s (36Cl/35Cl)	36Cl/37Cl	s (36Cl/37Cl)	37Cl/35Cl	s (37Cl/35Cl)		37Cl/35Cl	s (37Cl/35Cl)
1	c3373-nat	LNAT	1.746E-15	2.952E-16	1.742E-15	2.945E-16	0.2892	0.0000	R_natural	0.3198	0.0000
2	c3393-nat	LNAT	3.076E-15	1.229E-15	3.065E-15	1.225E-15	0.2896	0.0000			
3	c3413-nat	LNAT	9.0246E-16	2.745E-16	9.0127E-16	2.741E-16	0.2888	0.0000			
PSB										37Cl/35Cl	s (37Cl/35Cl)
1	c3383-spike	LPSB	3.564E-15	1.083E-15	2.117E-14	6.420E-15	0.0485	0.0000	R_spike	0.0506	0.0013
2	c3403-spike	LPSB	1.734E-17	1.734E-17	1.043E-16	1.043E-16	0.0479	0.0000			
3	c3423-spike	LPSB	6.792E-16	1.284E-16	4.081E-15	7.715E-16	0.048	0.0000			
BATCH NO.	20	Samples associated:								
DATE RUN	OCT 2016	LU317-LU318								37Cl/35Cl	s (37Cl/35Cl)
NAT									R_natural	0.3198	0.0000
1	c3735-nat	LNAT	8.598E-17	4.964E-17	8.632E-17	4.984E-17	0.2882	0.0000			
2	c3757-nat	LNAT	4.453E-16	1.683E-16	4.477E-16	1.692E-16	0.2878	0.0000			
3	c3778-nat	LNAT	4.3588E-16	1.78E-16	4.3885E-16	1.792E-16	0.285	0.0000		37Cl/35Cl	s (37Cl/35Cl)
PSB									R_spike	0.0503	0.0013
1	c3746-spike	LPSB	3.765E-16	1.087E-16	2.355E-15	6.799E-16	0.0462	0.0000			
2	c3768-spike	LPSB	6.546E-16	1.588E-16	4.082E-15	9.902E-16	0.046	0.0000			
3	c3779-spike	LPSB	5.145E-16	1.819E-16	3.152E-15	1.115E-15	0.0468	0.0000			

Figure A11: AMS Blank measurements

Analytical blanks: no processing has been applied, these blanks are used for correcting AMS-specific results

NAT	Sample ID	Material type	36Cl/35Cl	s (36Cl/35Cl)	36Cl/37Cl	s (36Cl/37Cl)	37Cl/35Cl	s (37Cl/35Cl)
BATCH NO.	17	Samples associated:						
DATE RUN	JUN 2016	LU270-LU273						
NAT								
1	c3654-nat	LNAT	5.701E-16	4.032E-16	5.731E-16	4.053E-16	0.2907	0.0000
2	c3535-nat	LNAT	5.701E-16	4.032E-16	5.731E-16	4.053E-16	0.2907	0.0000
PSB								
1	c3644-spike	LPSB	2.453E-15	3.470E-16	1.484E-14	2.099E-15	0.0485	0.0000
2	c3655-spike	LPSB	1.174E-15	1.751E-16	7.163E-15	1.068E-15	0.0475	0.0000
3	c3676-spike	LPSB	1.260E-15	3.369E-16	7.583E-15	2.027E-15	0.048	0.0000
BATCH NO.	18	Samples associated:						
DATE RUN	JUN 2016	LU276-LU289						
NAT								
1	c3654-nat	LNAT	5.701E-16	4.032E-16	5.731E-16	4.053E-16	0.2907	0.0000
2	c3535-nat	LNAT	5.701E-16	4.032E-16	5.731E-16	4.053E-16	0.2907	0.0000
PSB								
1	c3644-spike	LPSB	2.453E-15	3.470E-16	1.484E-14	2.099E-15	0.0485	0.0000
2	c3655-spike	LPSB	1.174E-15	1.751E-16	7.163E-15	1.068E-15	0.0475	0.0000
3	c3676-spike	LPSB	1.260E-15	3.369E-16	7.583E-15	2.027E-15	0.048	0.0000
BATCH NO.	23	Samples associated:						
DATE RUN	OCT 2016	LU360						
NAT								
1	c3791-nat	LNAT	3.518E-16	1.173E-16	3.524E-16	1.175E-16	0.2841	0.0000
2	c3811-nat	LNAT	1.024E-15	2.413E-16	1.030E-15	2.427E-16	0.2829	0.0000
3	c3831-nat	LNAT	2.8022E-15	3.154E-16	2.8151E-15	3.168E-16	0.2832	0.0010
PSB								
1	c3821-spike	LPSB2	1.036E-15	1.861E-16	6.388E-15	1.147E-15	0.0461	0.0000
2	c3832-spike	LPSB2	1.547E-15	5.495E-16	9.397E-15	3.334E-15	0.0469	0.0000
3	c3841-spike	LPSB2	1.324E-15	2.305E-16	8.253E-15	1.437E-15	0.0459	0.0000
BATCH NO.	24	Samples associated:						
DATE RUN	OCT 2017	LU373-LU386						
NAT								
	c3935-nat	LNAT	2.9208E-15	3.295E-16	2.926E-15	3.308E-16	0.2899	0.0024
	c3949-nat	LNAT	1.5763E-15	2.173E-16	1.5849E-15	2.185E-16	0.2883	0
	c3968-nat	LNAT	3.6823E-15	4.089E-16	3.6865E-15	4.094E-16	0.2898	0
PSB								
	c3940-spike	LPSB	1.7317E-15	1.889E-16	1.0565E-14	1.152E-15	0.0475	0
	c3959-spike	LPSB	2.5302E-15	2.431E-16	1.5289E-14	1.469E-15	0.048	0
	c3979-spike	LPSB	1.8772E-15	2.271E-16	1.1451E-14	1.385E-15	0.0474	0

	37Cl/35Cl	s (37Cl/35Cl)
R_natural	0.3198	0.0000

	37Cl/35Cl	s (37Cl/35Cl)
R_spike	0.0503	0.0013

	37Cl/35Cl	s (37Cl/35Cl)
R_natural	0.3198	0.0000

	37Cl/35Cl	s (37Cl/35Cl)
R_spike	0.0503	0.0013

	37Cl/35Cl	s (37Cl/35Cl)
R_natural	0.3198	0.0000

	37Cl/35Cl	s (37Cl/35Cl)
R_spike	0.0504	0.0013

	37Cl/35Cl	s (37Cl/35Cl)
R_natural	0.3198	0.0000

	37Cl/35Cl	s (37Cl/35Cl)
R_spike	0.0505	0.0013

Figure A12: AMS Blank measurements

Analytical blanks: no processing has been applied, these blanks are used for correcting AMS-specific results

NAT	Sample ID	Material type	36Cl/35Cl	s (36Cl/35Cl)	36Cl/37Cl	s (36Cl/37Cl)	37Cl/35Cl	s (37Cl/35Cl)
BATCH NO.	25	Samples associated:						
DATE RUN	OCT 2017	LU389-LU402						
NAT								
	c3992-nat	LNAT	1.7902E-15	2.464E-16	1.7975E-15	2.474E-16	0.288	0
	c4002-nat	LNAT	2.1938E-15	2.476E-16	2.1849E-15	2.465E-16	0.2904	0
	c4012-nat	LNAT	1.7619E-15	2.631E-16	1.7503E-15	2.613E-16	0.2911	0
PSB								
	c3993-spike	LPSB	1.265E-15	2.579E-16	7.7125E-15	1.573E-15	0.0476	0
	c4003-spike	LPSB	7.7629E-16	1.443E-16	4.6803E-15	8.7E-16	0.048	0
	c4013-spike	LPSB	3.2826E-15	4.652E-16	1.8859E-14	2.672E-15	0.0503	0
BATCH NO.	26	Samples associated:						
DATE RUN	OCT 2017	LU405-LU410						
NAT								
	c3935-nat	LNAT	2.9208E-15	3.295E-16	2.926E-15	3.308E-16	0.2899	0.0024
	c3949-nat	LNAT	1.5763E-15	2.173E-16	1.5849E-15	2.185E-16	0.2883	0
	c3968-nat	LNAT	3.6823E-15	4.089E-16	3.6865E-15	4.094E-16	0.2898	0
PSB								
	c3940-spike	LPSB	1.7317E-15	1.889E-16	1.0565E-14	1.152E-15	0.0475	0
	c3959-spike	LPSB	2.5302E-15	2.431E-16	1.5289E-14	1.469E-15	0.048	0
	c3979-spike	LPSB	1.8772E-15	2.271E-16	1.1451E-14	1.385E-15	0.0474	0

	37Cl/35Cl	s (37Cl/35Cl)
R_natural	0.3198	0.0000

	37Cl/35Cl	s (37Cl/35Cl)
R_spike	0.0505	0.0013

	37Cl/35Cl	s (37Cl/35Cl)
R_natural	0.3198	0.0000

	37Cl/35Cl	s (37Cl/35Cl)
R_spike	0.0505	0.0013

Figure A13: AMS Blank measurements

A3 Terrestrial laser scan slope pick data

I picked the TLS profile 10 times for each sample site. I record the parameters that resulted from each one of these picks in the tables below. This gives some idea of the uncertainty introduced into model geometry parameters that result from using this method.

Table A1: CF1 TLS slope picks

Iteration	Throw	Heave	Alpha	Beta	Gamma
1	9.1476	7.0626	31.1666	51.2204	35.2923
2	9.229	7.1293	31.9953	51.2121	35.2374
3	8.1115	6.2168	32.0039	51.2608	36.7594
4	9.5753	7.3835	32.1942	51.2976	34.527
5	9.9315	7.6753	32.3996	51.2762	33.9983
6	9.2521	7.1496	33.2999	51.2014	35.3534
7	9.8062	7.5736	33.1448	51.2833	34.1416
8	9.9652	7.7309	33.1013	51.1745	34.1403
9	9.4484	7.2448	32.6563	51.493	35.4592
10	9.8454	7.6287	32.9553	51.1903	34.1024
Average	9.43	7.27	32.49	51.26	34.90
Standard deviation	0.53	0.42	0.63	0.09	0.84

Table A2: CF2 TLS slope picks

Iteration	Throw	Heave	Alpha	Beta	Gamma
1	19.4214	14.7988	33.8341	52.6931	34.0674
2	19.5827	13.9046	33.5546	54.6236	33.4092
3	19.1762	13.6794	32.2814	54.4977	34.0232
4	21.2181	15.136	31.6562	54.4977	32.0989
5	19.8849	14.1849	33.526	54.4977	32.6409
6	19.9206	14.7835	33.3268	53.4201	32.7735
7	20.3209	14.8982	32.1266	53.7532	33.1756
8	19.0909	13.8151	32.5836	54.1086	33.7435
9	18.923	13.6936	33.4477	54.1086	34.2269
10	19.3833	14.3125	33.9247	53.5581	33.6953
Standard deviation	0.65	0.51	0.75	0.59	0.67
Average	19.69	14.32	33.03	53.98	33.39

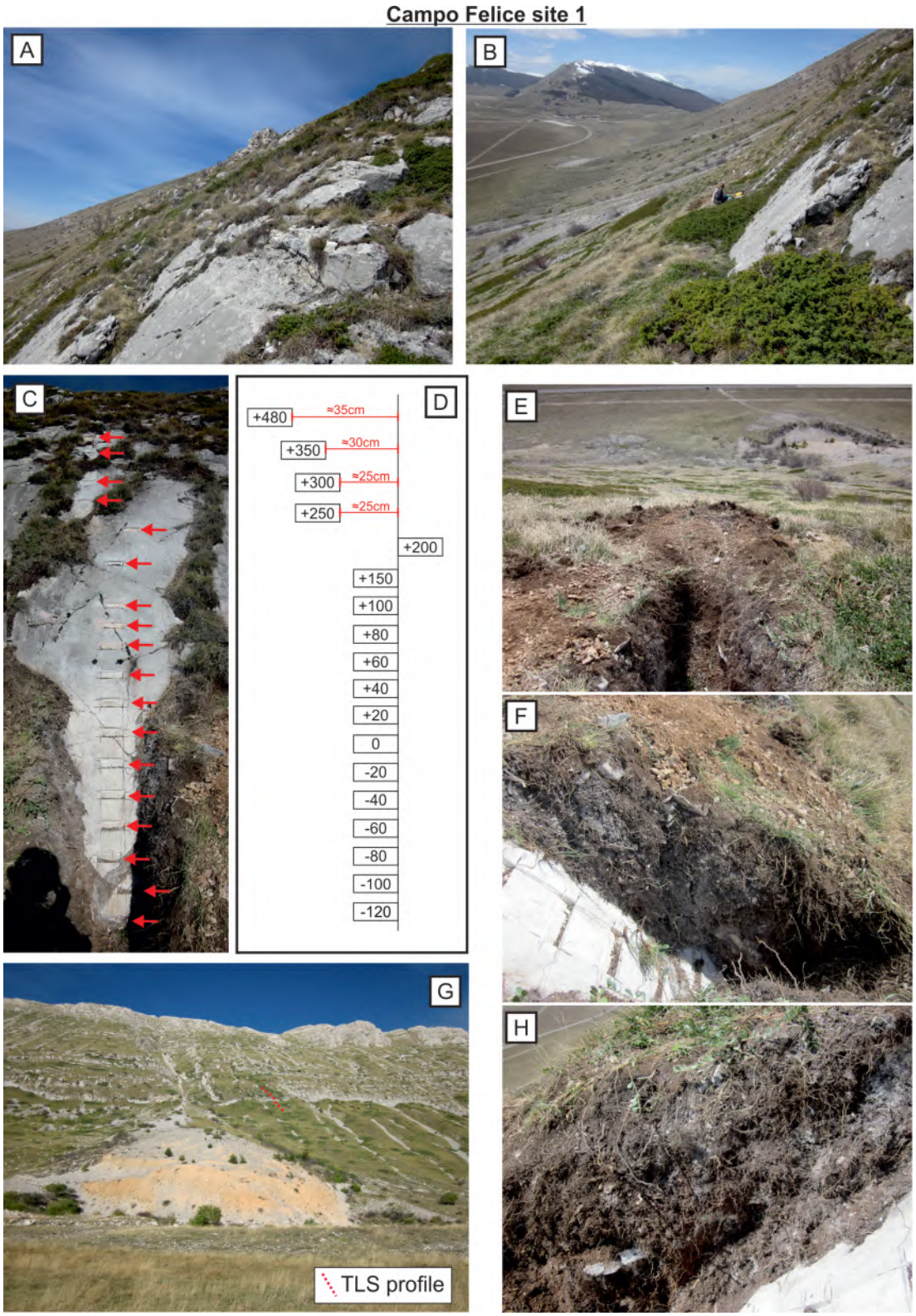
Campo Felice site 1
A
B
C
D
+480
≈35cm
+350
≈30cm
+300
≈25cm
+250
≈25cm
+200
+150
+100
+80
+60
+40
+20
0
-20
-40
-60
-80
-100
-120
E
F
G
TLS profile
H

Figure A14

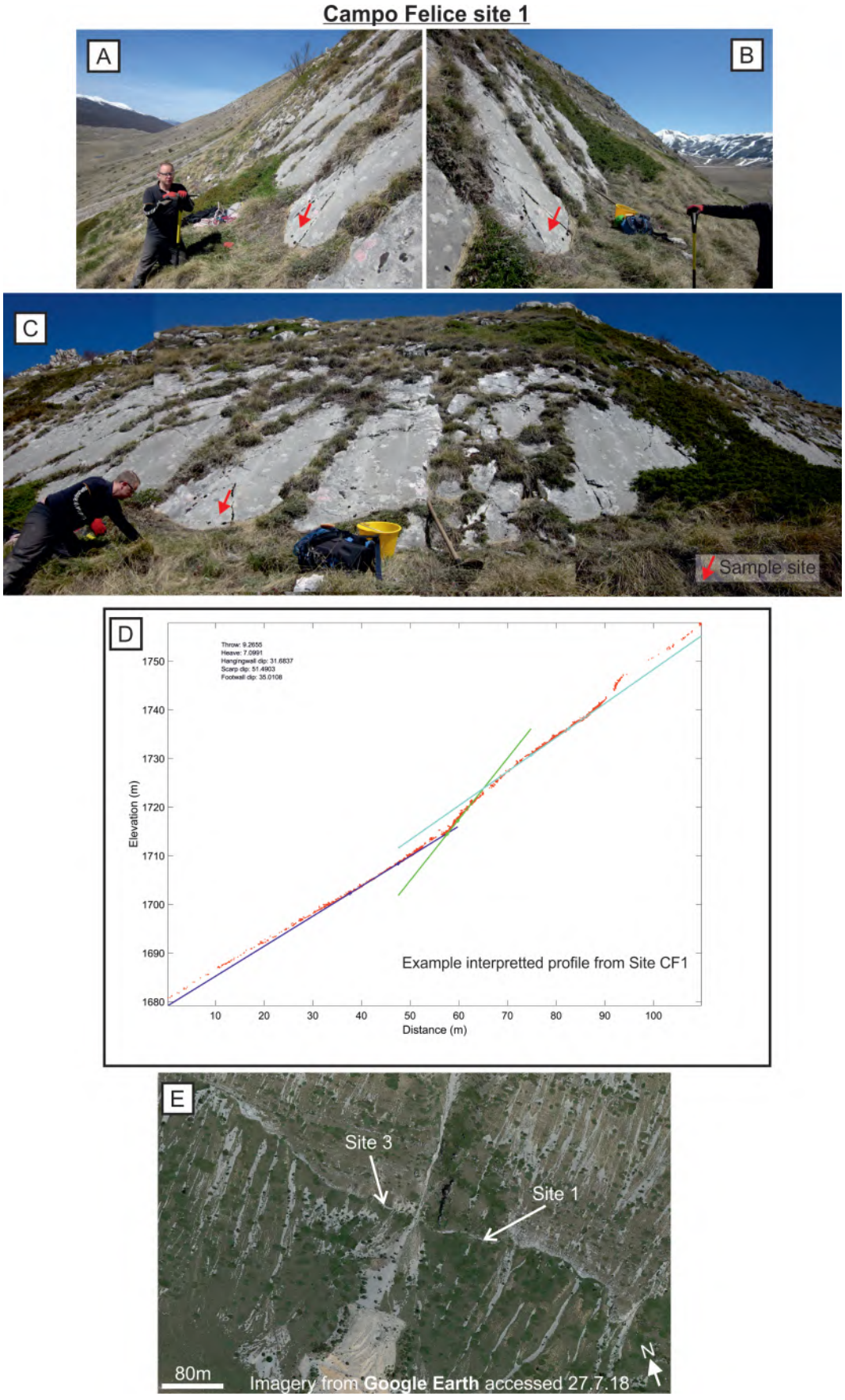
Campo Felice site 1
A
B
C
Sample site
D
Throw: 9.2655
Heave: 7.0991
Hangingwall dip: 31.6837
Scarp dip: 51.4903
Footwall dip: 35.0106
Elevation (m)
1750
1740
1730
1720
1710
1700
1690
1680
10
20
30
40
50
60
70
80
90
100
Distance (m)
Example interpretted profile from Site CF1
E
Site 3
Site 1
80m
Imagery from Google Earth accessed 27.7.18
N

Figure A15

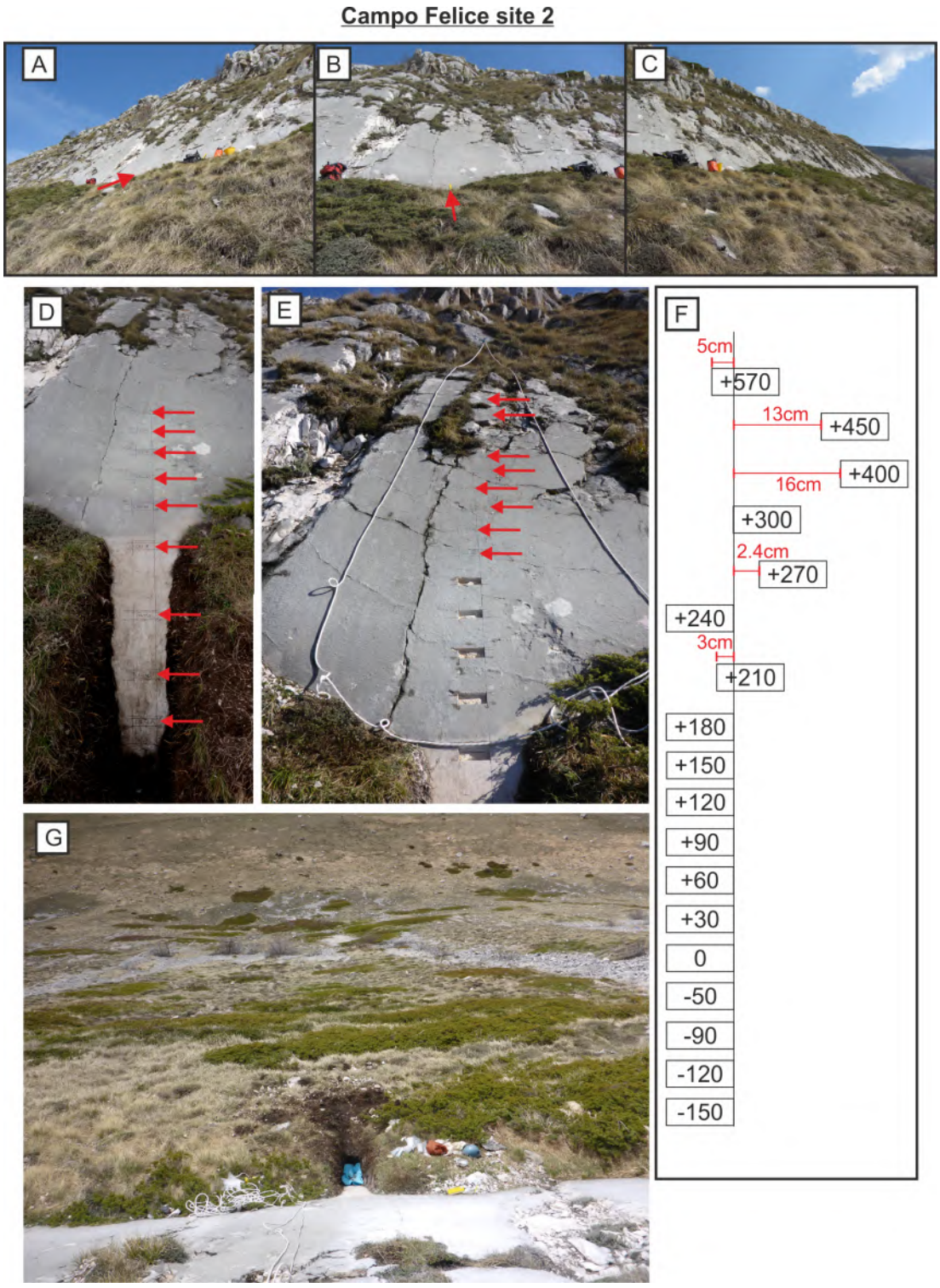
Campo Felice site 2
A
B
C
D
E
F
5cm
+570
13cm
+450
+400
16cm
+300
2.4cm
+270
+240
3cm
+210
+180
+150
+120
+90
+60
+30
0
-50
-90
-120
-150
G

Figure A16

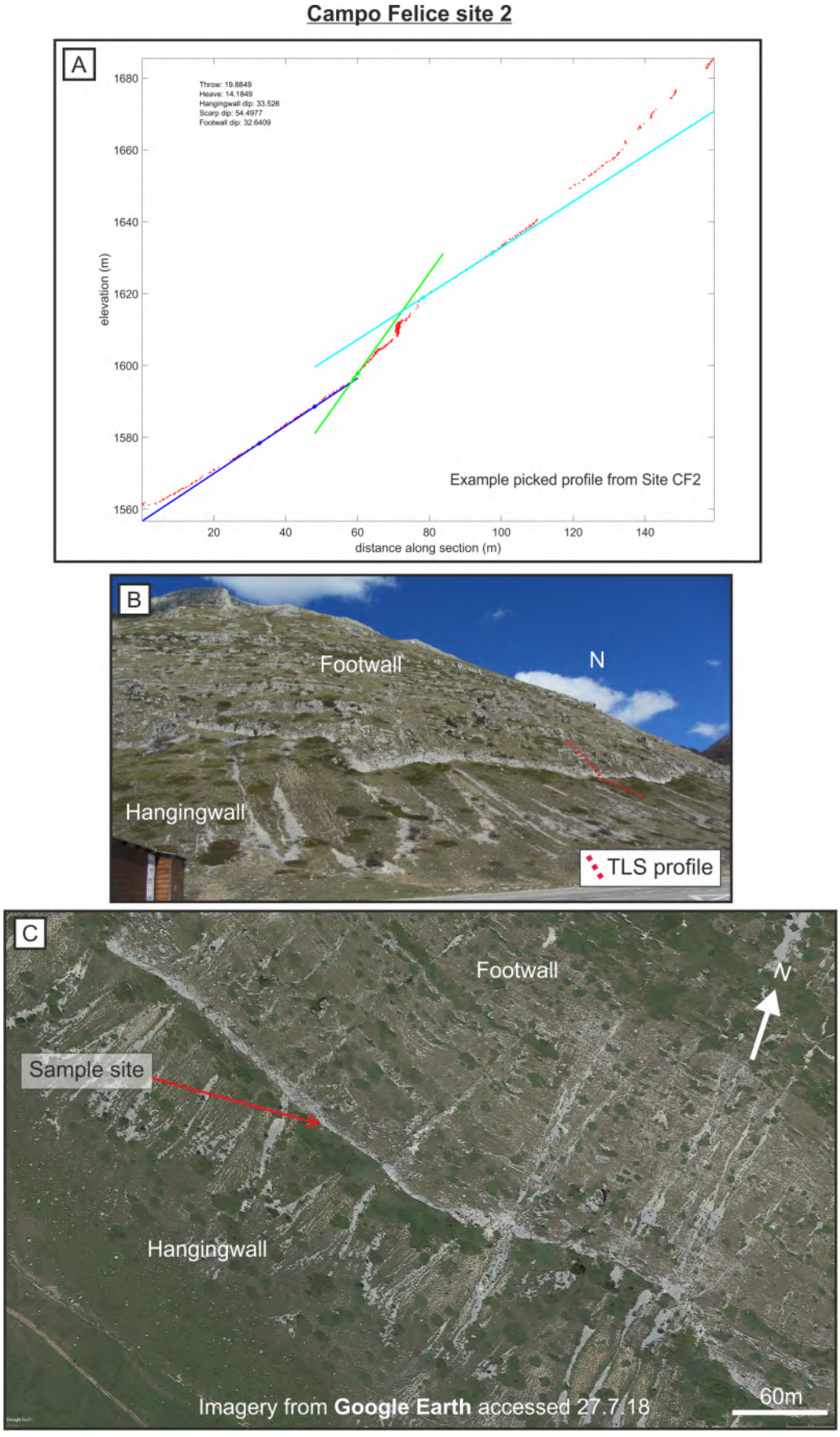
Campo Felice site 2
A
Throw: 19.8849
Heave: 14.1849
Hangingwall dip: 33.526
Scarp dip: 54.4977
Footwall dip: 32.6409
elevation (m)
distance along section (m)
Example picked profile from Site CF2
B
Footwall
N
Hangingwall
TLS profile
C
Footwall
N
Sample site
Hangingwall
Imagery from Google Earth accessed 27.7.18
60m

Figure A17

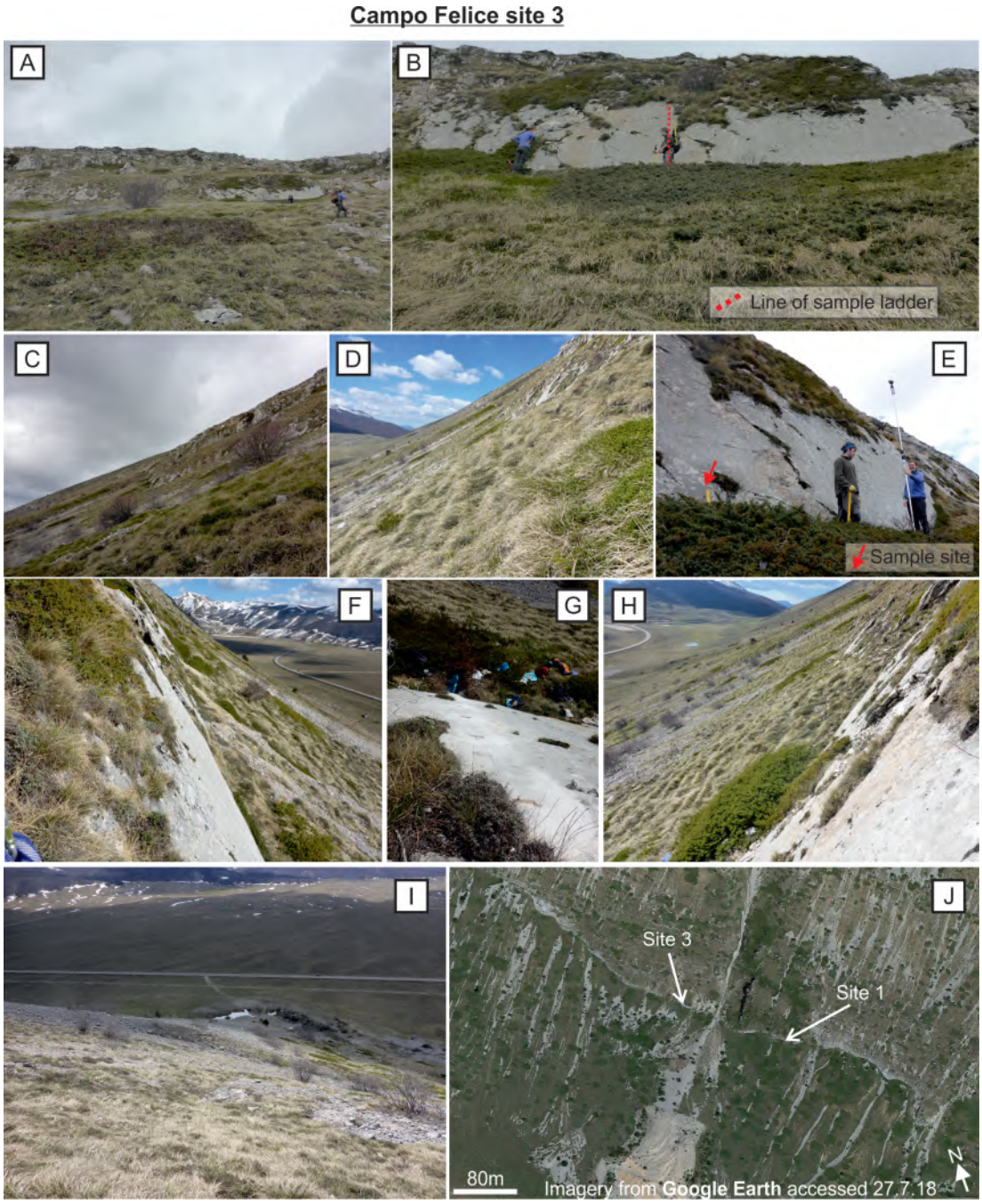
Campo Felice site 3
A
B
Line of sample ladder
C
D
E
Sample site
F
G
H
I
J
Site 3
Site 1
80m
Imagery from Google Earth accessed 27.7.18
N

Figure A18

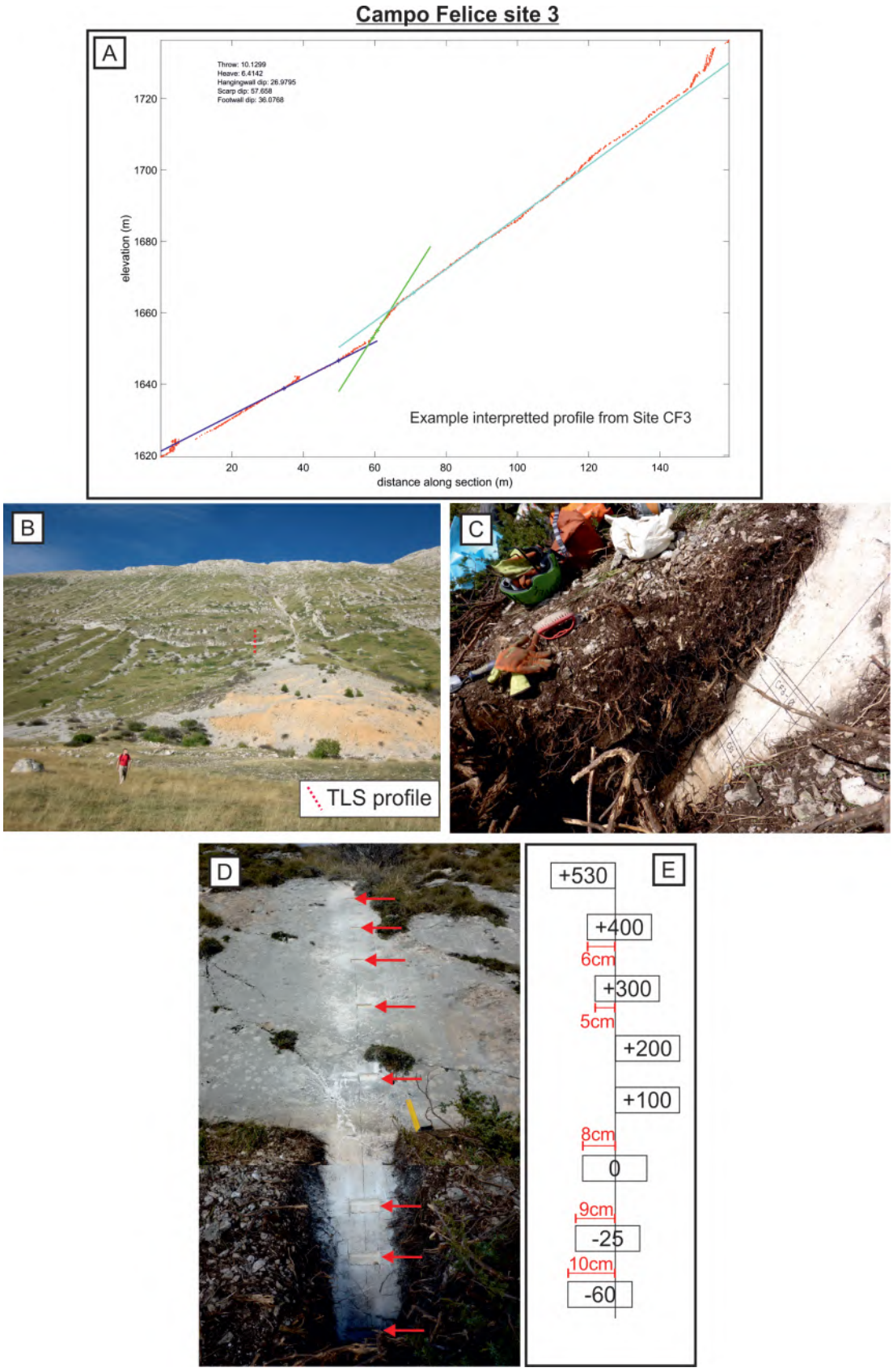
Campo Felice site 3
A
Throw: 10.1299
Heave: 6.4142
Hangingwall dip: 26.9795
Scarp dip: 57.658
Footwall dip: 36.0768
elevation (m)
distance along section (m)
Example interpretted profile from Site CF3
B
TLS profile
C
D
E
+530
+400
6cm
+300
5cm
+200
+100
8cm
0
9cm
-25
10cm
-60

Figure A19

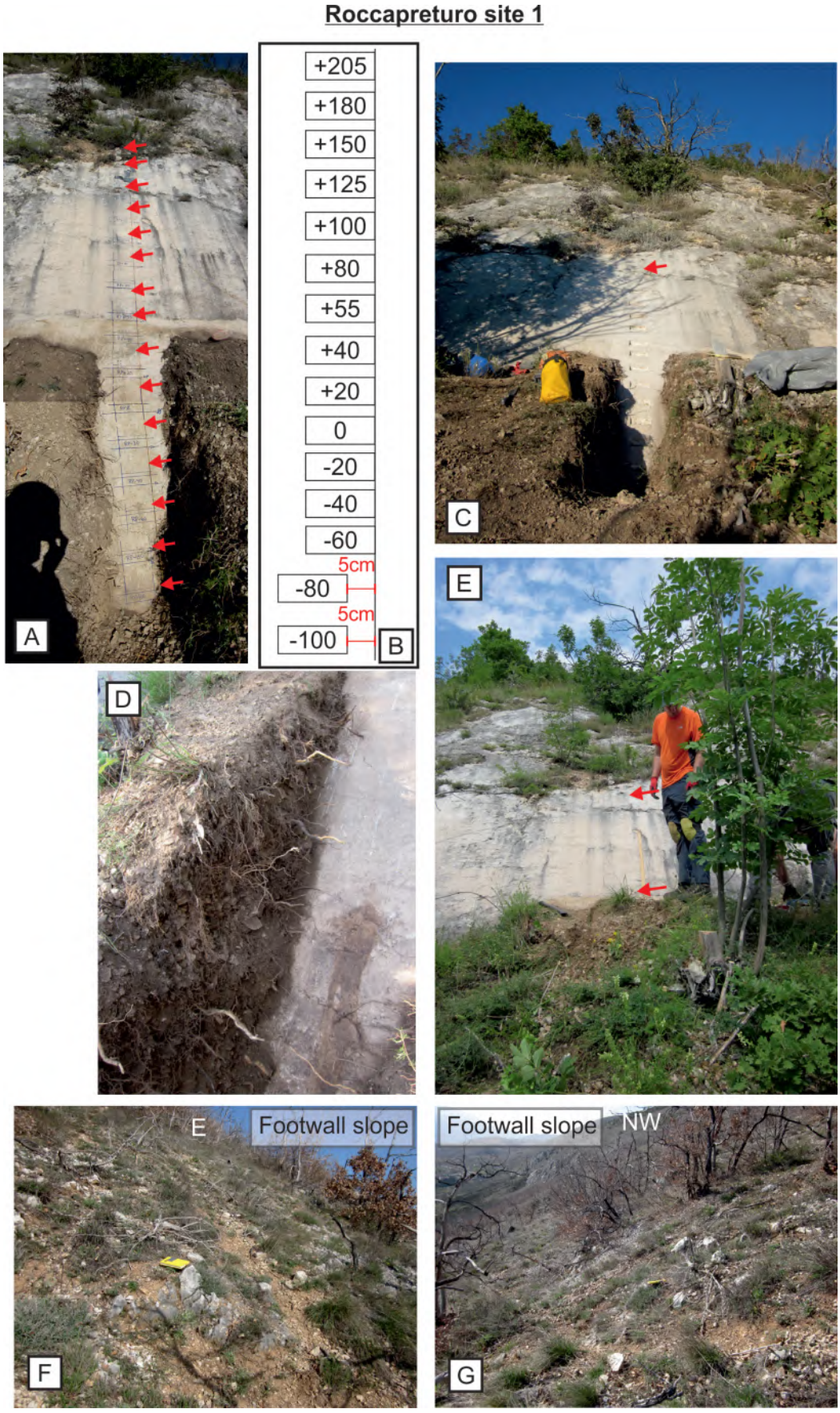
Roccapreturo site 1
+205
+180
+150
+125
+100
+80
+55
+40
+20
0
-20
-40
-60
5cm
-80
5cm
-100
A
B
C
D
E
E
Footwall slope
F
Footwall slope
NW
G

Figure A20

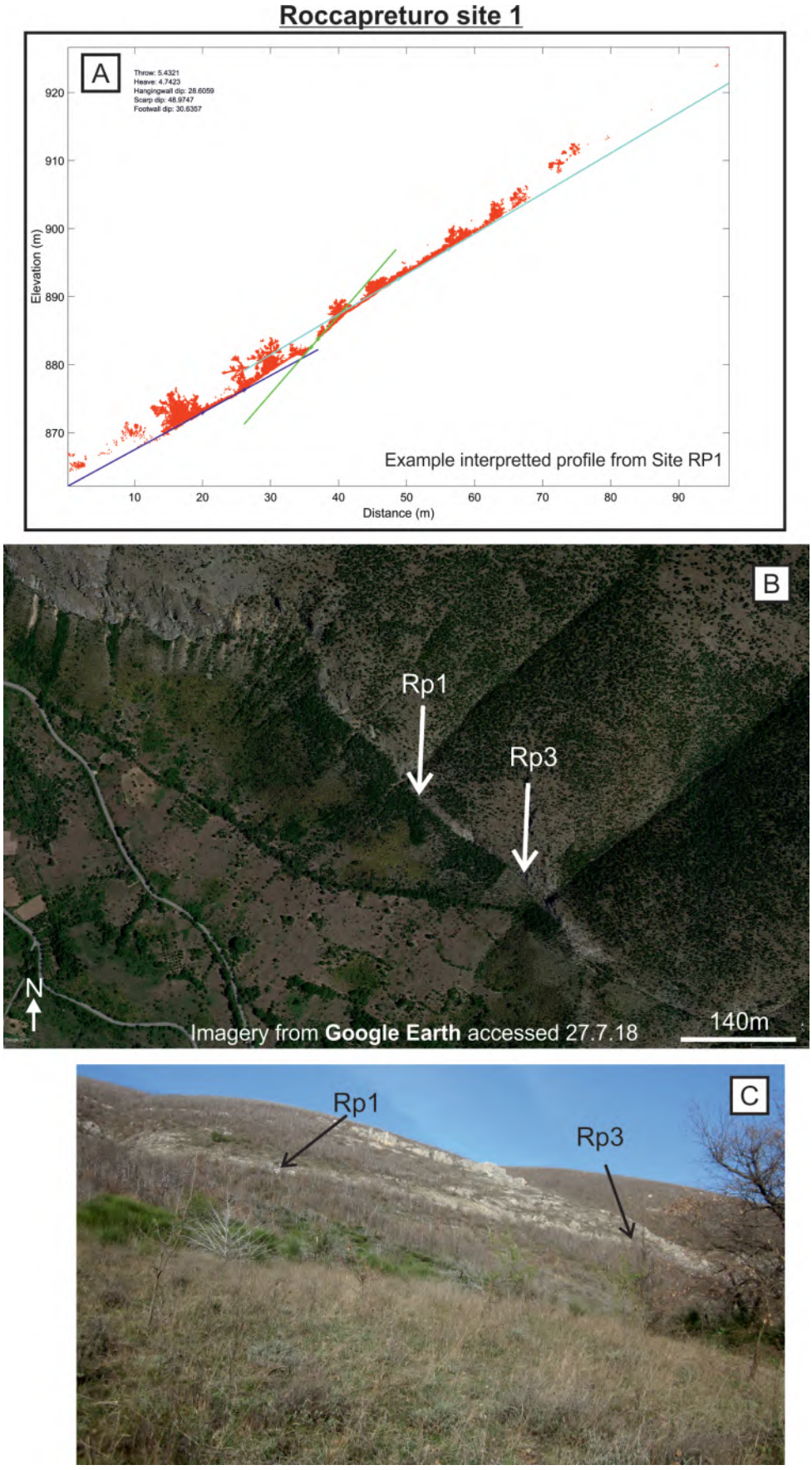
Roccapreturo site 1
A
Throw: 5.4321
Heave: 4.7423
Hangingwall dip: 28.6059
Scarp dip: 48.9747
Footwall dip: 30.6357
Elevation (m)
920
910
900
890
880
870
10
20
30
40
50
60
70
80
90
Distance (m)
Example interpretted profile from Site RP1
B
Rp1
Rp3
N
Imagery from Google Earth accessed 27.7.18
140m
C
Rp1
Rp3

Figure A21

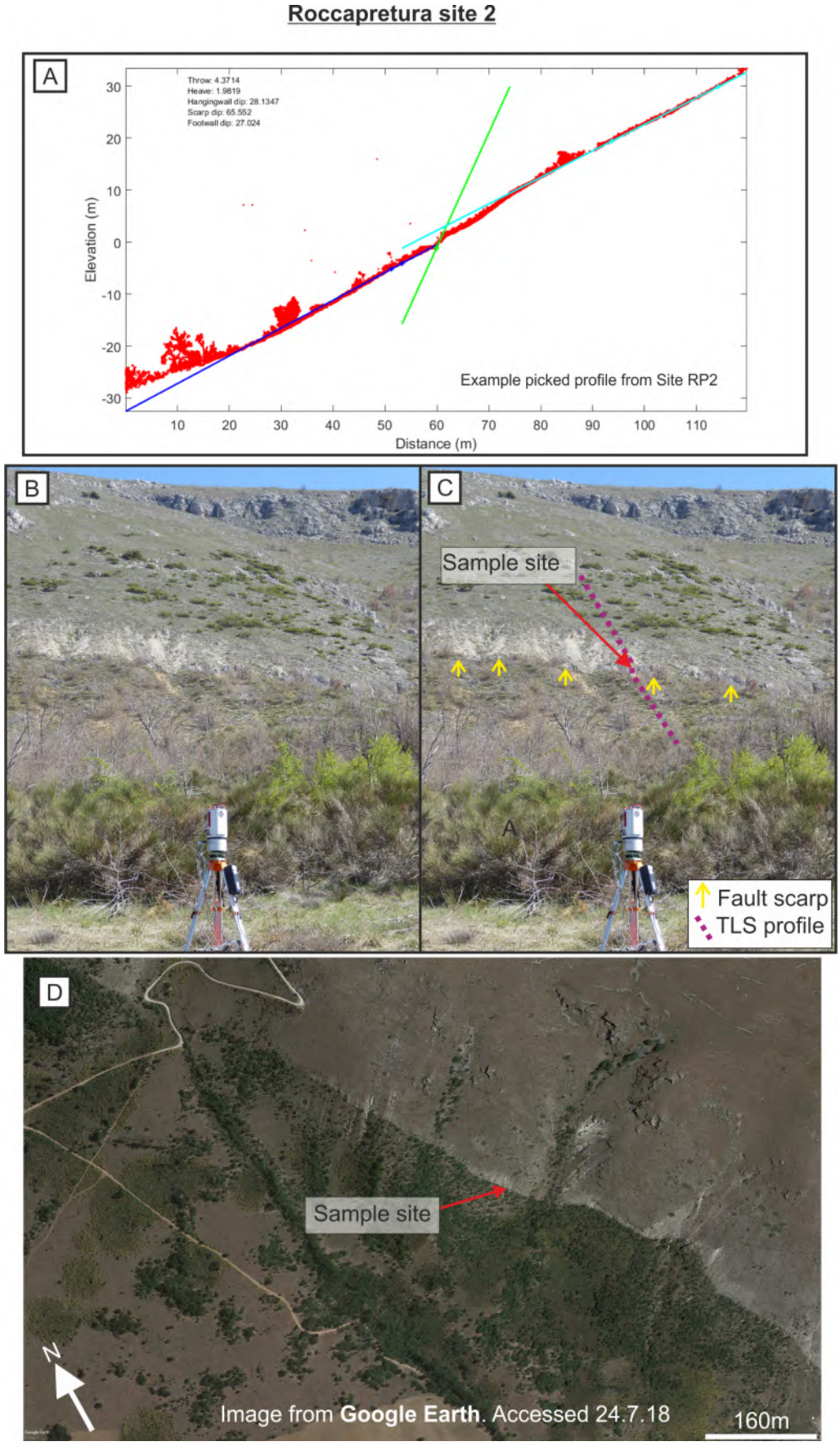
Roccapretura site 2
A
Throw: 4.3714
Heave: 1.9819
Hangingwall dip: 28.1347
Scarp dip: 65.552
Footwall dip: 27.024
Elevation (m)
Distance (m)
Example picked profile from Site RP2
B
C
Sample site
A
Fault scarp
TLS profile
D
Sample site
N
Image from Google Earth. Accessed 24.7.18
160m

Figure A22

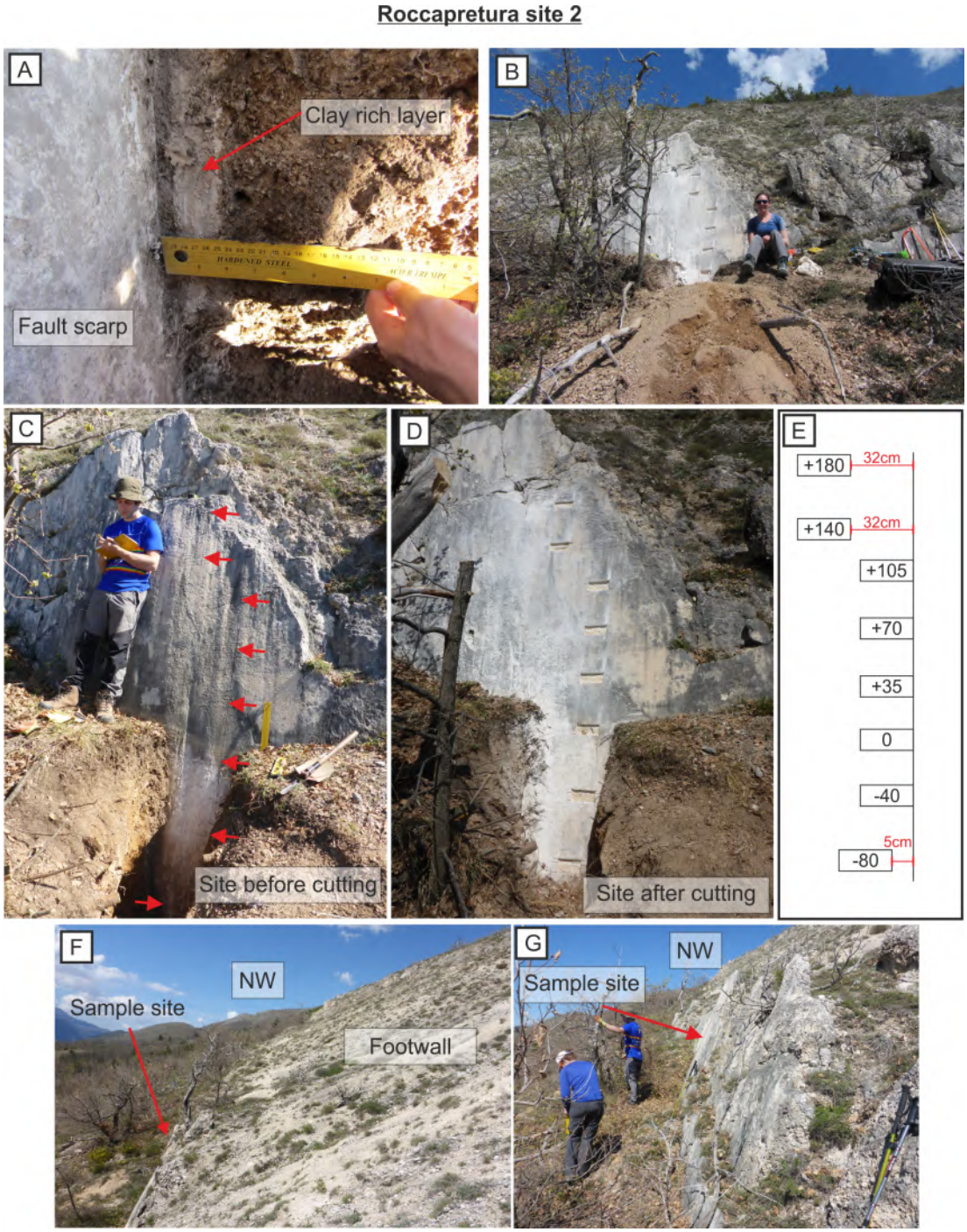
Roccapretura site 2
A
Clay rich layer
Fault scarp
B
C
Site before cutting
D
Site after cutting
E
+180
32cm
+140
32cm
+105
+70
+35
0
-40
5cm
-80
F
NW
Sample site
Footwall
G
NW
Sample site

Figure A23

Table A3: CF3 TLS slope picks

Iteration	**Throw**	**Heave**	**Alpha**	**Beta**	**Gamma**
1	10.3383	6.6131	28.1018	57.3941	34.6196
2	9.5757	6.1772	27.2244	57.1745	36.5643
3	9.8544	6.2398	28.621	57.658	35.7979
4	10.6322	6.8511	26.0529	57.2032	35.8259
5	10.5822	6.7147	27.1938	57.6039	35.3444
6	10.0543	6.4788	28.7162	57.2032	35.8605
7	10.1299	6.4142	26.9795	57.658	36.0768
8	10.5616	6.7606	26.7931	57.327	35.9398
9	9.9483	6.1273	27.2784	58.3705	36.1785
10	10.8904	7.014	26.927	57.2165	35.3484
Standard deviation	0.39	0.29	0.8	0.35	0.51
Average	10.26	6.54	27.39	57.48	35.76

Table A4: CF4 TLS slope picks

Iteration	**Throw**	**Heave**	**Alpha**	**Beta**	**Gamma**
1	19.1715	14.005	29.7489	53.8516	35.4755
2	18.7983	14.0907	32.0378	53.1456	34.124
3	18.7575	13.5707	31.3353	54.115	34.6453
4	18.8386	13.9769	30.8031	53.4273	34.7636
5	19.2192	14.2871	31.3307	53.3739	34.4846
6	19.1793	14.3686	31.7524	53.1604	34.1678
7	17.7645	13.0342	32.0384	53.7317	34.848
8	17.7291	12.8566	32.592	53.8973	34.8372
9	19.025	14.3155	32.4205	53.0402	34.3349
10	18.9126	14.076	31.2634	53.3409	34.8236
Standard deviation	0.52	0.51	0.8	0.35	0.38
Average	18.74	13.86	31.53	53.51	34.65

Table A5: RP1 TLS slope picks

Run	**Throw**	**Heave**	**Alpha**	**Beta**	**Gamma**
1	5.7425	4.9984	28.7157	49.0396	30.9068
2	5.5553	4.8537	28.6496	49	30.5254
3	5.3809	4.7378	29.2279	48.6972	30.877
4	5.8796	5.1065	28.601	49.1259	30.1281
5	5.4321	4.7423	28.6059	48.9747	30.6357
6	5.0019	4.3918	30.8583	48.7477	31.3227
7	5.491	4.8018	29.6952	48.909	30.5721
8	5.1071	4.4616	31.4749	48.9602	31.1141
9	4.874	4.2352	30.617	49.1353	31.6014
10	5.0632	4.4329	30.6532	48.8651	31.1207
Average	5.35	4.68	29.71	48.93	30.88
Standard deviation	0.33	0.28	1.10	0.15	0.43

Table A6: RP2 TLS slope picks

Run	**Throw**	**Heave**	**Alpha**	**Beta**	**Gamma**
1	4.2756	1.8062	28.3921	67.0858	26.9571
2	4.128	1.9211	27.8842	64.9523	27.2275
3	4.0218	1.7019	27.4326	67.0776	27.3508
4	4.7476	2.0843	26.247	66.2578	26.4795
5	4.3714	1.9819	28.1347	65.552	27.024
6	3.7617	1.6471	28.3827	66.2392	27.5527
7	4.3143	1.8015	27.0298	67.303	26.9648
8	4.4866	1.9658	24.9353	66.2396	26.8113
9	4.5472	1.9858	27.4445	66.315	26.8129
10	4.1606	1.7217	26.9213	67.6444	27.0708
Average	4.28	1.86	27.28	66.47	27.03
Standard deviation	0.28	0.15	1.07	0.83	0.30

B Modelling

B1 CRONUS and scaling factors

The code of Schlagenhauf et al., (2009), which provides the forward model used in this study, uses a scaling factor for the cosmogenic particle flux at the location of the sample site. This is to account for the differing flux of cosmogenic particles on the surface of the earth. There numerous ways to calculate this scaling factor, however it is usually a function of the lattitude, longitude and elevation of the site. Some of these methods for calculating scaling factors incorporate variation through time, which is primarily a function of fluctuating magnetic field strength with time as well as flux of solar particles. I use the CRONUS calc published by Marrero et al., (2016) using the LSD model as it takes into account the time variation in cosmogenic particle flux which will improve accuracy of our results. The scaling factors for each site can be found in a separate file.

Inspection of the whole model output vs data is key, it allows us to gain an understanding of what the distribution of likely models is and how well they fit the data. As well as running the MCMC flexible change point models I also run a more simple model which allows us to test which constant slip rate best fits the data. This allows us to see if a variable slip rate fits the data significantly better than a constant slip rate (figures

B1 and B3). A summary of the models used in this paper can be found in Table B2. In our results I present the average slip rate of models that fit the data to within 2 or 3 standard deviations. I use the RMSw values which means that if all the data fit to within 1 standard devation (SD), the RMSw value is equal to the square root of the number of samples. I multiply this value and use it to select models that have RMSw values less than or equal to the multiplied value. A table of number of models that fit to within 1-4 standard deviations can be found here (Table B1). Each model ran for 10^5 iterations and I removed a burn in of 10,000 iterations. I use these plots of model fit to data for each for 2,3 and 4 standard deviations to justify only using subsets of our models to calculate slip rates on the faults (figures B4 to B10.)

Figure B4 shows that models in SD3 and SD4 are generally not fitting well the two data points highest up the scarp, but models within 2 SD do seem to be fitting these reasonably well. Figure B5 shows similar and Figure B6 shows that it is primarily the highest data point that is not being fit well by models in SD3 and SD4. Figure B7 shows similar results between SD3 and SD4 in terms of slip history. These results indicate that sampling bias towards the bottom of the scarp may leads to the large variation in slip histories and average slip rate between SD 2,3 and 4 at Campo Felice sites 1-3. This sampling bias is unfortunately difficult to correct as it is more difficult to find well preserved places on the scarp higher up to sample, so there are necessarily fewer samples. It also demonstrates the importance of sampling as high up the well preserved scarp as possible, as these data are extremely informative about the slip history of a fault. I therefore use 2SD for sites CF1-CF3 and 3SD for site CF4.

RP1 does not appear to be particularly well fitted by the models (Figure B8), and some models in SD4 appear to be passing through only 1 or 2 data points. RP2 does have better agreement between models and data (Figure B9). RP3 appears to fit the data reasonably well in all subsets of the model output, the largest discprency is in the top few points (Figure B10). This suggests that there is some deficiency in the modeling of sites RP1 and RP2.

Standard deviations	CF1	CF2	CF3	CF4	RP1	RP2	RP3
1	0	0	147	0	0	3769	0
2	1686	621	6145	0	29	24864	530
3	28073	11351	18400	3688	57203	51353	28130
4	52459	33772	31086	16019	89058	71497	59000

Table B1: Number of models that fit within a number of standard deviations

Site and model name	Scarp height (cm)	Trench Depth (cm)	Hfinal (cm)	Offset(cm)	Elapsed time distribution type (years)	ET Mean (years)	ET stand. Dev. (years)	Alpha	Beta	Gamma	rho_coll	Scarp age distribution	Range/Mean	Range/Std dev	Number of runs
CF1	1560	120	1680	100	Uniform	2000	500	32	51	35	1.5	normal	15000	2500	100000
CF2	2440	150	2590	100	Uniform	2000	500	33	54	33	1.5	normal	15000	2500	100000
CF3	1230	60	1290	100	Uniform	2000	500	27	57	36	1.5	normal	15000	2500	100000
CF4	1870	0	1870	100	Uniform	2000	500	32	54	35	1.5	normal	15000	2500	100000
RP1	720	120	880	100	Uniform	2000	500	30	49	31	1.5	normal	15000	2500	100000
RP2	470	80	550	100	Uniform	2000	500	27	66	27	1.5	normal	15000	2500	100000
RP3	1020	0	1020	100	Uniform	2000	500	25	55	35	1.5	normal	15000	2500	100000
CF2 uniform	2440	150	2590	100	Uniform	2000	500	33	54	33	1.5	Uniform	0	24000	100000
RP1_20cm_slip	540	720	660	20	Uniform	2000	500	30	49	31	1.5	normal	15000	2500	100000
RP1_uniform_20cm_slip	720	120	880	20	Uniform	2000	500	30	49	31	1.5	uniform	0	24000	100000
RP1_1m_et	720	120	880	100	Uniform	5630	1856	30	49	31	1.5	normal	15000	2500	100000

Table B2: Table of parameters used in MCMC models.

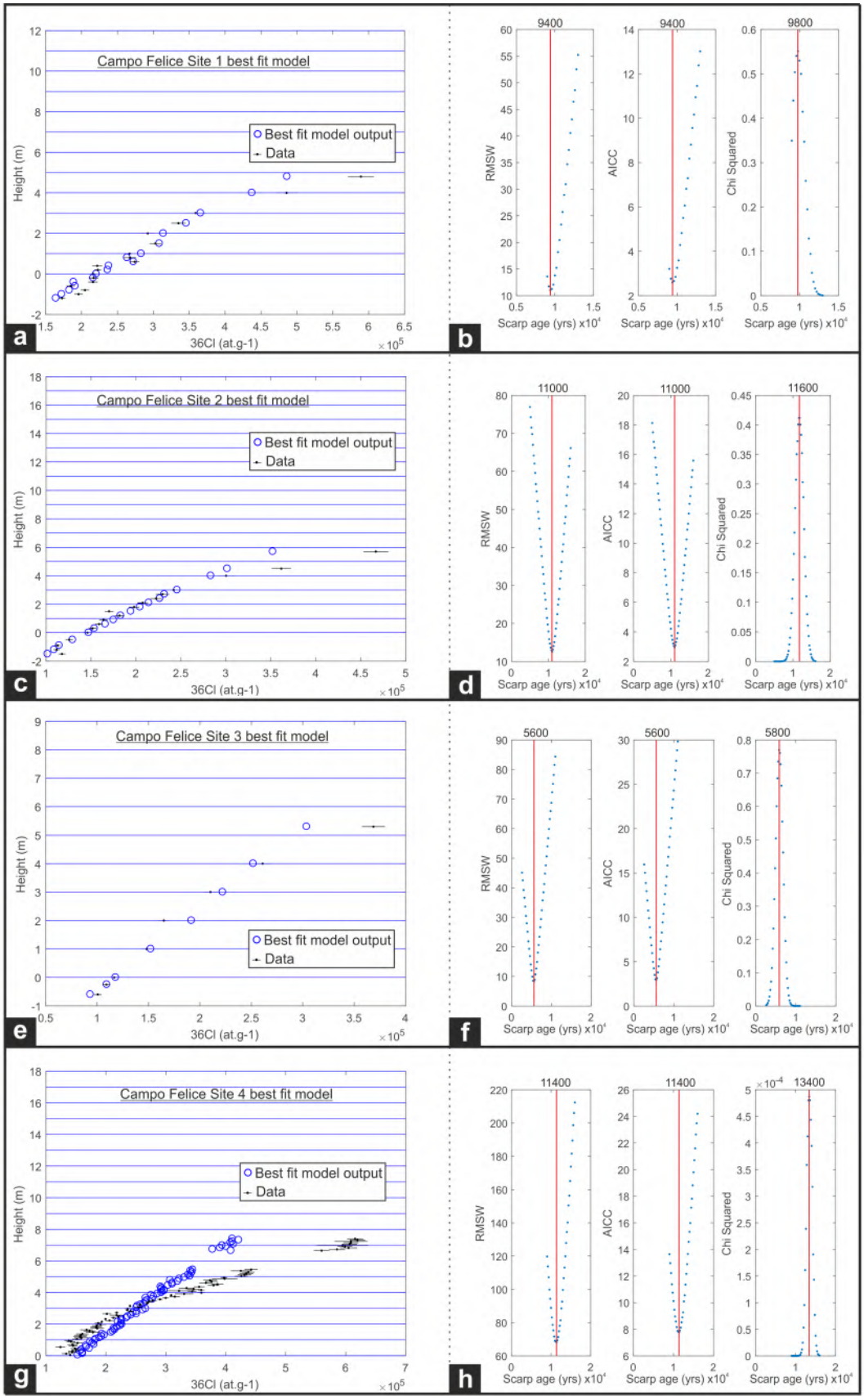

Figure B1: Panels on left show best fit constant slip rate model (lowest RMSw value), panels on right show the scarp age values that produce this as well as values for the lowest AICC and highest Chi squared scarp age.

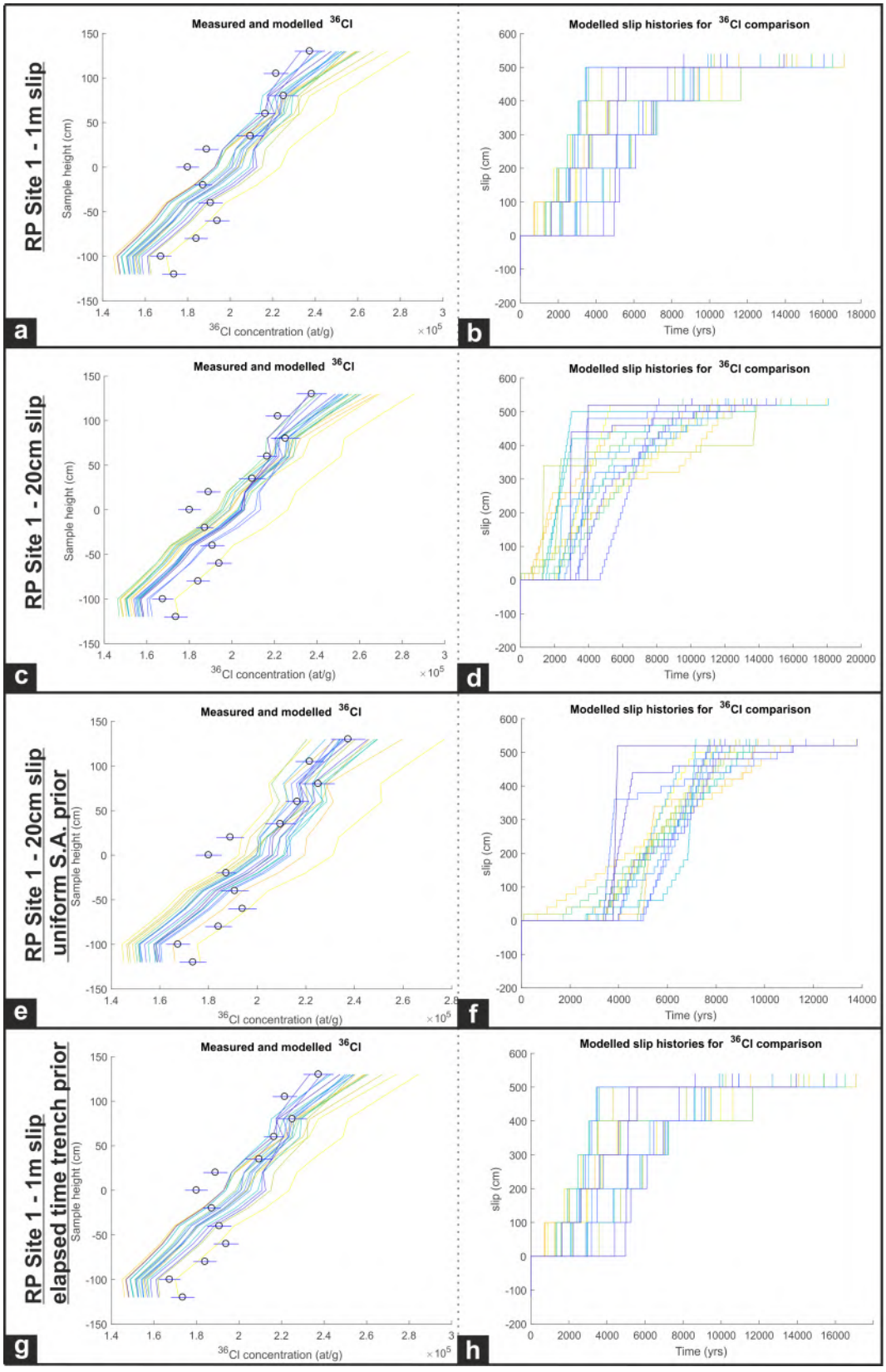

Figure B2: a,c,e and g show fit to data of every 5000th model (when ranked by likelihood) for models of site RP1 using different parameters. Circles represent data points and colored lines show model values, going from the highest likelihood in dark blue to the lowest likelihood in yellow. b,d,g and h show the corresponding slip histories using the same color scheme. These results show that it is unlikely to be the priors that are controlling the lack of fit to data. Details of the modeling can be found in Table B3.

Figures	Slip increment	Scarp age prior	Elapsed time prior
a-b	1m	normal	normal
c-d	20cm	normal	normal
e-f	20cm	uniform	normal
g-h	1m	normal	uniform

Table B3: Model parameters used for models shown in Figure B2

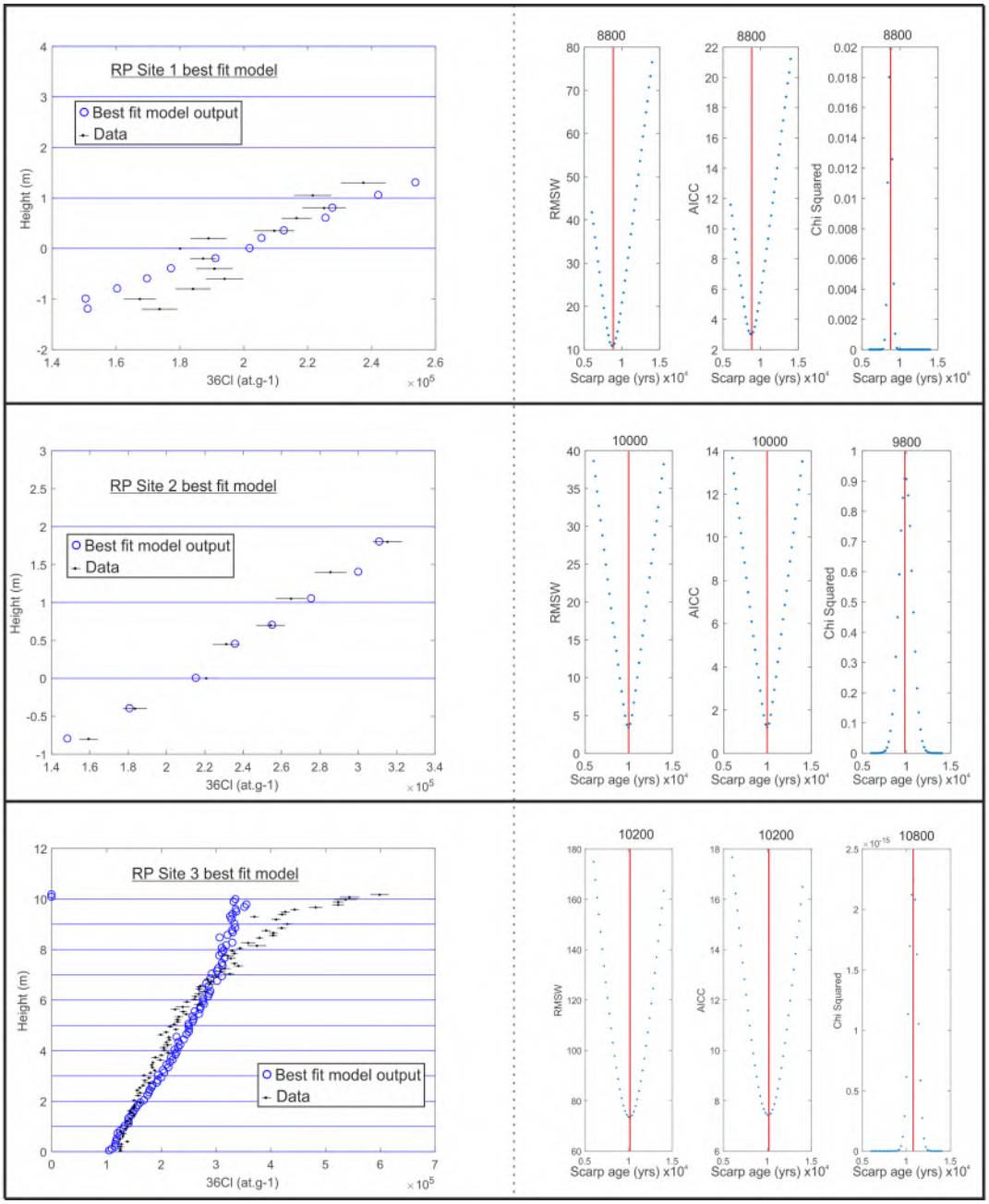

Figure B3: Panels on left show best fit constant slip rate model (lowest RMSw value), panels on right show the scarp age values that produce this as well as values for the lowest AICC and highest Chi squared scarp age.

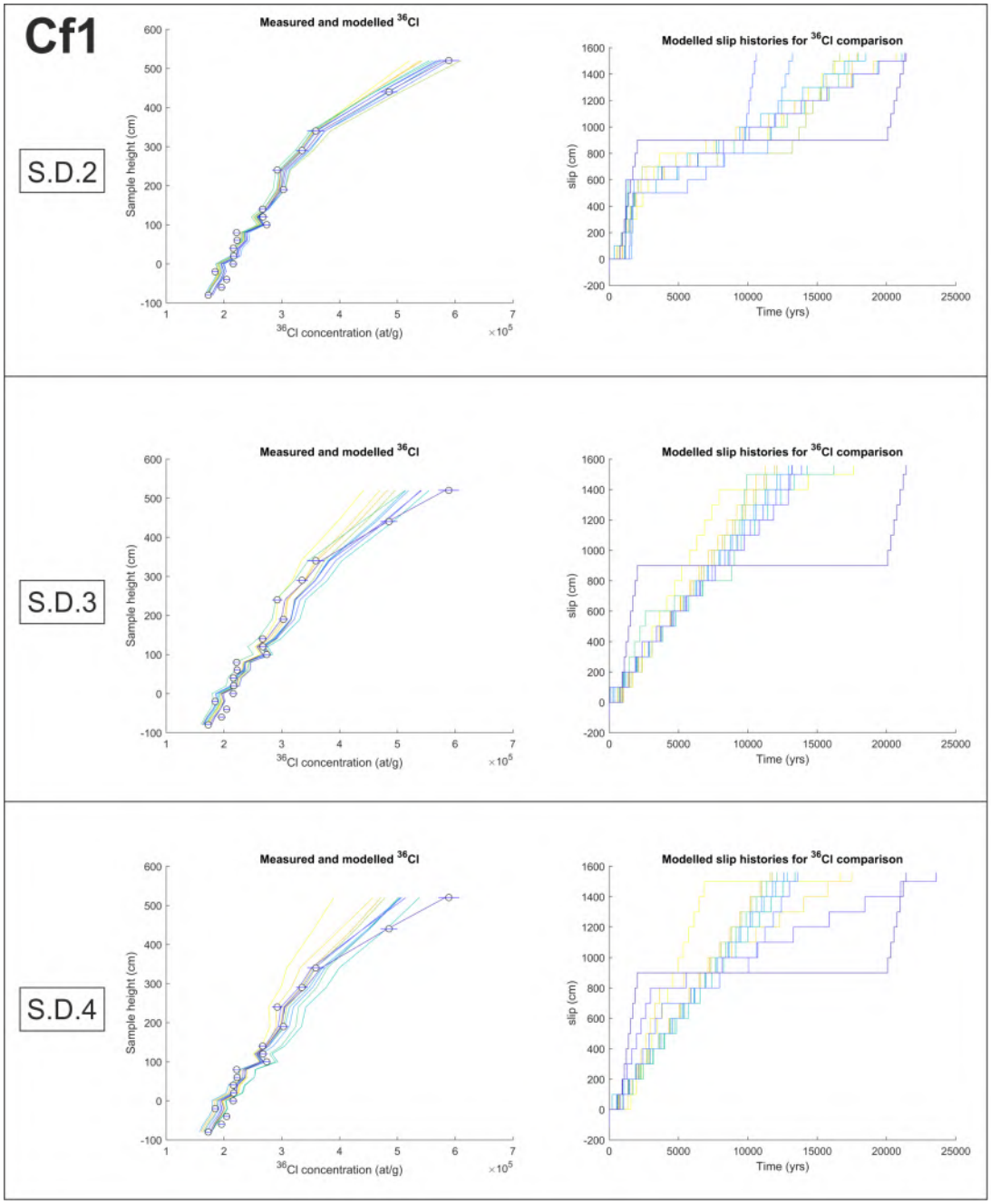

Figure B4: Plots on left show data and measurement errors in black circles and blue error bars for site CF1. Colored lines show data points of models, with each line representing one model. Darker colours are higher likelihood and lighter colours show lower likelihood. I plot different selections of models; models that fit within 2,3 or 4 standard deviations. I present 10 models for each subset of models, ranging from the highest likelihood likely to lowest likelihood of the models at equal intervals through the distribution. Plots on the right show the equivalent model slip histories.

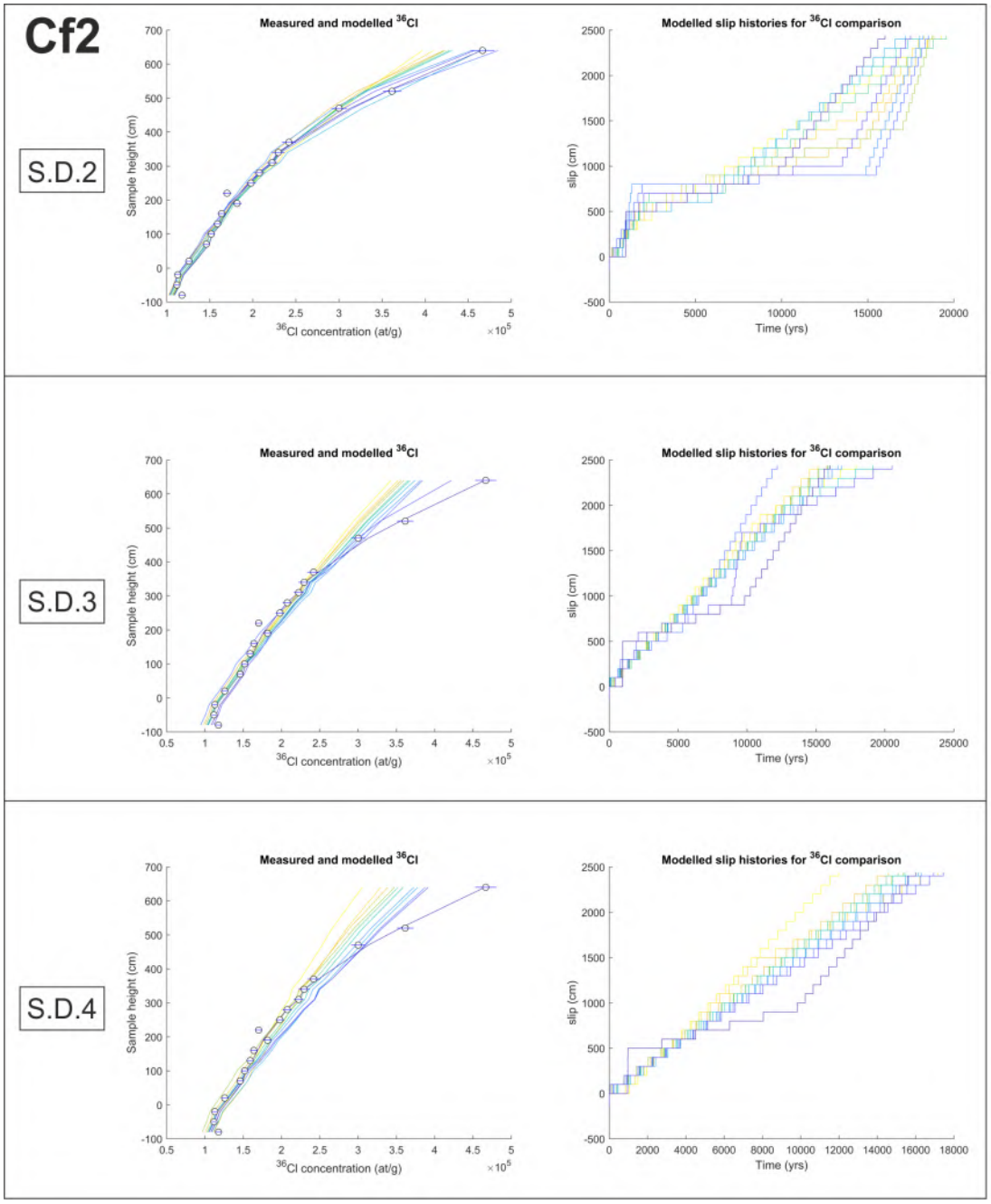

Figure B5: Plots on left show data and measurement errors in black circles and blue error bars for site CF2. Colored lines show data points of models, with each line representing one model. Darker colours are higher likelihood and lighter colours show lower likelihood. I plot different selections of models; models that fit within 2,3 or 4 standard deviations. I present 10 models for each subset of models, ranging from the highest likelihood likely to lowest likelihood of the models at equal intervals through the distribution. Plots on the right show the equivalent model slip histories.

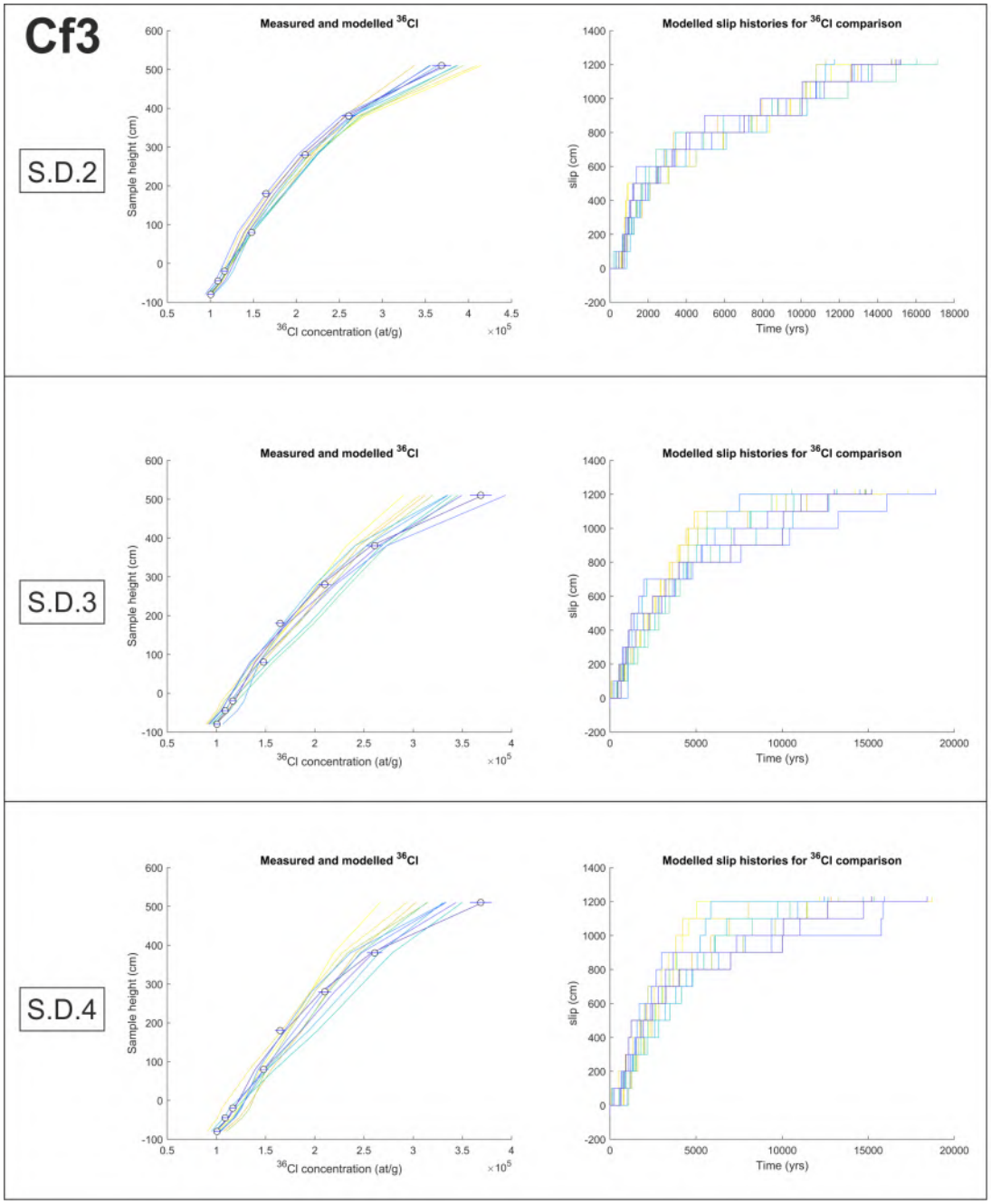

Figure B6: Plots on left show data and measurement errors in black circles and blue error bars for site CF3. Colored lines show data points of models, with each line representing one model. Darker colours are higher likelihood and lighter colours show lower likelihood. I plot different selections of models; models that fit within 2,3 or 4 standard deviations. I present 10 models for each subset of models, ranging from the highest likelihood likely to lowest likelihood of the models at equal intervals through the distribution. Plots on the right show the equivalent model slip histories.

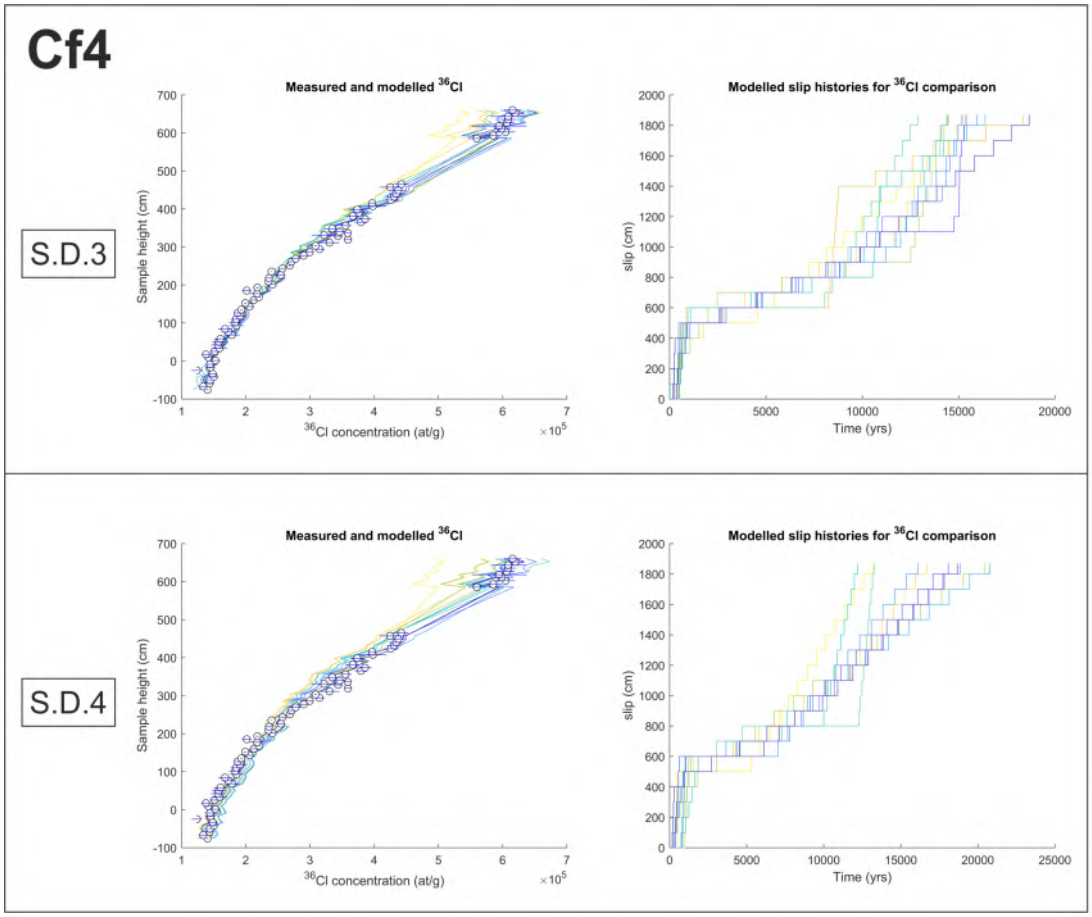

Figure B7: Plots on left show data and measurement errors in black circles and blue error bars for site CF4. Colored lines show data points of models, with each line representing one model. Darker colours are higher likelihood and lighter colours show lower likelihood. I plot different selections of models; models that fit within 2,3 or 4 standard deviations. I present 10 models for each subset of models, ranging from the highest likelihood likely to lowest likelihood of the models at equal intervals through the distribution. Plots on the right show the equivalent model slip histories.

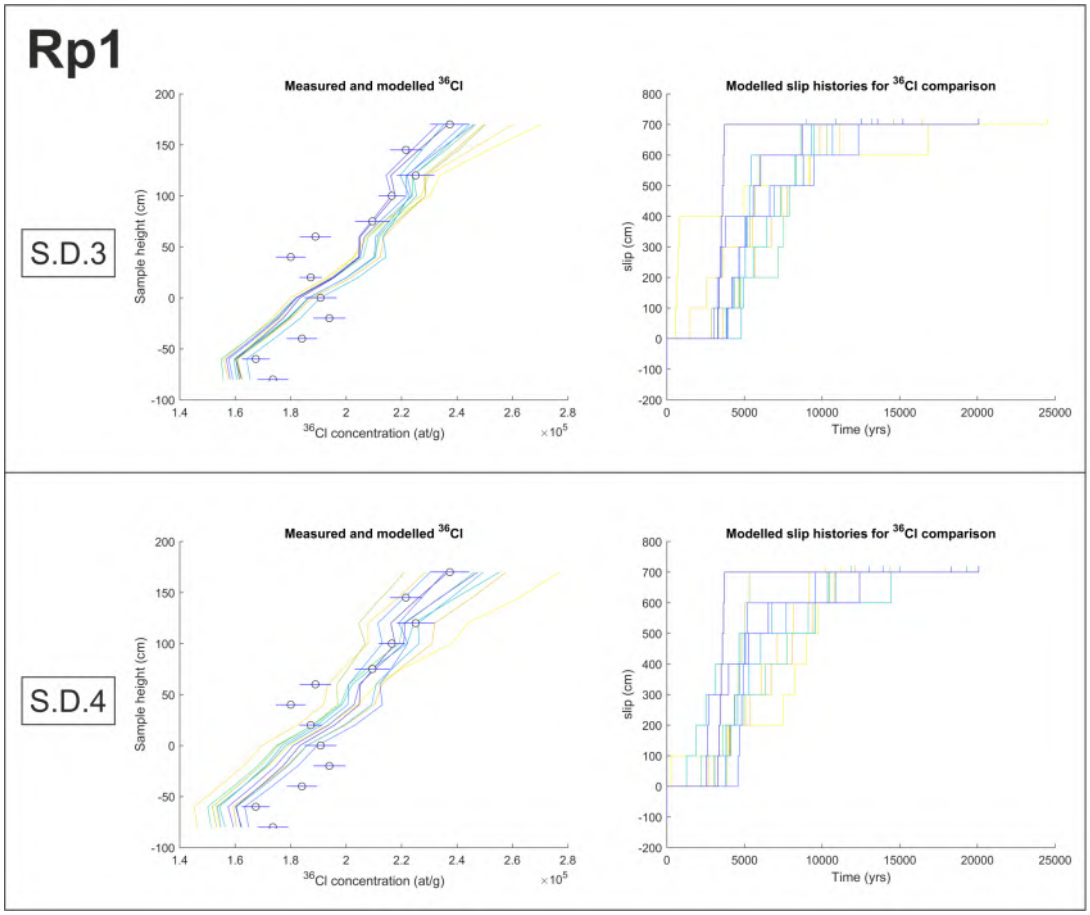

Figure B8: Plots on left show data and measurement errors in black circles and blue error bars for site RP1. Colored lines show data points of models, with each line representing one model. Darker colours are higher likelihood and lighter colours show lower likelihood. I plot different selections of models; models that fit within 2,3 or 4 standard deviations. I present 10 models for each subset of models, ranging from the highest likelihood likely to lowest likelihood of the models at equal intervals through the distribution. Plots on the right show the equivalent model slip histories.

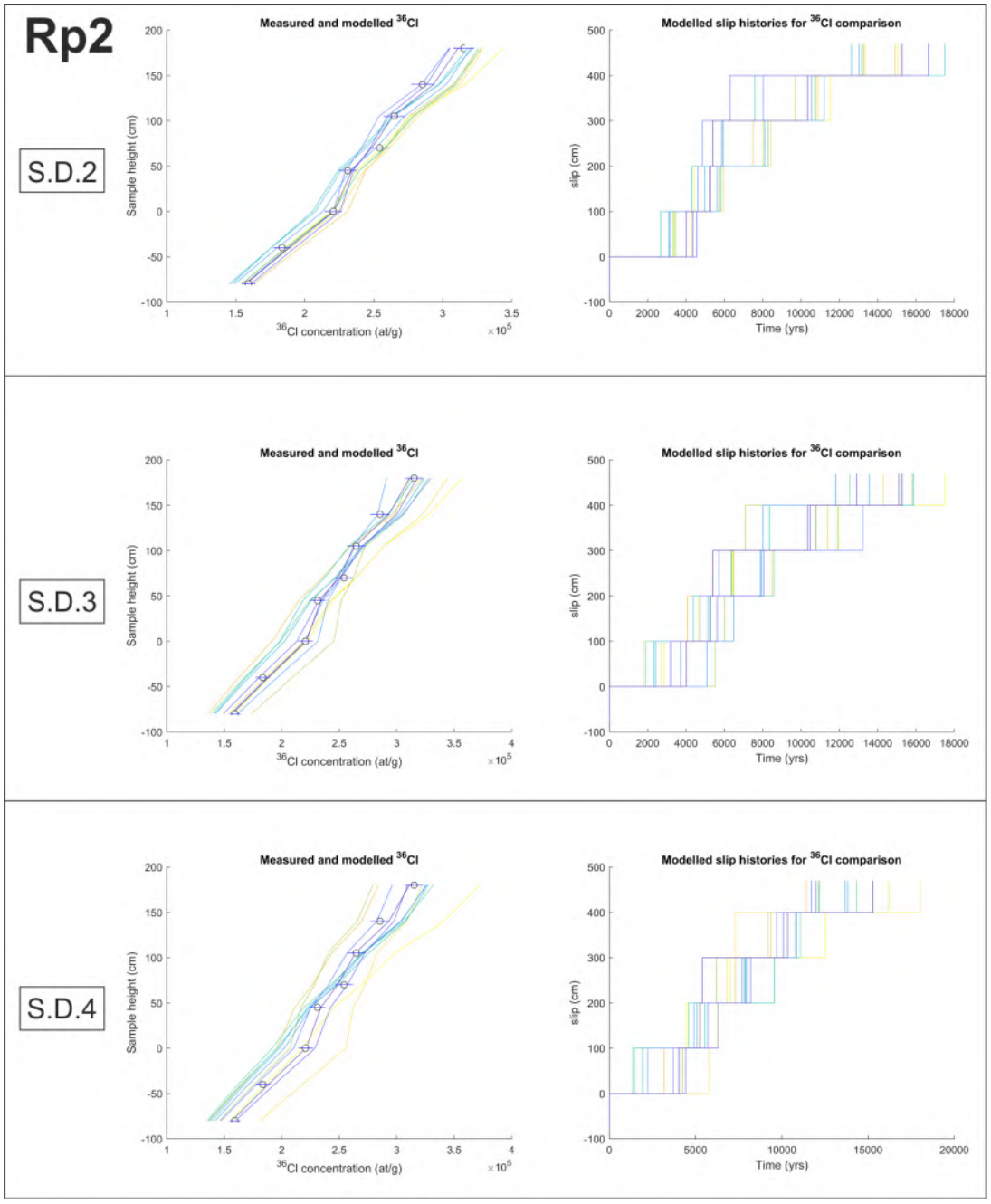

Figure B9: Plots on left show data and measurement errors in black circles and blue error bars for site RP2. Colored lines show data points of models, with each line representing one model. Darker colours are higher likelihood and lighter colours show lower likelihood. I plot different selections of models; models that fit within 2,3 or 4 standard deviations. I present 10 models for each subset of models, ranging from the highest likelihood likely to lowest likelihood of the models at equal intervals through the distribution. Plots on the right show the equivalent model slip histories.

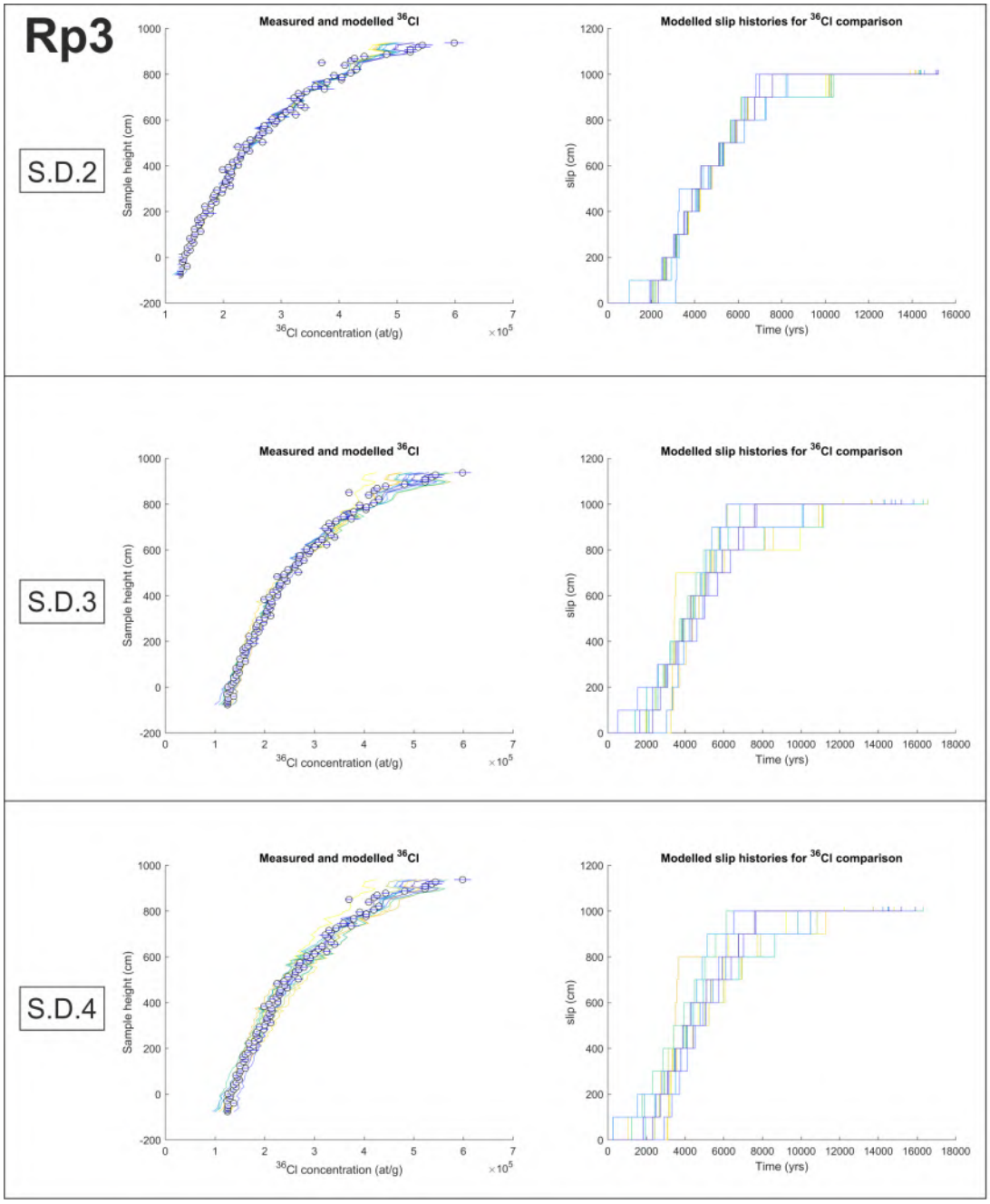

Figure B10: Plots on left show data and measurement errors in black circles and blue error bars for site RP3. Colored lines show data points of models, with each line representing one model. Darker colours are higher likelihood and lighter colours show lower likelihood. I plot different selections of models; models that fit within 2,3 or 4 standard deviations. I present 10 models for each subset of models, ranging from the highest likelihood likely to lowest likelihood of the models at equal intervals through the distribution. Plots on the right show the equivalent model slip histories.

B2 Calculation of incremental slip rate

To calculate the incremental slip rate of each sample site I use the mean slip rate of our selected slip histories. I calculate it using the following method:

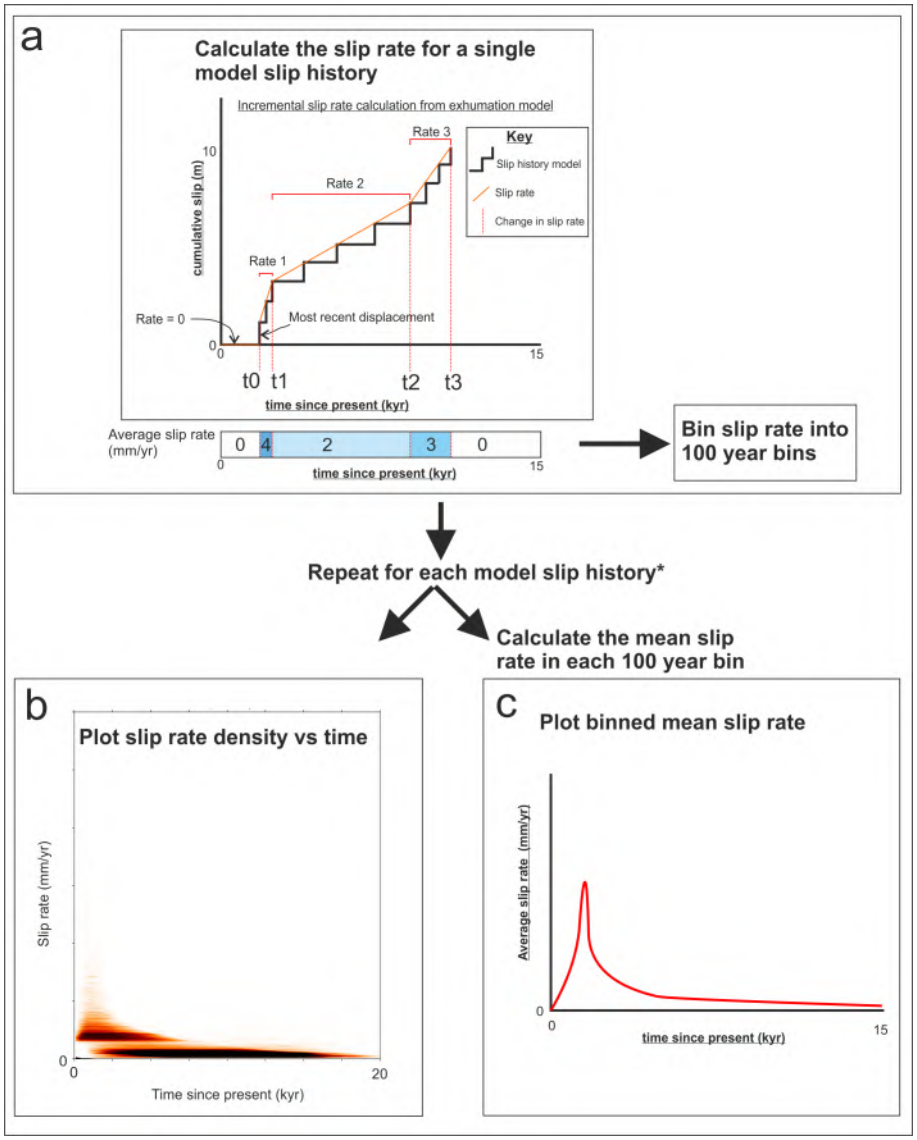

Figure B11: Schematic of how I calculate the mean slip rate and construct plots seen elsewhere in this paper.

The effect of using different sections of the model output, i.e. models that fit the data to within 2,3 or 4 standard deviations are shown in the plots below in the rest of this subsection:

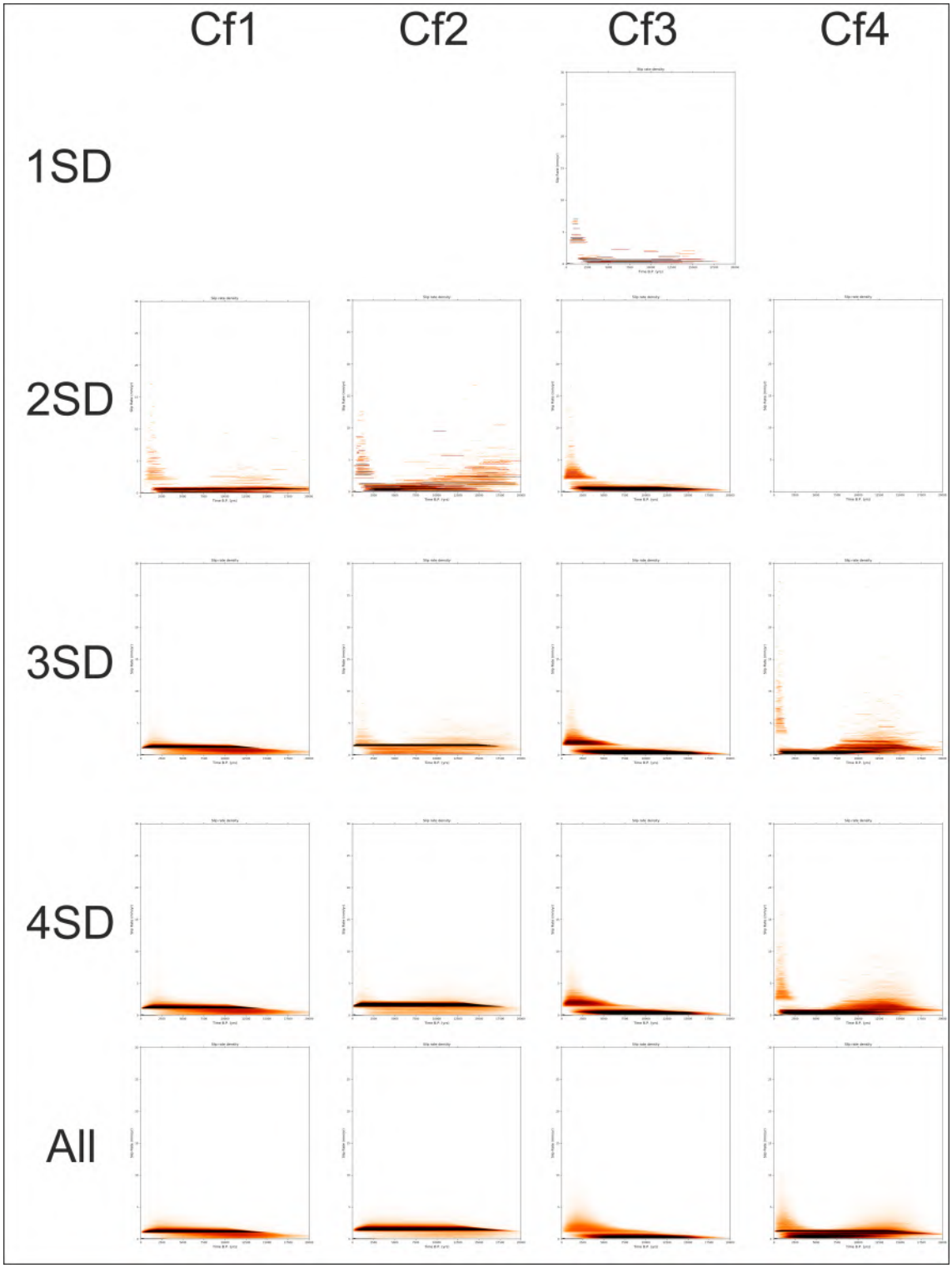

Figure B12: 2d histogram of slip rate through time for models that fit within 2,3 or 4 standard deviations or all models for all sites on the CF fault.

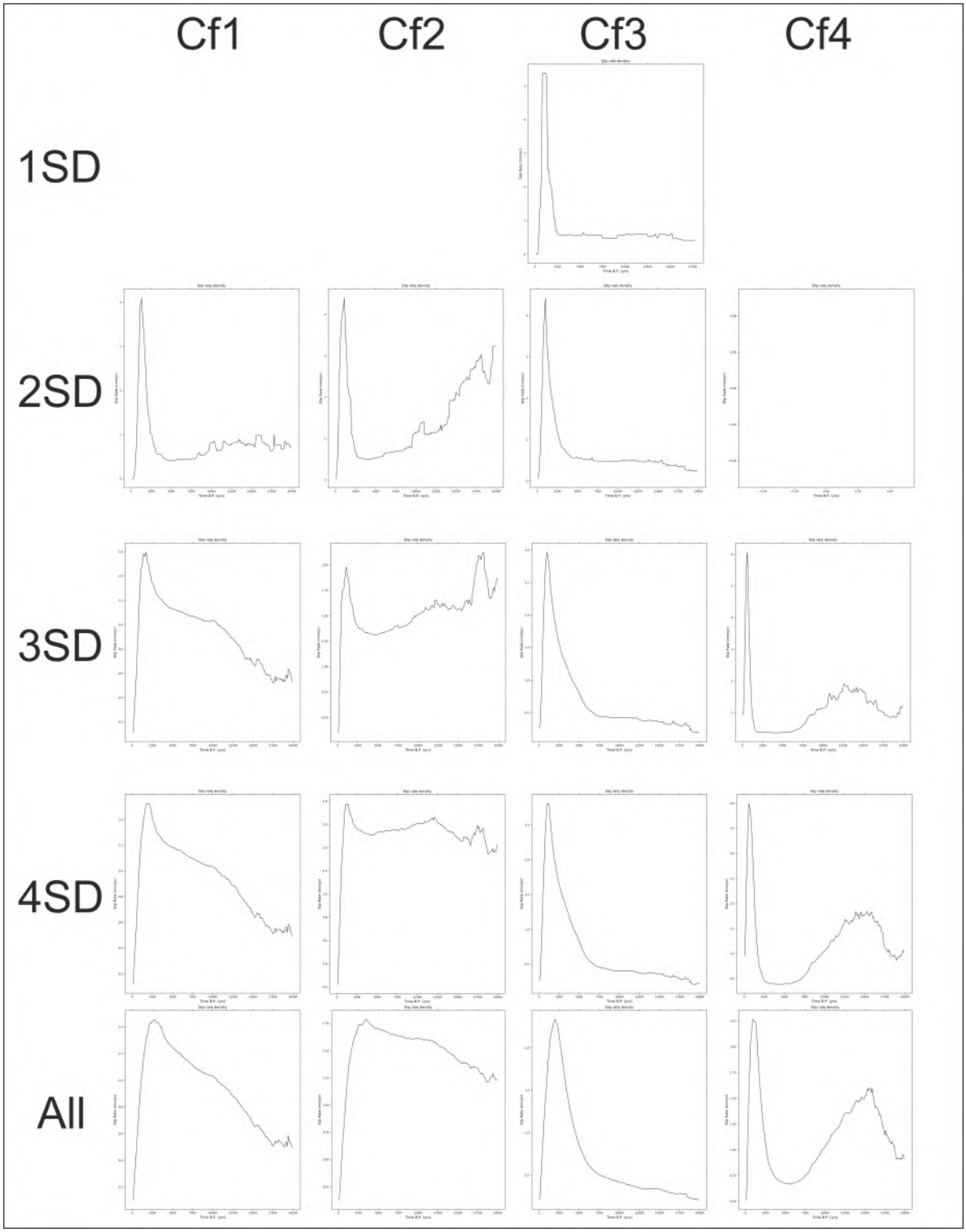

Figure B13: Average incremental slip rate for models that fit within 2,3 or 4 standard deviations or all models for all sites on the CF fault. Note: scale on y axis varies.

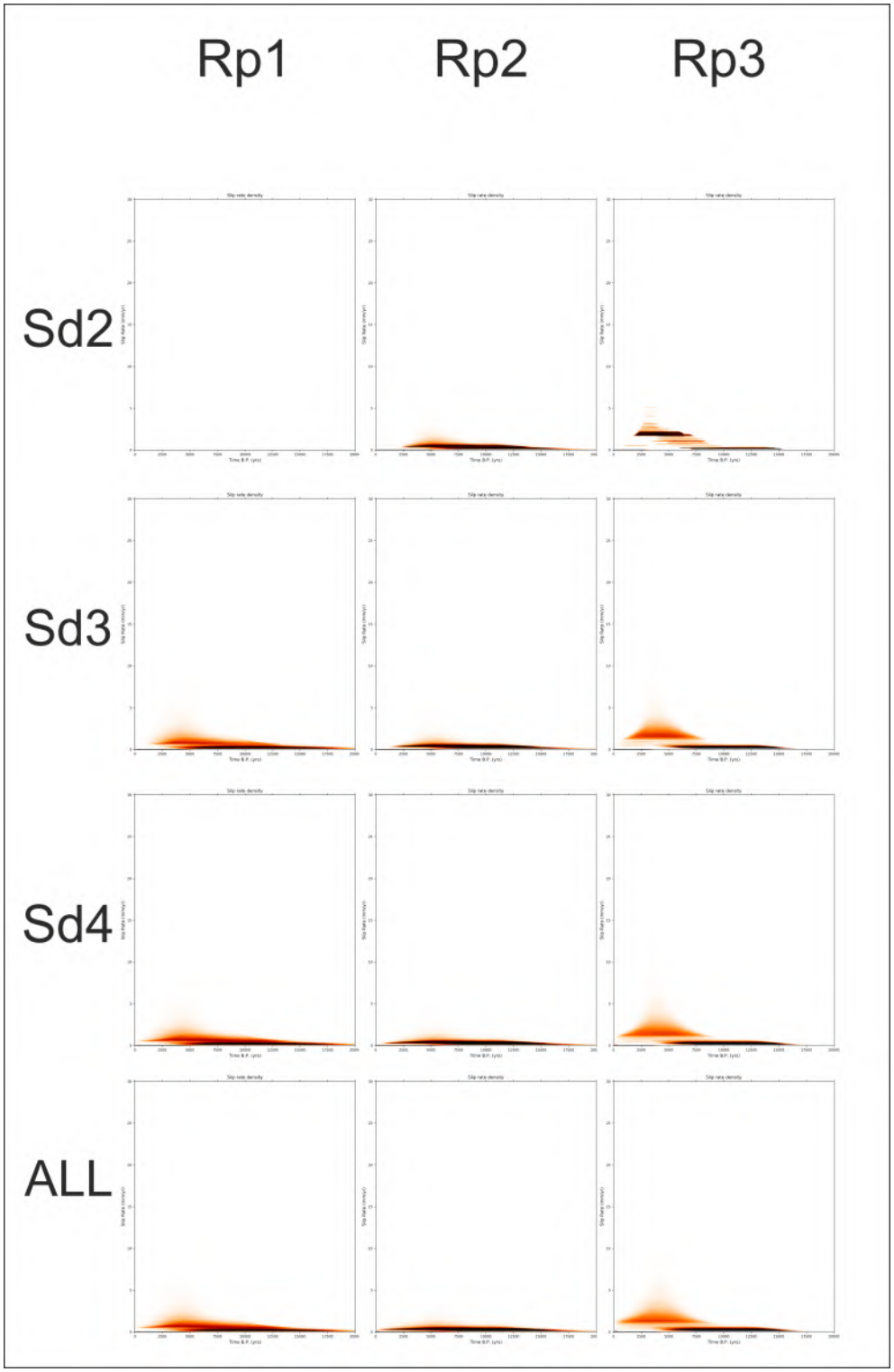

Figure B14: 2d histogram of slip rate through time for models that fit within 2,3 or 4 standard deviations or all models for all sites on the RP fault.

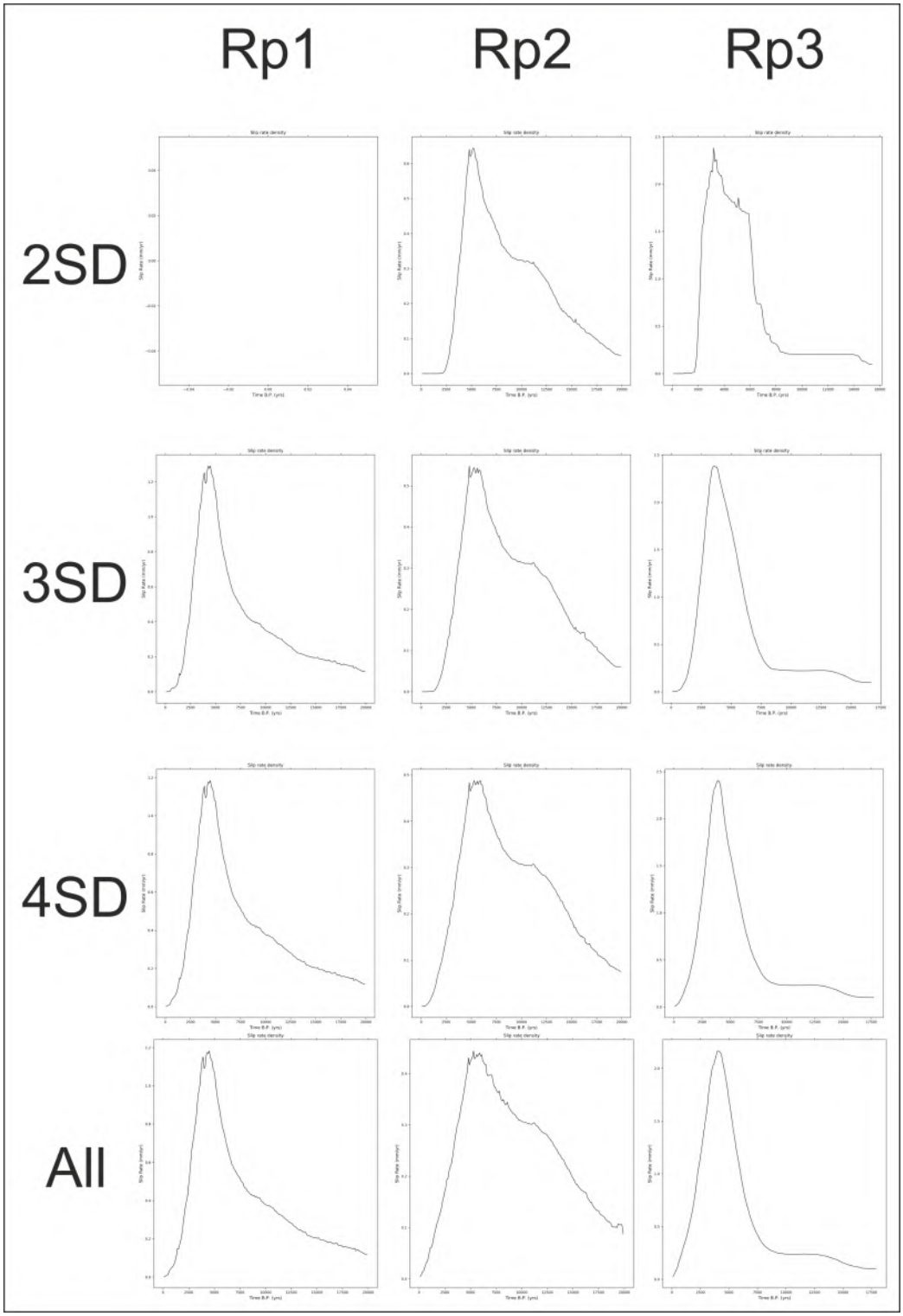

Figure B15: 2d histogram of slip rate through time for models that fit within 2,3 or 4 standard deviations or all models for all sites on the RP fault. Note: scale on y axis varies.

B3 Calculation of recurrence intervals

I use the formula derived by Wesnousky et al., 2008 to calculate the maximum surface displacement of the fault given its length. This takes the form:

$$D_{max} = C * L$$

- D_{max} Maximum displacement due to one earthquake (meters)
- C A constant, 0.09 for normal faults (Wesnousky et al., 2008)
- L Length of fault (km)

To calculate the average displacement (D_{avg}) I use the ratio derived by Wesnousky et al,2008 where:

$$D_{avg} = 0.41 * D_{max}$$

I obtain values of L for the Campo Felice and Rocapretturo faults using their surface trace on Google earth. I calculate the long term slip rate using:

$$\frac{H}{A} = R$$

- H Slip, known as model parameter Scarp height (mm)
- A Mean scarp age (yr)
- R Slip rate (mm/yr)

I use the slip at sites CF2 and RP1, as these are the tallest sites with reliable geomorphology on both faults. I calculate the recurrence interval for the fastest average slip rate for the fault and for the long term slip rate of the fault, I discount site RP3 as I believe the exhumation to be related to a combination of tectonic and slope processes. For the long term average slip rate I use the mean of values that fit the data to within 2 standard deviations on CF2 and 3 standard deviations at RP1. I also present the mean scarp age values of the whole distribution for comparison. To calculate the recurrence interval I use:

$$\frac{D_{max}}{R} = Int$$

Fault	C	L (km)	Dmax (m)	Davg (m)
CF	0.09	14	1.26	0.52
RP	0.09	20	1.8	0.74

Table B4: Parameters for calculating D_{max}.

- D_{avg} displacement (mm)
- R Slip rate (mm/yr)
- Int Recurrence interval

The values I used to calculate D_{max} and D_{avg} can be found in Table B4 and the values I used to calculate the recurrence interval are in Table B5.

I use the slip rates and the D_{max} values to calculate the recurrence interval at RP1 and CF2. Results for these are found in Table B5.

Site and scarp age type	Scarp age	Scarp height (mm)	slip rate (mm/yr)	Recurrence interval (yr)
CF2 (sd2 mean)	17557	24400	1.39	372
CF2 (all mean)	15537	24400	1.58	328
CF2 fast slip			4	130
RP1 (all mean)	14366	7200	0.55	1473
RP1 (sd3 mean)	12594	5400	0.43	1721
RP1_fast		7200	1.2	615

Table B5: Parameters for calculating earthquake recurrence intervals.

Estimations of recurrence intervals for given earthquake magnitudes are commonly used to represent the hazard posed by a particular fault (e.g. Pace et al., 2006), but these estimates are commonly calculated assuming a fault has a constant slip rate, which I have shown is not always true. I calculate a range of recurrence intervals based on the long-term time-averaged slip rate and the fastest average incremental slip rate modelled for each fault. At Campo Felice, the shortest recurrence interval is at site CF2, because it has the highest displacement, and I base our calculations on this site. Using an average displacement of 0.52 m based on empirical rupture length-displacement scaling laws, the average earthquake recurrence based on the long term slip rate (1.4 mm yr^{-1}) is 370 years. Using a peak slip rate of 4 mm yr^{-1}, the recurrence interval is 130 years. Details of the calculation can be found in the Supplementary Materials. The recurrence interval calculation has numerous assumptions, primarily that the whole

fault ruptures in every event with the empirically derived average displacement. Whilst this is unlikely to be the case, the calculation provides a simple base for assessing relative seismic hazard. A recurrence interval of 370 years for the Campo Felice fault agrees with that of Pace et al.,2006, who suggest recurrence intervals in the of range 320-689 years. The peak slip recurrence interval is shorter than the shortest recurrence interval suggested by Pace et al.,2006, highlighting the challenge of incorporating variable slip rates into seismic hazard assessments.

On the Roccapreturo fault I use site RP1 to determine the recurrence interval, because it has the greatest displacement with acceptable geomorphology, and I calculate the recurrence interval based on the post LGM slip rate (0.4 mm yr^{-1}) and the peak incremental slip rate of the models (1 mm yr^{-1}). I use an average displacement of 0.6 m, which results in recurrence intervals of 1720 years and 615 years, for average and peak recurrence respectively. One consistent feature of the average incremental slip rate, show in the main text, is the drop to 0 mm yr^{-1} in recent times; this is simply a function of representing episodic fault slip with a continuous slip rate and including an estimate of elapsed time as described in the modeling section in the main text. The drop to 0 mm yr^{-1} is just a function of the modelling so should not be over interpreted as it does not reflect the current slip rate of the fault.

C Sample preparation

C1 Pre-crushing Preparation

The aims of this section are to; record the sample before crushing, remove non-rock material, remove weathered rock and remove secondary calcite.

1. Rinse the sample with water and clean using a medium stiff brush (nailbrush).
2. Photograph each side of sample whilst wet (this allows features to be seen and photographed more clearly).
3. Make a sample description.
4. Using a rock saw remove a small amount of rock for preservation for producing

thin section in the future, normally a 10 mm wide segment cut perpendicular to the longest axis (Figure C1).

5. Note on the offcut the fault face and the top of the sample

6. Remove surface weathering and secondary calcite from sample using a tile cutter. Cut the rock into pieces up to 2−3cm.

7. Leave samples to dry overnight.

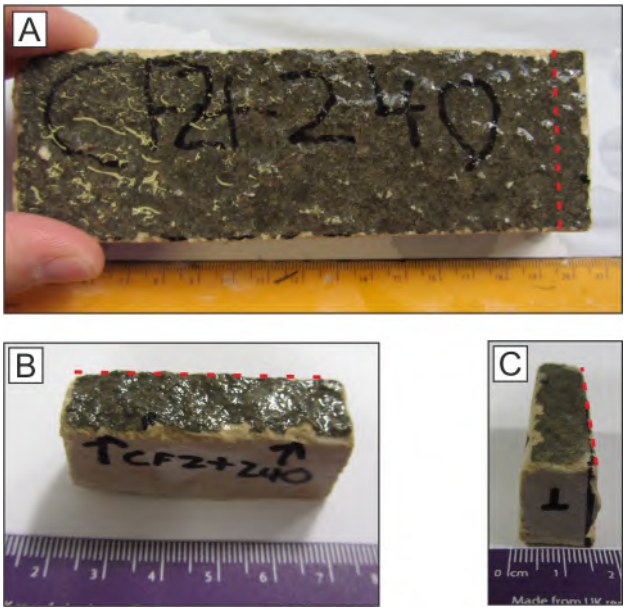

Figure C1: An example sample tile before I cut a section to preserve for future work (A) and the section saved (B and C). Red dotted line indicates line of cutting.

C2 Crushing

The aim of this section is to produce 65-80g of material with a grain size between 250-500 microns from the sample.

1. Record weight of sample

2. Crush the sample in a jaw crusher with a relatively wide separation between the jaws

3. Sieve the sample using 500micron and 250 micron sieve to capture the 250-500 micron portion produced. Retain all fractions of seived material.

4. Reduce the jaw separation and repeat the above two steps. Do not keep reducing the jaw separation, below a critical value it will only produce a fraction <250. Crushing should continue until at least 65-80g of material of grain size 250-500 microns has been produced.

5. Record the weight of each fraction of crushed material and then store in a dry area out of direct sunlight.

6. **Thoroughly** clean the work area and crushing equipment, remove any trace of the crushed sample (mainly done with compressed air and a wire brush).

7. Repeat steps 1-6 for each sample.

C3 Chlorine Extraction

C3.1 Rinse

The aim is to remove material finer than 250 microns, which could be cross contamination.

1. Weigh out 60g of 250-500 micron fraction of the sample into a labeled 500ml plastic beaker that has been washed rinsed 3 times with 18Ω water. This is usually done in batches of 14 for logistical reasons.

2. Add 18Ω water to the beaker until the sample is well covered and swirl the beaker to mobilize the sediment.

3. Wait until the sample has settled (typically the same time it takes to repeat the previous step for a further 6 samples) and then pour the water away, not losing any sample, just fines. Do this for each of the samples.

4. Repeat this rinsing 8-10 times, until the water is no longer visibly cloudy.

5. If moving on to next step on the same day there is no need to dry samples. Otherwise dry in oven at 70 degrees Celsius.

C3.2 First Leach

The aim is to remove altered grain boundaries to remove the influence of meteoric fluids on the measured chemistry. This is usually done on 1 or 2 batches at the same time.

1. Remove samples from oven and place in fumehood
2. Add 100ml 18 Ω water to each beaker, rinsing down the side of the beaker to catch any grains not in the bottom.
3. Use extra 18 Ω water to rinse beaker sides if grains remain.
4. Add 30ml of 0.33M HNO_3, pouring acid onto side of beaker to reduce vigor of reaction.
5. Add 45ml 0.33M HNO_3 for every 10g of sample, in 30ml aliquots, swirling the beaker gently so all grains are exposed to acid. Wait 10-15 minutes between additions.
6. Leave for 12-24 hours and if possible genrtly swirl samples 2-3 times during this period.

C3.3 Second Leach

The aim is to remove altered grain boundaries to remove the influence of meteoric fluids on the measured chemistry.

1. Pour of supernatant liquid waste.
2. Repeat steps 2 onwards of the first leach.

C3.4 Leach rinse

The aim is to remove all fines and contaminated acid.

1. Pour off and dispose of supernatant liquid.
2. Rinse samples with 18 Ω water 7 times or more if liquid is not clear.
3. Dry samples in foil lined oven overnight at 70 degrees Celsius.

To prepare for the following stage:

1. Label 14 nalgene beakers with sample name identifying number.
2. Label 2 nalgene beakers with BLK1 and BLK2 and identifying number.
3. Rinse all beakers and with 18 Ω water
4. Dry in oven overnight at 70 degrees Celsius
5. Weigh beakers individually (with lid on) to nearest 0.0001g. Anti static fans are very useful.

C3.5 Weighing out and Spike

The aim is to weigh out the samples, spike the samples and then dissolve the samples.

Weighing

1. Inspect small plastic weigh boat and visually check for any dirt. If any seen dispose of and try the next one.
2. Check scales are clean - if not clean with 18 Ω water.
3. Place inspected weigh boat into scales and weigh 30-32g of leached sample into weigh boat and record weight.
4. Transfer grains from weigh boat into new labeled and cleaned nalgene beaker (prepared in previous step) by pouring in.
5. Use 18 Ω water to slurry any remaining grains from weigh boat into beaker.
6. Place beaker into pre-prepared ice bath.
7. Repeat for all samples using a new inspected weigh boat each time.
8. Add a similar amount of water to blank bottles and add to ice bath.

Spike

9. Weigh spike bottle

10. Double glove and add appropriate amount of spike to sample. Each sample requires 1mg of Cl. Note the mg Cl/g of solution in lab book.

11. Weigh spike bottle again, to calculate exact amount of spike added

12. Repeat previous 2 steps, using a new pipette tip for each sample and blank.

C3.6 Dissolution

The aim is to dissolve the leached sample as slowly as possible.

1. Add 10ml of HNO_3 to each sample, adding to the side of beaker and not directly on to sample. Do not swirl sample.

2. Wait 10-15 minutes and repeat previous step until 100ml has been added.

3. Add 20ml of HNO_3 to each sample until samples have approximately 10ml of HNO_3 per g of sample.

4. It is necessary to add more if sample is still present and reacting, ie effervescing. This is typically a further 100ml when using 30g of leached material. Add this in 20ml increments.

5. Remove beakers from ice-bath once reaction has stopped and leave in fume hood overnight.

6. If reaction is still occurring the next day, add further HNO_3 in 20ml increments until reaction has stopped.

C3.7 Decanting

The aim is to remove all the sample in liquid form, leaving behind any undissolved sediments.

1. Wash with Ω water and label a conical flask and watch glass for each sample and blank. Dry overnight in oven.

2. Wash with 18 Ω water and label 4 50ml centrifuge tube for each sample and blank. Label with sample name and number and label one with S, one with * for each sample. Dry overnight.
3. Wash 3 10ml centrifuge tubes per sample blank, labeling with ICP 1:10, ICP 1:100 and ICP 1:1000 as well as sample number and name.
4. Weigh conical flask and watch glass and record weight.
5. Pour supernatant liquid (sample) from nalgene beaker into respective conical flask, very slowly, until sediment approaches lip of beaker. Stop pouring.
6. Place watch-glass on top of flask.
7. Mobilise sediment in beaker by swirling and pour into labeled 50ml centrifuge.
8. Repeat this for each sample.
9. Centrifuge 50ml centrifuge tube for 3 minutes at 3000rpm.
10. Pour the liquid from the centrifuge tube into the respective conical flask.
11. If the sediments mobilise then repeat previous 2 steps.
12. Repeat previous 7 steps until all solution from nalgene is in the conical flask and all sediment is in the centrifuge tube.
13. Place centrifuge tub in oven at 70°C until sample residue is dry (typically left in oven overnight).
14. Weigh the conical flasks containing solution and note weight as 'flask full weight'.

C3.8 $AgNO_3$ addition

ICP preparation

1. Remove sediment filled centrifuge tubes from oven and store.
2. Pipette 5ml using a digital pipette from the sample into respective 10ml centrifuge tube labeled ICP 1:10.

3. Using a different pipette tip for each sample repeat the previous step until all samples have an ICP aliquot.

4. Weigh the ICP tube to 6 significant figures and note weight as ICP tube and lid full weight.

$AgNO_3$ addition

1. Place flasks with watchglasses on on top on hotplate and heat to 150°C for 1 hour in fume cupboard.
   Whilst waiting for heating

2. Pipette 100ul of ICP aliquot into ICP tube labelled with same sample ID and 1:1000.

3. Weigh the 1:1000 centrifuge tube with aliquot and note weight.

4. Add 9.9ml 2% HNO_3 using a pipette.

5. Weigh the 1:1000 centrifuge tube with aliqout and HNO_3 and note weight.

6. Repeat previous 4 steps until all samples have been diluted, using a different pipette tip for each sample. The same pipette tip can be used for 2%HNO_3 addition unless contaminated.

7. Weigh centrifuge tubes containing sediment that were in oven overnight and note weight as 'centrifuge tube and lid full'.

8. Store sediment tubes.

9. Check the liquid in the conical flasks on the hot plate is hot (convecting with bubbles forming on walls and condensation on necks).

10. Laboratory must now go into red light conditions. No white light should be present in the lab.

11. Add 1ml of 10% $AgNO_3$ per 1mg of Cl added to the sample, using pipette.

12. Repeat for all samples using a new pipette tip for each sample.

13. Turn off hotplate and leave to cool for 30 minutes.

14. Remove from hotplate and leave in fume cupboard overnight or if possible 36 hours.

C3.9 Silver Chloride precipitation

(minimum 5 hours).

1. Conical flasks in fume hood should appear clear with a white AgCl scum precipitated on the base. When moving conical flasks do as slowly and carefully as possible, taking care to avoid dislodging the AgCl 'scum' from bottom of flask.

2. Clean 20ml disposable pipette inside by rinsing inside with 18Ω water.

3. Remove nascent liquid using cleaned disposable 20ml pipette and put in waste beaker until approximately 50ml of liquid is left. Do not disturb the AgCl scum and remove liquid from the same point in beaker to minimise impact of removal of liquid with pipette.

4. Once ¡40ml of liquid remains swirl flask to take up the precipitate in suspension.

5. Pour liquid carefully into the correct labeled 50ml centrifuge tube

6. Rinse the flask with <10ml 18Ω water and pour the rinse into the same centrifuge tube.

7. If any crystals are left a further rinse will have to be undertaken at a later stage.

8. Repeat steps 1-6 for each sample.

9. Centrifuge the centrifuge tubes containting liquid and AgCl precipitate at 3000rpm for 5 minutes.

10. Check for white pellet (often very small).

11. Pour supernatant solution from centrifuge tube into waste beaker taking extreme care not to loose pellet or any white precipitate.

12. If not all precipitate was removed from conical flask, repeat steps 6-11. It is imperative to remove all AgCl precipitate.

13. If precipitate breaks up not allowing supernatant fluid to be removed by pouring, centrifuge again and use a disposable pipette cleaned using 18Ω water to remove fluid. Do not touch precipitate.

C3.10 Dissolving AgCl

After removing supernatant fluid from centrifuge tubes:

1. Add 5ml of 14% NH_4OH using a pipette.

2. For samples with diffuse AgCl around the centrifuge tube (no good white pellet) add 10ml 14% NH_4OH and note sample number.

3. 30. For any flasks that did not produce a white pellet, add 10ml 14% NH_4OH to flask and then swirl very well as this should dissolve any precipitate. Pour this solution into the correct centrifuge tube. Note this sample number.

4. Vortex strongly to break up all black residue.

5. Centrifuge each sample for 5 minutes at 3000rpm.

6. If there is any residue remaining transfer the solution to a labeled and rinsed new centrifuge tube as this residue is likely excess Ag or sediment or Fe/Mn hydroxide and is not wanted. Note in the lab book any samples that require this. If the residue is loose or not compacted, pipette the solution into a new tube using a 5ml digital pipette.

C3.11 Sulphate Removal

1. Add 3ml $Ba(NO_3)_2$ to each sample tube using pipette. If you have added extra 14% NH_4OH during the previous subsection, add 3ml of $Ba(NO_3)_2$ perm 5ml 14% NH_4OH.

2. Cap centrifuge tube and leave in fridge for at least 48 hours to allow $BaSO_4$ to precipitate.

C3.12 Filtering, precipate AgCl and cleaning

Continuing in red light conditions

1. Remove tubes from fridge and centrifuge.
2. Place sample centrifuge tubes into fume hood with labeled centrifuge tubes with asterisk on.
3. Take up the liquid from the centrifuge tube into a disposable syringe
4. Attach a 0.2μm Anatop inorganic membrane filter on to the disposable syringe to the disposable syringe, touching only the sides of the filter to avoid contamination.
5. Place syringe into labeled centrifuge tube with asterisk on it and depress until all liquid is transferred. If there is very little or no resistance then it is most likely that the filter is broken and steps 1 to 5 should be repeated with a new cleaned labeled asterisked centrifuge tube, syringe and filter.
6. Dispose of syringe and filter.
7. Repeat steps 2-6 for all samples.
   AgCl Precipitation
8. Add 10ml 5M HNO_3 to sample tube using pipette. If precipitation is not visible as white cloudiness add more 5m HNO_3 in 1ml increments until precipitation occurs. If you have doubled sample volume at any point add a further 10ml of 5M HNO_3.
9. Screw lid on loosely to tube as reaction is exothermic and produces gas.
10. Repeat steps 8-9 for each sample.
11. Add 200 μl 10% $AgNO_3$ to each sample tube. If 2 tubes have been combined at an earlier stage, double the volume of $AgNO_3$.
12. Screw lids on tightly and vortex.

13. Leave floc to settle for at least 1 hour.

    Cleaning AgCl

14. If there is precipitate on the side of the centrifuge tube, knock it off (e.g. with the handle of a knife).

15. Centrifuge for 5 minutes at 3000rpm.

16. If white precipitate is still floating, tab tube base a few times and re-centrifuge.

17. If precipitate is diffuse round the edges, tap tap edges to dislodge then re centrifuge.

18. If there is no visible plug in base of tube add 5ml 14% NH_4OH and cortex and check everything has dissolved. If it hasn't add 1ml extra 14% NH_4OH and vortex until it does dissolve. Then go back to 8 and repeat all steps.

19. Pour off supernatant waste watching white pellet in bottom of tube. Take special care when meniscus pulls over pellet. If pellet starts moving use an 18Ω cleaned disposable pipette to remove to remove liquid. Some scum floating off is acceptable. DO NOT LOSE SAMPLE (PELLET).

20. Add 10 ml 18Ω water to each sample.

21. Add 100 μl 5M HNO_3 to each tube using pipette. Clean pipette tip internally using 100 μl 5M HNO_3 before using. The same pipette tip can be used for each sample.

22. Vortex gently until AgCl pellet disintegrates, avoid liquid touching the centrifuge tube lid.

23. Centrifuge for 5 mins at 3000rpm/

24. Pour off waste liquid from centrifuged tubes, being careful of the pellet.

25. Add 10ml 18Ω

26. Vortex gently until AgCl pellet disintegrates, avoid liquid touching the centrifuge tube lid.

27. Centrifuge for 5 minutes at 3000rpm.

28. Repeat steps 24-27

29. Pour off supernatant waste being careful of pellet.

30. Place tubes in 70°C oven, with lids by side, overnight or over the weekend.

C3.13 Storage

Continuing in red light conditions.

1. Lid the sample tubes once cool.

2. Store in darkness (typically in taped shut blackout bags in specific sample cupboard).

Table C1: TLS picks for the Mugla fault

Iteration	Throw (m)	Heave (m)	Alpha (°)	Beta (°)	Gamma (°)
1	6.36	6.78	21.09	43.11	19.21
2	6.41	6.84	21.11	43.08	18.93
3	6.13	6.33	21.27	43.95	19.87
4	6.47	6.92	21.36	42.97	18.63
5	6.48	6.93	21.23	43.01	18.55
6	6.14	6.16	21.78	44.72	19.24
7	6.53	7.13	21.25	42.49	18.68
8	6.36	6.79	21.10	43.05	19.29
9	6.55	7.02	21.20	42.99	18.25
10	6.17	6.59	21.30	43.06	20.39
Mean	6.36	6.75	21.27	43.24	19.10
St. dev.	0.15	0.29	0.19	0.60	0.62

Table C2: TLS picks for the Yatagan fault

Iteration	Throw (m)	Heave (m)	Alpha (°)	Beta (°)	Gamma (°)
1	8.53	2.47	23.13	73.87	36.62
2	8.78	2.59	23.31	73.58	34.33
3	8.86	2.60	23.36	73.64	34.04
4	9.40	2.83	23.76	73.26	34.82
5	8.67	2.56	22.80	73.57	34.86
6	8.59	2.50	22.64	73.76	36.29
7	8.83	2.62	24.41	73.48	34.39
8	8.56	2.47	20.25	73.88	35.83
9	8.56	2.56	23.16	73.34	35.42
10	9.05	2.77	23.17	72.98	33.66
Mean	8.78	2.60	23.00	73.54	35.03
St. dev.	0.26	0.11	1.03	0.27	0.93

Modelling bonus results

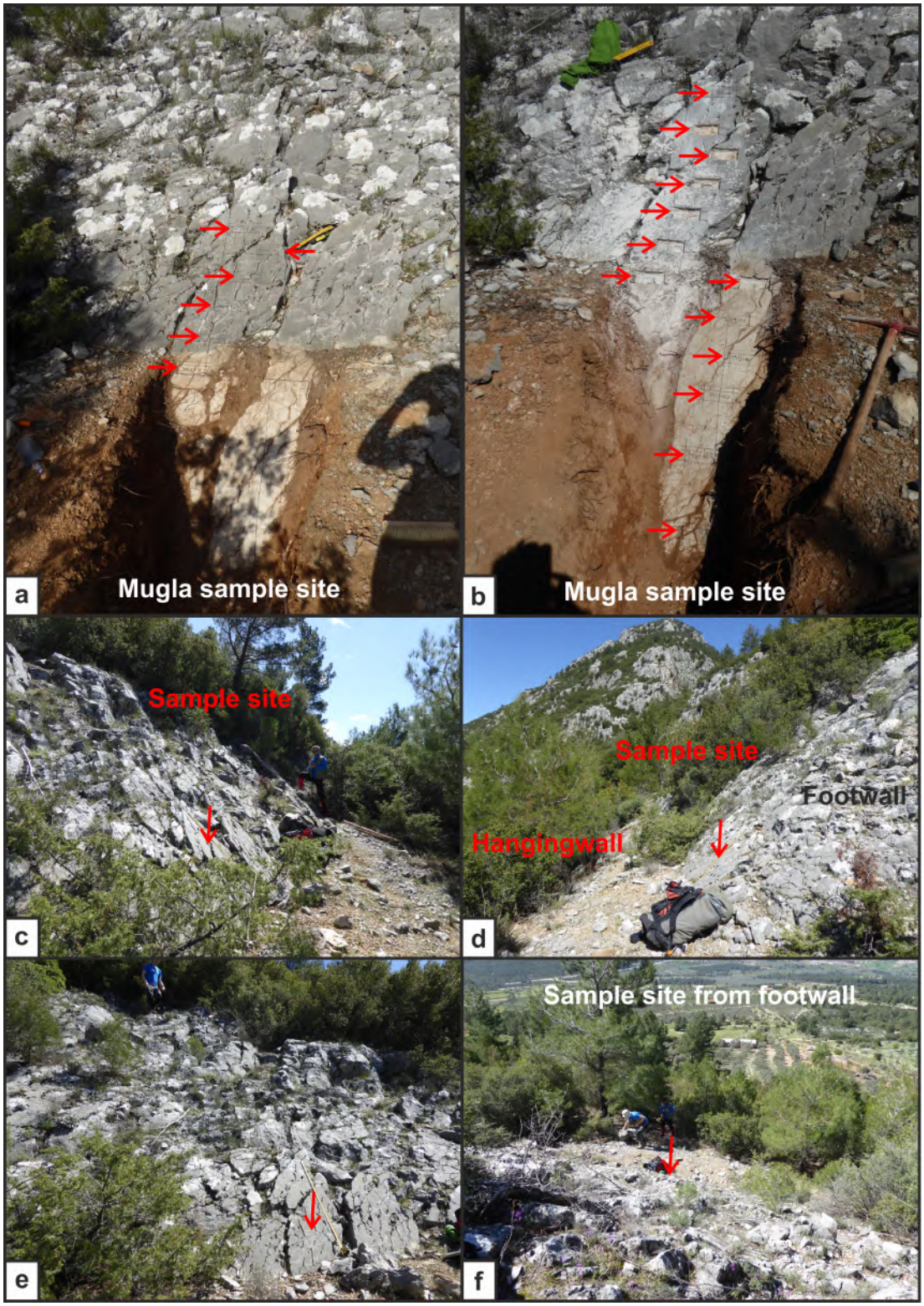

Figure C2: a)-e)Photos of the sampled fault scarp on the Mügla fault, f) A view of the sample site from above. Arrows indicate sampling locations.

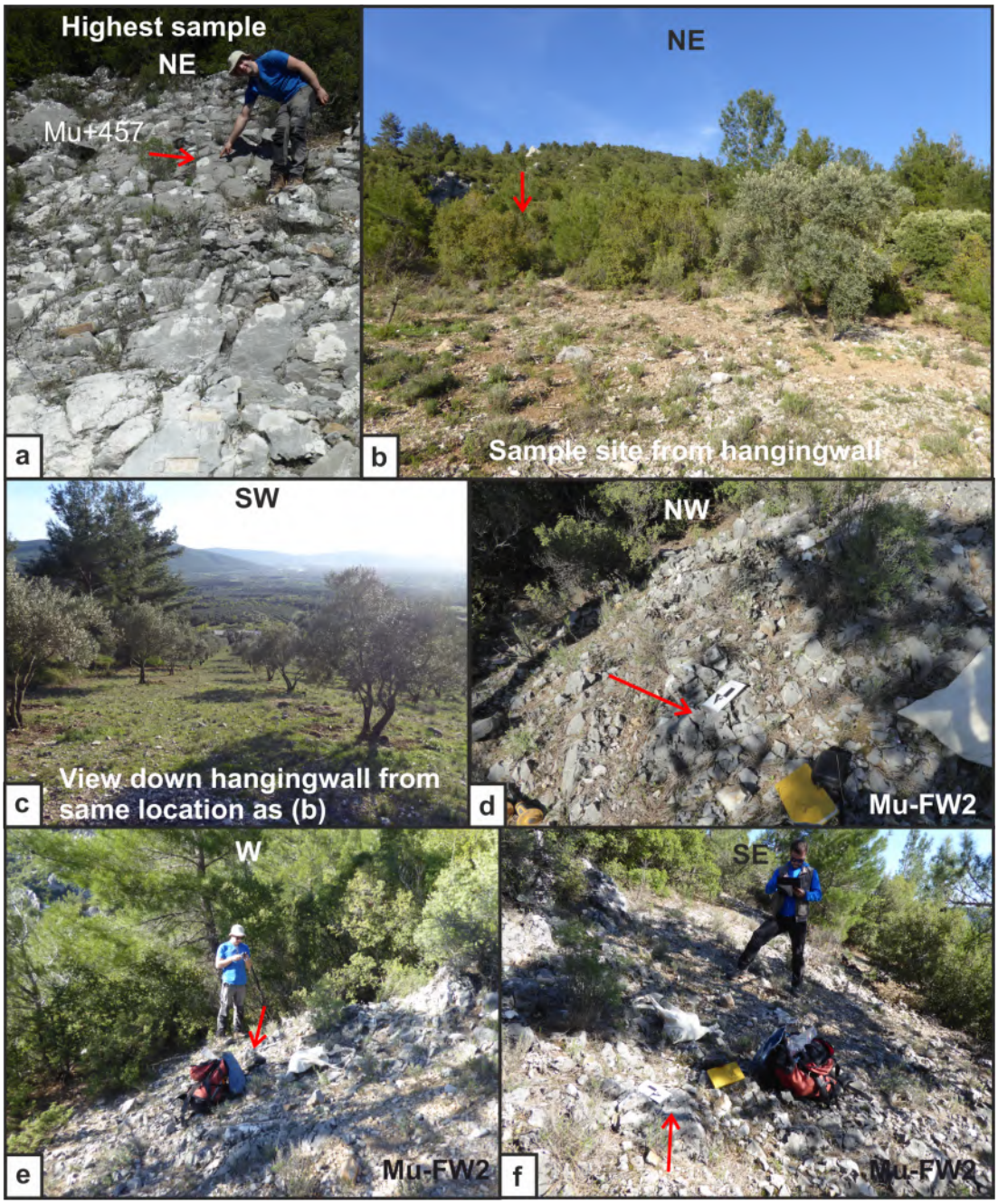

Figure C3: Photos of the Muğla sample site. a) The sample taken furthest up the scarp. b) A view from the hangingwall of the sample site. c) The view west. d)-f) Views of the footwall sample Mu-FW2. Arrows indicate sampling locations.

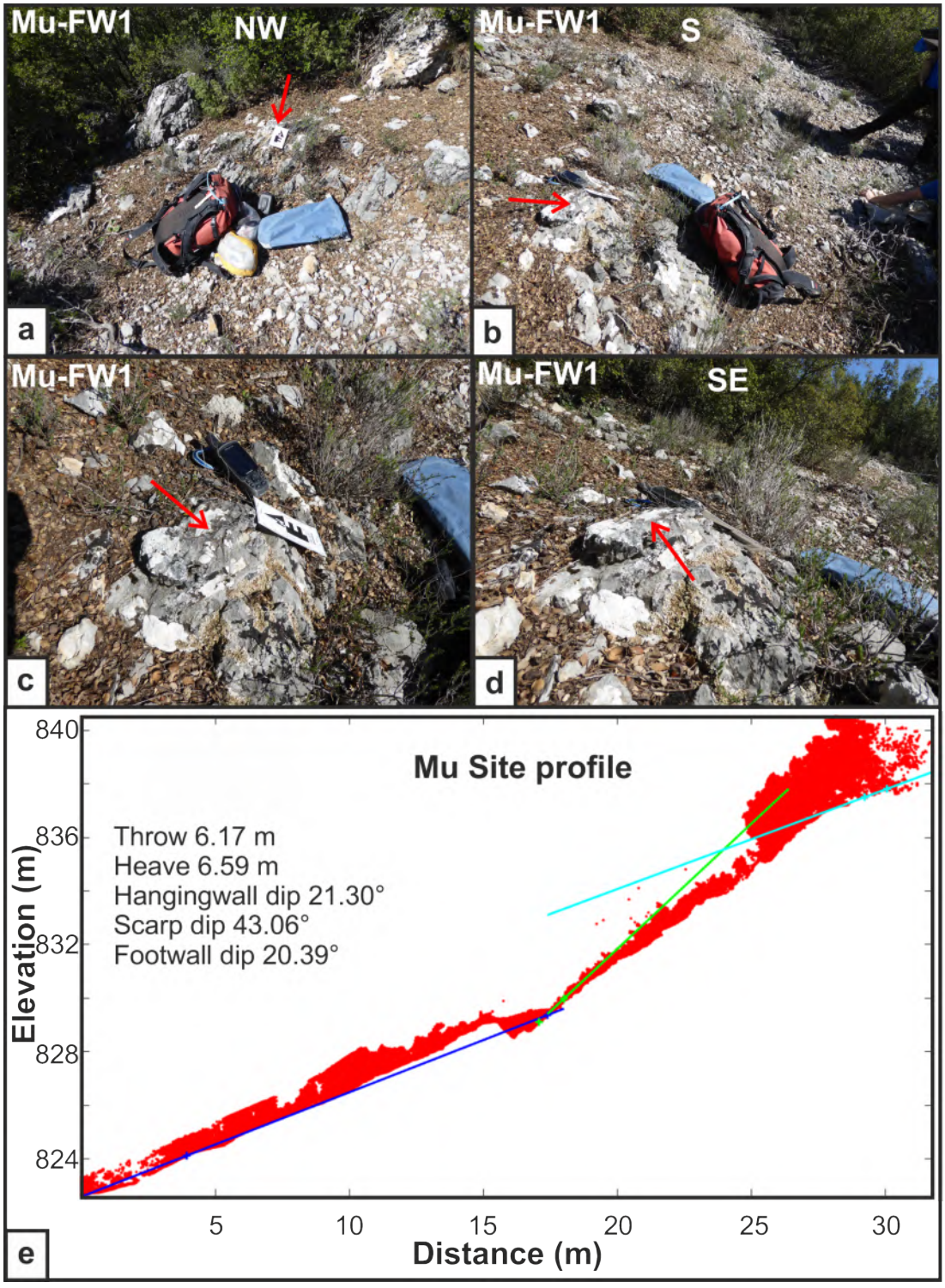

Figure C4: Photos of the Muğla footwall sample site Mu-FW1 and an interpreted TLS profile of the Muğla site, produced using *crossint* (*Wilkinson et al.*, 2015, *Cowie et al.*, 2017). Arrows indicate sampling locations. The data from all TLS slope interpretations is in Table C1.

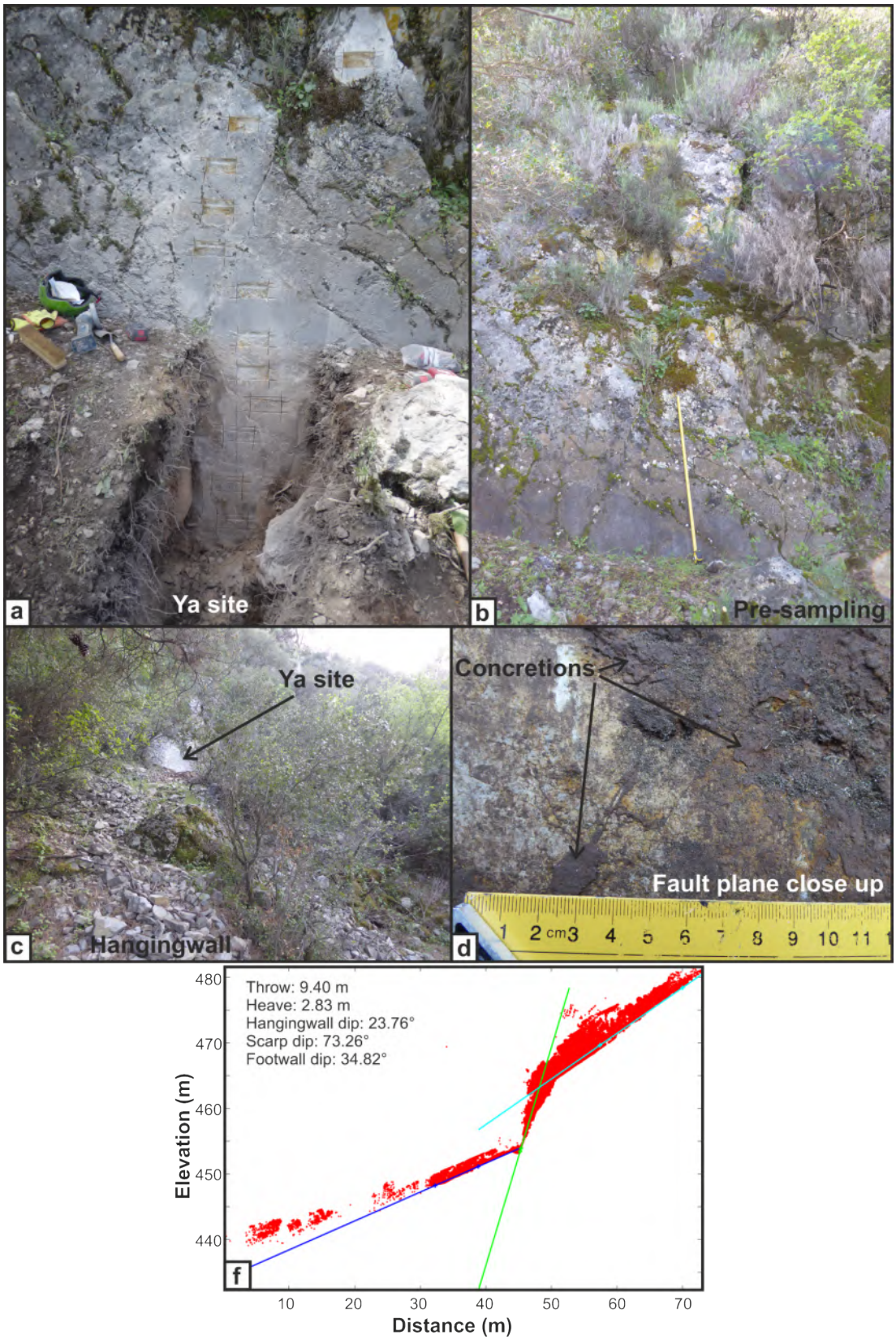

Figure C5: The Yatağan sampling site. a-d) photos of the fault plane,f) an interpreted TLS data cross section of of the fault scarp. Data from all TLS slope interpretations is in Table C2.

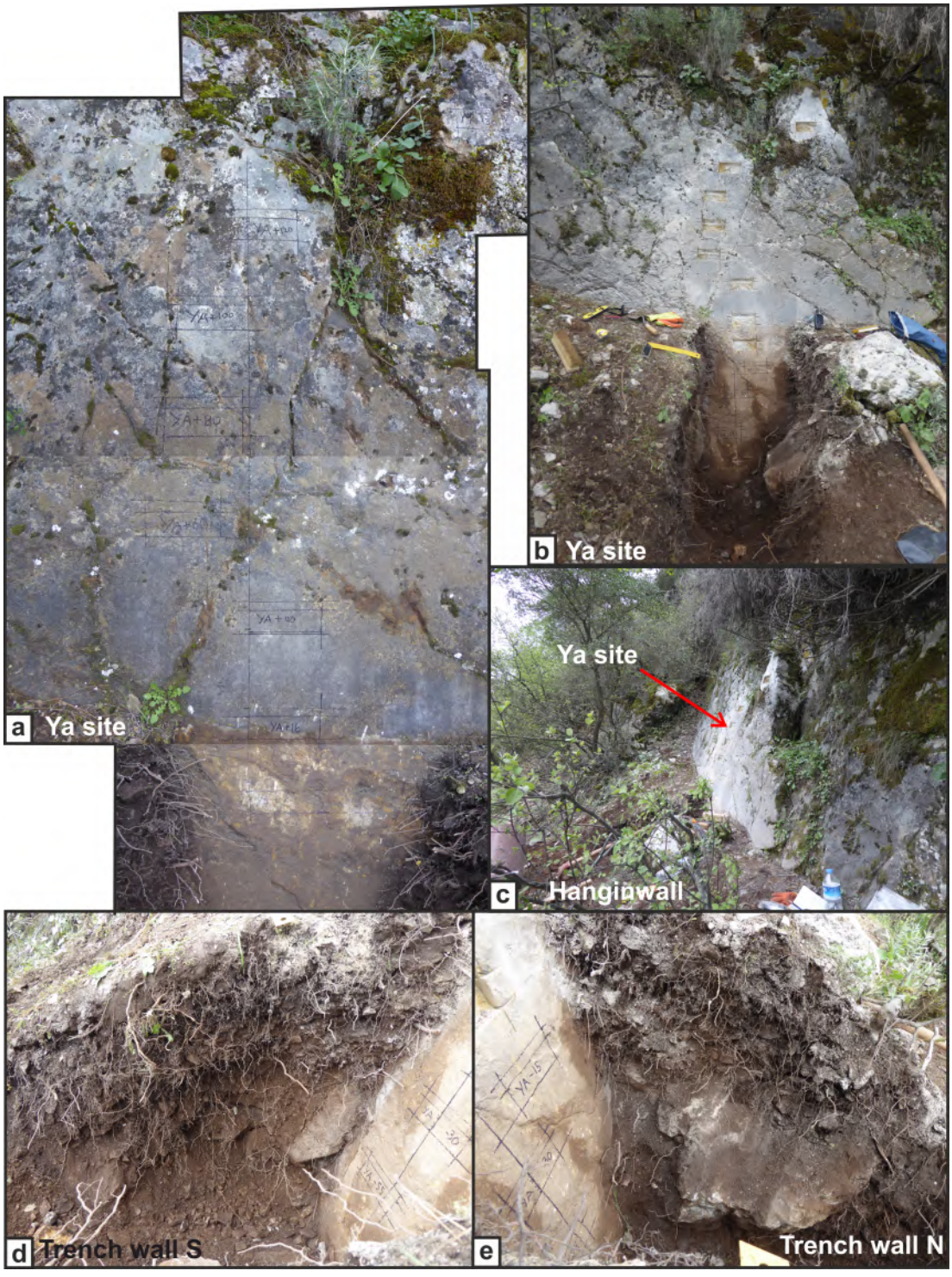

Figure C6: The Yatağan sample site. a-c) photos of the fault plane d-e) side walls of the excavated trench. Note the sample tiles are 16cm across for scale) and the layered stratigraphy, indicating a stable Holocene slope.

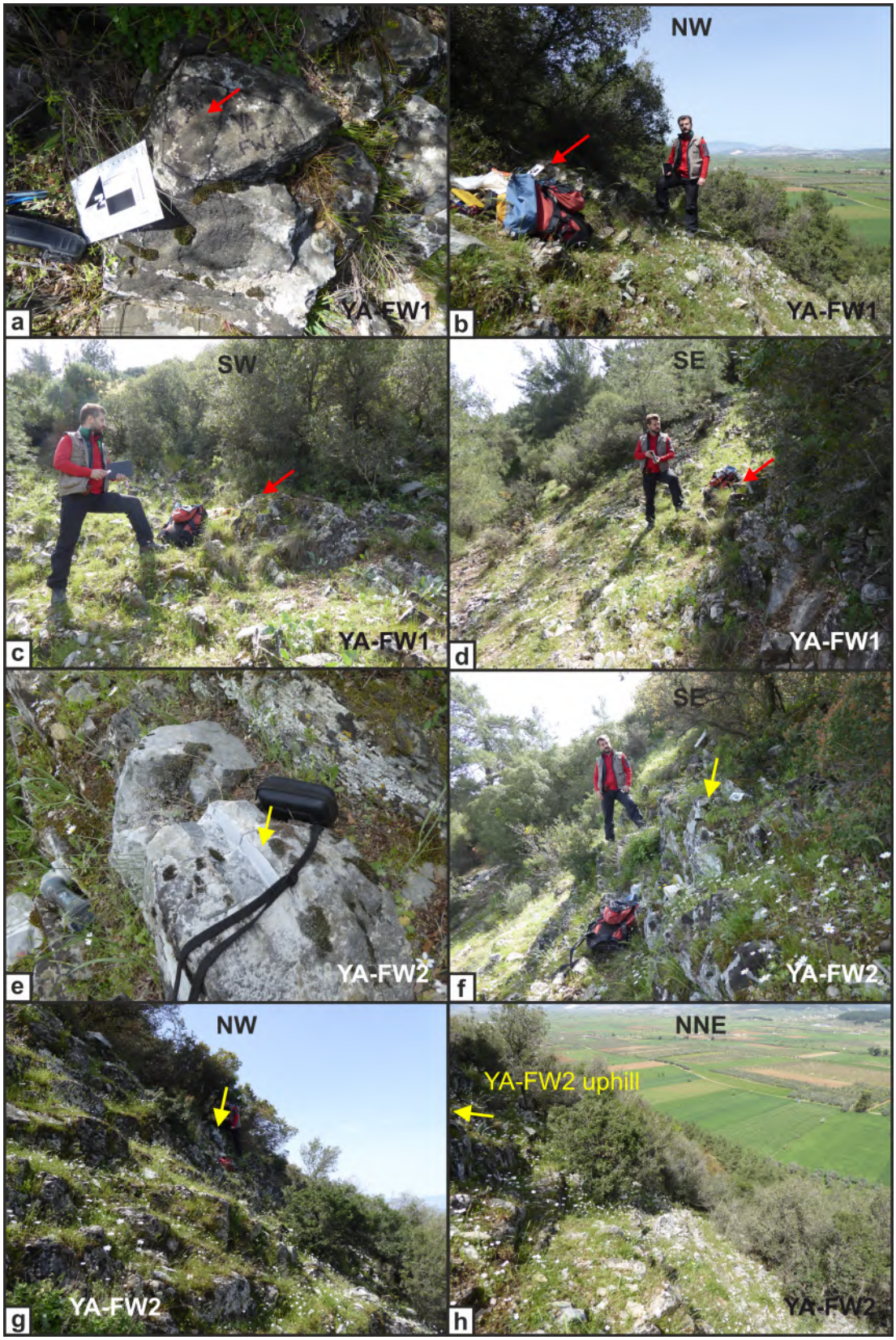

Figure C7: Photos of the Yatağan footwall sample sites YA-FW1 and YA-FW2, with my collaborator Bora Uzel for scale in b,c,d,f and g. Arrows indicate sampling locations.

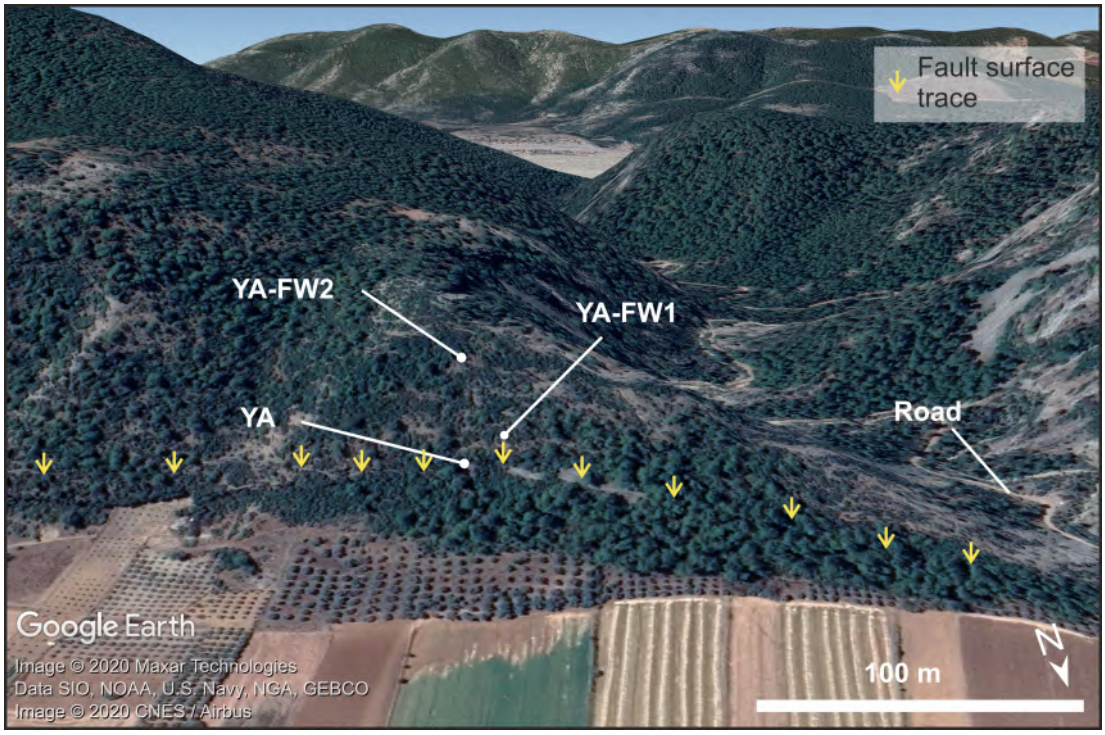

Figure C8: 3D imagery of the Yatgan sample sites.

Table C3: TLS picks for the Yilanli fault

Iteration	Throw (m)	Heave (m)	Alpha (°)	Beta (°)	Gamma (°)
1	4.44	2.90	22.79	56.85	23.76
2	4.14	2.69	22.40	57.03	24.15
3	3.24	2.09	22.77	57.49	28.30
4	3.67	2.43	25.17	56.54	26.19
5	4.02	2.54	24.24	57.92	24.52
6	2.66	1.70	22.93	57.85	30.56
7	3.44	2.31	24.23	56.22	27.72
8	3.34	2.14	24.33	57.35	27.66
9	3.49	2.27	24.76	57.03	27.43
10	3.28	2.14	24.79	56.83	28.31
Mean	3.57	2.32	23.84	57.11	26.86
St. dev.	0.49	0.32	0.96	0.52	2.06

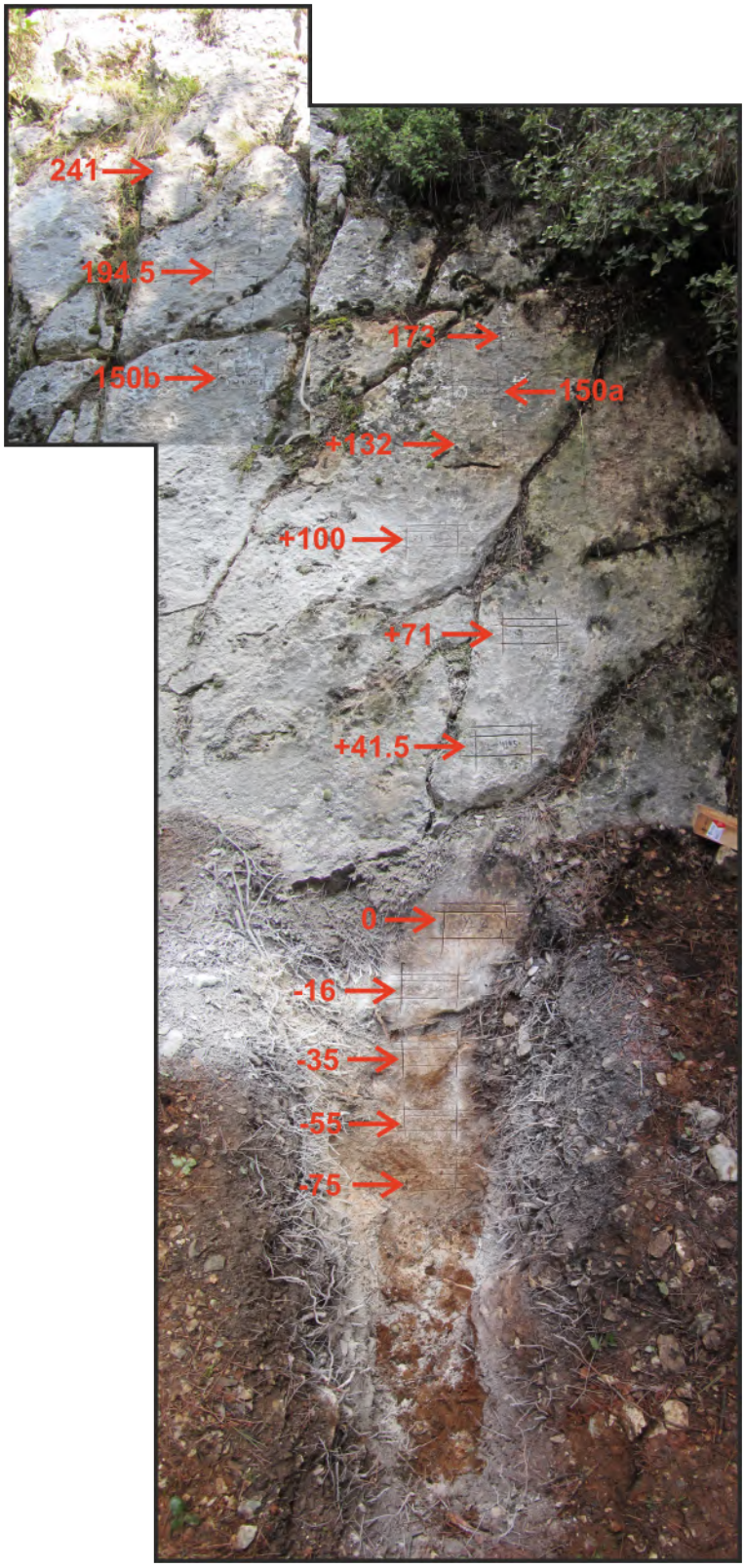

Figure C9: Photos of the Yilanli sample site before samples were removed. White powder on scarp and ground is dust from cutting of lower samples. Arrows indicate sampling locations.

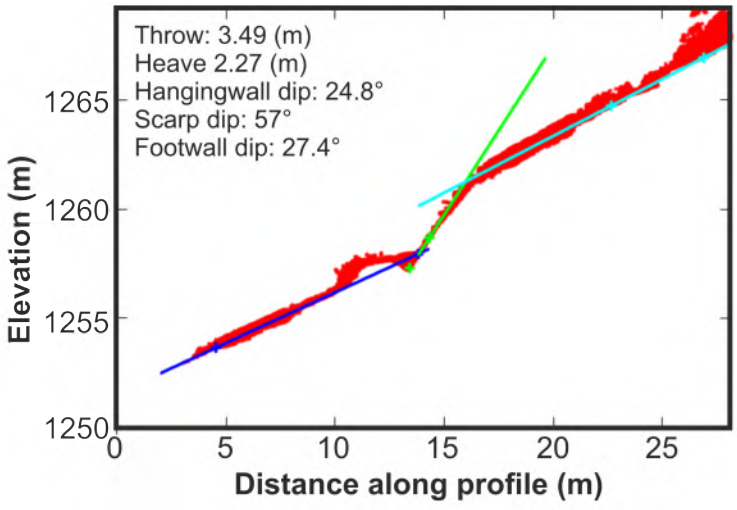

Figure C10: Interpretted TLS data from the Yilanli sample site, data from all TLS slope interpretations is in Table C3.

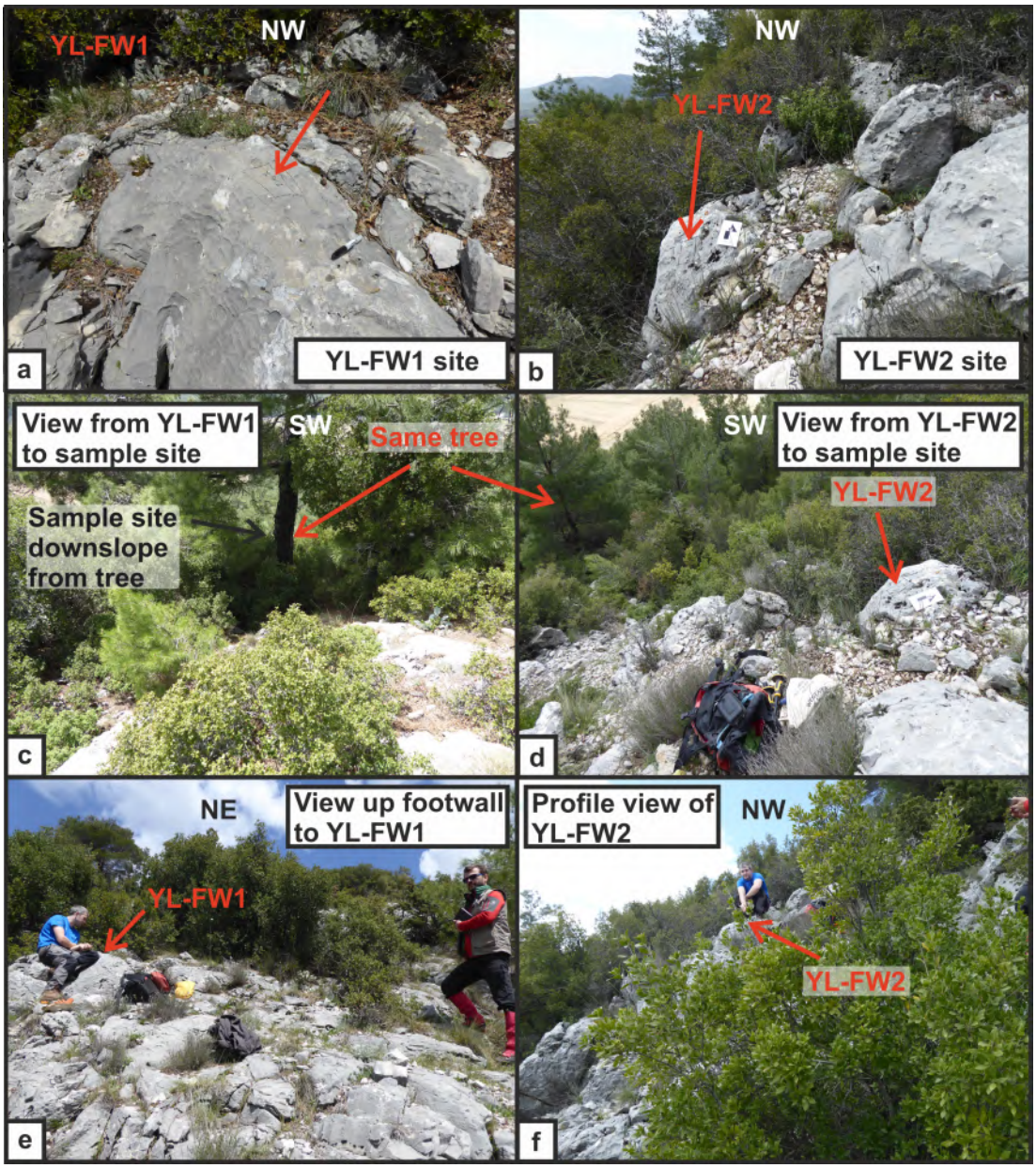

Figure C11: Photos of the footwall sample sites on the Yilanli fault. Locations can be seen in Figure 5.8. Arrows indicate sampling locations.

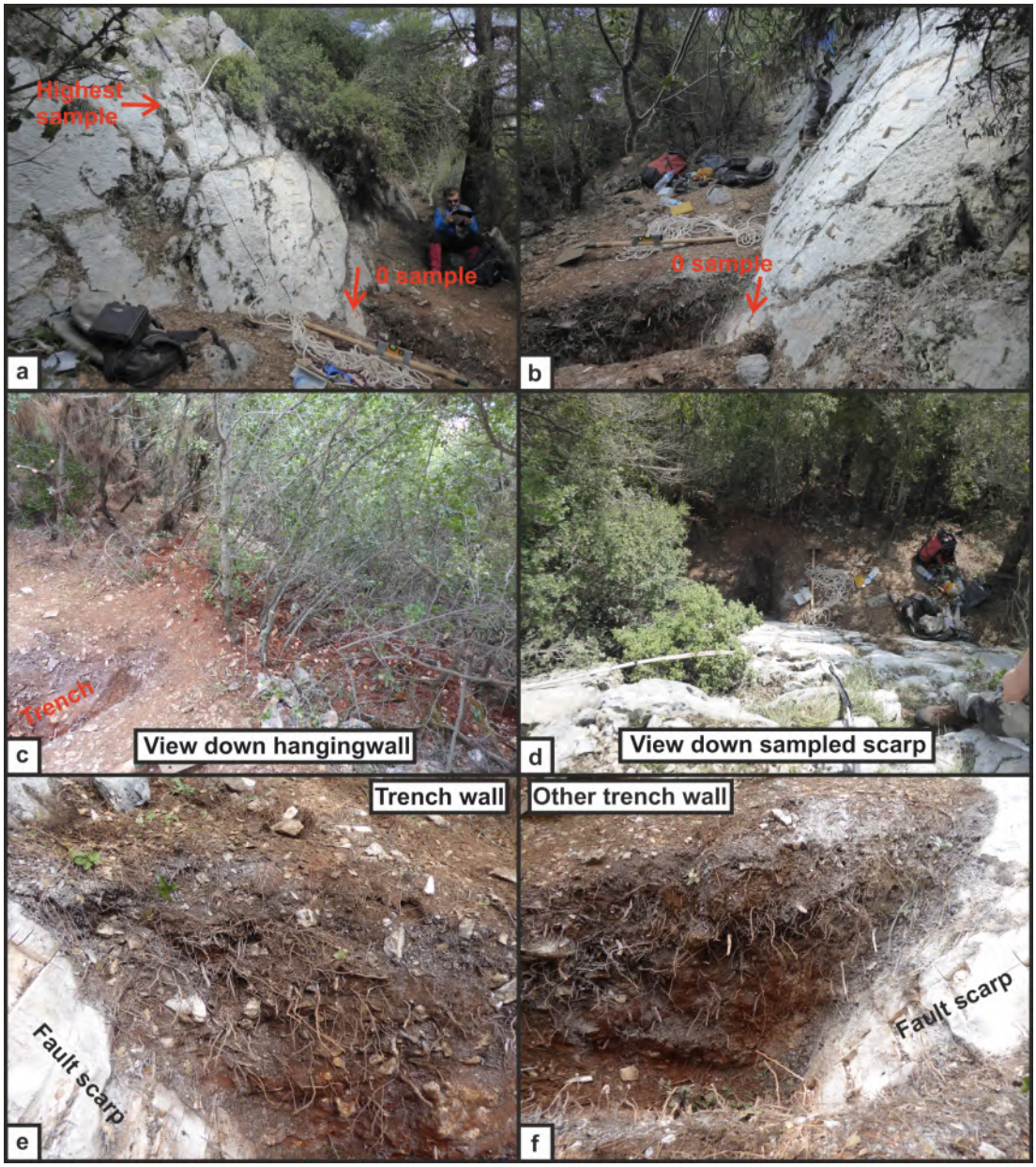

Figure C12: Photos of the Yilanli sample site before samples were removed. White powder on scarp and ground is dust from cutting of lower samples.

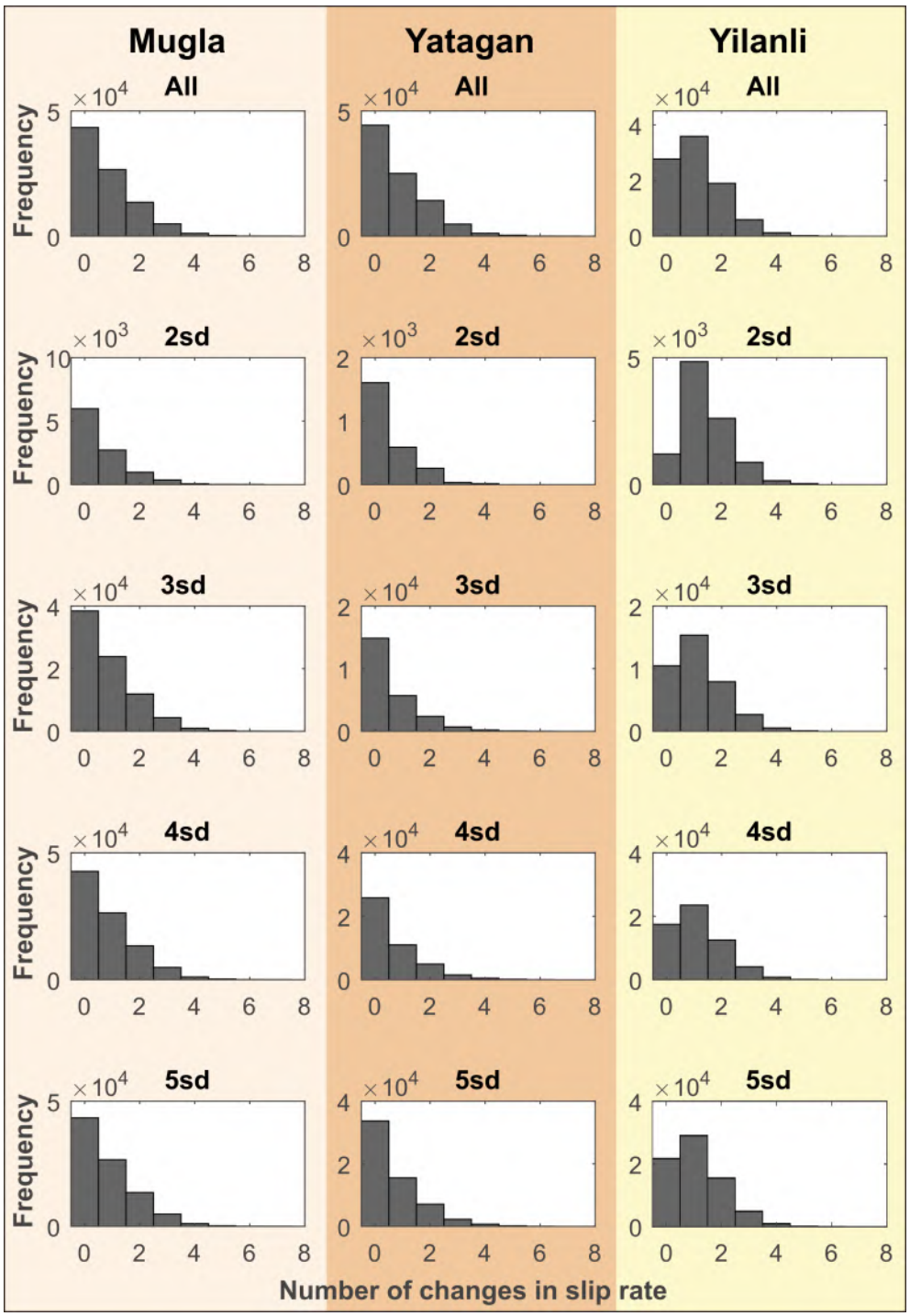

Figure C13: Histograms of the number of change points (changes in slip rate) for the normal scarp age prior. Plots are of all models, and models that fit within 2, 3, 4 and 5 standard deviations. Yatağan in this case is modelled omitting the top sample. The number of models in each histogram can be found in Table 5.9.

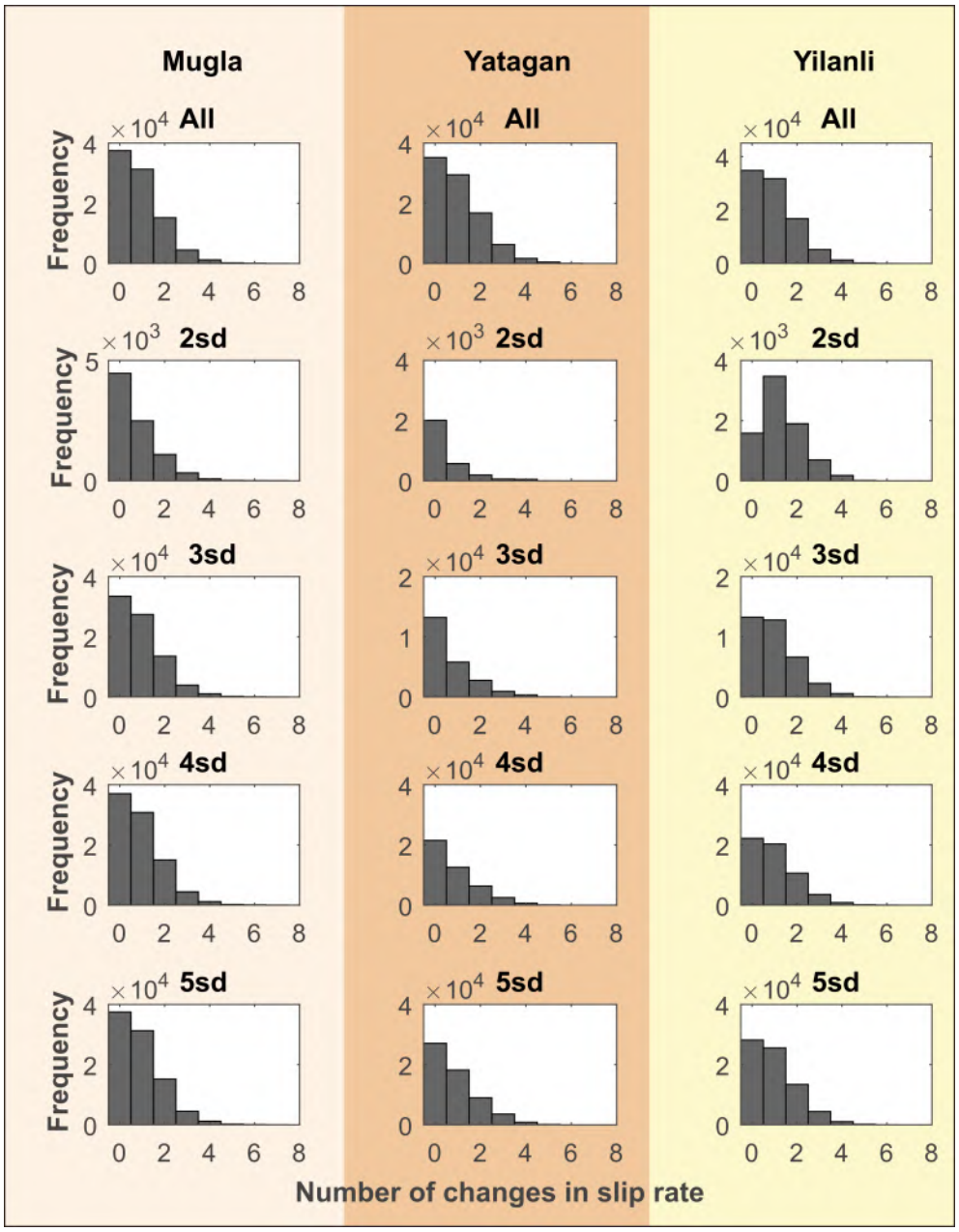

Figure C14: Histograms of the number of change points for the uniform scarp age prior. Plots are of all models, and models that fit within 2, 3, 4 and 5 standard deviations. Yatağan in this case is modeled omitting the top sample. The number of models in each histogram can be found in Table 5.10.

Sample Measurements

Sample Name	Scaling	Latitude	Longitude	Elevation	Pressure	Atmospheric Pressure	Sample Thickness	Bulk Density	Shielding Factor	Erosion Rate	Conc. 36Cl
		decimal degrees	decimal degrees	meters	hPa	or elevation	cm	g/cm^3	unitless	mm/kyr	Atoms/g of sample
YA-FW1	SF	37.26514	28.18956	441	962.56	Both	2.5	2.5	0.9704	0	3.63E+05
YA-FW2	SF	37.26452	28.18958	488	957.22	Both	2.5	2.5	0.9360	0	3.05E+05
YL-FW1	SF	37.25033	28.42705	1272	871.69	Both	2.5	2.5	0.9790	0	1.00E+06
YL-FW2	SF	37.24997	28.42662	1244	874.64	Both	2.5	2.5	0.9695	0	7.51E+05
MU-FW1	SF	37.19433	28.4538	826	919.57	Both	2.5	2.5	0.9810	0	9.51E+05
MU-FW2	SF	37.19436	28.45366	817	920.56	Both	2.5	2.5	0.9810	0	5.93E+05

Sample Name	Attenuation length	Depth to Top of Sample	Year Collected	Water Content in Pores	Mineral Separation	SiO2 Bulk Rock	TiO2 Bulk Rock	Al2O3 Bulk Rock	Fe2O3 Bulk Rock
	g/cm^2	g/cm^2	Year A.D.	Volume Fraction		oxide weight %	oxide weight %	oxide weight %	oxide weight %
YA-FW1		0	2018	0	No	0.01	0.01	0.004581037	0.006476851
YA-FW2		0	2018	0	No	0.01	0.01	0.004439945	0.00529413
YL-FW1		0	2018	0	No	0.01	0.01	0.008822225	0.006204015
YL-FW2		0	2018	0	No	0.01	0.01	0.009691276	0.006836516
MU-FW1		0	2018	0	No	0.01	0.01	0.009343398	0.026125795
MU-FW2		0	2018	0	No	0.01	0.01	0.004794461	0.007767264

Sample Name	MnO Bulk Rock	MgO Bulk Rock	CaO Bulk Rock	Na2O Bulk Rock	K2O Bulk Rock	P2O5 Bulk Rock	Analytical Water	CO2 Bulk Rock	Cl Bulk Rock	B Bulk Rock
	oxide weight %	oxide weight %	oxide weight %	oxide weight %	oxide weight %	oxide weight %	weight %	oxide weight %	ppm	ppm
YA-FW1	0.000677623	0.646074447	58.834	0.008253137	0	0.005793957	0	43	5.451516061	1
YA-FW2	0.000302021	1.103895741	55.801	0.008997067	0	0.003167958	0	43	4.240631674	1
YL-FW1	0.001368356	0.225704016	59.446	0.008058867	0	0.056561466	0	43	1.655103312	1
YL-FW2	0.004482168	0.294658901	59.585	0.008004291	0	0.045964975	0	43	2.647489943	1
MU-FW1	0.00247061	0.314033301	58.937	0.008411229	0	0.01282463	0	43	0.992995919	1
MU-FW2	0.002294283	0.380665453	58.869	0.009206565	0	0.014669767	0	43	2.751761418	1

Sample Name	Sm Bulk Rock	Gd Bulk Rock	U Bulk Rock	Th Bulk Rock	Cr Bulk Rock	Li Bulk Rock	Target K2O	Target CaO	Target TiO2	Target Fe2O3	Target Cl
	ppm	ppm	ppm	ppm	ppm	ppm	weight %	weight %	weight %	weight %	ppm
YA-FW1	0	0	0	0	0	0	0	58.83382531	0	0.006476851	5.451516061
YA-FW2	0	0	0	0	0	0	0	55.80105139	0.01	0.00529413	4.240631674
YL-FW1	0	0	0	0	0	0	0	59.4460957	0.01	0.006204015	1.655103312
YL-FW2	0	0	0	0	0	0	0	59.58496978	0.01	0.006836516	2.647489943
MU-FW1	0	0	0	0	0	0	0	58.93667443	0.01	0.026125795	0.992995919
MU-FW2	0	0	0	0	0	0	0	58.86898841	0.01	0.007767264	2.751761418

Figure C15: Data used for calculating footwall ages of faults in the Mugla-Yatagan basin, in the format used for the CRONUS calculator (*Marrero et al.*, 2016) . Table continues in Figure C16.

Uncertainties on measurements

Sample Name	Latitude	Longitude	Elevation	Pressure	Sample Thickness	Bulk Density	Shielding Factor	Erosion-Rate	Conc. 36Cl	Attenuation Length	Depth to Top of Sample
	decimal degrees	decimal degrees	meters	hPa	cm	g/cm^3	unitless	mm/kyr	Atoms/g of sample	g/cm^2	g/cm^2
YA-FW1	0	0	10	1	0	0.2	0.005	0	9389.483267	10	0
YA-FW2	0	0	10	1	0	0.2	0.005	0	8607.847341	10	0
YL-FW1	0	0	10	1	0	0.2	0.005	0	28248.17077	10	0
YL-FW2	0	0	10	1	0	0.2	0.005	0	17148.66652	10	0
MU-FW1	0	0	10	1	0	0.2	0.005	0	24530.95194	10	0
MU-FW2	0	0	10	1	0	0.2	0.005	0	21860.2361	10	0

Sample Name	Year Collected	Water Content in Pores	Bulk Rock SiO2	Bulk Rock TiO2	Bulk Rock Al2O3	Bulk Rock Fe2O3	Bulk Rock MnO	Bulk Rock MgO	Bulk Rock CaO	Bulk Rock Na2O
	Year A.D.	Volume %	oxide weight %	oxide weight %	oxide weight %	oxide weight %	oxide weight %	oxide weight %	oxide weight %	oxide weight %
YA-FW1	0	0	0	0	0	0	0	0	0	0
YA-FW2	0	0	0	0	0	0	0	0	0	0
YL-FW1	0	0	0	0	0	0	0	0	0	0
YL-FW2	0	0	0	0	0	0	0	0	0	0
MU-FW1	0	0	0	0	0	0	0	0	0	0
MU-FW2	0	0	0	0	0	0	0	0	0	0

Sample Name	Bulk Rock K2O	Bulk Rock P2O5	Analytical Water	Bulk Rock CO2	Bulk Rock Cl	Bulk Rock B	Bulk Rock Sm	Bulk Rock Gd U	Bulk Rock U
	oxide weight %	oxide weight %	weight %	oxide weight %	ppm	ppm	ppm	ppm	ppm
YA-FW1	0	0	0	0	0	0.1	0	0	0
YA-FW2	0	0	0	0	0	0.1	0	0	0
YL-FW1	0	0	0	0	0	0.1	0	0	0
YL-FW2	0	0	0	0	0	0.1	0	0	0
MU-FW1	0	0	0	0	0	0.1	0	0	0
MU-FW2	0	0	0	0	0	0.1	0	0	0

Sample Name	Bulk Rock Th	Bulk Rock Cr	Bulk Rock Li	Target K2O	Target CaO	Target TiO2	Target Fe2O3	Target Cl	Covariance
	ppm	ppm	ppm	weight %	weight %	weight %	weight %	ppm	unitless
YA-FW1	0	0	0	0	0	0	0	0.1	0
YA-FW2	0	0	0	0	0	0	0	0.1	0
YL-FW1	0	0	0	0	0	0	0	0.1	0
YL-FW2	0	0	0	0	0	0	0	0.1	0
MU-FW1	0	0	0	0	0	0	0	0.1	0
MU-FW2	0	0	0	0	0	0	0	0.1	0

Figure C16: Uncertainties of data used for calculating footwall ages of faults in the Mugla-Yatagan basin, in the format used for the CRONUS calculator (*Marrero et al.*, 2016). Continuation of table in Figure C15.

Sample Name	LU code	Al2O3 (Al)	Fe2O3 (Fe)	MnO (Mn)	MgO (Mg)	CaO (Ca)	Na2O(Na)	K2O(K)	TiO2(Ti)	P2O5(P)	B	Li	H2Otot (H)	Stot (S)
		%	%	%	%	%	%	%	%	%	ppm	ppm	%	%
Yilanli														
YL-75	LU418	0.204772029	0.112578512	0.004555345	0.099852481	58.16962529	0.012801732	0	0	0.04150965	0	0	0.219	0.000
YL-55	LU419	0.072349762	0.035099498	0.001324232	0.074399238	59.20208853	0.012254958	0	0	0.030293212	0	0	0.219	0.000
YL-35	LU420	0.025869994	0.012265287	0.00030656	0.054987916	59.53596308	0.010940532	0	0	0.022923202	0	0	0.219	0.000
YL-16	LU421	0.031682452	0.012822723	0.000398228	0.060939423	60.37331354	0.011681784	0	0	0.026737824	0	0	0.219	0.000
YL-0	LU422	0.023236161	0.008536343	0.000279016	0.053884302	61.09025353	0.010814281	0	0	0.022124227	0	0	0.219	0.000
YL+45.1	LU423	0.007765401	0.001470037	5.29438E-05	0.040809867	60.82265159	0.010515477	0	0	0.01939002	0	0	0.219	0.000
YL+71	LU424	0.021997194	0.006388048	0.000360613	0.056682607	61.65074048	0.011282431	0	0	0.01904821	0	0	0.219	0.000
YL+100	LU425	0.013706021	0.004284232	0.000188229	0.066009596	60.90336368	0.011029946	0	0	0.020466995	0	0	0.219	0.000
YL+132	LU426	0.031600589	0.011799555	0.000682537	0.070151989	60.58738303	0.010825934	0	0	0.023070684	0	0	0.219	0.000
YL+150a	LU427	0.038131193	0.01435942	0.000857055	0.085116795	59.22783873	0.01032887	0	0	0.024155915	0	0	0.219	0.000
YL+150b	LU428	0.008871455	0.001802848	0.000112615	0.050784774	59.17116446	0.010741386	0	0	0.021415873	0	0	0.219	0.000
YL+173	LU429	0.040791602	0.016877484	0.000831942	0.060555473	61.04219899	0.010463428	0	0	0.023037312	0	0	0.219	0.000
YL+194	LU430	0.015604492	0.003803307	0.000200095	0.03932908	60.44618972	0.009667218	0	0	0.0164025	0	0	0.219	0.000
YL+241	LU431	0.007879474	0.001184192	2.39502E-05	0.041918111	61.42183156	0.010475972	0	0	0.016983236	0	0	0.219	0.000
Mugla														
MU-125	LU434	0.008862637	0.02507086	0.009375557	0.274674008	63.5445618	0.009848324	0	0	0.013837468	0	0	0.219	0.000
MU-90	LU435	0.008210632	0.032801685	0.010947781	0.290794752	62.24298765	0.009465555	0	0	0.014794925	0	0	0.219	0.000
MU-60	LU436	0.01031158	0.09873371	0.014706399	0.259097322	59.69516192	0.009937755	0	0	0.023403668	0	0	0.219	0.000
MU-40	LU437	0.010327328	0.094010057	0.013463573	0.293033079	57.53076429	0.010200441	0	0	0.022322804	0	0	0.219	0.000
MU-20	LU438	0.010358196	0.088449248	0.011782178	0.266466738	53.58757407	0.009483568	0	0	0.022418219	0	0	0.219	0.000
MU-0A	LU439	0.006899478	0.065802135	0.008271408	0.247263745	63.64852523	0.009244599	0	0	0.019677568	0	0	0.219	0.000
MU-0B	LU440	0.008994086	0.061098454	0.006792242	0.2718431	28.73576606	0.009783804	0	0	0.020695367	0	0	0.219	0.000
MU+20	LU441	0.007189885	0.053678163	0.006438752	0.252532553	53.4670341	0.008753671	0	0	0.017593648	0	0	0.219	0.000
MU+40	LU442	0.013040894	0.076681968	0.010549206	0.245039772	53.95750468	0.0087866	0	0	0.024050583	0	0	0.219	0.000
MU+60	LU443	0.01201703	0.109035205	0.009158196	0.242423748	51.64881393	0.00980617	0	0	0.028854234	0	0	0.219	0.000
MU+80	LU444	0.010419586	0.106852918	0.006999086	0.274680665	62.53511879	0.010570431	0	0	0.02562499	0	0	0.219	0.000
MU+96	LU445	0.013496971	0.124165853	0.006082943	0.270386986	61.28893618	0.010101951	0	0	0.026710664	0	0	0.219	0.000
MU+123	LU446	0.010214884	0.079006794	0.004569553	0.250932135	59.44046715	0.008976288	0	0	0.023416589	0	0	0.219	0.000
MU+189	LU447	0.012222406	0.113893818	0.005647654	0.247631408	62.06198568	0.009448786	0	0	0.02607943	0	0	0.219	0.000
Yatagan														
YA-75	LU450	0.006691029	0.012666654	0.006363807	0.174052195	59.41215854	0.007938031	0	0	0.010193713	0	0	0.219	0.000
YA-55	LU451	0.006727029	0.015805003	0.005939945	0.188977004	59.72133863	0.007866898	0	0	0.007784461	0	0	0.219	0.000
YA-30	LU452	0.006855758	0.019010837	0.005620401	0.242348759	59.15155933	0.007909784	0	0	0.008225442	0	0	0.219	0.000
YA-15	LU453	0.007813342	0.024744875	0.005946068	0.22147845	57.33454414	0.008900434	0	0	0.005925647	0	0	0.219	0.000
YA-0	LU454	0.00734636	0.025965978	0.005187818	0.225575695	47.8237388	0.008268364	0	0	0.007403233	0	0	0.219	0.000
YA+16	LU455	0.007592109	0.029443417	0.004972099	0.218157908	55.99899614	0.008448222	0	0	0.010474224	0	0	0.219	0.000
YA+40	LU456	0.007951385	0.033396887	0.004825394	0.234143111	58.20364544	0.008753083	0	0	0.015557308	0	0	0.219	0.000
YA+60	LU457	0.008759328	0.039438367	0.004920597	0.273886538	58.26782899	0.0095443	0	0	0.010642122	0	0	0.219	0.000
YA+80	LU458	0.0867575	0.041529355	0.004505504	0.214648956	60.2566801	0.009361746	0	0	0.014820567	0	0	0.219	0.000
YA+100	LU459	0.007605903	0.0384467	0.003645743	0.234012934	60.69944473	0.008131718	0	0	0.014296956	0	0	0.219	0.000
YA+120	LU460	0.009135818	0.048491756	0.004034173	0.261225187	59.40149398	0.009681688	0	0	0.012605563	0	0	0.219	0.000
YA+150	LU461	0.009888902	0.054854941	0.004013701	0.246810584	59.73262937	0.010392042	0	0	0.023883749	0	0	0.219	0.000
YA+378	LU462	0.009506633	0.054888389	0.00353716	0.321828117	60.52540917	0.009910457	0	0	0.018007097	0	0	0.219	0.000
YA+457	LU463	0.010498297	0.062869784	0.003569541	0.237722652	56.48005807	0.0108606	0	0	0.016303251	0	0	0.219	0.000
Mean value	-	0.01909	0.04462	0.00481	0.18660	58.33427	0.00986	0	0	0	0	0	0.21900	0.00000

Figure C17: Data rock file for Turkey sites

Sample Name	CO2 tot (C)	O,rock	O,water	Cl nat AMS	Ca ICP	Sample Thickness	[36Cl] AMS	Uncertainty	Z(HEIGHT)	Z (position, z<0 = buried)
	%			ppm	ppm	cm	at/g.rock		cm	cm
Yilanli										
YL-75	43	16.21	0.19	0.8424	415738	2.5	2.1270E+05	6488.716	0	-75
YL-55	43	16.21	0.19	0.5294	423117	2.5	2.2333E+05	6915.918	20	-55
YL-35	43	16.21	0.19	0.6655	425503	2.5	2.4245E+05	8945.294	40	-35
YL-16	43	16.21	0.19	0.7739	431488	2.5	2.5971E+05	8026.223	59	-16
YL-0	43	16.21	0.19	0.5058	436612	2.5	2.7823E+05	7176.533	75	0
YL+45.1	43	16.21	0.19	0.2162	434699	2.5	3.0165E+05	9320.848	117	42
YL+71	43	16.21	0.19	0.4493	440618	2.5	3.1398E+05	9656.874	146	71
YL+100	43	16.21	0.19	5.9187	435276	2.5	3.7437E+05	11396.862	175	100
YL+132	43	16.21	0.19	0.3139	433018	2.5	3.8375E+05	11835.868	207	132
YL+150a	43	16.21	0.19	0.3734	423301	2.5	4.1779E+05	4288.771	225	150
YL+150b	43	16.21	0.19	0.3479	422896	2.5	3.9333E+05	12064.241	225	150
YL+173	43	16.21	0.19	0.3361	436268	2.5	4.5978E+05	14060.303	248	173
YL+194	43	16.21	0.19	0.1400	432009	2.5	4.7435E+05	14613.615	269	194
YL+241	43	16.21	0.19	0.2396	438982	2.5	5.5753E+05	17045.882	316	241
Mugla										
MU-125	43	16.21	0.19	1.5396	454153	2.5	1.5000E+05	6302.583	0	-125
MU-90	43	16.21	0.19	1.5939	444850	2.5	1.5637E+05	7140.962	35	-90
MU-60	43	16.21	0.19	1.2996	426641	2.5	1.6775E+05	7708.599	65	-60
MU-40	43	16.21	0.19	1.7064	411172	2.5	1.7776E+05	8170.121	85	-40
MU-20	43	16.21	0.19	1.5423	382990	2.5	2.0475E+05	9298.933	105	-20
MU-0A	43	16.21	0.19	1.2875	454896	2.5	192923.0237	8719.262176	125	0
MU-0B	43	16.21	0.19	1.4220	205374	2.5	190292.7406	8939.143832	125	0
MU+20	43	16.21	0.19	0.8510	382129	2.5	197141.8245	8711.344923	145	20
MU+40	43	16.21	0.19	0.8708	385634	2.5	219540.4203	10287.63649	129	4
MU+60	43	16.21	0.19	1.1318	369134	2.5	213784.0791	9455.275454	185	60
MU+80	43	16.21	0.19	0.8092	446938	2.5	211540.7973	9633.278307	205	80
MU+96	43	16.21	0.19	1.5239	438032	2.5	254986.3923	11181.28319	225	100
MU+123	43	16.21	0.19	0.8281	424821	2.5	272906.5009	12665.65527	248	123
MU+189	43	16.21	0.19	1.1882	443557	2.5	300445.551	13318.02023	314	189
Yatagan										
YA-75	43	16.21	0.19	1.3076	424618	2.5	50294.52482	1983.252199	0	-75
YA-55	43	16.21	0.19	2.2237	426828	2.5	60923.94577	2504.168955	20	-55
YA-30	43	16.21	0.19	1.8197	422756	2.5	61271.59686	2236.538104	45	-30
YA-15	43	16.21	0.19	2.0819	409770	2.5	66011.09326	2522.530897	60	-15
YA-0	43	16.21	0.19	2.5276	341796	2.5	72263.48947	2705.697509	75	0
YA+16	43	16.21	0.19	2.1234	400225	2.5	79240.07787	2876.815484	91	16
YA+40	43	16.21	0.19	4.4764	415981.2604	2.5	84424.52278	3027.98324	115	40
YA+60	43	16.21	0.19	2.4720	416440	2.5	86520.18602	3582.409758	135	60
YA+80	43	16.21	0.19	3.7248	430654	2.5	101110.9388	3780.118473	155	80
YA+100	43	16.21	0.19	5.2077	433819	2.5	113653.2603	4353.512995	175	100
YA+120	43	16.21	0.19	2.2291	424542	2.5	128065.7376	4056.261107	195	120
YA+150	43	16.21	0.19	2.5703	426908.9035	2.5	131167.9541	4303.779571	225	150
YA+378	43	16.21	0.19	2.1660	432575	2.5	228155.4918	8667.369555	453	378
YA+457	43	16.21	0.19	0.9861	403663	2.5	496683.7455	18810.28558	582	457
Mean value	43.00000	16.21	0.19	1.55149	416915					

Figure C18: Data rock file for Turkey sites

AMS Analytical data for YL,MU and YA

Sample ID	Leeds University Code	AMS ID SUERC-	Z [cm]	m sample [g]	m_cl spike[a] [mg]	36Cl/Cl[b] derived from	± 1 sigma 36Cl/35Cl	36Cl/Cl[b] derived from	± 1 sigma 36Cl/37Cl	37Cl/35Cl	Clnat AMS [ppm]	N_Cl36,rock 36Cl [atoms/g]	s36Cl [atoms/g]
YL-75	LU418	c4324	-75	28.8622	1.0692	2.59E-13	7.59E-15	1.49E-12	4.35E-14	0.0490	0.84	2.127E+05	6.49E+03
YL-55	LU419	c4325	-75	29.8504	1.0551	2.87E-13	8.43E-15	1.69E-12	4.97E-14	0.0476	0.53	2.233E+05	6.92E+03
YL-35	LU420	c4326	-35	29.9894	1.0589	3.11E-13	1.11E-14	1.81E-12	6.46E-14	0.0483	0.67	2.425E+05	8.95E+03
YL-16	LU421	c4327	-16	30.1279	1.0512	3.36E-13	9.81E-15	1.93E-12	5.64E-14	0.0489	0.77	2.597E+05	8.03E+03
YL-0	LU422	c4333	0	30.2057	1.0589	3.61E-13	1.03E-14	2.13E-12	4.12E-14	0.0475	0.51	2.782E+05	7.18E+03
YL+45	LU423	c4334	45	30.3647	1.0551	3.97E-13	1.16E-14	2.42E-12	7.08E-14	0.0460	0.22	3.017E+05	9.32E+03
YL+71	LU424	c4335	71	30.0254	1.0557	4.06E-13	1.18E-14	2.42E-12	7.04E-14	0.0472	0.45	3.140E+05	9.66E+03
YL+100	LU425	c4336	100	31.2359	1.0622	4.46E-13	1.30E-14	1.71E-12	5.00E-14	0.0733	5.92	3.744E+05	1.14E+04
YL+132	LU426	c4342	132	30.0308	1.0538	4.99E-13	1.46E-14	3.02E-12	8.79E-14	0.0465	0.31	3.838E+05	1.18E+04
YL+150a	LU427	c4343	150	31.5158	1.0570	5.67E-13		3.40E-12		0.0469	0.37	4.178E+05	4.29E+03
YL+150b	LU428	c4344	150	30.5927	1.0602	5.17E-13	1.51E-14	3.11E-12	9.08E-14	0.0467	0.35	3.933E+05	1.21E+04
YL+173	LU429	c4345	173	30.0993	1.0660	5.92E-13	1.73E-14	3.57E-12	1.04E-13	0.0466	0.34	4.598E+05	1.41E+04
YL+194	LU430	c4346	194	30.5504	1.0557	6.28E-13	1.83E-14	3.87E-12	1.13E-13	0.0456	0.14	4.744E+05	1.46E+04
YL+241	LU431	c4347	241	29.9496	1.0609	7.19E-13	2.09E-14	4.38E-12	1.27E-13	0.0461	0.24	5.575E+05	1.70E+04
MU-125	LU434	c4354	-125	28.8622	1.0318	1.88E-13	3.95E-15	1.02E-12	2.14E-14	0.0517	1.54	1.500E+05	6.30E+03
MU-90	LU435	c4355	-90	29.8504	1.0624	1.96E-13	5.76E-15	1.06E-12	3.11E-14	0.0520	1.59	1.564E+05	7.14E+03
MU-60	LU436	c4356	-60	29.9894	1.0586	2.14E-13	6.25E-15	1.19E-12	3.47E-14	0.0506	1.30	1.678E+05	7.71E+03
MU-40	LU437	c4357	-40	30.1279	1.0535	2.26E-13	6.66E-15	1.21E-12	3.55E-14	0.0527	1.71	1.778E+05	8.17E+03
MU-20	LU438	c4364	-20	30.2057	1.0675	2.59E-13	7.58E-15	1.41E-12	4.11E-14	0.0518	1.54	2.048E+05	9.30E+03
MU-0A	LU439	c4365	0	30.3647	1.0784	2.44E-13	7.16E-15	1.36E-12	3.99E-14	0.0505	1.29	1.929E+05	8.72E+03
MU-0B	LU440	c4366	0	30.0254	1.0324	2.48E-13	7.26E-15	1.36E-12	3.97E-14	0.0514	1.42	1.903E+05	8.94E+03
MU+20	LU441	c4367	20	31.2359	1.1103	2.51E-13	7.37E-15	1.46E-12	4.29E-14	0.0483	0.85	1.971E+05	8.71E+03
MU+40	LU442	c4374	30	30.0308	1.0439	2.86E-13	8.38E-15	1.66E-12	4.85E-14	0.0485	0.87	2.195E+05	1.03E+04
MU+60	LU443	c4375	60	31.5158	1.1040	2.75E-13	8.06E-15	1.55E-12	4.54E-14	0.0498	1.13	2.138E+05	9.46E+03
MU+80	LU444	c4376	80	30.5927	1.0841	2.71E-13	8.07E-15	1.58E-12	4.71E-14	0.0481	0.81	2.115E+05	9.63E+03
MU+96	LU445	c4377	96	30.0993	1.1091	3.09E-13	9.08E-15	1.70E-12	4.97E-14	0.0514	1.52	2.550E+05	1.12E+04
MU+123	LU446	c4378	123	30.5504	1.0567	3.58E-13	1.05E-14	2.08E-12	6.11E-14	0.0483	0.83	2.729E+05	1.27E+04
MU+189	LU447	c4379	189	29.9496	1.1014	3.68E-13	1.08E-14	2.08E-12	6.09E-14	0.0498	1.19	3.004E+05	1.33E+04

[a]Mass of $^{35/37}$Cl spike added to sample prior to dissolution. Spike concentration on next page.
[b]36Cl/Cl is based on either the measured $^{36}Cl/^{35}Cl$ or $^{36}Cl/^{37}Cl$ ratios assuming natural $^{35}Cl/^{37}Cl$ ratios.

Figure C19: ^{36}Cl data from AMS for sites Ya, Yl, and Mu

AMS Analytical data for YL,MU and YA

Sample ID	Leeds	AMS ID	Z	m sample	m_cl spike[a]	36Cl/Cl[b]	± 1 sigma	36Cl/Cl[b]	± 1 sigma	37Cl/35Cl	Clnat AMS	N_Cl36,rock	
	University	SUERC-	[cm]	[g]	[mg]	derived from 36Cl/35Cl		derived from 36Cl/37Cl			[ppm]	36Cl [atoms/g]	s36Cl [atoms/g]
YA-75	LU450	c4389	-75	30.0468	1.0682	6.451E-14	1.995E-15	3.699E-13	1.143E-14	0.0499	0.99	5.036E+04	1.98E+03
YA-55	LU451	c4390	-55	30.2572	1.0976	7.606E-14	2.629E-15	4.232E-13	1.462E-14	0.0514	1.31	6.099E+04	2.50E+03
YA-30	LU452	c4391	-30	30.2750	1.0822	7.608E-14	2.155E-15	3.886E-13	1.100E-14	0.0560	2.22	6.134E+04	2.24E+03
YA-15	LU453	c4392	-15	30.3982	1.0439	8.581E-14	2.473E-15	4.513E-13	1.299E-14	0.0544	1.82	6.610E+04	2.52E+03
YA-0	LU454	c4399	0	30.1050	1.0567	9.150E-14	2.608E-15	4.712E-13	1.341E-14	0.0555	2.08	7.232E+04	2.71E+03
YA+16	LU455	c4400	16	30.4386	1.0841	9.798E-14	2.779E-15	4.873E-13	1.380E-14	0.0575	2.53	7.933E+04	2.88E+03
YA+40	LU456	c4401	40	30.1996	1.0707	1.057E-13	2.859E-15	5.435E-13	1.468E-14	0.0556	2.12	8.449E+04	3.03E+03
YA+60	LU457	c4402	60	30.2700	1.0643	1.039E-13	3.605E-15	4.459E-13	1.546E-14	0.0667	4.48	8.666E+04	3.58E+03
YA+80	LU458	c4407	80	30.2002	1.0880	1.237E-13	3.706E-15	6.196E-13	1.854E-14	0.0571	2.47	1.012E+05	3.78E+03
YA+100	LU459	c4408	100	31.3742	1.0656	1.430E-13	4.403E-15	6.400E-13	1.969E-14	0.0639	3.72	1.138E+05	4.35E+03
YA+120	LU460	c4409	120	30.0232	1.0656	1.501E-13	3.375E-15	6.162E-13	1.383E-14	0.0697	5.21	1.282E+05	4.06E+03
YA+150	LU461	c4410	150	30.0394	1.0567	1.648E-13	3.673E-15	8.392E-13	1.867E-14	0.0562	2.23	1.314E+05	4.30E+03
YA+378	LU462	c4411	378	30.3159	1.0714	2.832E-13	8.547E-15	1.401E-12	4.223E-14	0.0578	2.57	2.284E+05	8.67E+03
YA+457	LU463	c4412	457	30.0519	1.0765	6.130E-13	1.845E-14	3.149E-12	9.467E-14	0.0557	2.17	4.974E+05	1.88E+04
YA-FW1	LU474	c4435		30.111	1.0528	4.28E-13	1.03E-14	1.71E-12	4.11E-14	0.0715	5.43	3.617E+05	9.35E+03
YA-FW2	LU475	c4436		30.364	1.0567	3.69E-13	9.79E-15	1.59E-12	4.22E-14	0.0662	4.20	3.022E+05	8.53E+03
YL-FW1	LU476	c4437		30.211	1.0541	1.28E-12	3.38E-14	6.78E-12	1.79E-13	0.0540	1.65	9.984E+05	2.82E+04
YL-FW2	LU477	c4438		30.2854	1.0567	9.41E-13	1.96E-14	4.57E-12	9.48E-14	0.0589	2.64	7.504E+05	1.71E+04
MU-FW1	LU478	c4439		30.1747	1.0586	1.22E-12	2.93E-14	6.91E-12	1.65E-13	0.0506	0.99	9.461E+05	2.44E+04
MUFW2	LU479	c4440		30.3437	1.0516	7.42E-13	2.61E-14	3.57E-12	1.27E-13	0.0594	2.73	5.887E+05	2.17E+04

[a]Mass of ^{35,37}Cl spike added to sample prior to dissolution. Spike concentration on next page.
[b]36Cl/Cl is based on either the measured ^{36}Cl/^{35}Cl or ^{36}Cl/^{37}Cl ratios assuming natural ^{35}Cl/^{37}Cl ratios.

Figure C20: ^{36}Cl data from AMS for sites Ya, Yl, and Mu cont.

Processed blanks: run alongside each batch of samples to correct for contamination during sample processing

Corresponding Sample Ids[a]	Leeds Uni Code	AMS ID SUERC-	m_cl spike[a] [mg]	36Cl/Cl[b] ± 1 sigma uncertainty derived from 36Cl/35Cl		derived from 36Cl/37Cl		37Cl/35Cl
LU418-LU431	LU432	c4323	1.0538	3.76E-16	1.19E-16	2.37E-15	7.48E-16	0.0448
LU418-LU431	LU433	c4332	1.0454	4.56E-16	1.52E-16	2.86E-15	9.54E-16	0.0449
LU434-LU447	LU448	c4353	1.0893	8.678E-16	2.893E-16	5.543E-15	1.848E-15	0.044
LU434-LU447	LU449	c4363	1.0362	2.223E-16	1.572E-16	1.427E-15	1.009E-15	0.0438
LU450-LU463	LU464	c4388	1.0733	3.588E-16	1.794E-16	2.306E-15	1.153E-15	0.0445
LU450-LU463	LU465	c4398	1.0375	4.958E-16	1.496E-16	3.147E-15	9.493E-16	0.045
LU466-LU479	LU480	c4417	1.0548	1.486E-15	3.607E-16	9.302E-15	2.258E-15	0.0457
LU466-LU479	LU481	c4426	1.0586	1.612E-15	3.164E-16	1.022E-14	2.007E-15	0.0451

(a) Each processed blank corresponds to a batch of samples (listed below) and the 36Cl concentrations are propagated as errors through the calcutation of 36Cl in at/g. from raw AMS data.

Analytical blanks: no processing has been applied, these blanks are used for correcting AMS-specific results

	Leeds Uni Code	AMS ID SUERC-	m_cl spike[a] [mg]	36Cl/Cl[b] ± 1 sigma uncertainty derived from 36Cl/35Cl		derived from 36Cl/37Cl		37Cl/35Cl			
BATCH NO.	27	**Samples associated:**		**LU418-LU431**							
DATE RUN											
NAT											
										37Cl/35Cl	s (37Cl/35Cl)
	c3935-nat	LNAT	5.152E-17	5.152E-17	5.165E-17	5.165E-17	0.2805	0	R_natural	0.3198	0.0000
	c3949-nat	LNAT	5.4339E-16	2.054E-16	5.4438E-16	2.058E-16	0.2808	0			
	c3968-nat	LNAT	4.0328E-16	1.646E-16	3.9937E-16	1.631E-16	0.284	0			
PSB											
										37Cl/35Cl	s (37Cl/35Cl)
	c4352-spike	LPSB	2.47E-16	9.32E-17	1.58E-15	5.99E-16	0.0438	0.0000	R_spike	0.0505	0.0013
	c4362-spike	LPSB	8.53E-17	8.53E-17	5.42E-16	5.42E-16	0.0443	0.0000			
	c4373-spike	LPSB	2.21E-16	1.27E-16	1.43E-15	8.24E-16	0.0435	0.0000			
BATCH NO.	28	**Samples associated:**		**LU434-LU447**							
DATE RUN											
NAT											
										37Cl/35Cl	s (37Cl/35Cl)
	c4340-nat	LNAT	5.15E-17	5.15E-17	5.17E-17	5.17E-17	0.2805	0.0000	R_natural	**0.3198**	**0.0000**
	c4361-nat	LNAT	5.43E-16	2.05E-16	5.44E-16	2.06E-16	0.2808	0.0000			
	c4371-nat	LNAT	4.03E-16	1.65E-16	3.99E-16	1.63E-16	0.2840	0.0000			
PSB											
										37Cl/35Cl	s (37Cl/35Cl)
	c4352-spike	LPSB	2.47E-16	9.32E-17	1.58E-15	5.99E-16	0.0438	0.0000	R_spike	0.0505	0.0013
	c4362-spike	LPSB	8.53E-17	8.53E-17	5.42E-16	5.42E-16	0.0443	0.0000			
	c4373-spike	LPSB	2.21E-16	1.27E-16	1.43E-15	8.24E-16	0.0435	0.0000			

Figure C21: Process and AMS blank measurements

Analytical blanks: no processing has been applied, these blanks are used for correcting AMS-specific results

	Leeds Uni Code	AMS ID SUERC-	m_cl spike[a] [mg]	36Cl/Cl[b] ± 1 sigma uncertainty derived from 36Cl/35Cl		derived from 36Cl/37Cl		37Cl/35Cl			
BATCH NO.	29	Samples associated:		LU450-LU463							
DATE RUN											
NAT										37Cl/35Cl	s (37Cl/35Cl)
	c4396-nat	LNAT	7.93E-16	1.66E-16	7.89E-16	1.65E-16	0.2872	0.0016	R_natural	**0.3198**	**0.0000**
	c4416-nat	LNAT	1.97E-15	3.29E-16	1.98E-15	3.30E-16	0.2853	0.0016			
	c4434-nat	LNAT	1.22E-15	2.79E-16	1.23E-15	2.81E-16	0.2837	0.0000			
PSB										37Cl/35Cl	s (37Cl/35Cl)
	c4386-spike	LPSB	1.25E-15	2.32E-16	7.87E-15	1.46E-15	0.0453	0.0000	R_spike	0.0505	0.0013
	c4406-spike	LPSB	1.60E-15	3.34E-16	1.02E-14	2.13E-15	0.0448	0.0000			
	c4425-spike	LPSB	1.69E-15	3.14E-16	1.07E-14	1.99E-15	0.0451	0.0000			
BATCH NO.	30	Samples associated:		LU466-LU479							
DATE RUN											
NAT										37Cl/35Cl	s (37Cl/35Cl)
	c4396-nat	LNAT	7.93E-16	1.66E-16	7.89E-16	1.65E-16	0.2872	0.0016	R_natural	**0.3198**	**0.0000**
	c4416-nat	LNAT	1.97E-15	3.29E-16	1.98E-15	3.30E-16	0.2853	0.0016			
	c4434-nat	LNAT	1.22E-15	2.79E-16	1.23E-15	2.81E-16	0.2837	0.0000			
PSB										37Cl/35Cl	s (37Cl/35Cl)
	c4386-spike	LPSB	1.25E-15	2.32E-16	7.87E-15	1.46E-15	0.0453	0.0000	R_spike	0.0505	0.0013
	c4406-spike	LPSB	1.60E-15	3.34E-16	1.02E-14	2.13E-15	0.0448	0.0000			
	c4425-spike	LPSB	1.69E-15	3.14E-16	1.07E-14	1.99E-15	0.0451	0.0000			

Figure C22: Process and AMS blank measurements cont.

Site parameters

Site ID	Elevation (m)	Latitude (°N)	Longitude (°E)	α	β	γ	Scarp Height[1] (cm)	Trench Depth (cm)	HW density (g/cm^3)	Production rate[2]
LIRI	867	41.97532	13.3661	7	78	36	790	80	1.5	48.8
CF1	1674	42.233597	13.437885	32	51	35	1560	120	1.5	48.8
CF2	1603	42.22777	13.445166	33	54	33	2440	150	1.5	48.8
CF3	1667	42.234344	13.436509	27	57	36	1230	60	1.5	48.8
RP1	839	42.192420°	13.71068	30	49	31	720	120	1.5	48.8
RP2	923	42.206124	13.686017	27	66	27	470	80	1.5	48.8

(1) Calculated in the plane of the fault

(2) Spallation production rate from ^{40}Ca used in modelling (Stone et al., 1996). Other spallation production rates (K, Ti, Fe) and slow muon stopping rates are the same as in Schlagenhauf et al., 2001.

Figure C23: Site parameters used for modelling ^{36}Cl fault scarp data.